## Faculdade de Engenharia da Universidade do Porto



# The effect of heat treatment on the mechanical and metallurgical characteristics of aluminium-steel joints used in transportation industries

Tiago Oliveira Gonçalves Teixeira

Master's in Mechanical Engineering

Supervisor: Reza Beygi (INEGI) Co-supervisors: Eduardo A. S. Marques (FEUP) Lucas F. M. da Silva (FEUP)

March, 2024

© Tiago O. G. Teixeira, 2024

# The effect of heat treatment on the mechanical and metallurgical characteristics of aluminium-steel joints used in transportation industries

Tiago Oliveira Gonçalves Teixeira

Dissertation for the Degree of Master in Mechanical Engineering

### Resumo

Para reduzir o peso dos veículos e consequentemente melhorar a eficiência energética, é cada vez mais comum encontrar processos de ligação de materiais dissimilar na indústria automóvel. Esta mudança é também motivada pelo complexo processo de fabrico e pela limitada capacidade de reciclagem das estruturas leves, o que resulta numa redução das emissões e da pegada de carbono.

A junção de metais dissimilares surge como uma estratégia convincente para obter estruturas leves e robustas. No entanto, o uso deste processo pode trazer dificuldades devido à formação de compostos intermetálicos frágeis (IMCs) na interface de juntas dissimilares. Estes IMCs afetam significativamente a resistência da junta sob carga, resultando frequentemente em falhas frágeis. Os tratamentos térmicos apresentam uma solução viável para modificar a espessura e a natureza dos IMCs, alterando assim as propriedades da junta. Este estudo apresenta um projeto simples para unir uma chapa de aço fina (2 mm de espessura) a uma chapa de alumínio (5 mm de espessura) numa configuração de topo, resultando numa interface Al/St em forma de S devido ao desvio da ferramenta FSW para o aço.

Este estudo teve como objetivo investigar o impacto de vários tratamentos térmicos em juntas de aço e alumínio fabricadas por soldadura por fricção (FSW). Foi efetuada uma análise exaustiva de uma série de amostras de aço-carbono St37/alumínio Al1050. Esta análise inclui o exame da microestrutura da interface da junta soldada utilizando Microscopia Eletrónica de Varrimento (SEM) e Espectroscopia Dispersiva de Eletrões (EDS) para análise da composição química e medições da espessura da camada IMC, e as propriedades mecânicas serão avaliadas através de ensaios de tração, enquanto o comportamento de fratura durante o carregamento será examinado através da análise das superfícies de fratura e da distribuição da dureza ao longo da junta. Por fim, foi utilizado um modelo numérico, usando um modelo inverso de contacto coesivo, para simular o carregamento da junta, utilizando as propriedades da camada de IMC da literatura e estudadas.

O principal objetivo do estudo foi determinar sistematicamente a temperatura e a duração ótimas para obter as melhores propriedades mecânicas, controlando simultaneamente a formação de IMC na interface da junta, anteriormente nunca estudada. A cinética do crescimento do IMC foi investigada, correlacionando a temperatura e o tempo com a espessura da camada de IMC e a resistência da junta.

Este estudo revelou um aumento da espessura da camada de IMC ao longo dos tratamentos térmicos, particularmente notável com temperaturas mais elevadas e maior duração, em particular o período de recozimento de 90 minutos, que influenciou significativamente a integridade da junta.



## **Abstract**

The automotive industry is adopting dissimilar welding techniques, particularly for light alloys, to reduce vehicle weight and improve fuel efficiency. This shift is driven by the intricate manufacturing process and limited recyclability of lightweight structures, resulting in reduced emissions and a reduced carbon footprint.

Joining dissimilar metals, such as aluminium and steel, emerges as a compelling strategy to achieve lightweight yet robust structures. However, challenges arise from the formation of brittle intermetallic compounds (IMCs) at the interface of dissimilar joints. These IMCs significantly impact joint strength under load, often resulting in brittle failure. Heat treatments present a viable solution in modifying the thickness and nature of IMCs, thereby altering the joint properties. This study introduces a straightforward design to join a thin steel sheet (2 mm thickness) to an aluminium sheet (5 mm thickness) in a butt configuration, resulting in an S-shaped Al/St interface due to the offset of the FSW tool into the steel.

This study aimed to investigate the impact of various heat treatments on Steel and Aluminium joints fabricated via Friction Stir Welding (FSW). A comprehensive analysis was conducted on a series of St37 carbon steel/ Al1050 aluminium specimens. This analysis included the examination of the microstructure of the welded joint interface using Scanning Electron Microscopy (SEM) and Electron-dispersive Spectroscopy (EDS) for chemical composition analysis and IMC layer thickness measurements, and mechanical properties were evaluated through tensile testing, while fracture behaviour during loading will be examined by analysing fracture surfaces and hardness distribution across the joint. At last, a numerical model, using a reverse cohesive contact model, was employed to simulate joint loading, using the IMC layer properties studied.

The primary objective of the study was to determine systematically the optimal temperature and duration for achieving the best mechanical properties while controlling IMC formation at the joint interface, previously unexamined. The kinetics of IMC growth will be investigated, correlating temperature and time with IMC layer thickness and joint strength.

This study revealed an increase in IMC layer thickness along the heat treatments, particularly notable with higher temperatures and longer duration, in particular the 90-minute annealing period, which significantly influenced joint integrity.



## Acknowledgements

I would like to express my gratitude to Prof. Reza Beygi, supervisor (INEGI), for his invaluable guidance and support throughout my thesis journey. Despite not being able to be present in Portugal during this period, his unwavering assistance, helpfulness, and availability were truly remarkable. His expertise and encouragement have been instrumental in shaping the direction of my research.

I am also deeply thankful to co-supervisor Prof. Eduardo Marques (FEUP) for his support and dedicated involvement in the progress of my work. His guidance and presence during the experimental work have been invaluable, contributing significantly to the success of this thesis.

Furthermore, I would like to extend my appreciation to AJPU for providing me with the opportunity to embark on this academic journey and for their continuous support and encouragement throughout the process.

Also, I would like to thank my family and all my dearest friends for the unconditional support, not only throughout my Master's thesis, but also along all the academic years spent together as a second family to me.

Tiago O. G. Teixeira

"Sempre chega a hora em que descobrimos que sabíamos muito mais do que antes julgávamos." José Saramago

## Table of contents

Chapter 1 Introduction	
1.1 - Motivation and background	
1.2 - Objectives	
1.3 - Research methodology	
1.4 - Thesis overview	
Chapter 2 Literature review	
2.1 - Aluminium-steel joints	
2.1.1 - Fusion and low dilution welding of Al-steel joints	
2.1.2 - Solid-state welding of aluminium-steel joints	
2.2 - Friction Stir Welding	
2.2.1.1 - Tool specifications	
2.2.1.2 - Welding parameters	
2.2.1.3 - Joint configurations and machine options	
2.2.1.4 - Weld zones	
2.2.1.5 - Material flow	
2.2.1.6 - Defects and challenges	22
2.2.2 - FSW of aluminium-steel joints	
2.3 - Intermetallic Compounds in FSW	
2.3.1 - Iron Aluminides IMCs	
Chapter 3 Experimental work	
3.1 - Experimental details	
3.1.1 - Joint manufacturing	
3.1.2 - Heat treatment	
3.1.3.1 - SEM/EDS interface analysis	
3.1.3.2 - Tensile Testing	
3.1.3.3 - Fractography	
3.1.3.4 - Microhardness analysis	
3.2 - Experimental results	
3.2.1 - IMC layer thickness	
3.2.2 - Interface microstructure	
3.2.3 - Load vs. Extension results	
3.2.4 - Fractography results	
Chapter 4 Numerical model	
4.1 - Introduction	
4.2 - Properties	
4.4 - Results	
Chapter 5 Conclusion and future work	93
References	95
Appendices	
A Paper	
B Load vs extension curves	123
C Tensile tests video frames	. 127
D Microhardness plots	. 129

# List of figures

Figure 2.1 -Commonly implemented techniques of welding for dissimilar welds diagram [10]3
Figure 2.2 - Schematic representation of GTAW process [18]
Figure 2.3 - Schematic representation of GMAW process [19]6
Figure 2.4 - Weld cross-section, representing a base metal and a weld bead, where (A) is indicative the weight of the filler material, and (B) and (C) of the weight of the base metals, at the weld bead [24]. (edited)
Figure 2.5 - Heat-affected zone schematic for Fusion and Low Dilution Welding processes
Figure 2.6 - Schematic representation of a current-time diagram [19]. (edited)
Figure 2.7 - Roll Bonding process representation [42]. (edited)10
Figure 2.8 - Explosion Welding detonation and joining procedure representation [46]. (edited)11
Figure 2.9 - Explosion Welding wave interface, resultant of the process [47]11
Figure 2.10 - Impact welding window based on impact velocity and angle along with various types of interfaces formed depending on the conditions [49]
Figure 2.11 - Rotary Friction welding (a) [52] and Linear Friction Welding (b) [53] representations. (edited)
Figure 2.12 - Schematic representation of three stages of FSW: Plunge (1) and Dwell (2), Traverse welding (3), and Retracting (4); tool pin (A) and shoulder (B) [57]. (edited)14
Figure 2.13 - Schematic of the FSW process and main parameters and weld zone [59]. (edited)15
Figure 2.14 - Example of a FSW keyhole, caused by the retracting tool at the end of the weld process [62]
Figure 2.15 - Tool's shoulder designs and features [64]17
Figure 2.16 - Tool's pin designs [64]
Figure 2.17 - Representation of tool dimensions translated as FSW parameters [66]18
Figure 2.18 - Main joint configurations possible to obtain in FSW [71]. (edited)19
Figure 2.19 - Representation of the FSW weld zones [59]. (Edited)
Figure 2.20 - Metal flow patterns (a) and metallurgical processing zones developed during friction stir welding (b) [55]
Figure 2.21 - Plane view of friction stir welded, studied by Liu et al. [75] (a) and material flow pattern around the probe during steady state FSW (b) [76]. (edited)22
Figure 2.22 - Example of tunnel defect in a FSW weld [77]22
Figure 2.23 - Flash defect in the surface of friction stir weld [78]
Figure 2.24 - Examples of void defect (A), and cavity (B)23
Figure 2.25 - Kissing bond examples in an Al alloy weld [79]. (edited)24
Figure 2.26 - Example of root defect due to lack of pin penetration24
Figure 2.27 - Representation of an Intermetallic crystal structure and a Alloy crystal structure [90]
Figure 2.28 - Calculated bulk modulus versus shear modulus (B/G) ratios of Al-Fe IMCs [91]27
Figure 2.29 - Periodic table regarding the electronegativity of the atomic elements28
Figure 2.30 - Iron-Aluminium phase diagram
Figure 2.31 - Theoretical model showing mechanism of Al-Fe IMC formation during FSW [95]31

Figure 3.1 - Experimental workflow diagram.	34
Figure 3.2 - Schematic representation of the FSW mount apparatus used to manufacture the Al-St joints.	34
Figure 3.3 - Schematic representation detail of the tool's shoulder and pin, with the respective dimensions.	35
Figure 3.4 - Top view schematic representation of the joint substrate plates after welding, with the WEDM cut specimens, represented in red	36
Figure 3.5 - Section of a manufactured joint, showing the S-shape interface.	36
Figure 3.6 - Schematic matrix of the heat treatment pairs	37
Figure 3.7 - Specimens and sample configuration (a) with a thermocouple attached one of the specimens at the interface of the joint (b). Close-up of the thermocouple tip located at the joint (c).	38
Figure 3.8 - Preparation for heat treatment, with the aluminium foil wrap (a) and steel plate (b). In (c) we have the thermometer used in the preparation.	39
Figure 3.9 - Images of the oven used in the heat treatments (a), oven temperature display (b), and thermocouple thermometer (c)	40
Figure 3.10 - Example of the specimens used for tensile testing and fractography (a), and sample for microstructure analysis and hardness measurements (b)	40
Figure 3.11 - Sample preparation for the as-welded Al/St joint (a) and joint interface - SEM image in BSE mode of the joint, at 35x magnification (b)	42
Figure 3.12 - Heat treated sample preparations for the second SEM/EDS session, (a) sample preparation photography and (b) schematic representation and identification	42
Figure 3.13 - Tensile test setup.	44
Figure 3.14 - Tensile test clamps (a) and detail of a specimen mounted in the tensile machine clamping system (b)	44
Figure 3.15 - Schematic representation of the microhardness lines measurements U, M and B, for the as-welded sample <b>00</b>	46
Figure 3.16 - Average IMC thickness of the U, M2 and L zones for the measured as-welded and heat treated samples, and linear regressions	47
Figure 3.17 - SEM images in BSE mode of the joint interfaces, taken from the Zones M1 (a), M2 (b), M3 (c), U (d), L (e) and B (f), at 10 000x magnification.	49
Figure 3.18 - Line-scan EDS analysis taken across the IMC layer of the zones U (a), M1 (b), M2 scan line 1 (c) and scan line 2 (d), and SEM images, 30 000x magnification, of the irregular microstructures of zone M3 (e), zone L (f) and zone B (g)	50
Figure 3.19 - Sample II (100 °C / 60 min) SEM images in BSE mode of the joint interfaces, taken from the zone U (b) and (c); zone M2 (d), (e) and (h); and zone L (f) and (g)	51
Figure 3.20 - Sample III (100 °C / 90 min) SEM images in BSE mode of the joint interfaces, taken from the zone U (c) and (d); zone M2 (e) and (f); and zone L (g) and (h). Line-scan EDS analysis taken across the IMC layer of the zone M2 (b)	52
Figure 3.21 - Sample IV (250 °C / 30 min) SEM images in BSE mode of the joint interfaces, taken from the zone U (c) and (d); zone M2 (e) and (f); and zone L (g) and (h). Line-scan EDS analysis taken across the IMC layer of the zone M2 (b)	53
Figure 3.22 - Sample VI (250 °C / 90 min) SEM images in BSE mode of the joint interfaces, taken from the zone U (c) and (d); zone M2 (e) and (f); and zone L (g) and (h). Line-scan EDS analysis taken across the IMC layer of the zone M2 (b)	54
Figure 3.23 - Sample VIII (400 °C / 60 min) SEM images in BSE mode of the joint interfaces, taken from the zone U (c) and (d); zone M2 (e) and (f); and zone L (g) and (h). Line-scan EDS analysis taken across the IMC layer of the zone M2 (b).	55

Figure 3.24 - SEM images in BSE mode of the joint interfaces of samples V (250 °C / 60 min) (a), VII (400 °C / 30 min) (b), and IX (400 °C / 90 min) (c), and details of the zone M2 (d), (e) and (f), respectively
Figure 3.25 - Line-scan EDS analysis taken across the IMC layer of the zone M2 of the samples <b>V</b> (a), <b>VII</b> (b), and <b>IX</b> (c)
Figure 3.26 - Load vs. Extension curve of the 100 $^\circ$ C / 30 min heat treatment specimens58
Figure 3.27 - Failure instants video frames of the specimen I • • tensile test59
Figure 3.30 - Failure instants video frames of the specimen II • tensile test60
Figure 3.31 - Failure instants video frames of the specimen II • • tensile test61
Figure 3.32 - Specimen II • • • tensile test video frame before the secondary failure instance, at the top zone of the joint61
Figure 3.34 - Specimens III • • and III • • • tensile test video frames before loading (a) and (e), at main failure zone (b) and (f), and at the yielding of the Al1050 tips of the joint interface (c) and (g), respectively
Figure 3.36 - Failure instants video frames of the specimen IV • tensile test64
Figure 3.37 - Localized yielding after main failure at the middle zone of the joints IV • • (a) and IV • • • (b)65
Figure 3.39 - Failure instants video frames of the specimen V $ullet$ tensile test66
Figure 3.42 - Failure instants video frames of the specimen VI • • • tensile test67
Figure 3.47 - Before and after failure instants video frames of the specimen VIII • • • tensile test
Figure 3.49 - Failure instants video frames of the specimen IX • • • tensile test69
Figure 3.50 - Average max loads of each heat treatment pair and as-welded specimens (blue), and trendline (dotted black)70
Figure 3.51 - Average max. loads by temperature, grouped by heat treatment duration70
Figure 3.52 - Schematic representation of the applied forces in the bottom (a), middle (b) and top (c) zones of the joint interface. The IMC layer is represented in yellow71
Figure 3.53 - Plotted average main failure loads and IMC layer thickness at the middle zone, with respective trendlines72
Figure 3.54 - Images after tensile test of the III • • (100 °C / 90 min) (a), VI • (250 °C / 90 min) (b), and IX • (400 °C / 90 min) (c) specimens73
Figure 3.55 - SEM imaging, in secondary mode, of the III, VI and IX specimens' fracture surfaces, at 35x magnification
Figure 3.56 - SEM imaging, in backscattering mode, and EDS zone analysis of specimen III (100 °C / 90 min) steel side75
Figure 3.57 - SEM imaging, in backscattering mode, and EDS zone analysis of specimen III (100 °C / 90 min) aluminium side76
Figure 3.58 - SEM imaging, in backscattering mode, and EDS zone analysis of specimen <b>IX</b> (400 °C / 90 min) steel side77
Figure 3.59 - SEM imaging, in backscattering mode, and EDS zone analysis of specimen <b>IX</b> (400 °C / 90 min) aluminium side78
Figure 3.60 - SEM images, in secondary mode, of two sections of the top zone of the IX sample,  Al side, (a) at 200x magnification and (b) at 2000x magnification
Figure 3.61 - SEM images, in secondary mode, at the bottom zone of the Al side of sample IX,  100x magnification

Figure 3.62 - SEM imaging, in backscattering mode and 35x magnification of specimen VI (250 °C / 90 min) steel side (a) and aluminium side (b) fracture surfaces	
Figure 3.63 - Optical image of the as-welded sample interface, 10x magnification, during the Vicker's microhardness measurements. Noting three indentations: one at the St side and two at the Al side	80
Figure 3.64 - Vickers microhardness of the as-welded sample along the upper, middle, and bottom measured lines	82
Figure 3.65 - Vickers microhardness of the middle zones of the measured samples	86
Figure 4.1 - Joint geometry used in the numerical model, in Abaqus CAE / Explicit	88
Figure 4.2 - Bilineal traction-separation law diagram	89
Figure 4.3 - Model boundary conditions (a), and variable meshing of the part (b)	89
Figure 4.4 - Cohesive surface damage initiation (CSMAXSCRT) results, at the Al1050 substrate interface, of the tensile test simulation.	90
Figure 4.5 - Plastic strain equivalent (PEEQ) results of the tensile test simulation	91
Figure 4.6 - Cohesive damage (CSDMG) results for the joint interface. View cut of the last simulation frame	91

## List of tables

Table 2.1 - FSW advantages [34]	15
Table 2.2 - Defects and challenges of FSW	25
Table 2.3 - Reactions in the Fe-Al binary system	29
Table 2.4 - Effective activation energy Q of the commonly formed phases in FSW of Al-Fe	32
Table 3.1 - Mechanical properties and chemical compositions of St37 carbon steel and 1050 Aluminium	34
Table 3.2 - FSW parameters and tool specifications	35
Table 3.3 - Imaging magnification used in each zone of the sample	43
Table 3.4 - Max. Load and Extension at Max. Load of the specimen I • (100 °C / 30 min)	58
Table 3.5 - Max. Load and Extension at Max. Load of the specimen I $\bullet$ $\bullet$ (100 $^{\circ}$ C / 30 min)	58
Table 3.6 - Max. Load and Extension at Max. Load of the specimen I $\bullet$ $\bullet$ • (100 $^{\circ}$ C / 30 min)	59
Table 3.7 - Max. Load and Extension at Max. Load of the specimen II • (100 °C / 60 min)	60
Table 3.8 - Max. Load and Extension at Max. Load of the specimen II • • (100 °C / 60 min)	60
Table 3.9 - Max. Load and Extension at Max. Load of the specimen II • • • (100 °C / 60 min)	61
Table 3.10 - Max. Load and Extension at Max. Load of the specimen III • (100 °C / 90 min)	62
Table 3.11 - Max. Load and Extension at Max. Load of the specimen III • • and III • • • (100 °C / 90 min).	62
Table 3.12 - Max. Load and Extension at Max. Load of the 250 °C / 30 min heat treatment specimens	63
Table 3.13 - Max. Load and Extension at Max. Load of the 250 °C / 60 min heat treatment specimens	65
Table 3.14 - Max. Load and Extension at Max. Load of the 250 °C / 90 min heat treatment specimens	66
Table 3.15 - Max. Load and Extension at Max. Load of the 400 °C / 30 min heat treatment specimens	67
Table 3.16 - Max. Load and Extension at Max. Load of the 400 °C / 60 min heat treatment specimens.	
Table 3.17 - Max. Load and Extension at Max. Load of the 400 °C / 90 min heat treatment specimens.	69
Table 3.18 - Upper zone Vickers' microhardness values for the as-welded sample <b>00</b>	81
Table 3.19 - Middle zone Vickers' microhardness values for the as-welded sample <b>00</b>	81
Table 3.20 -Bottom zone Vickers' microhardness values for the as-welded sample <b>00</b>	82
Table 3.21 -Upper zone Vickers' microhardness values for the sample III (100 °C / 90 min)	83
Table 3.22 - Middle zone Vickers' microhardness values for the sample III (100 °C / 90 min)	83
Table 3.23 - Bottom zone Vickers' microhardness values for the sample III (100 $^{\circ}$ C / 90 min)	83
Table 3.24 - Upper zone Vickers' microhardness values for the sample <b>VI</b> (250 $^{\circ}$ C / 90 min)	84
Table 3.25 - Middle zone Vickers' microhardness values for the sample VI (250 °C / 90 min)	84
Table 3.26 - Bottom zone Vickers' microhardness values for the sample VI (250 °C / 90 min)	84
Table 3.27 - Middle zone Vickers' microhardness values for the sample IX (400 °C / 90 min)	85

Table 4.1 - Basic material properties inputted in numerical model for the substrates.	88

## **Acronyms and Symbols**

#### **Acronyms**

Al Aluminium
AS Advancing Side

Au Gold

At. % Atomic Percentage

BCC Body Centered Cubics

C Carbon

CFRP Carbon Fiber Reinforced Polymers

Cu Copper

CZM Cohesive-zone Model

DOF Degrees of Freedom

EBW Electron Beam Welding

EDS Energy-dispersive Spectroscopy

FCC Face Centered Cubics

Fe Iron

FSW Friction Stir Welding

FSSW Friction Stir Spot Welding
GMAW Gas Metal Arc Welding
GTAW Gas Tungsten Arc Welding

HAZ Heat Affect Zone

HCP Hexagonal Close Packing

HV Vicker's Hardness

IMC Intermetallic Compound
LBW Laser Beam Welding

MAG Metal Active Gas
MIG Metal Inert Gas

Mg Magnesium
Mn Manganese
P Phosphorus

RPM Rotations Per Minute RS Retreating Side

S Sulphur

SAW Submerged Arc Welding

SEM Scanning Electron Microscope

Si Silicon

SMAG Shielded Metal Arc Welding

SSW Solid State Welding

Ti Titanium

TIG Tungsten Inert Gas

TMAZ Thermo-Mechanically Affected Zone
WEDM Wire Electrical Discharge Machining

Zn Zinc

#### **Symbols**

 $\beta$  Dynamic collision angle

*E<sub>IMC</sub>* IMC stiffness

e IMC layer thickness

 $F_n$  Axial force

F<sub>x</sub> Transverse force

F<sub>y</sub> Side force

Gc Fracture energy  $k_{eff}$  Initial stiffness

M Torque
m Metres
mm Millimetres

MPa Megapascal R Gas constant

s Seconds

*T* Temperature

*T<sub>ult</sub>* Cohesive strength

t Time

 $\begin{array}{ll} \theta & & Tool \ tilt \ angle \\ \mu m & & Micrometres \end{array}$ 

 $V_c$  Collision velocity  $V_p$  Impact velocity

 $V_x$  Tool traverse speed

Q Effective activation energy

 $\omega$  Tool rotation speed

## Chapter 1

## Introduction

The main subject of this dissertation is introduced in this chapter, which includes some background on the motivation, the objectives, the methodology used, and the structure of the present work.

### 1.1 - Motivation and background

The automotive sector is experiencing an increase in the use of dissimilar welding of materials, notably light alloys to the detriment of Carbon Fiber Reinforced Plastics (CFRP), due to their complex and expensive manufacturing and low recyclability [1]. Reducing the weight of the vehicles being produced assumes a pivotal importance in today's global context, correlating with decreased fuel or electrical energy consumption, thereby resulting in reductions in emissions and a diminished carbon footprint [2].

Joining dissimilar metals is a compelling approach to achieve lightweight structures that are strong and durable. When joining dissimilar metals, a brittle intermetallic compound at the interface is formed. These dissimilar joints have particular characteristics, having a significant impact on joint strength when loaded, failing brittlely [3]. The application of heat treatments in dissimilar metal welds can change the thickness and type of these intermetallic compounds (IMC), enhancing the properties obtained in these joints.

## 1.2 - Objectives

This work has the intended objective of studying the effect of a group of heat treatments in Steel and Aluminium joints by Friction Stir Welding (FSW).

A number of specimens manufactured of Carbon Steel/Pure Aluminium will be studied through the analysis of the microstructure of the interface of the welded joint tensile, with the assistance of Scanning Electron Microscopy (SEM) imaging and Electron-dispersive Spectroscopy (EDS) chemical composition acquisition analysis, the study of the mechanical properties of welded specimens with the assistance of tensile testing, with study of the fracture behaviour during this loading being carried out by examining the fracture surface and hardness distribution throughout the joint.

The optimal temperature and duration of the treatment will be determined in this investigation in order to evaluate the best mechanical properties, with control of the intermetallic compound at the interface of the joint. The kinetics of IMC growth will be determined, correlating the temperature and time with the final IMC layer thickness and joint strength.

#### 1.3 - Research methodology

To achieve the intend objectives set for the thesis, a methodology was carried out following the steps presented below:

- A comprehensive literature study, focused on the dissimilar aluminium-steel solid state welds, more
  precisely by FSW, its technological challenges, and the consequential inherent formation of the IMC
  layer at the interface of the two base metals, was carried out.
- Through past research work on the area of solid-state welding (SSW) of Al-steel and heat treatments
  applied in these joints, a set of temperatures and times was chosen to for treatment of the FSW
  joints manufactured in the context of this thesis, and a study their impact on the formation of IMC
  and the strength of the joint.
- A set of experimental work comprised of tensile tests, with the intention of obtaining results on the
  strength of the heat-treated joints and Scanning Electron Microscope (SEM) analysis of the IMC at
  the interface of the base metals, before and after the heat treatments, in order to correlate the grow
  of the IMC layer with the annealing temperatures and times, as well as the study of the fracture
  behaviour of the joint.
- Numerical modelling of the experimental work, through the use of a reverse cohesive contact model
  to simulate the joint interface of IMC layer with the steel surface, with the implementation of the
  experimental results to interactively obtain a simulation model as similar as the experimental results.

#### 1.4 - Thesis overview

The thesis follows a five chapter structure, as follows:

**Chapter 1:** The introduction of the dissertation, presenting the research topic and providing a comprehensive overview of the significance of dissimilar welding techniques in the automotive sector. The chapter also outlines the research objectives, aims, and the methodology employed to address the research questions.

Chapter 2: A review of legacy and novel welding technologies capable of producing dissimilar metal joint, discussing the challenges and the mechanisms of IMC formation associated with the technologies, with special attention to FSW. The chapter synthesizes key findings and identifies gaps in the current literature, paving the way for the experimental and numerical investigations conducted in subsequent chapters.

**Chapter 3:** This chapter details the experimental procedures conducted to investigate the effect of heat treatments on Steel and Aluminium joints fabricated via Friction Stir Welding (FSW). It describes the sample preparation, welding parameters, and heat treatment employed in the study. The chapter also discusses the analytical techniques used for microstructure examination, chemical composition analysis, mechanical testing, and fracture behaviour analysis. The results obtained from the experimental work are presented and analysed in detail.

**Chapter 4:** In this chapter, the dissertation discusses the development and implementation of a

numerical model using a reverse cohesive contact model to simulate the interface between intermetallic compounds (IMCs) and the Steel surface. The chapter outlines the theoretical framework, assumptions, and mathematical formulations underlying the numerical model. It describes the validation process and discusses the insights gained from numerical simulations. The chapter also explores the correlation between experimental findings and numerical predictions, providing a comprehensive understanding of IMC growth kinetics and its impact on joint properties.

**Chapter 5:** The final chapter presents the conclusions drawn from the research findings and discusses their implications for the automotive industry. It summarizes the key findings and contributions of the study, highlighting the significance of dissimilar welding techniques in achieving lightweight yet robust structures. The chapter also reflects on the limitations of the study and suggests avenues for future research. Overall, it underscores the importance of interdisciplinary approaches in addressing complex engineering challenges and driving innovation in the automotive sector.

## Chapter 2

## Literature review

### 2.1 - Aluminium-steel joints

In today's global context, a continuous increase in environmental concerns has been observed, accompanied by the reinforcement of increasingly restrictive regulations in this regard, leading the automotive sector and many other globalized industries to prioritize the development of sustainable technologies, materials and designs [4]. The demand for lighter materials and design solutions is not a novel topic in the automotive industry, with a growing use of CFRP and other lightweight composite materials, with the aim of enhancing a vehicle's performance, obtaining better vehicle dynamics, and reducing the energy consumption, being the rather a current focus [5, 6].

However, CFRP represents a challenge regarding the complex and limited recyclability - the presence of dissimilar multilayered and thermoset materials - and the high manufacturing costs of CFRP parts [1, 7], leading the automotive industry to research technological sustainable solutions, which implement lightweight and recyclable materials, such as lower specific weight metals and dissimilar metal joints, and Aluminium and Steel designs consequently[4], as in the context of this thesis. Moreover, safety standards mandate that the cabin around the passenger cannot collapse upon the occupants, the appropriate material for the passenger compartment, commonly known as the "safety cage," is predominantly hot-stamped high-strength martensitic steel. However, the regions surrounding this cage from the front and back require a significant amount of energy absorption in either of these structures, in case of frontal or back impacts. Also, in some areas, stiffness is also important for avoiding handling and ride quality problems. Aluminium alloys with moderate to high strengths are a great choice because of these attributes: strong energy absorption, low density, high strength, and high stiffness [8], raising the question of how to join the two metals in an efficient way that doesn't compromise engineering requirements.

Efforts are being made in order to combine the desirable properties of Aluminium and Steel in the design of structures for the automotive industries, in order to obtain lightweight bodies due to the increasing demands in a sustainability point of view as a result of lower power consumption, without compromising structural integrity offered by Steel at the price point that this metal is implemented in the industry [9].

Although the idea of joining dissimilar metals, such as Aluminium and Steel, represents a good approach for the concerns mentioned, the real-life implementation of the concept faces some engineering problems. To start, the feasibility of combining these dissimilar metals by conventional fusion welding

processes is low, where we encounter incompatibilities, such as the distinct melting points of the metals, thermal expansion coefficients and thermal conductivity values, leading to vastly different thermal cycles for the Steel and Aluminium, which adds to the insolubility problem found when combining these metals, where the formation of hard and brittle intermetallic compounds (IMCs) occurs in the interface of the welds. Furthermore, there is also the possibility of facing galvanic corrosion, resulting in less than desirable joint properties for structural designs [9].

Alternatives to fusion welding of distinct metals can be found in forms of Low Dilution Welding and Solid-state Welding, also known as Non-fusion Welding. Furthermore, other joining techniques commonly implemented include fastening, riveting and adhesive bonding, where the impact of thermal and electrochemical dissimilarities are less severe. In this sub-chapter, we'll discuss in more depth fusion and Solid-state Welding processes for Aluminium and Steel joints.

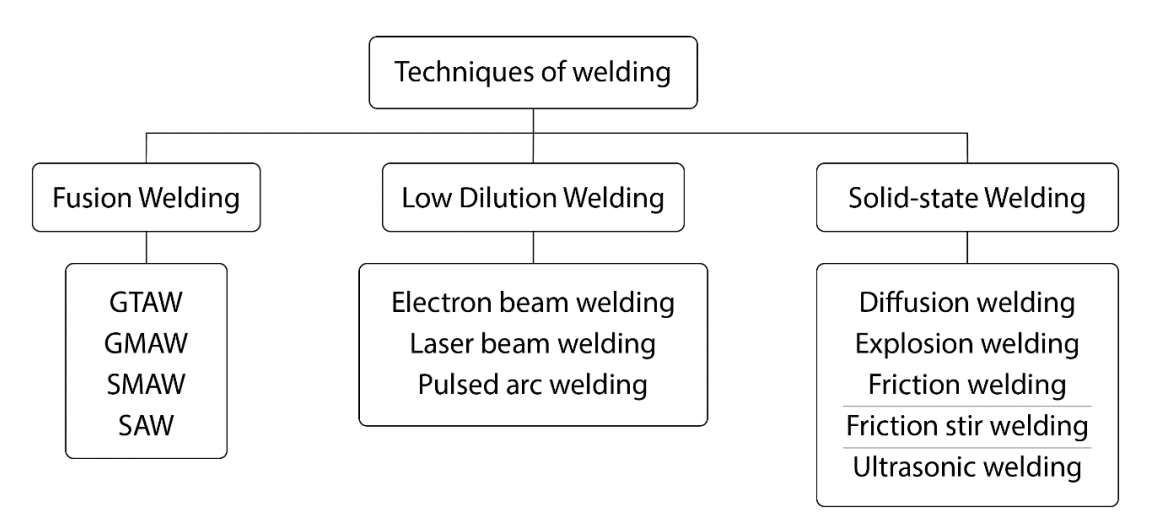


Figure 2.1 –Commonly implemented techniques of welding for dissimilar welds diagram [10]

### 2.1.1 - Fusion and low dilution welding of Al-steel joints

Welding is a manufacturing process characterized by the joining of two or more materials, usually metals or thermoplastics, using a combination of heat, pressure, or both, in order to obtain a permanent coalescence [11]. Fusion welding is achieved by heating the material, and a filler material in the cases that those are used, until the melting point is reached, and a joint is formed as the materials cool.

Fusion welding processes can be categorized by the heating source and protective gas used. The major fusion welding techniques are Gas Tungsten Arc Welding (GTAW), Gas Metal Arc Welding (GMAW), Shielded Metal Arc Welding (SMAW), Submerged Arc Welding (SAW), following ASME designations (also known as Tungsten Inert Gas (TIG), Metal Inert Gas/Metal Active Gas (MIG/MAG) and Flux Shielded Welding, respectively), and their applications can be material and design oriented, having a set of particular advantages and disadvantages. Resistance Welding can also be classified as a fusion welding technique, taking in account that at the interface of the two base metals to be welded, a pool of fused metal forms, and a nugget is created after it cools.

Typically, the process is conducted in materials with the similar characteristics to ensure that the properties obtained in the weld are consistent with those of the base metal, taking in account that high dissimilarities in the base and filler materials, such as those referenced before, can have a negative

impact in the joints and cause a wide range of defects [12].

#### **GTAW**

One of the most commonly implemented welding method is Gas Tungsten Arc Welding due to the high controllability and precision capable to be achieved, and the versability of welding configurations and base metals used, allowing high quality joints and seams. The process is particularly suitable for applications where a high level of control and precision is necessary, such as in the automotive and aerospace industries [13]. The TIG process can be used to weld a wide variety of materials and it is particularly suitable for welding highly reactive materials with which defect-free welds can be obtained.

It involves joining metals using a non-consumable tungsten electrode while protecting the welding area with an inert gas. The welding parameters for TIG welding include metal gauge, joint type, tungsten size, filler rod size, cup size, shield inert gas flow, welding amperes, and travel speed [14]. The parameters vary based on the specific base metals being welded and the joint configuration. Even though argon is the most widely used inert gas in GTAW, suitable for welding steels, including stainless steel, aluminium and titanium, helium and the inclusion of hydrogen is also used for specific purposes such as when we have a high heat input or for welding austenitic stainless steels, respectively [14, 15].

Despite being suitable for joining Aluminium and Steel, the applicability of this technique to join the two metals directly is extremely low, consequence of the distinct material properties in a technique which sound results dependent on the appropriate parameters chosen. As discussed before, the specific thermal properties are one of the biggest drawbacks in order to choose GTAW as an efficient method to weld Al to St – the two metals have significantly different melting points and thermal conductivities, representing challenges in controlling the heat input, and consequently adjustment of welding parameters such as current, voltage, and travel speed, during the welding process, as the materials require different energy inputs ranges for proper fusion [16]. Furthermore, Aluminium TIG welds are performed using Alternate Current (AC), allowing the cleaning of the refractory oxide layer and providing good heat balance between the workpiece and the tungsten electrode, resulting in a stable arc and good weld penetration for this metal, contrary to the Steel welds that require Direct Current (DC), providing the higher output and deeper penetration needed, resulting in more efficient welds, adding to the parameter incompatibilities for these dissimilar metals [17].

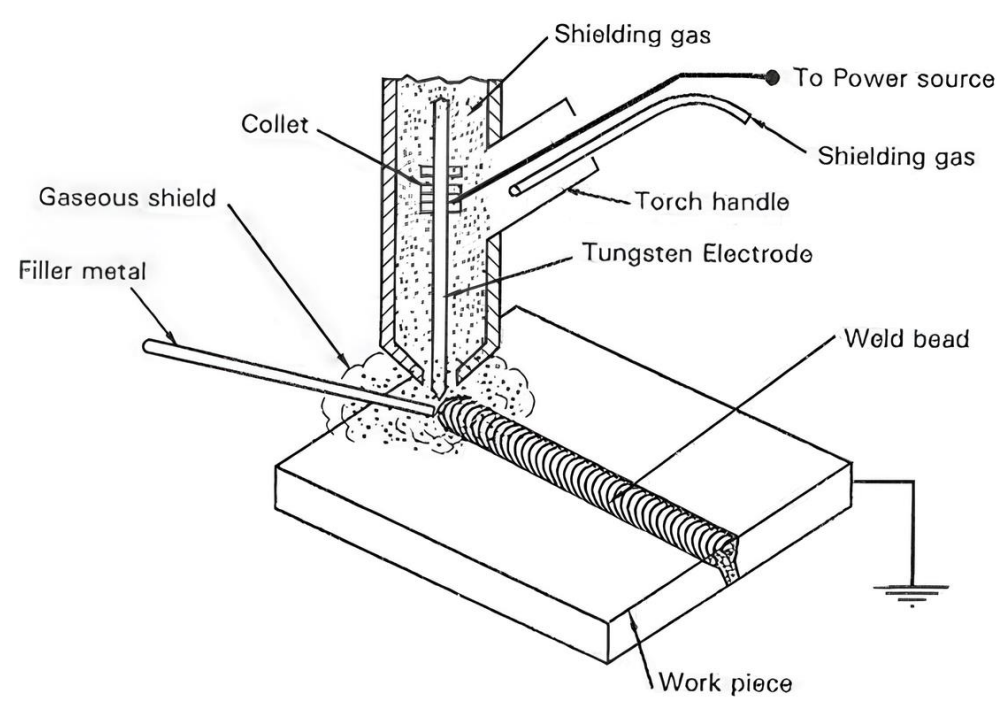


Figure 2.2 - Schematic representation of GTAW process [18].

#### **GMAW**

GMAW welding is a one-hand continuous process and is thought a more accessible technique, requiring less expertise to operate than other methods such GTAW, and therefore it is a versatile and common technique employed in numerous industries [19]. Multiple metals and alloys can be welded with it. Additionally, a variety of filler wire electrode materials are available, supporting a wide range of welds. The process is semi-automatic, as the consumable wire is feed and arc length are controlled by power, while travel speed and positioning are controlled manually by the welding technician [20]. The shielding gas mixture used in GMAW differs according to the base metal to be joined – for the MIG process, an inert gas mixture is employed, Argon and Argon + Helium are commonly used in the industry, for Aluminium alloys and other non-ferrous base metals, as they are chemically stable, protecting the weld pool from atmospheric contamination and preventing the oxidation of the metals at high temperature, as well as creating a stable arc and minimizing spatter. For MAG, a mix of Argon and active gases such Carbon Dioxide (CO2) and Oxygen, as the gases chemically react with the molten metal, providing benefits such as increased arc stability, deeper penetration, and faster welding speeds for ferrous metals [20, 21]. Therefore, GMAW is not suitable for welding Al-steel joints since the variants of the technology are not compatible to both simultaneously. Additionally, GMAW welds for dissimilar joints experience the same challenges caused by the inherent thermal properties of the two metals, as in GTAW and other Fusion Welding methods, mentioned previously [16].

Even though welding Aluminium and Steel by fusion represents serious challenges, successful attempts were made, as Jamalundin et al. [17] demonstrated via thorough optimization of the welding parameters, these welds are not without defects that compromises the joints' integrity. Residual stresses and crack formation are frequent, where the substantial differences in the coefficient of thermal expansion and thermal conductivity between aluminium and steel can result in the generation of residual stresses in the weld region, propitious to cracking issues, particularly during the cooling phase of the

weld, due to the differential contraction rates of the two metals [16]. Moreover, Spatter, characterized by the ejection of molten metal droplets during welding, can be caused by a disturbance in the weld pool as the wire is transferred into the weld, caused by incorrect energy density of the weld, as well as improper welding gas selection for a certain base material [22], common when working with dissimilar metals with incompatible material properties, such as Al-steel fusion welds.

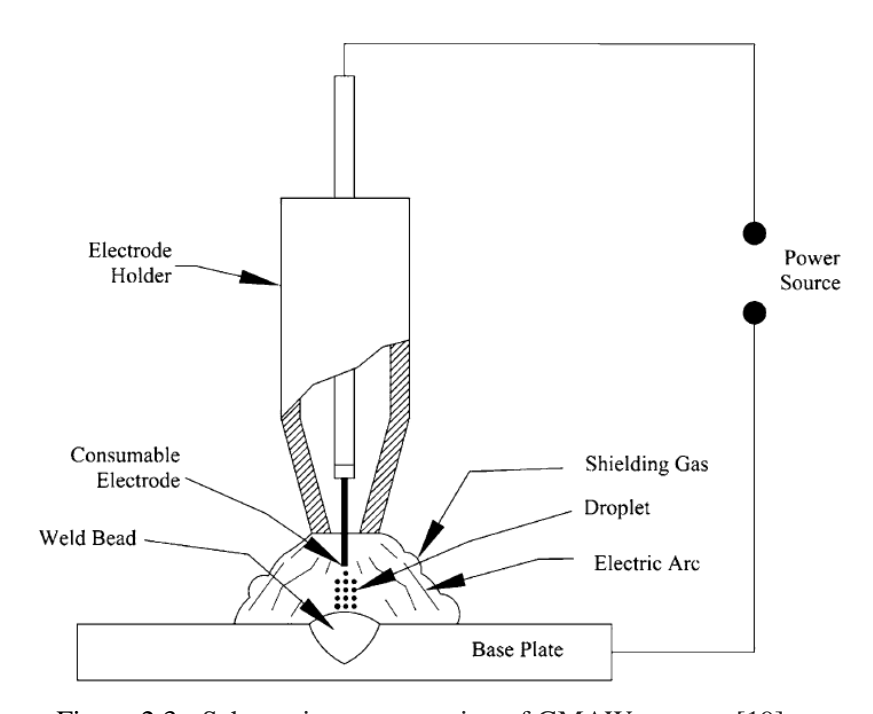


Figure 2.3 - Schematic representation of GMAW process [19].

An alternative to the conventional Fusion welding techniques is the Low Dilution Welding technologies. Dilution in welding refers to the change in the chemical composition of the welding filler material caused by the admixture of the base material or previously deposited weld metal [23]. The dilution can be calculated by quotient of the sum of the weights of the base metals (represented in Figure 2.4 by (a) and (c)), and the total weight of the weld bead, this is, the combined total of the weights of the filler material (a) and the base metals (b) and (c), at the weld bead, expressed in percentage [24], expressed in Equation 1.

Dilution (%) = 
$$\frac{\text{weight of base metals at the weld bead}}{\text{weight of the weld bead}} * 100$$
 (1)

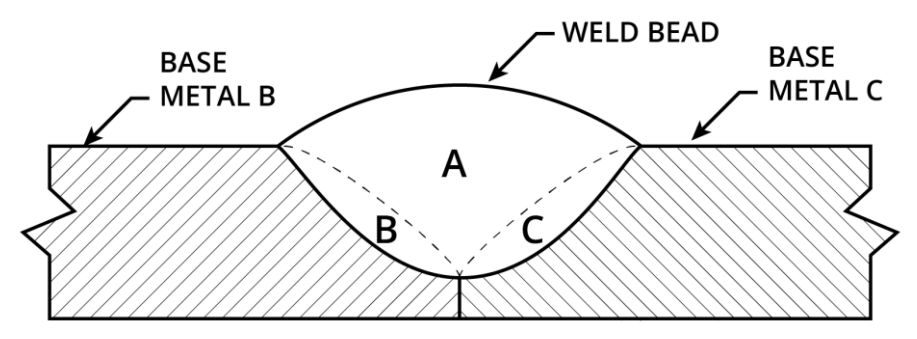


Figure 2.4 – Weld cross-section, representing a base metal and a weld bead, where (A) is indicative the weight of the filler material, and (B) and (C) of the weight of the base metals, at the weld bead [24]. (edited)

In particular, low dilution welding methods are necessary for reducing the undesirable effects caused by dilution during the welding process when combining dissimilar metals [25] in order to control the mixing of the dissimilar metals, the diffusion of alloying elements, which increased proportionally with the welding temperature, and consequent formation of excessive brittle IMCs phases that occurs in the welding process which compromises the mechanical properties and the integrity of the dissimilar joints [26]. Furthermore, these techniques are much important in the control of the size of the heat-affected zone (HAZ), minimizing the extent to which the base metals are affected by the welding process [27].

The Heat Affected Zone (HAZ) is a part of base metal that is heated to an elevated temperature below the melting temperature during fusion welding, preventing phase change. HAZ is located around the weld metal and does not contain filler metal, as seen in Figure 2.5. Due to the thermal cycle, metallurgical and mechanical properties of the HAZ can vary significantly from that of the base metals. However, the chemical composition matches with that of the base metal (excluding composition change owing to small scale of diffusive atom transfer) [28] . HAZ geometry is usually defined by its width, which varies with the welding process, selected parameters, extent of heating, base metal properties, and number of passes.

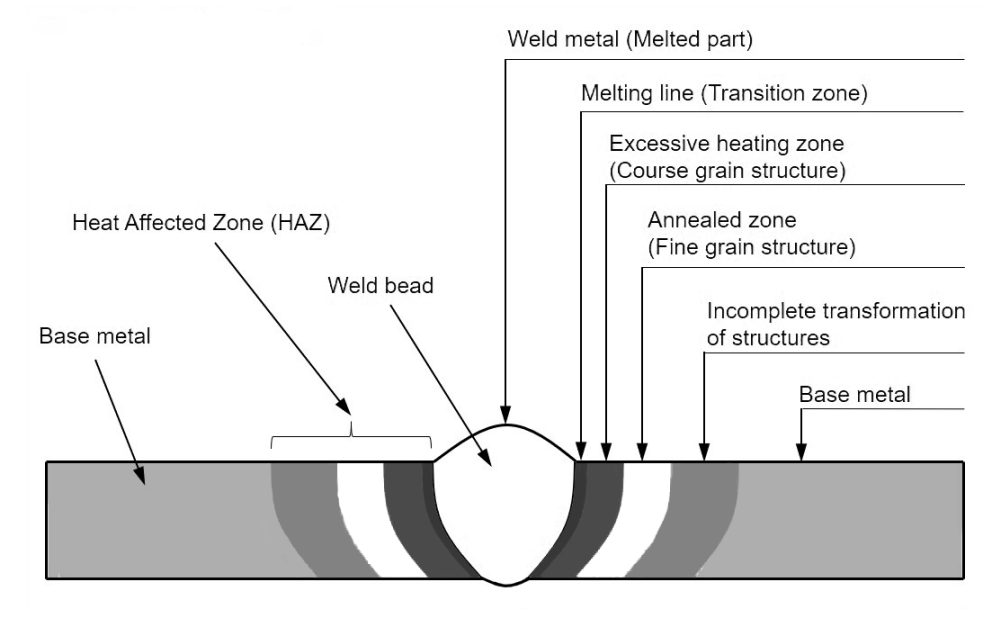


Figure 2.5 - Heat-affected zone schematic for Fusion and Low Dilution Welding processes.

The reference techniques for Low Dilution Welding are Electron Beam Welding (EBW), Laser Beam Welding (LBW), and Pulsed Arc Welding.

The EBW is a method of joining two materials via fusion welding that uses a high-velocity electron beam. The method is applying a focused beam of fast electrons to the materials that need to be connected. These electrons are usually accelerated to speeds of 0.3 to 0.7 times the speed of light. The workpieces melt and flow together as a consequence, converting the electrons' kinetic energy into heat and producing a weld in the process. Vacuum environments are frequently used for EBW in order to limit beam contact with air, which might scatter electrons, and to prevent the electron beam from dissipating. It is suitable for a variety of industry sectors and applications since it is especially good at bonding metals in similar and dissimilar combinations. High degrees of automation are possible, and weld quality is usually excellent, with remarkable high efficiency values [29].

LWB is a precise and efficient fusion welding process that uses a concentrated beam of light to join metal parts. The laser beam, produced by a CO2 laser, provides a highly localized heat source, allowing for narrow, deep welds with minimal heat-affected zones and distortion. This process is frequently used in high-volume and precision-requiring applications, particularly in the automotive, aerospace, and electronics industries since it can also be automated and allows high welding rates [30].

In the Pulsed Arc Welding, with short bursts, or pulses, of high current to melt the weld pool, which reduces the amount of time that the base material can mix with the filler material, thus minimizing dilution [31]. Usually a non-consumable tungsten electrode is used, however unlike traditional electric arc welding processes, such as GTAW and GMAW, pulse welding involves a current that continuously fluctuates from low (background current) to high (peak current), as seen in the current-diagram representation in Figure 2.6, providing more control over the welding process [19, 32].

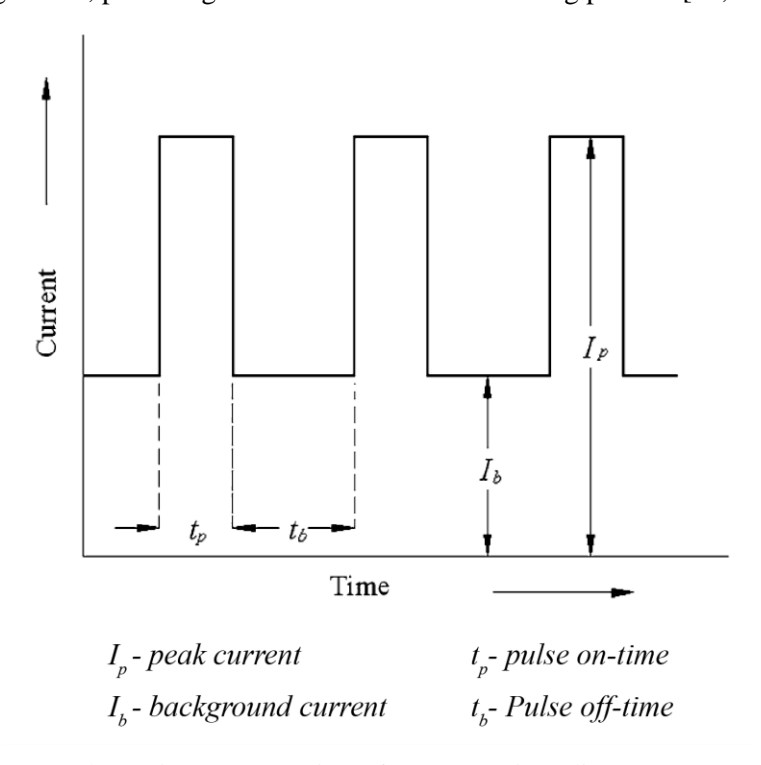


Figure 2.6 - Schematic representation of a current-time diagram [19]. (edited)

#### 2.1.2 - Solid-state welding of aluminium-steel joints

Facing the challenges presented in welding metallic parts by fusion welding processes, as discussed in the previous section, Solid State Welding (SSW) represents an alternative to the conventional welding technologies, diminishing a great number of defects inherent to these method [33, 34]. This process is commonly used in cutting edge industries such as those operating in the aerospace and automotive sectors, where high-quality, defect-free welds are required.

SSW processes are characterized by the coalescence at temperatures below the melting point of the base materials being joined [35]. These processes produce a bond between materials without melting them, and they are based on the principle that the driving force for two pieces of metal to weld can be achieved without the requirement for molten metal. These joining technologies include Diffusion Welding, Explosion Welding, Ultrasonic Welding, Linear and Rotating Friction Welding, and Friction Stir Welding [34]. They utilize a combination of heat, pressure, and time to overcome the barriers to bonding, resulting in a metallurgical bond between the workpieces [33, 35]. By avoiding melting, solid-state joining allows the welding of intricate metals and dissimilar metal pairings, which are frequently difficult or impossible to join by fusion welding [36]. To begin with, due to the low temperatures reached in SSW processes, relatively to the conventional welding technologies, heat-affected zones and thermal distortion can be minimized and often negligible. Thus, advantages such chemical stability and microstructural homogenization of the joint is promoted, leading to reduced problems inherent in welding dissimilar materials, such as Al-steel joints, such as decreased probability of galvanic corrosion and intergranular corrosion [37, 38].

Diffusion Welding is characterized by being a solid state based pressure method, where the interdiffusion of atoms occurs at the joint interface in three phases: firstly, interfacial voids are decreased via plastic deformation of surface asperities, with the applied loads being typically lower than the yielding loads of the parent material, the second phase involves the shrinking of voids due to rapid creep and grain boundary migration brought on by high temperature and pressure, being the first typically 50% to 90% of the melting point of the base metals. Elevated temperature encourages the diffusion of fluid over faying surfaces and increases the area of contact asperities [39].

Some relevant variants of this process are implemented in the industry, mainly Solid-phase Diffusion Bonding and Roll Bonding. The Solid-phase Diffusion Bonding process entails connecting materials within a controlled vacuum environment, regulating temperature and pressure. Heat application methods, including resistance heating, radiant heating, and induction heating, are employed. Pressure is commonly uniaxial or isostatic, and achieving a high-quality surface is essential for effective atomic diffusion. Hot isostatic pressing, a variant of solid-state diffusion bonding, is employed for intricate geometries [34]. This technique allows for the adjustment of stress distributions after bonding and minimizes the formation of intermetallic compounds, a feature further improved by incorporating single or multiple interlayers [40]. Alternatively, the Roll Bonding process involves joining metals by rolling them at different temperatures. Similar bond formation mechanisms are shared by Roll Bonding and other diffusion bonding techniques, despite different settings and temperatures during the process [41]. When two or more sheets of similar or different materials are processed by two rollers under enough pressure breaking up oxide layers, causing the fresh materials of the sheets and base materials to share electrons and leading to a welded surface [41]. This process is represented in

Figure 2.7.

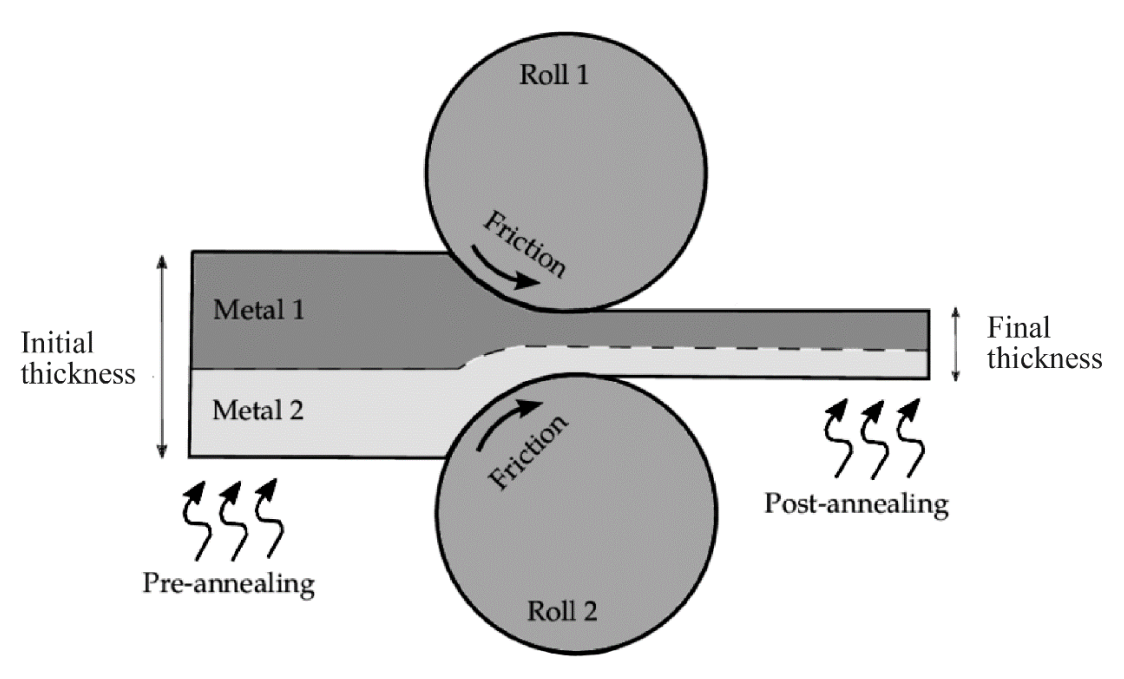


Figure 2.7 - Roll Bonding process representation [42]. (edited)

However, the strength of the rolled bonds depends on the rolling conditions and the pre-rolling treatment, namely the surface treatments and thorough cleaning, and pre-annealing procedure. Based on temperature ranges, the procedure is classified as Cold, Warm, or Hot Roll Bonding. Welding temperatures below half of the melting temperature are used for Cold Roll Bonding, over 50% of the melting temperature is used for hot roll bonding, and processing temperatures beginning below and finishing above half of the melting temperature are used for warm roll bonding [41]. Diffusion bonding offers several advantages, including the ability to produce high-quality joints without metallurgical discontinuities or porosity across the interface. By controlling process variables, the strength of the diffusion-bonded joint can be comparable to that of the parent material [43]. This technique is versatile in joining dissimilar materials and is effective for intricate shapes or cross sections. However, diffusion bonding has its limitations. The primary bonding interface is the weak area of the bonded parts, often requiring post-bonding heat treatment to enhance mechanical properties. Adequate surface preparation is crucial, as excessive oxidation or contamination can decrease joint strength. Achieving high bond strength may necessitate the application of high bonding pressure (20–100 MPa) and a long bonding time (1-2 hrs) [44].

Another SSW process commonly implemented is Explosion Welding, where two or more pieces of metal collide at high speeds, resulting in a bond at the impact surfaces. Because of the high-speed energy transmitted at the contact, impurities on the surface like oils and oxides are removed. The creation of a metallic joint between the sheets is then facilitated by the high-pressure contact between the now-clean metal surfaces [45]. The Explosion Welding procedure involves a flyer plate and a stationary target plate, and an explosive charge that accelerates the flyer plate in the direction of the target plate when detonated, as seen in Figure 2.8.

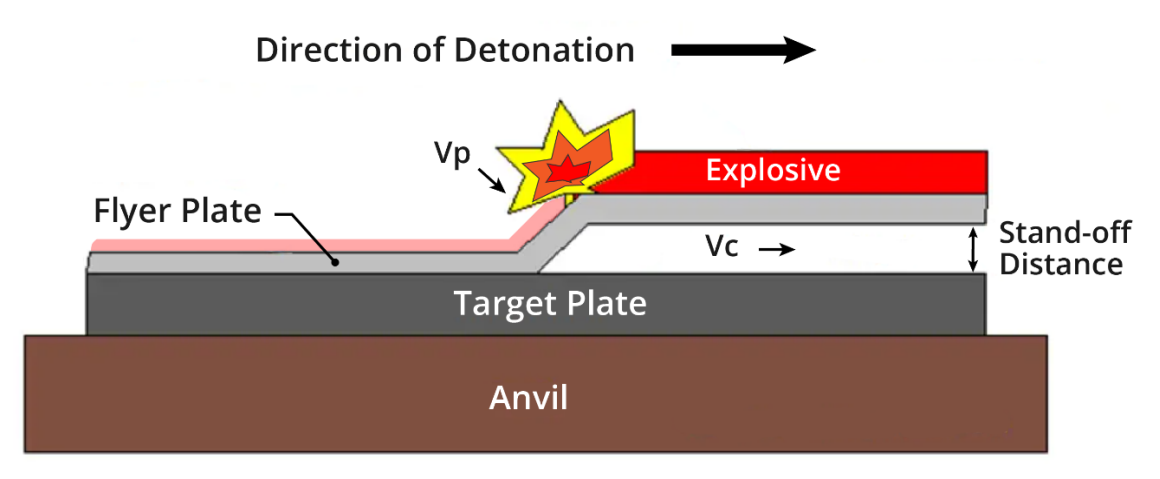


Figure 2.8 - Explosion Welding detonation and joining procedure representation [46]. (edited)

Since the flyer must attain a high enough velocity and experience rapid deformation, the alloy with a lower areal density and greater ductility is usually used for this role. A stand-off distance in the explosive welding configuration is essential given that it allows the flyer plate to reach the required impact speed, which is usually between 200 and 1000 m/s. Rather than collapsing instantly, the explosion wave collapses gradually as it moves across the flyer plate's surface, resulting in an wavy interface, as seen in Figure 2.8.



Figure 2.9 - Explosion Welding wave interface, resultant of the process [47].

An oblique impact is produced by this gradual collapse, which permits shear deformation at the collision surfaces and the subsequent removal of oxide [48]. The collision velocity  $V_c$  can be calculated by the Equation 2, where  $V_p$  is impact velocity and  $\beta$  the dynamic collision angle (Figure 2.8).

$$V_c = \frac{V_p}{2\sin\left(\frac{\beta}{2}\right)} \tag{2}$$

Resultant wave-like interface from this technology is influenced by the collision velocity  $V_c$  and by the dynamic collision angle  $\beta$ . The weldability window of the process and the formed morphology of the interface, dependent of the referenced welding conditions can be seen in Figure 2.10.

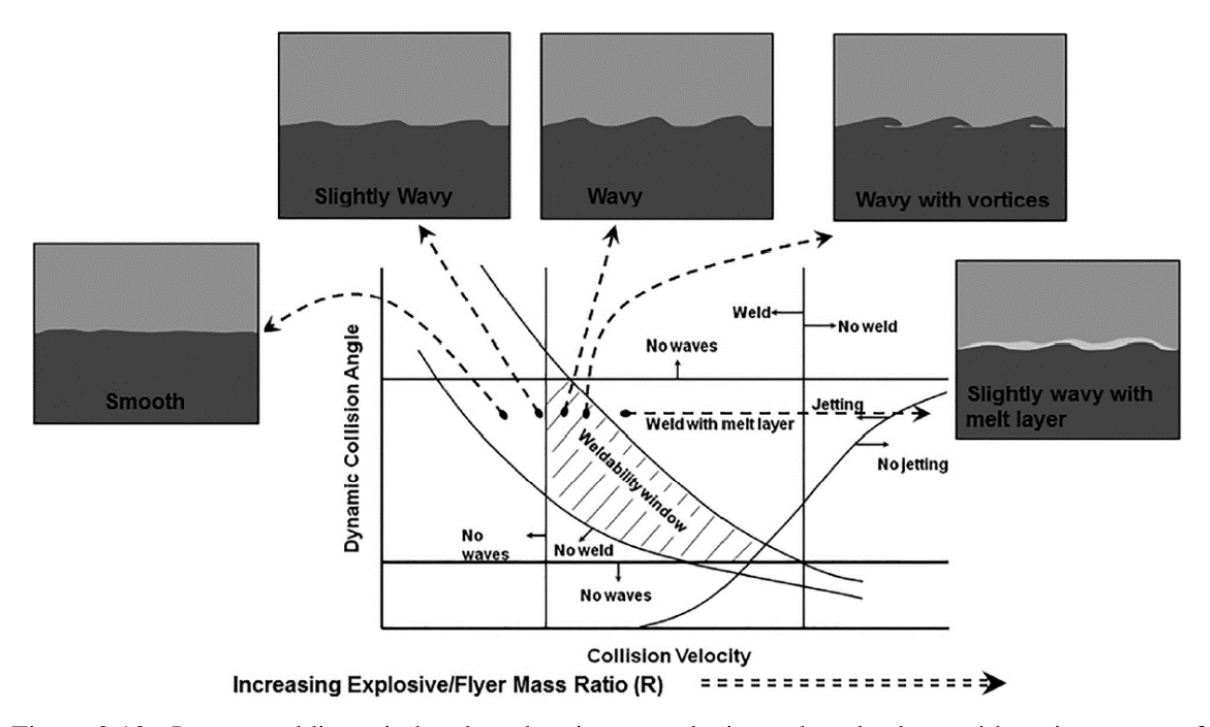


Figure 2.10 - Impact welding window based on impact velocity and angle along with various types of interfaces formed depending on the conditions [49].

The welding method offers significant advantages, allowing for the welding of extremely large areas exceeding 25 m² and accommodating thicknesses greater than 50 mm. Moreover, it is versatile in welding widely disparate material combinations, and the parameters can be easily modified to suit specific requirements. The process minimizes the need for complicated fixtures and offers flexibility with several possible configurations, there are certain limitations to consider. However, automating the process on a production line proves challenging, and the critical volume effect reduces repeatability at smaller scales. Additionally, the cost per cycle is relatively high, and the process necessitates the use of secluded facilities [45].

Ultrasonic Welding is an SSW process in which a high frequency of acoustic vibrations is used to generate relative motion between the parts to be welded and consequently heat. This method is typically used to join small electronic circuits, semiconductors devices, and more recently is being implemented in the manufacturing of battery packs for the automotive industry, in the assembly of terminals and bus bars [50]. This process is the most efficient in Copper and other high thermal conductive metals [51].

Friction Welding is one of the earliest processes of SSW and consists in a combination of pressure and rotational and/or linear oscillation motion between the two base materials to generate heat through the conversion kinetic energy to friction energy, reaching a plasticized regime in order to achieve coalescence of the two materials upon cooling, forming a welded joint. This technique can be categorized in two main variants, Rotary Friction Welding (RFW) illustrated in Figure 2.11 (a), Linear Friction Welding (LFW) and Friction Stir Welding, represented in Figure 2.11 (b) [34].

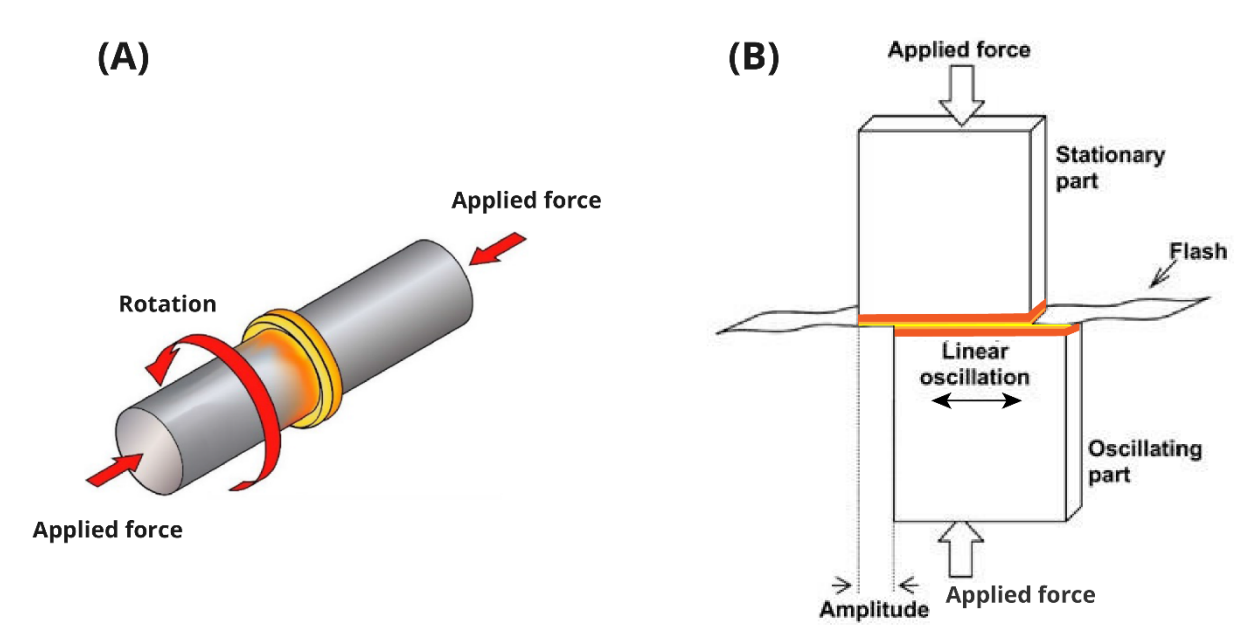


Figure 2.11 - Rotary Friction welding (a) [52] and Linear Friction Welding (b) [53] representations. (edited)

Whitin the scope of this study, we will focus solely on FSW, and a detailed review of the process will be undertaken in the next section.

# 2.2 - Friction Stir Welding

In the context of this this work, a more detailed discussion of the Friction Stir Welding (FSW) process will be conducted in this subchapter. At first, a comprehensive overview of technology where the concept will be explained, as well as the advantages offered by the process over the legacy alternatives, followed by the in-depth description parameters, focusing on tool specifications and selection, welding parameters, joint configurations, and machine options for different applications and scales of production.

The mechanics of material flow for the base metals during welding will also be discussed, followed by a summary of the common challenges and defects present in these types of welds. In the end of this section, a review of aluminium to steel FSW joint will be conducted.

# 2.2.1 - Overview of the FSW process

Friction Stir Welding was originally developed at the Welding Institute (TWI), United Kingdom, in 1991 as an aluminium SSW technique [54].

The process of Friction Stir Welding (FSW) involves utilizing a non-consumable rotating tool with distinct pin and shoulder components. This tool is inserted into the adjacent faces of the plates to be welded, making full contact with the workpiece surface, being the shoulder responsible for the application of the axial load, generating the frictional due to the rotation of the tool. Subsequently, the tool traverses along the joint line, forming the weld. Through the combined action of rotational and linear movements, the tool generates frictional heat, softening the material without reaching its melting point. The softened material is then transferred from the front to the back of the tool, with the tool

shoulder containing the softened material beneath it. Additionally, the shoulder of the tool prevents the plasticized material to ascend and flash out of the welding zone [55].

To go further into the comprehensive discussion of the FSW process, some fundamental terminology and key parameters must be explained. The process unfolds in three stages: tool plunging into the top faces of the base metals and initial stationary dwell until the target plasticity is reached; followed by traverse linear motion of the tool, forming the welding line; and finishing in the retracting of the tool from the joint [56]. A variant of the process is Friction Stir Spot Welding (FSSW), comprising only the tool plunge, dwell, and retract stages without traverse movement, creating a single point connection. The Figure 2.12 represents the main three stages of FSW - Plunge (1) and Dwell (2), Traverse welding (3), and Retracting (4), as well as the tool pin (A) and shoulder (B)

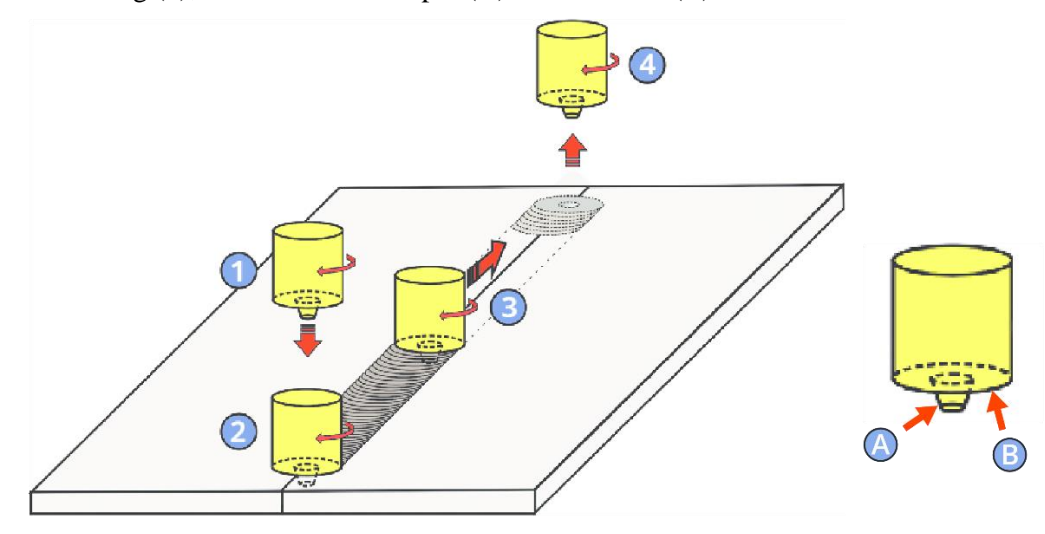


Figure 2.12 - Schematic representation of three stages of FSW: Plunge (1) and Dwell (2), Traverse welding (3), and Retracting (4); tool pin (A) and shoulder (B) [57]. (edited)

Key parameters governing the FSW process include the tool rotation rate (rpm), tool traverse speed (mm/min), tool plunge depth, tool tilt angle, and the dimensions and features of the shoulder and pin, as observed in Figure 2.13. The advancing side (AS) designates the side where the tool rotation aligns with the tool traverse direction, while the retreating side (RS) pertains to situations where these directions oppose each other. FSW applications can be in either butt or lap format.

In Friction Stir Butt Welding, material flow assumes critical importance, particularly when joining dissimilar metals and alloys. Special consideration must be given to the placement of the hard metal, which does not plasticize at the same temperature as the softer one. To address this, the hard metal is strategically positioned on the AS, while the tool offset is directed into the softer metal to mitigate tool wear and excessive heating [58].

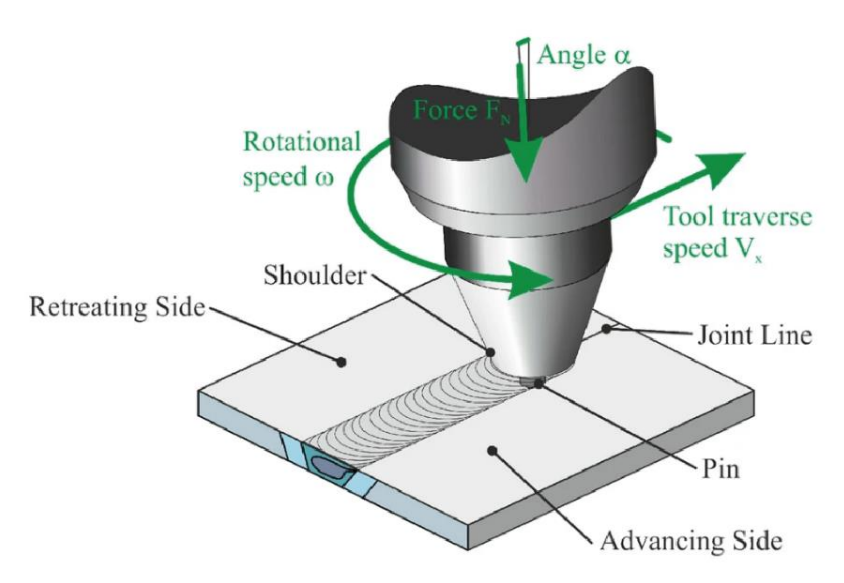


Figure 2.13 - Schematic of the FSW process and main parameters and weld zone [59]. (edited)

The process offers a considerable number of general advantages. In many aspects, it offers a range of opportunities in comparison with traditional welding technologies, in terms of sustainability, potential for defect reduction and in material selection.

Table 2.1 - FSW advantages [34]

Technical advantages	Economic and environmental advantages
- Possible dissimilar material joining	- Low energy consumption
- Largely defect free welding process	- Low preparation times
- Low thermal cycle effects	- No consumable tools
- Good dimensional stability	- No filler material is required
- Low welding distortion.	- No flux or shielding gases are required
- Low residual stresses.	- No UV radiation and fumes emissions
- Low risk of hot cracking	
- Low risk of solidification cracking	
- Good surface appearance.	
- Easly automated process	
- No requirement for special edge preparations	
- Good overall mechanical properties	
- Welding position versability	

## 2.2.1.1 - Tool specifications

The tool, which consists primarily of the pin and shoulder, is essential for generating both the frictional heat, in order to achieve a plastic regime of the substrate, and the material flow and mixing, responsible for the weldability. When the pin is inserted into the workpiece during the first phase of

FSW, friction between the pin and the base material is what produces heat, until the shoulder enters in contact with the surface of the workpiece. From this stage on, the shoulder is responsible for the majority of the heat generated, consequence of the friction and axial loads applied to the top of the workpiece, besides containing the softened material in the welding region. Furthermore, the pin in this stage is now responsible for the mixing of the base material, creating as a consequence a complex material flow around itself. In the AS, the advancing tool velocity and the rotation velocity are in concordance, as in the RS the two velocities have an opposite direction, resulting in an asymmetry in the flow of the welding zone [60]. Also, at the bottom of the tool's pin, a swirl motion caused by the asymmetric flow of the plasticised material, generating rotation and translation of the materials from the advancing side to the retreating side of the joint [61]. In the final stage, while the tool is retracting from the workpiece, a hole is left in its place, commonly known as the *keyhole*. The keyhole can be avoided by using run off tabs at the end of the workpiece, which are not part of the welded piece.

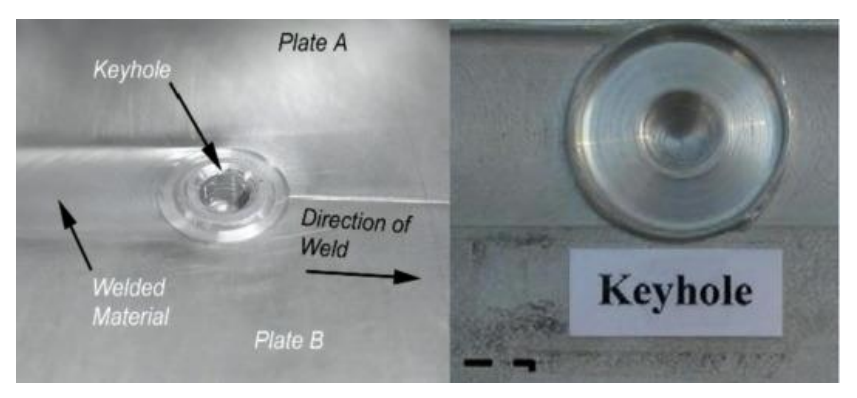


Figure 2.14 – Example of a FSW keyhole, caused by the retracting tool at the end of the weld process [62].

Heat generation, plastic flow, power consumption, and the consistency of the welded joint are all greatly impacted by its design. The ratio between the shoulder and pin dimensions of tool is proportional to heat transferred to the substrate. Therefore, diverse tool designs, consisting in a range of pin length and profiles, shoulder diameters and angles, and other designs are available commercially, used in the industry, and continually being optimized to fulfil the desirable welds results for a number of particular joints [55].

The maximum height of the weld is determined by the geometry of the tool, namely the pin length. Different tool designs, such adding a threaded pin, can affect how voids occur close to the pin's end. The material is pushed to descend when a screw is inserted into the pin, which stops voids from forming. Tool shoulders have a variety of forms and characteristics, including concave, convex, and flat surfaces, which affect the weld integrity and material flow.

In order to improve workpiece mixing and weld quality, shoulder end surfaces may include features such concentric circles, ridges, knurling, grooves, and scrolls to increase material friction, shear, and deformation. Often employed, scrolls allow material to flow more easily from the edge of the shoulder to the probe, saving the tool from having to be tilted. Concave shoulders combined with scrolling features help reduce and even eliminate tool lift during high-speed welding [63], represented in Figure 2.15.

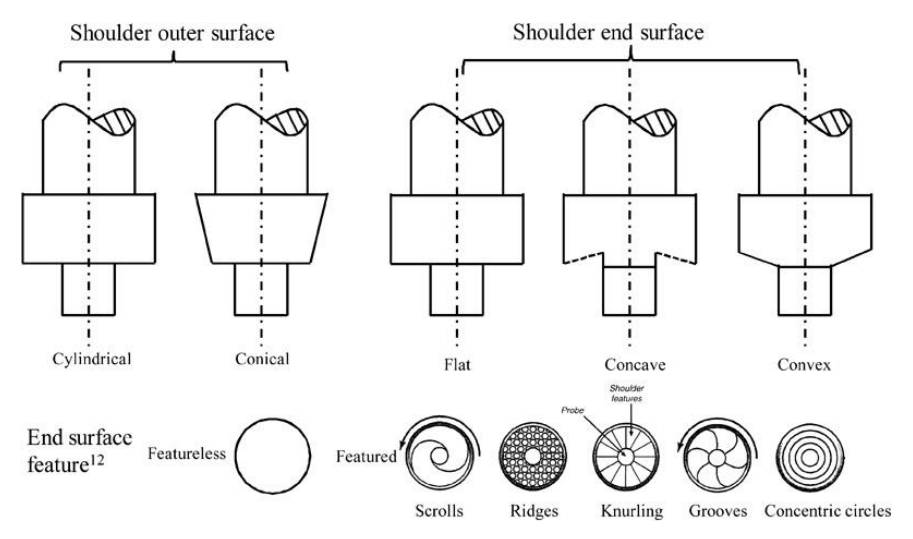


Figure 2.15 – Tool's shoulder designs and features [64].

The tool pins can have a variety of geometries, including flat or domed ends, and are responsible for producing deformational and frictional heating. Material flow, stirring, and overall weld quality are influenced by the selection of probe geometry, outer surface form, and features, such as threads, flats, or flutes. The ratio of dynamic volume to static volume, or swept rate, is a crucial factor that affects the nugget's ability to reduce voids and effectively disrupt and disperse surface oxides [63].

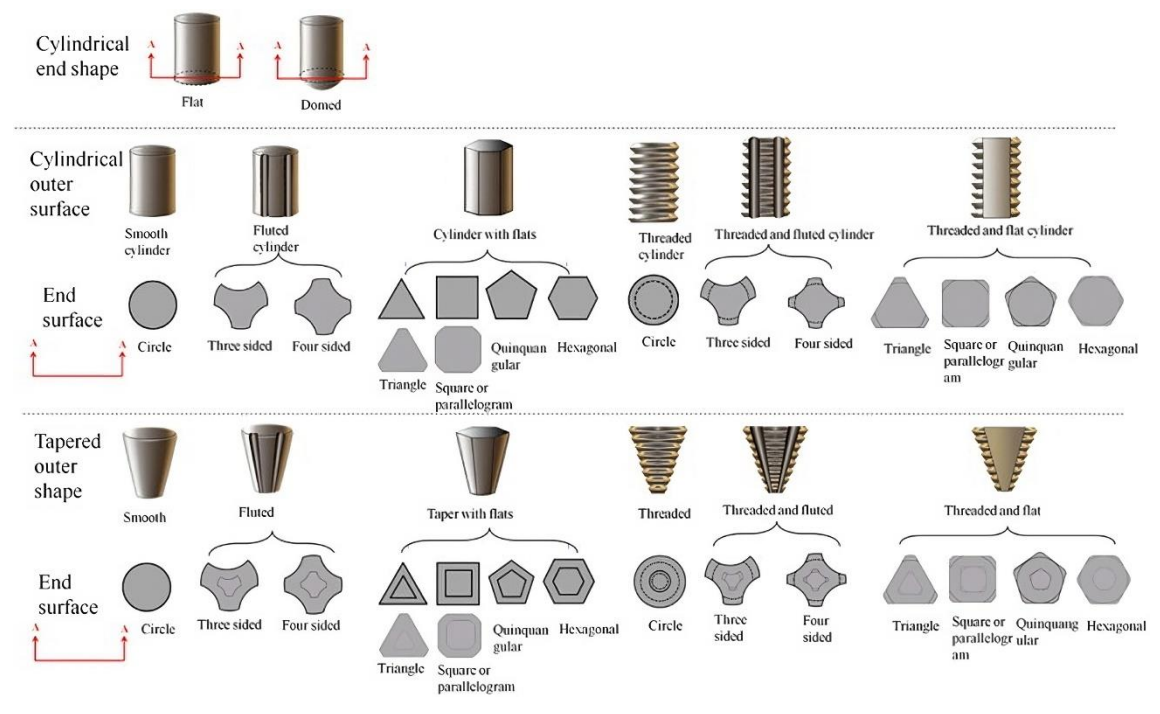


Figure 2.16 – Tool's pin designs [64].

The heat input in the friction stir welding process is intricately related to the shoulder radius, as the axial force is also determined by the shoulder radius, emphasizing the significant impact of shoulder dimensions on the energy dynamics of the process [65]. The equation representing this relationship is given as follows:

$$q_0 = \frac{4}{3\pi^2 \mu P \omega R^3} \tag{3}$$

Here,  $q_0$  represents the net power (W),  $\mu$  is the effective friction coefficient between the workpiece and the tool, P denotes the pressure (MPa),  $\omega$  is the rotation speed (rev min<sup>-1</sup>), and R stands for the shoulder radius (mm).

## 2.2.1.2 - Welding parameters

As discussed previously, the weld quality is highly dependent on the FSW parameters, and their selection should be considered for the particular weld to be manufactured, as materials, thickness, and even joint configuration. The main FSW parameters include tool rotation, traverse speed, and axial force, which can be seen in Figure 2.13, and pin and heel plunge depth, as well as the tool tilt angle, represented in Figure 2.17:

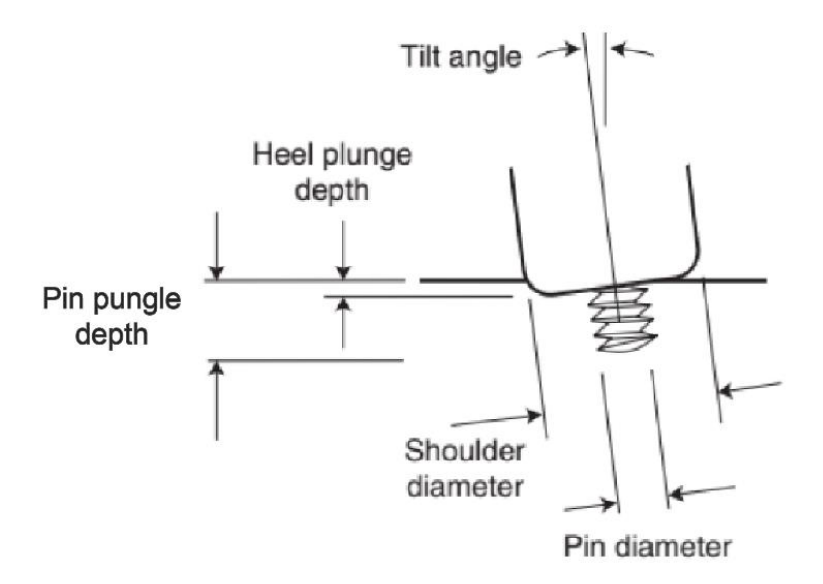


Figure 2.17 – Representation of tool dimensions translated as FSW parameters [66].

### **Friction Stir Welding Parameters [67]:**

- Tool rotation speed  $(\omega)$  in RPM, Clockwise or Counter-clockwise direction
- Tool traverse speed (Vx) in mm/min or mm/s
- Tool tilt angle ( $\theta$ )
- Axial force (Fn)
- Pin plunge depth
- Heel plunge depth
- Friction coefficient

The process involves the intricate interplay of rotational and translational movements, which induces the stirring and blending of softened material around the pin. This stirred material is subsequently transferred from the leading edge to the back of the pin, where it undergoes cooling and solidification. The pivotal role of rotational speed in the welding process is evident. Elevating rotation speed increases temperatures due to enhanced friction, thereby intensifying the stirring and mixing of the material [55].

The complex heat input thermodynamics presents a correlation between the tool surface and the workpiece. There is no significant increase in heating with rotation speed, attributed to the varying friction coefficient at the interface [68]. Non-linear effects manifest with the acceleration of rotation speed. Instead of expanding, the welding zone experiences a reduction in size, and the deformation zone exhibits a non-continuous increase. The rising rotation speed compromises the flow strength of the workpiece material [55].

Critical parameters shaping the welding process include tool angle and tilt. A seamless tilt of the tool towards the trailing direction ensures the efficient retention of stirred material. Additionally, adopting a scroll shaped tool shoulder enables the creation of high-quality FSW welds even with a 0° tool tilt [63]. The depth of pin insertion is an important parameter, consequent of the pin height in tool design. Shallow insertion limits the efficacy of moving stirred material, potentially resulting in defects like inner channels or surface grooves. In the other hand, excessive insertion leads to the generation of flash, resulting in a noticeably concave weld and localized thinning of welded plates [69].

## 2.2.1.3 - Joint configurations and machine options

The joint configurations for friction stir welding (FSW) include various geometries such as single and two sided butt joints, lap joint, lap-butt, T and corner joints, and circumferential butt joints. The majority of FSW studies have been based on butt joint geometry, with the lap joint configuration also being widely used in conventional FSW [70] . The following Figure 2.18 represents the most common FSW joint configurations.

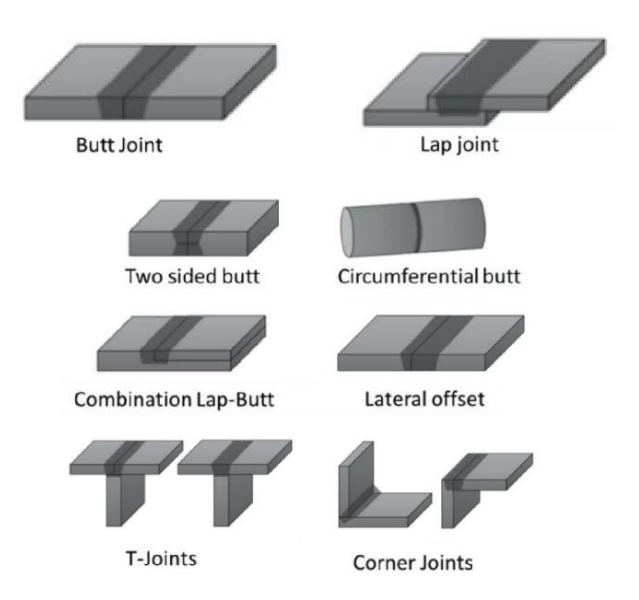


Figure 2.18 - Main joint configurations possible to obtain in FSW [71]. (edited)

The load capability in Friction Stir Welding (FSW) machines is a critical design consideration, influenced by factors such as material type and thickness. Relevant loads during FSW include axial force (Fn), traverse force (Fx), side force (Fy), and torque (M). Axial force facilitates friction and forging pressure for weld formation, traverse force supports material resistance, side force arises from process asymmetry, and torque is responsible for friction [55]. Stiffness is a key concern in FSW equipment design to withstand loads without deformation or deflection, ensuring minimal vibrations and maintaining weld quality. Sensing capability is crucial for precise process control, with sensors providing data for feedback and process automation. Flexibility, determined by the machine's degrees of freedom (DOF), dictates the complexity of weld paths—1D, 2D, or 3D. The number of DOF influences machine flexibility [72].

In terms of machine types, three major groups are identified: conventional machines like milling or CNC machines, although these suffer from limited power and low stiffness, not indicate to weld high strength material, and dedicated FSW gantry machines and industrial robots [72]. Some of the common FSW machine types include:

### - C-type Friction Stir Welding Machine:

This type of machine is designed with a C-shaped configuration and is suitable for specific FSW applications.

### - Dual Station FSW Machine:

These machines are equipped with two stations, allowing for simultaneous or sequential welding operations.

### - Static Gantry FSW Machine:

Static gantry machines are characterized by a stationary frame, and the welding tool is moved along the workpiece.

#### - Dynamic Gantry FSW Machine:

Dynamic gantry machines feature a movable frame, offering flexibility in the welding process.

### - 6-Axis FSW Machine:

This type of machine provides multi-axis movement, allowing for complex welding operations on non-planar surfaces.

### 2.2.1.4 - Weld zones

Friction stir welding (FSW) typically results in the formation of three main microstructural regions within the weld, each with distinct characteristics. These regions are the weld nugget, the central region of the weld experiences dynamic recrystallization, resulting in a refined and homogenized microstructure. It is the primary bonding area where the material is thoroughly mixed and joined; Thermo-Mechanically Affected Zone (TMAZ), surrounding the weld nugget and exhibits a microstructure that has been altered by the combined effects of heat and mechanical deformation during the FSW process. This zone plays a crucial role in the overall mechanical properties of the weld; and the Heat-Affected Zone (HAZ), located outside the TMAZ and experiences thermal effects without significant mechanical deformation [55]. The microstructure of this zone is influenced by the heat from

the welding process, but it does not undergo the same level of mechanical mixing as the TMAZ. The aforementioned zones are represented in Figure 2.19:

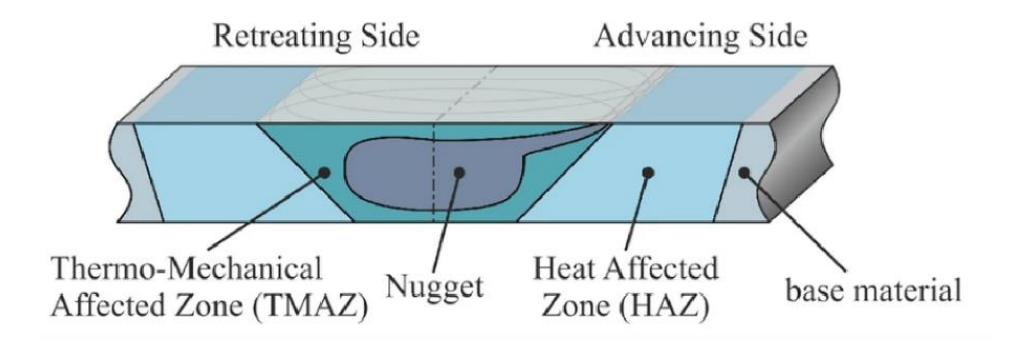


Figure 2.19 - Representation of the FSW weld zones [59]. (Edited)

These distinct regions are essential to consider when evaluating the microstructure and mechanical properties of a friction stir weld. The weld nugget is the primary bonding area, while the TMAZ and HAZ exhibit varying degrees of microstructural alteration due to the FSW process. Understanding and controlling the characteristics of these zones is crucial for ensuring the quality and integrity of FSW joints [73].

#### 2.2.1.5 - Material flow

Understanding the mechanics of joint formation relies on comprehending the complexities of material flow in FSW. The weld centre line is not symmetrical, and the final stirring material distribution is usually behind the initial location, with very little in front, especially on the AS [55].

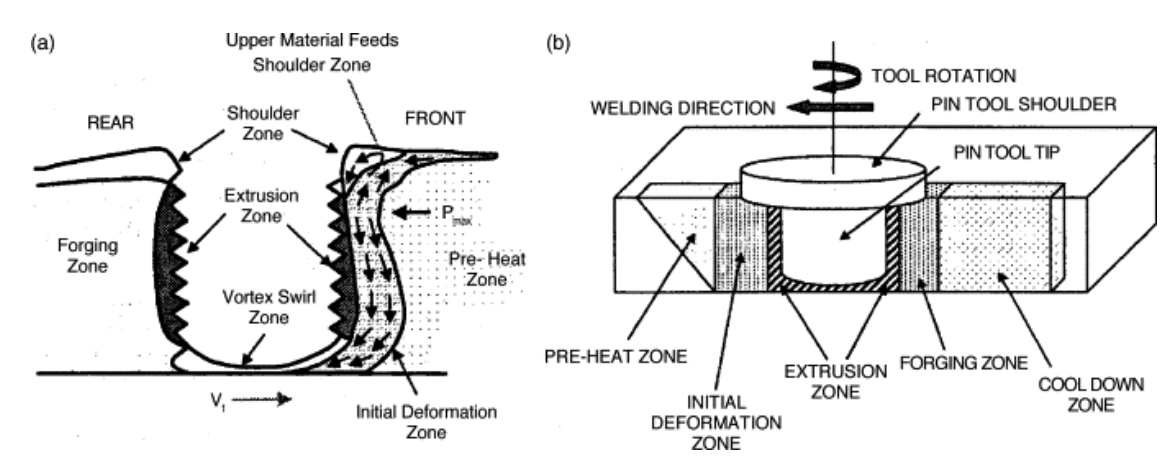


Figure 2.20 - Metal flow patterns (a) and metallurgical processing zones developed during friction stir welding (b) [55].

This last resting spot is matched to a volume equal to the pin behind it. On a larger scale, there is a visible border between the forward and backward sides, and there are no obvious indications of

significant stirring between these areas. The direction of the threads in the pin turns out to be crucial, causing the material to be forced downward, in the vortex swirl zone, on the forward-moving side and backward on the retreating side. In FSW, material movement occurs via two different mechanisms, as represented in Figure 2.20. The material on the AS, in front of a weld, enters a zone in the first stage where it spins and moves in tandem with the pin. This procedure creates arc-shaped characteristics behind the pin by significantly deforming the material [74]. The next step is to extrude material from the retreating front side of the pin between the parent metal and the rotational zone. The material that is produced fills the weld wake and is derived from the material that has sloughed off in the rotating zone [55], as represented in Figure 2.21.

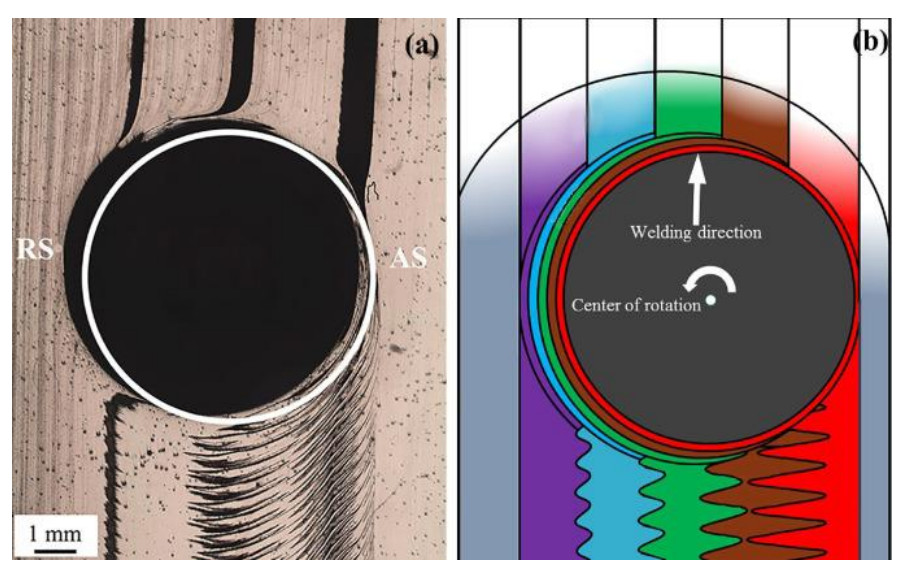


Figure 2.21 - Plane view of friction stir welded, studied by Liu et al. [75] (a) and material flow pattern around the probe during steady state FSW (b) [76]. (edited)

## 2.2.1.6 - Defects and challenges

**Tunnel defect** occurs in the AS, propagating through the welding line, and it's caused by insufficient heat input and material flow, Figure 2.22.

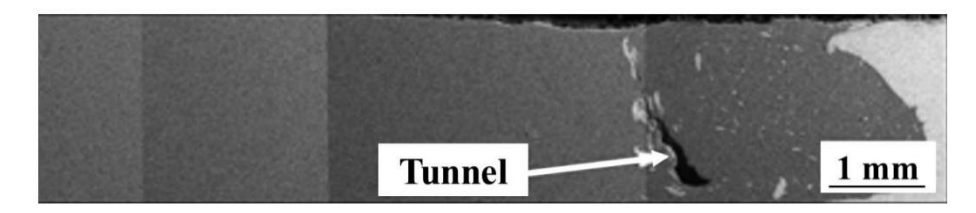


Figure 2.22 – Example of tunnel defect in a FSW weld [77].

**Flash defect** is caused by a large amount of softened material expelled by the shoulder of the tools, due to inadequate large heat input, Figure 2.23.

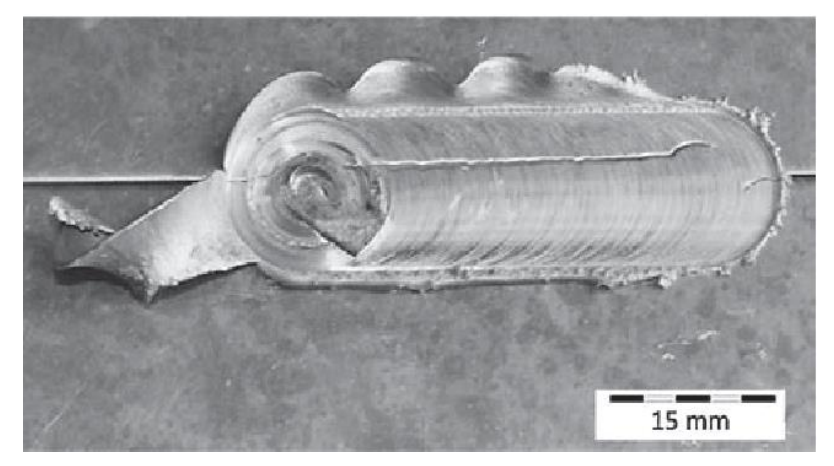


Figure 2.23 - Flash defect in the surface of friction stir weld [78].

**Voids** and **cavities** appear in a variable size and orientations and are caused by insufficient axial loads and inadequate fast welding speeds, Figure 2.24.

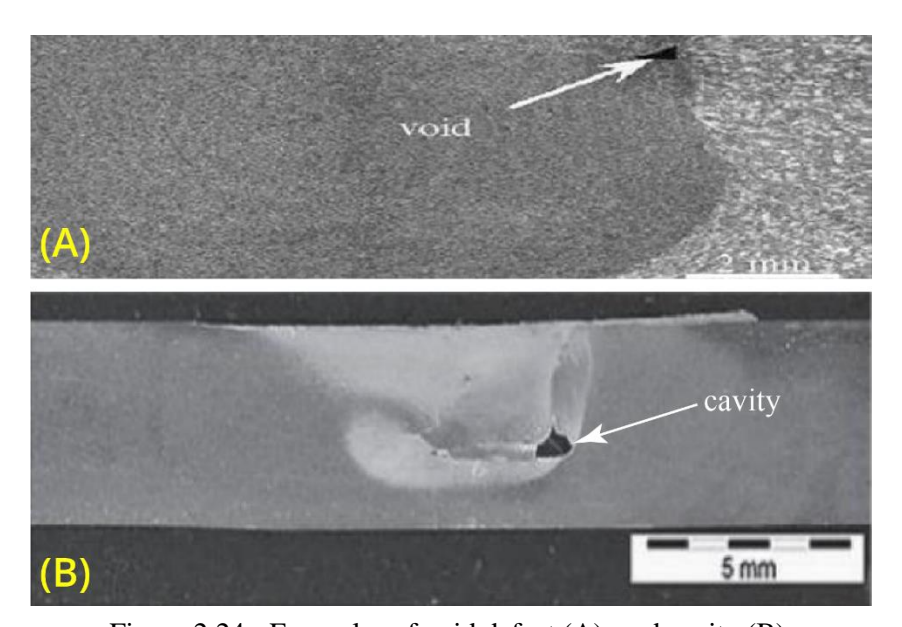


Figure 2.24 - Examples of void defect (A), and cavity (B).

**Kissing bond** is characterized by the partial breaking of the oxide layer, attributed to insufficient stirring of the metal and low heat input, results in a diminished flowability of plastic material. The broken oxide particles are incorporated, manifesting as either a zigzag line or a kissing bond defect, Figure 2.25.

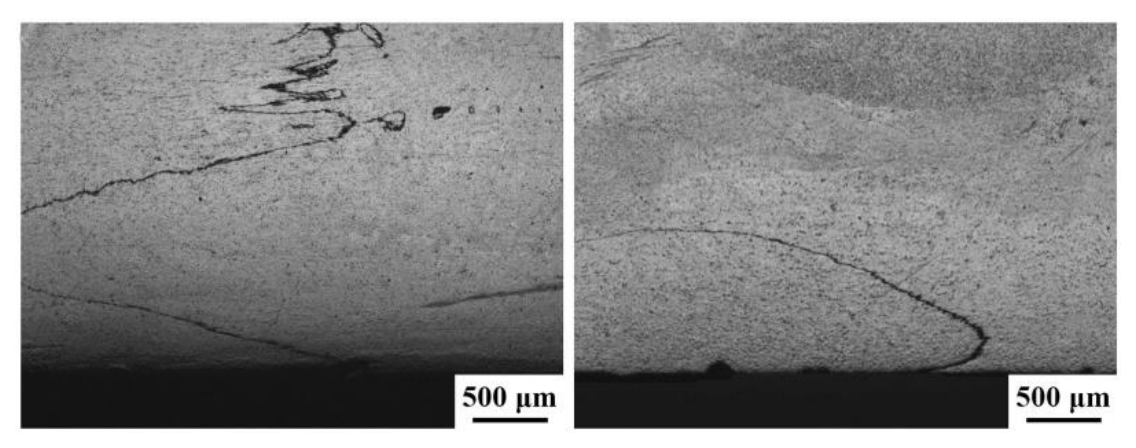


Figure 2.25 - Kissing bond examples in an Al alloy weld [79]. (edited)

**Root defect** occurs with insufficient heat input or incomplete breakup of surface oxide layers, combined with inadequate pin length for the thickness of the workpiece, can result in the development of a crack line root defect, Figure 2.26.

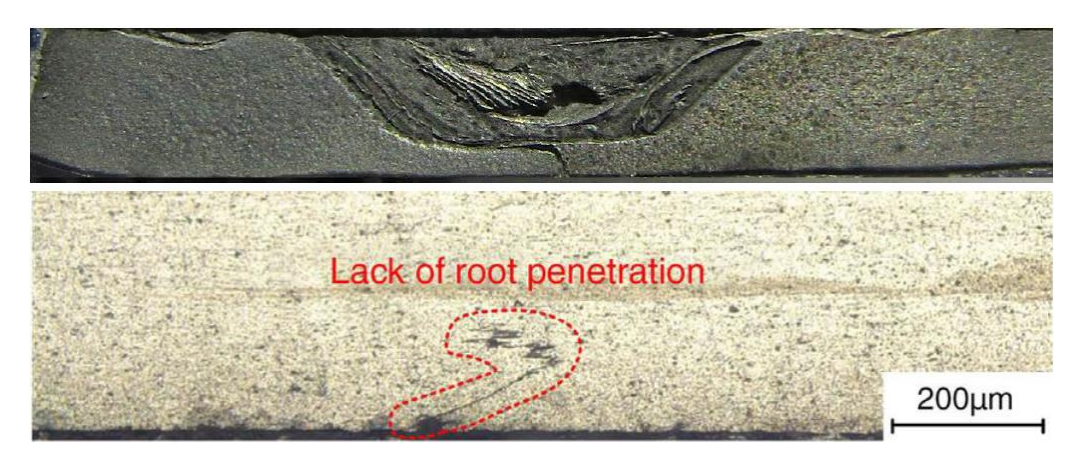


Figure 2.26 - Example of root defect due to lack of pin penetration.

FSW has a number of challenges that must be addressed for its adoption. These difficulties include the requirement for strong clamping mechanisms to maintain stability throughout the welding process and the large reaction forces that call for strong tools and structural support. Furthermore, FSW may result in a decrease in the maximum elongation at break, which would impact the welded material's overall ductility. Crucial components of process control include addressing root defects along the welding seam and controlling the development of exit pin extraction holes, or "keyholes." Furthermore, the upfront expenses linked to FSW equipment and tooling are substantial, underscoring the significance of weighing advantages versus investment issues [55].

Table 2.2 - Defects and challenges of FSW.

Defects	Challenges
- Tunnel defect	- Strong and stiff clamping systems required
- Flash defect	- High reaction forces
- Void formation	- Reduction of maximum elongation at break
- Cavity	- Root defects along the welding seam
- Kissing bond	- Exit pin extraction hole (keyhole)
- Root defect	- High initial costs

## 2.2.2 - FSW of Aluminium-Steel joints

Friction Stir Welding (FSW) finds predominant application in joining dissimilar materials across various industries. In the automotive sector, there is a growing need to weld materials like Al-steel and Al-Mg. Notably, Honda Motor Corporation has successfully employed dissimilar welding of aluminium and steel for a structural component in the Honda Accord [80]. Mazda Motor Corporation has also leveraged FSSW technology to join an aluminium deck lid to galvanized steel brackets, resulting in significant total body weight reduction and cost savings. In the healthcare sector [9], Siemens Medical Solutions utilizes FSW to join domed aluminium sheets to stainless steel sheets in their X-ray equipment [34].

In 2004, Kimapong K et al. [81] successfully butt-joint welded an aluminium alloy plate to a mild steel plate using friction stir welding. They observed the formation of intermetallic compounds at the steel/aluminium interface and noted fracture tendencies along these interfaces. Furthermore, the impact of tilt angle and pin diameter on lap joint strength between aluminium alloy and steel via FSW. They found that increasing tilt angle or pin diameter didn't enhance joint strength due to intermetallic compound formation. They also studied the effect of pre-holes, noting an improvement in joint strength with optimal pre-hole diameter.

Elrefaey et al. [82] investigated FSW of lap joints between aluminium and steel plates. They discovered that slight penetration of the pin tip into the steel surface significantly increased joint strength. Rotation speed positively affected joint strength, while traveling speed had a scattered effect. Takehiko Watanabe et al. [83] explored friction stir welding of aluminium alloy to mild steel plates. They investigated the effects of pin rotation speed and insertion position on tensile strength and microstructure. They observed the formation of intermetallic compounds at the interface and the rubbing motion of the rotating pin removing the oxide film from the steel faying surface. They also examined the effects of pin offset on joint strength and intermetallic compound formation, finding optimal conditions for sound joints.

The optimal operating conditions for FSW of dissimilar metals joints between aluminium alloy and low-carbon steel, by Chen [84]. He evaluated joint quality using impact value and tensile strength and employed ANOVA and Taguchi techniques for analysis, aiming to provide insights for weight reduction in transportation machinery.

In 2009, G. Figner et al. [85] investigated dissimilar Friction Stir Spot Welding (FSSW) of aluminium AA5754 and galvanized steel HX 340LAD, analysing the impact of spindle speeds and dwell times on microstructure and mechanical properties. They examined cross-section microstructures using light optical and scanning electron microscopes, evaluating weld strength through tensile shear and vibration fatigue tests. They also explored the appearance of intermetallic phases and their relation to mechanical properties.

Tsutomu Tanaka et al. [86] investigated the post-weld properties of dissimilar friction stir welds between mild steel and A7075-T6 aluminium alloy. They found that joint strength increased with a reduction in the thickness of intermetallic compounds (IMCs) at the weld interface. Their analysis using the heat input parameter revealed that joint failure depended on the heat input region, indicating challenges in obtaining sound welds that fail at the aluminium base metal.

In 2020, Mohamed Elnabi et al. [87] achieved a dissimilar joint between pure aluminium and annealed low carbon steel using friction stir welding. They utilized high rotational speed combined with low traverse speed to generate significant heat and maximize joint strength. Their study revealed the influence of parameters on intermetallic compound thickness and joint strength.

Reza Beygi et al. [3] studied friction stir welding of dissimilar materials, including aluminium and steel. It was observed the formation of intermetallic compound layers and analysed fracture behaviours under tensile loading conditions. Their findings highlighted the influence of IMC layer characteristics on joint strength and fracture energy. Additionally, they utilized a cohesion zone model to simulate fracture behavior and determine fracture energy values for different welding conditions and treatments. They found that irregularities and steel fragments within the IMC layer could delay crack propagation, affecting joint strength and fracture behavior. Furthermore, their research also involved the successful joining of AA1050 and carbon steel using friction stir spot welding (SSFSW). They observed microcracks at the FeAl-Al interface due to differences in thermal expansion coefficients, which influenced fracture behavior and joint strength. Heat treatment affected the uniformity of the IMC layer and fracture propagation, highlighting the importance of IMC layer characteristics in determining joint properties [88].

# 2.3 - Intermetallic Compounds in FSW

As seen above, the main challenge associated to welding dissimilar metals is the inherent formation of Intermetallic Compounds at the interface of the welded joint. IMCs are a solid-phase chemical compound that forms between two distinct metallic elements [89]. These compounds vary from the metal alloys formed by inclusions of other elements, considered a solid solution of metallic and non-metallic elements in a parent metallic matrix, with a range of variable compositions, where the IMCs presents a specific stoichiometry and unique crystal structures, with the atoms of the composing metallic elements are arranged in a well-defined structure, as seen in Figure 2.27, being a chemically combined compound. Therefore, IMC present their own set of material properties and behaviours, different from the metals formed by the constituents, on their own or in an alloying mixture [89].

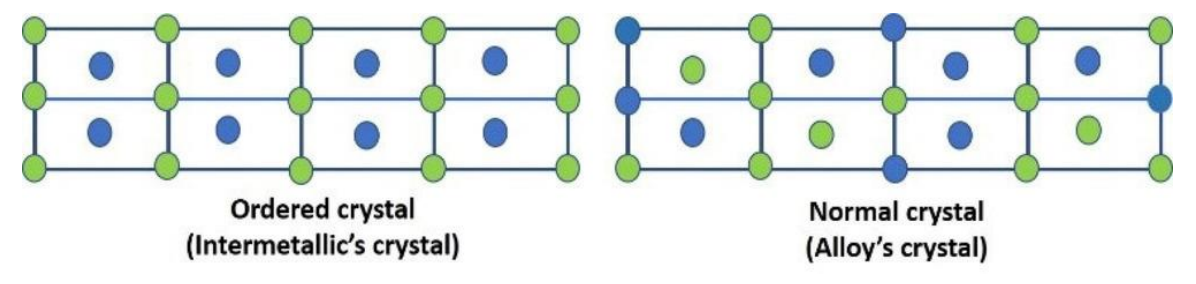


Figure 2.27 - Representation of an Intermetallic crystal structure and a Alloy crystal structure [90].

This class of materials is characterized by their exceptional hardness and their brittle nature at room temperatures, commonly undesirable for structural application due to the comprise of the joint integrity, with a ductility of less than 2% at the most [91], leading to less-than-desirable joint strengths, not viable in many engineered components in the automotive and aerospace. However, intermetallics present good thermal capabilities such as high melting points and reasonably good mechanical properties at elevated temperatures, making them suitable for non-structural uses under extremely high operating temperatures regimes and corrosive environments. Furthermore, these compounds are also often used for their, desirable electrical and magnetic properties. In Figure 2.28, we observed the calculated bulk modulus versus shear modulus (B/G) ratios of diverse Al–Fe IMC phases, denoting their ductility.

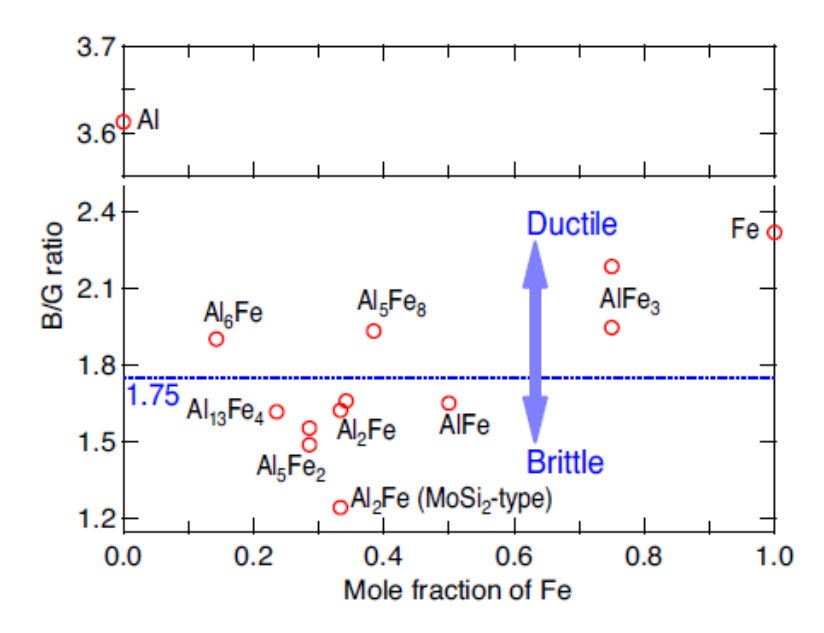


Figure 2.28 - Calculated bulk modulus versus shear modulus (B/G) ratios of Al–Fe IMCs [91].

Intermetallics exhibit a combination of metallic and ionic bonds, dependent on the electronegativity gap between constituent elements. A low gap results in predominantly metallic bonds, while a high gap leads to primarily ionic bonds. Bond nature is influenced by the periodic table pattern of increasing electronegativity from top to bottom and from left to right. When combined with metals from groups 13–16 on the right, transition metals (groups 4–12) on the left significantly enhance the chance of IMC production, seen in the Figure 2.29. Ionic bonds have a high melting temperature and are fragile. Different slip systems have different crystal structures, which affect ductility: face centred cubics (FCC) have 12, body centred cubics (BCC) have 48, and hexagonal close packing (HCP) has 3. Even though

BCC has several different slip systems, obstructions to the movement of the slip plane cause it to become brittle. At room temperature, FCC-based IMCs could be more ductile than BCC-based ones [90].

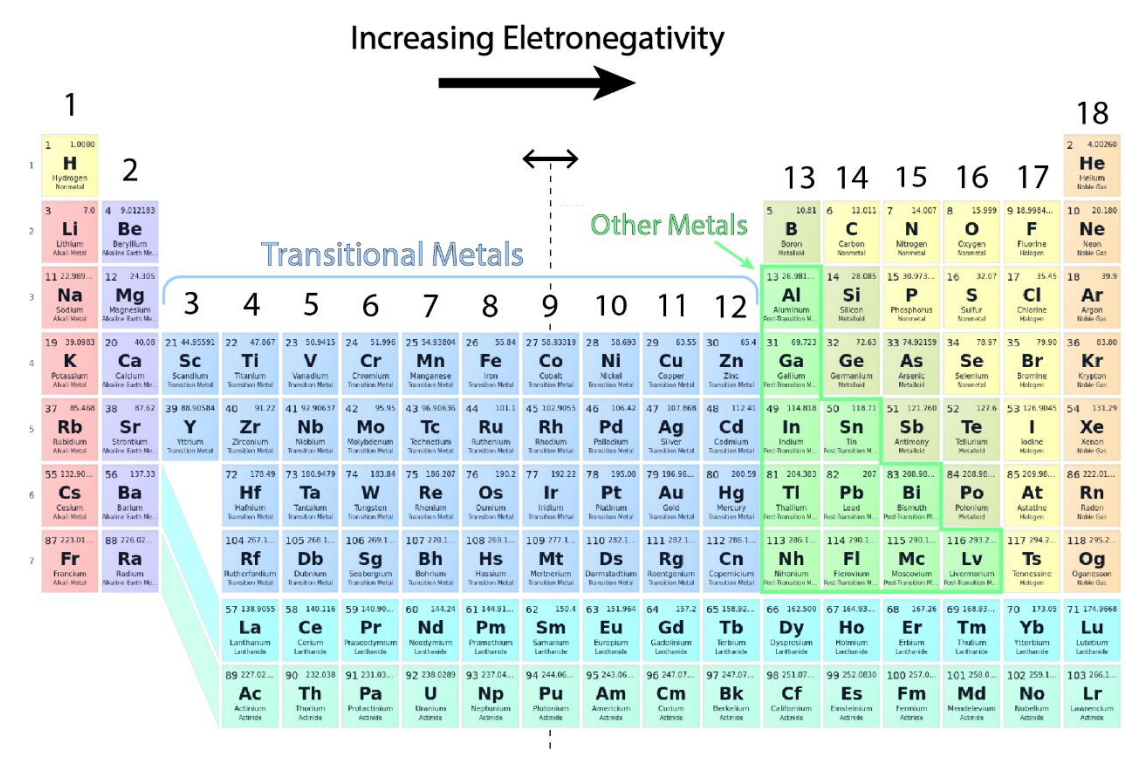


Figure 2.29 - Periodic table regarding the electronegativity of the atomic elements.

A homogeneous matrix free of cracks may form throughout the structure if the IMC phase has a crystal structure like that of its parent materials, such as FCC-FCC or BCC-Laves-BCC. Incompatible matrices, as FCC-BCC-FCC or BCC-FCC-BCC, might potentially result in interface fractures [90].

## 2.3.1 - Iron Aluminides IMCs

In the context of this thesis and the dissimilar material welding of Aluminium to Steel via FSW process, we will be dealing with Iron Aluminides (Fe-Al) IMCs. The Iron Aluminides contains Fe<sub>3</sub>Al, FeAl, FeAl<sub>2</sub>, Fe<sub>2</sub>Al<sub>3</sub>, Fe<sub>2</sub>Al<sub>5</sub>, and FeAl<sub>3</sub> phases. However those more commonly formed under the conditions produced by FSW are Fe<sub>2</sub>Al<sub>5</sub>, Fe<sub>3</sub>Al and FeAl, at temperatures below the melting points of these metals sustained in SSW the process [92]. Several reactions that take place in the Fe-Al binary system are shown in the Table 2.3 below.

Table 2.3 - Reactions in the Fe-Al binary system.

Reaction	Reaction type	Atomic % of Al
$ ext{L} +  ext{FeAl} \leftrightarrow arepsilon$	Peritectic	pprox 60
$\mathrm{L} + arepsilon \leftrightarrow \mathrm{Fe_2Al_5}$	Eutectic	pprox 70.5
$L \leftrightarrow Fe_2Al_5 + FeAl_3$	Unknown	pprox 72
$ ext{L} \leftrightarrow  ext{FeAl}_3 +  ext{Al}$	Eutectic	pprox 76.6
$arepsilon + \mathrm{Fe_2Al_5} \leftrightarrow \mathrm{FeAl_2}$	Peritectoid	pprox 66.5
$arepsilon \leftrightarrow \mathrm{FeAl} + \mathrm{FeAl}_2$	Eutectoid	55
$ ext{L} \leftrightarrow  ext{Fe}_2 ext{Al}_5$	Congruent	71
$lpha Fe \leftrightarrow  ext{FeAl}$	Tricritical	pprox 23.3
$FeAl \leftrightarrow Fe_3Al$	Allotropic	pprox 25

The Fe<sub>3</sub>Al, also known as θ-phase undergoes a structural transformation, maintaining its ordered D03 structure up to 540 °C, transitioning to an ordered B2 structure at higher temperatures, and becoming disordered above 760 °C. The D03 to B2 transition temperature decreases rapidly when the aluminium content surpasses 25%, and above 36% aluminium, the system becomes unstable, converting into FeAl, which has a B2 structure and forms in the range of 30-50% atomic aluminium. However, Fe<sub>3</sub>Al's room temperature ductility is sensitive to environmental factors, especially moisture content, with even a small amount of water vapor inducing embrittlement. Increasing aluminium concentration leads to intrinsic grain boundary instability, impacting ductility. Above 40% aluminium, intergranular fracture results in poor tensile ductility, whereas below 40%, transgranular fracture exhibits significant ductility at room temperature. Thermal vacancies are introduced in the system (>38% aluminium content) through rapid cooling from high temperatures. The severity of embrittlement is observed with an increase in thermal vacancies, reducing tensile ductility. Water vapor induces room-temperature embrittlement by introducing hydrogen. At intermediate temperatures (400-600 °C), the yield strength of increases, contrary to the expected decrease. The constitutional vacancy theory explains this abnormal behaviour, suggesting that at higher temperatures, a large number of vacancies act as pinning agents, increasing yield strength. After reaching peak yield strength, increasing temperature causes movable vacancies, assisting dislocation climb and resulting in softening [90].

The Fe<sub>2</sub>Al<sub>5</sub> structure, referred to as the  $\eta$ -phase, is a phase typically formed in FSW of Aluminium to Carbon Steel. Its existence interval falls within the range of 53 wt.% to 57 wt.% as indicated by the Fe-Al diagram, Figure 2.30. In Al-steel joining processes, a sequence of two IMCs is the monoclinic FeAl<sub>3</sub> initially forms with a needle-like morphology, followed by the orthorhombic Fe<sub>2</sub>Al<sub>5</sub> forming in the steel.

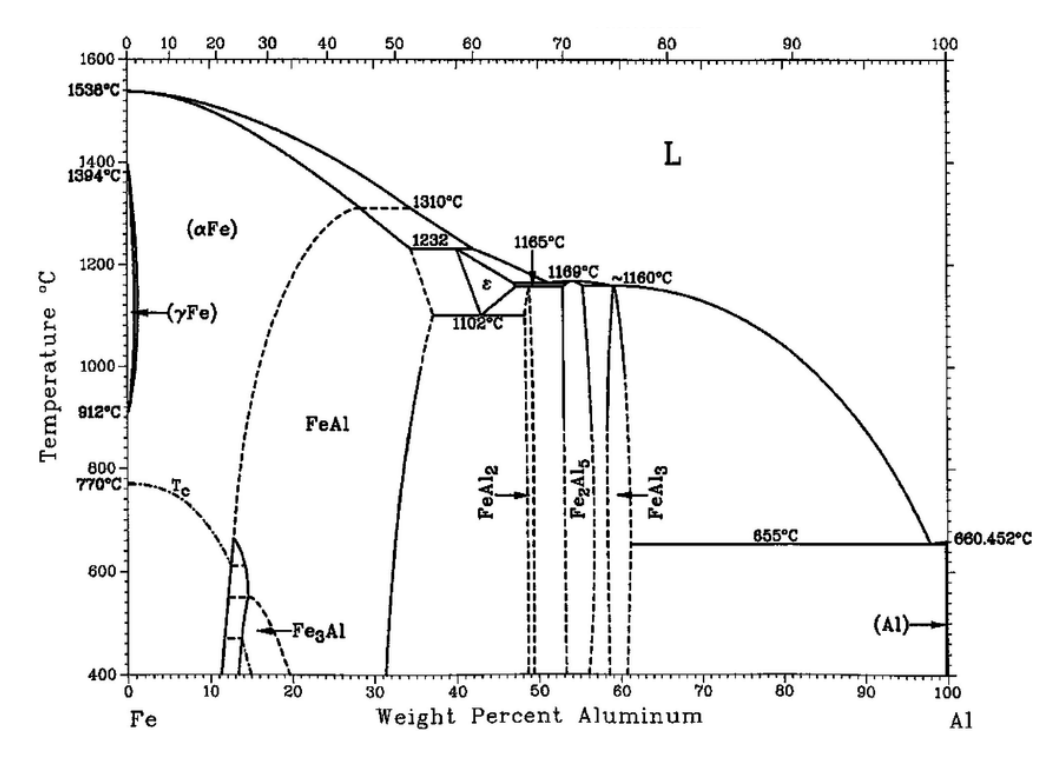


Figure 2.30 - Iron-Aluminium phase diagram.

Cracks within the Fe<sub>2</sub>Al<sub>5</sub> phase primarily consist of primary cracks propagating along the interface and secondary cracks approaching the steel side. The dominance of primary cracks increases with the thickness of the IMC layer. A distinctive feature of the Fe<sub>2</sub>Al<sub>5</sub> phase is the anisotropic network of partial-occupancy Al sites that run parallel to the c-axis in the [001] direction. These sites, having similar energy levels, facilitate greater diffusivity of Al along the c-axis [93].

As the thickness of the Fe<sub>2</sub>Al<sub>5</sub> layer increases, the textured and larger grain size of the Fe<sub>2</sub>Al<sub>5</sub> compound, coupled with diminishing iron phase between the Fe<sub>2</sub>Al<sub>5</sub> grains, leads to a layered IMC structure that is susceptible to crack propagation along the interface. This phenomenon generates primary cracks rather than branching to the steel side to form secondary cracks, ultimately compromising the weld strength [94].

## 2.3.2 - IMC formation mechanism

The formation and growth of IMCs in FSW of Fe-Al involves three main stages: nucleation, formation of intermetallic phases, and growth of the IMC layer at the interface. This is a thermomechanical induced chemical process [68]. Understanding the formation mechanisms of the intermetallic phases that occurs during the welding procedure, as well as having knowledge of the right tools to predict the thickness and phases of the IMC layer, controlling their formation at the interface of the joint, is fundamental for optimizing the welding parameters and to achieve the desirable mechanical properties, avoiding excessive brittleness of the joint, as well as potential defects [95].

• **Nucleation:** At first, the formation of IMC crystal nuclei at the interface between the stirred zone (SZ) and the thermo-mechanically affected zone (TMAZ), where the heat generated by the

FSW tool causes the material around the tool to enter a plasticized state. Fe<sub>2</sub>Al<sub>5</sub> first nucleates at the interface between the SZ and TMAZ, while FeAl<sub>3</sub> is the first to nucleate at the interface of the heat-affected zone (HAZ) due to the limitation of element concentration.

- **Formation of Intermetallic Phases:** After the formation of the IMC crystal nuclei, solute atoms in the solid solution at the interface precipitate out of the supersaturation state. As aluminium and iron atoms continue to diffuse to the interface, the solid solution transforms into a supersaturated state again, leading to the growth of the IMC nuclei.
- **Growth of IMC Layer:** The IMC nuclei continue to be generated at higher grain boundary energy, and the IMC grows along the interface, forming a continuous IMC layer. The growth of the IMC layer at the interface is mainly affected by the diffusion rate of aluminium and iron atoms. The growth of IMC is influenced by factors such as welding parameters, solid-phase diffusion of Fe and Al atoms, welding heat input, and cooling rate.

The two main IMC formation conditions in FSW are temperature and strain, leading to thermally assisted interdiffusion of atoms across the interface of the two metals, and deformation-induced interdiffusion, respectively. This results growth kinetics due to the diffusion of Al and Fe atoms to the interface and in chemical reaction between the two. In Figure 2.31, a theoretical model for IMC formation mechanism during FSW is represented.

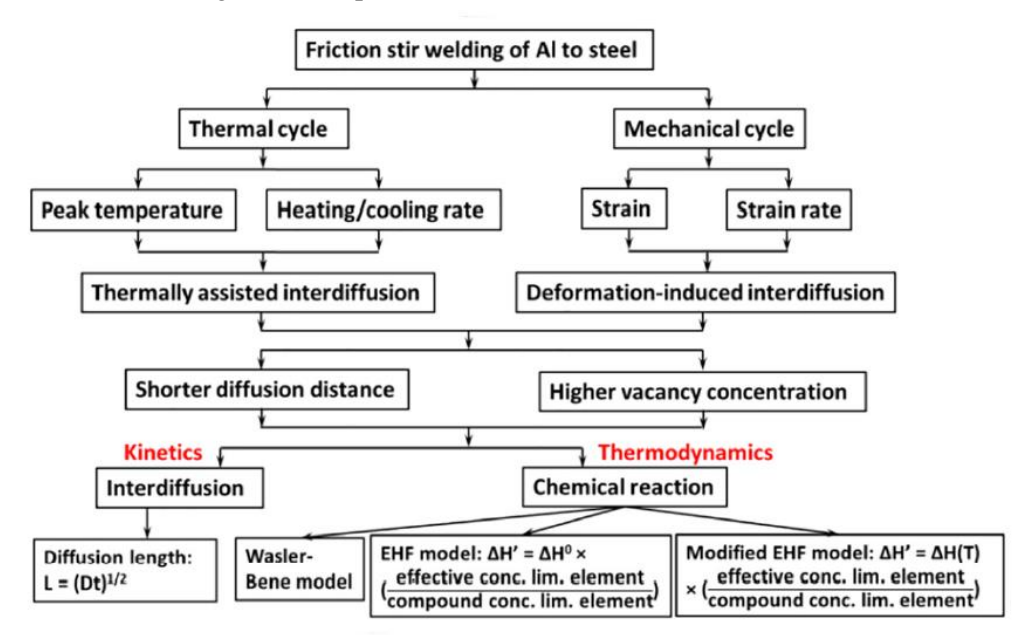


Figure 2.31 - Theoretical model showing mechanism of Al-Fe IMC formation during FSW [95]

Limited information exists regarding the kinetics of IMC growth during FSW due to the challenging synchronization of temperature measurements. Typically, interpreting IMC layer growth kinetics involves fitting thickness as a function of time to a parabolic law, expected for lattice diffusion-controlled growth:

$$x^2 = kt (4)$$

Here, x represents the thickness of the IMC layer (m) after a reaction time t, and k is the rate constant with dimensions of  $m^2 s^1$ . The rate constant, k, is temperature-dependent and is anticipated to follow an Arrhenius relationship:

$$k = k_0 \exp\left(\frac{-Q}{RT}\right) \tag{5}$$

Where  $k_0$  is the pre-exponential factor, Q is the effective activation energy (J mol<sup>-1</sup>), R is the gas constant (J K<sup>-1</sup> mol<sup>-1</sup>), and T is the reaction temperature (K).

Commonly, experimental data at various temperatures are fitted to derive values for  $k_{\theta}$  and Q. However, discrepancies in reported effective activation energies for Fe<sub>2</sub>Al<sub>5</sub> growth indicate a lack of consensus, with significant variations between the smallest and largest values. This inconsistency suggests that a simple parabolic law is not suitable for predictive purposes, as the calculated layer thickness is highly dependent on the chosen activation energy value.

The differences in activation energy values cannot be solely attributed to varying alloy compositions or the state of aluminium (liquid or solid). Additionally, there is no systematic variation in activation energy that correlates with aluminium state or alloy composition details. Studies using pure Al to pure Fe couples showed the lowest (74 kJ mol<sup>-1</sup>) and highest (281 kJ mol<sup>-1</sup>) activation energy values [92, 96, 97]. The typical values for the effective activation energy of the commonly formed phases in FSW of Al-Fe are shown in the Table 2.4 below.

Table 2.4 - Effective activation energy Q of the commonly formed phases in FSW of Al-Fe.

Fe-Al phases	Activation energy, Q [kJ/mol]	
Fe <sub>2</sub> Al <sub>5</sub>	167	
Fe₃Al	260	
FeAl	180	

# Chapter 3

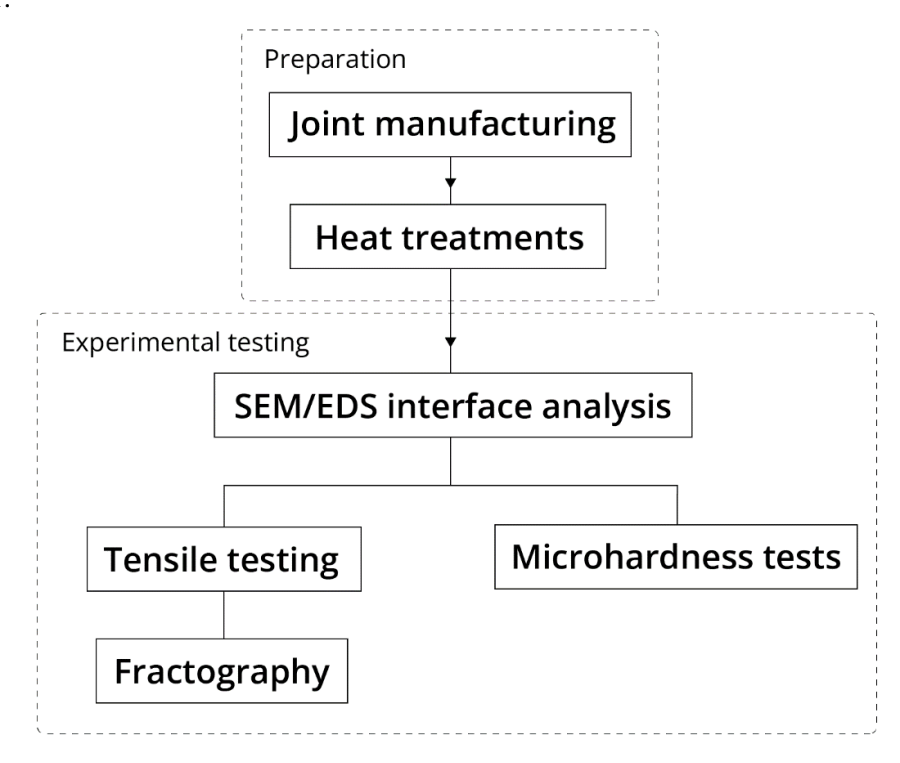
# **Experimental Work**

In this chapter, the experimental work will be presented and discussed, starting with experimental details of the preparation, namely the FSW joint manufacturing and the heat treatments performed to these, for the experimental tests that followed, starting with the analysis of the interface of the weld, where the thickness and the chemical composition of the IMC layer and surroundings were measured at different zones of the joint, by Scanning Electron Microscope (SEM) and Energy-Dispersive X-Ray Spectroscopy (EDS), respectively. Thereafter, quasi-static tensile testing was conducted for each aswelded samples and for a series of heat treatments, followed by the fractography of the failed specimens. Moreover, a Vickers microhardness analysis of the samples was also performed. In the end, the experimental results are presented by each test and correlated regarding each heat treatment, drawing the IMC layer growth kinetics.

# 3.1 - Experimental details

In this subchapter, the preparation, consisting in the manufacturing of the joints and heat treatments, and the experimental testing will be discussed in detail. The workflow diagram, as explained, is represented in

Figure 3.1.



# 3.1.1 - Joint manufacturing

In the scope of this dissertation, dissimilar 1050 aluminium / St37 steel metal butt joints were manufactured by FSW. Furthermore, the joints were manufactured with dissimilar substrate thicknesses, with 5 mm thick aluminium and 2 mm thick steel base metal plates.

The main substrates properties relevant to the work are present in the following Table 3.1.

Table 3.1 – Mechanical properties and chemical compositions of St37 carbon steel and 1050 Aluminium.

St37 carbon steel	1050 Aluminium	
Tensile strength - 370 MPa	Tensile strength - 100-135 MPa	
Yielding strength - 300 MPa	Yielding strength - 85 MPa	
Vicker's hardness - 120 HV	Vicker's hardness - 41 HV	
Chemical composition:	Chemical composition:	
Fe: 99.43 - 99.75%	Al: 99.5 % Mg: 0.05 %	
C: 0.08%	Si: 0.25 % Zn: 0.07 %	
Mn: 0.25 - 0.4%	Fe: 0.40 % Ti: 0.05 %	
S: 0.05%	Cu: 0.05 % Others: 0.03 %	
P: 0.04%	Mn: 0.05 %	

To obtain reliable joints with the desired dissimilar thickness, a FSW jig consisting in 1 mm and 2 mm aluminium support plates on the bottom and top of the St37 substrate plate, respectively, was used to eliminate the gaps to the welding table and to the shoulder of the tool, as seen in Figure 3.2.

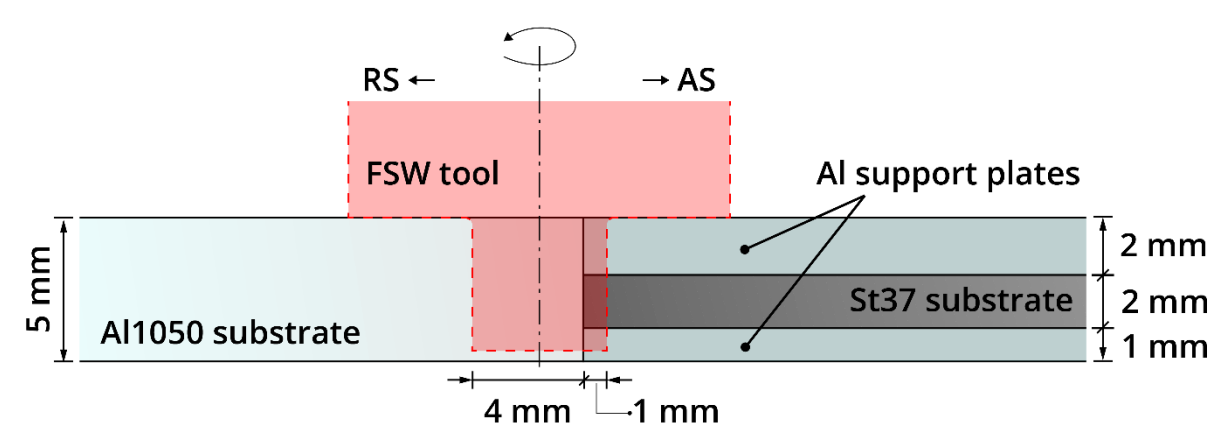


Figure 3.2 – Schematic representation of the FSW mount apparatus used to manufacture the Al-steel joints.

The tool pin had an offset to the RS, with 4 mm in the Al1050 substrate and 1 mm in the St37 substrate, and a tool tilt angle ( $\theta$ ) of 2.5 °.

A H13 tool-steel FSW tool used to weld the dissimilar joints has an 18 mm shoulder diameter, 4.7 mm pin length and 5 mm pin diameter, as seen in Figure 3.3.

Moreover, the tool rotation speed ( $\omega$ ) used was 950 RPM, counter clockwise (CCW) and the tool traverse speed (Vx) was between 10 and 20 mm/s.

Table 3.2 presents all the FSW parameters and tool specifications used in the manufacturing of the joints.

Table 3.2 - FSW parameters and tool specifications

FSW parameters	Tool specifications	
- Tool rotation speed (ω): 950 RPM, CCW	- Material: H13 tool steel	
- Tool traverse speed (Vx): 10-20 mm/s		
- Tool tilt angle ( $\theta$ ): 2.5 °	- Tool shoulder concavity: 2.5 °	
- Axial force (Fn):	- Tool pin diameter: Ø 5 mm	
- Pin plunge depth : 4.7 mm	- Tool pin length: 4.7 mm	
- Tool offset: 1.5 mm to RS		

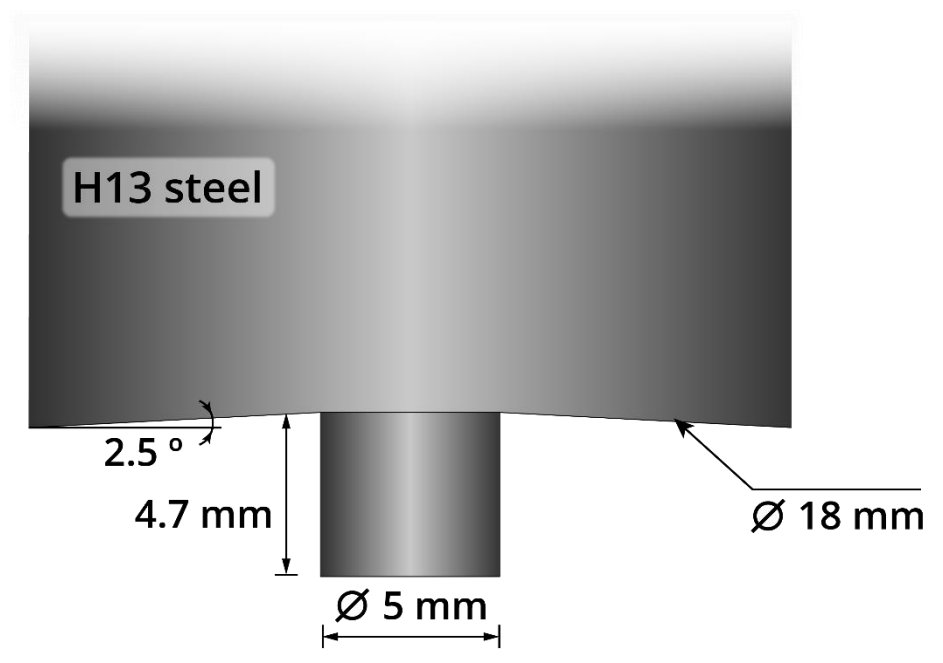


Figure 3.3 - Schematic representation detail of the tool's shoulder and pin, with the respective dimensions.

After the welding of the substrate plates, the steel support plates were removed, and the joint was cut into several specimens using Wire Electrical Discharge Machining (WEDM), represented in Figure 3.4.

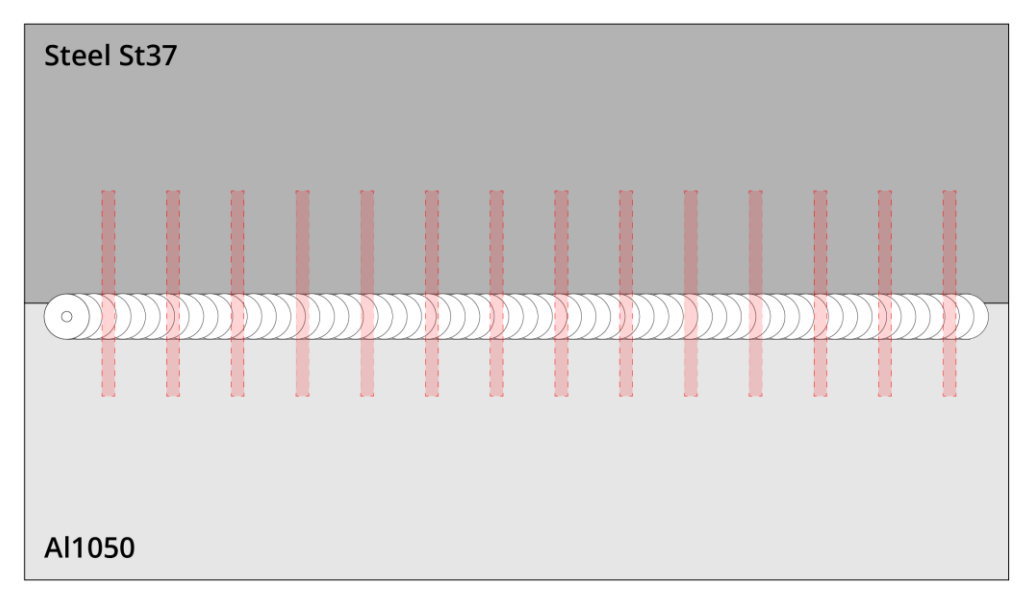


Figure 3.4 – Top view schematic representation of the joint substrate plates after welding, with the WEDM cut specimens, represented in red.

A weld with dissimilar thickness was manufactured, resulting in the joint geometry seen in Figure 3.5, where the image upper part coincides with the top side of the weld - a noticeable S-shape joint cross-section geometry, with the upper tip facing the steel substrate and the lower one facing the aluminium substrate, occurring in the penetration of this base metal.

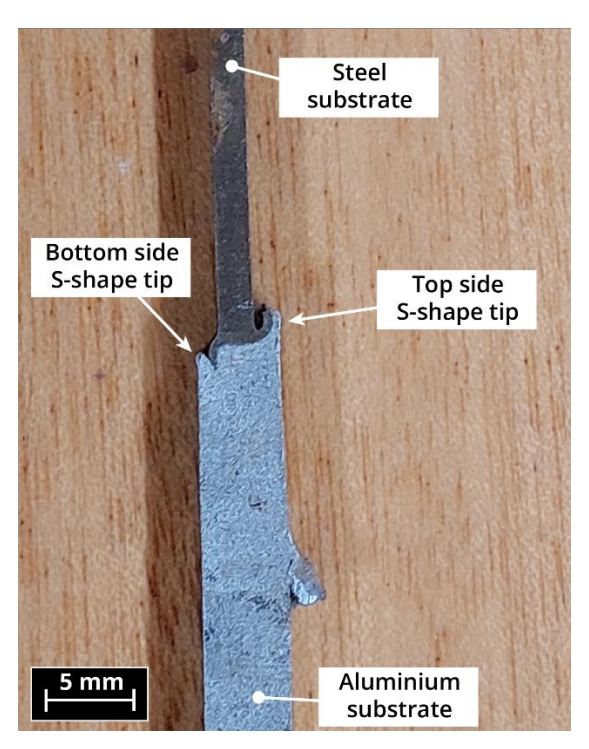


Figure 3.5 – Section of a manufactured joint, showing the S-shape interface.

This phenomenon is attributed to the material flow during the solid-state welding, characteristic of FSW. In the steel side of the joint, the advancing tool velocity and the rotation velocity are in concordance, having the same direction – advancing side (AS) of the weld, while in the aluminium side,

these two velocities have an opposite direction – retreating side (RS) of the weld, resulting in an asymmetry in the flow of the two materials, being in a plastic regime, and therefore a asymmetry in the microstructure of the joint after cooling [60].

The high hydrostatic pressure applied at the top side of the joint by the shoulder of the tool causes a displacement of the plasticised material from the tool outwards, leading to the observed unique upper tip of the S-shape. At the bottom of the tool's pin, a swirl motion caused by the asymmetric flow of the plasticised material, generating rotation and translation of the materials from the advancing side to the retreating side of the joint [61], resulting in the penetration of St in the Al substrate. Also, it is possible to observe, at the bottom side of the joint, an aluminium tip, with an approximately thickness of 0.6 mm, where no weld is present, and thus no IMCs are formed, as observed in Figure 3.5.

### 3.1.2 - Heat treatment

In the scope of this master's thesis, with the aim of analysing the impact of temperature in the degradation of Al-steel joint characteristics by FSW, a series of heat treatments were performed on the manufactured samples and specimens, annealing the joints, and promoting the growth of the IMC layer at the interface.

In order to trace the IMC layer growth kinetics, 9 temperature and time pairs were selected, varying from 100 °C, 250 °C and 400 °C, and 30 min, 60 min and 90 min. For each pair temperature/time, 3 specimens for tensile testing and 1 sample for SEM/EDS analysis were treated. The samples were allocated to each pair temperature/time in a controlled manner, with the aim of having a homogeneous distribution and minimizing the manufactured batch bias, that could lead to misleading results and incorrect correlations. The designation of each heat treatment pair is represented in the Figure 3.6.

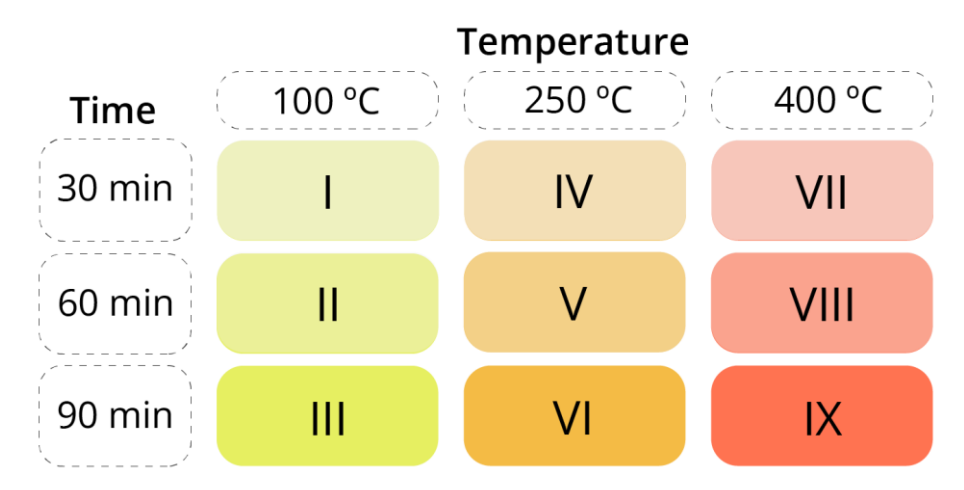


Figure 3.6 – Schematic matrix of the heat treatment pairs.

### Heat treatment procedure

For each temperature/time pair, the heat treatment procedure consisted on the following steps:

1. The tensile test specimens and SEM/EDS sample were placed in the configuration shown in Figure 3.7 (a). A thermocouple was placed at the joint interface, ensuring a correct measurement

of the temperature of each heat treatment, Figure 3.7 (b) and (c).

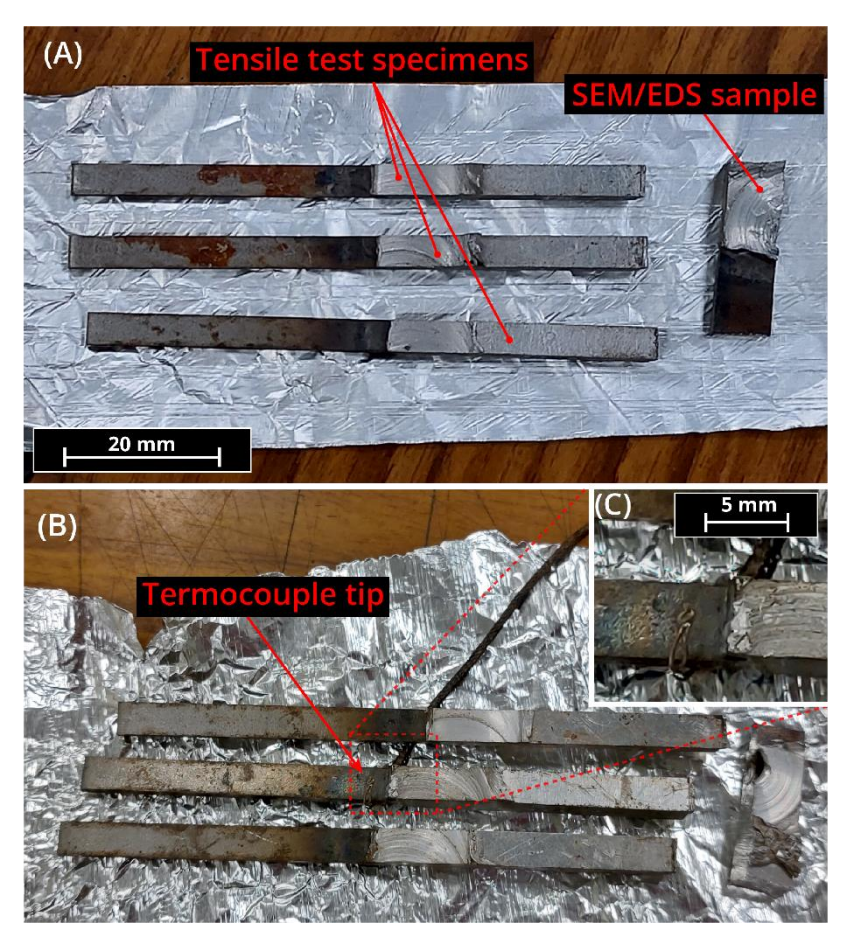


Figure 3.7 - Specimens and sample configuration (a) with a thermocouple attached one of the specimens at the interface of the joint (b). Close-up of the thermocouple tip located at the joint (c).

2. The joints were wrapped with aluminium foil, with the aim of diminishing the effects of the oxidizing atmosphere present in the oven, and a plate of steel was placed over the aluminium foil, guaranteeing that the thermocouple tip was in contact with the joint throughout the complete heat treatment. The preparation used for the heat treatments is shown in Figure 3.7, as described above.

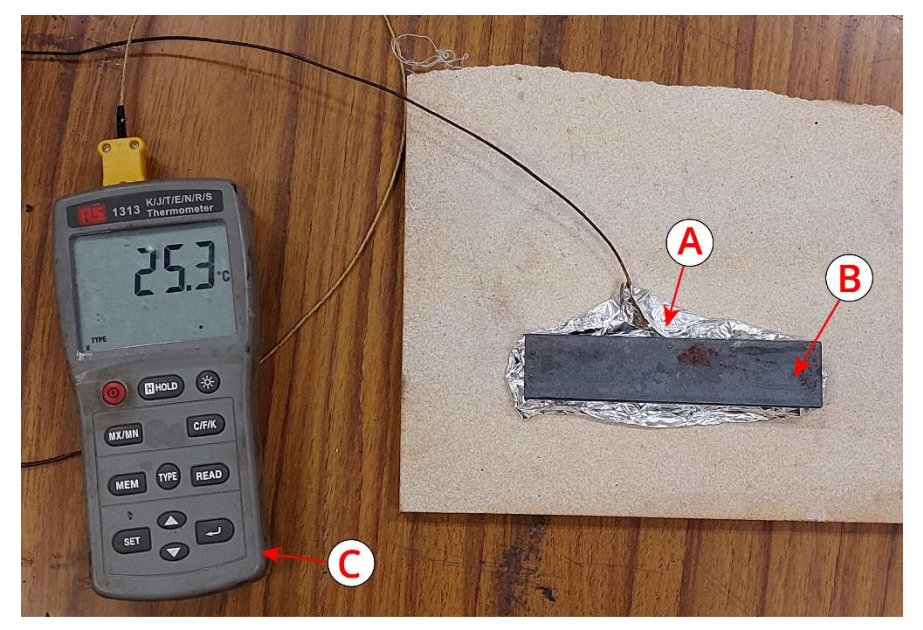


Figure 3.8 – Preparation for heat treatment, with the aluminium foil wrap (a) and steel plate (b). In (c) we have the thermometer used in the preparation.

- 3. The preparation was placed inside the oven when the target temperature was reached, measured by the oven's thermometer, Figure 3.9 (a) and (b), respectively.
- 4. At the end of the heat treatment time, the joints were left to cool at room temperature.

During the heat treatments, the temperature of the joint was regularly compared to the temperature displayed by the oven thermometer and the nominal temperature regarding the same pair temperature/time. During these procedures, offsets were observed between the measured temperatures at the joint and the nominal temperature for each the heat treatment. The maximum temperature offset recorded between the two was 9.9 °C for the pair **VII** (30 min at 400 °C), resulting in a heat treatment at 390.1 °C, as observed in Figure 3.9 (c). Addressing this maximum offset, an increase of 5 °C was set to oven temperature for the pairs **VIII** (60 min at 400 °C) and **IX** (90 min at 400 °C), resulting in a decrease between the nominal and joint temperatures difference approximately of 5 °C. For the remaining heat treatments, the temperature offset observed did not exceed 5 °C.

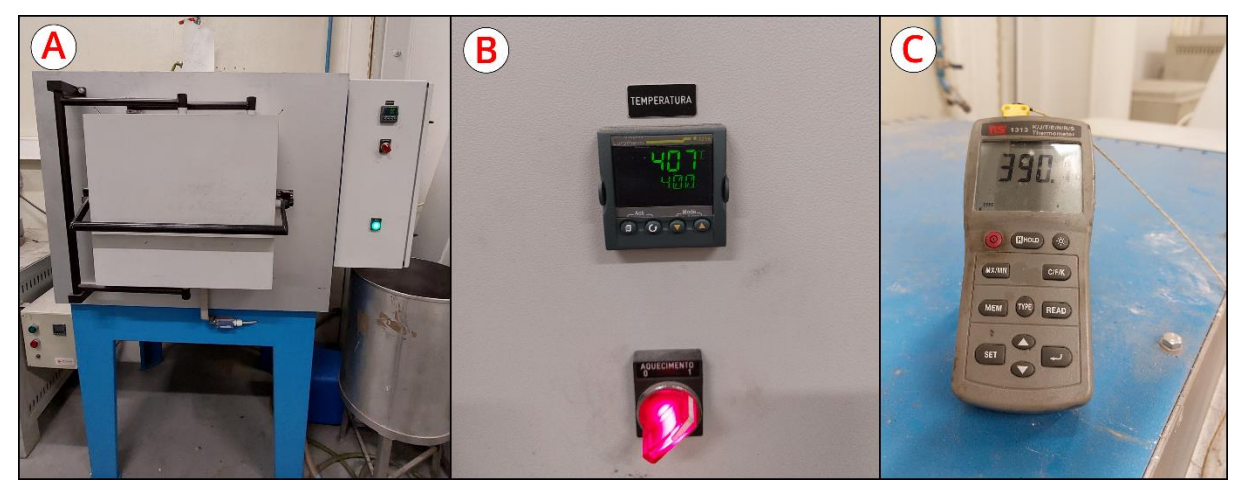


Figure 3.9 - Images of the oven used in the heat treatments (a), oven temperature display (b), and thermocouple thermometer (c)

# 3.1.3 - Experimental tests

With the aim of studying the degradation of the Al-steel joints, two types of joint were used for the analysis: complete joint specimens, for tensile testing and subsequent fractography, showing Figure 3.10 (a), and samples for the microstructure analysis of the joint and microhardness measurements, Figure 3.10 (b).

In this section, an extensive discussion of testing procedures will be presented.

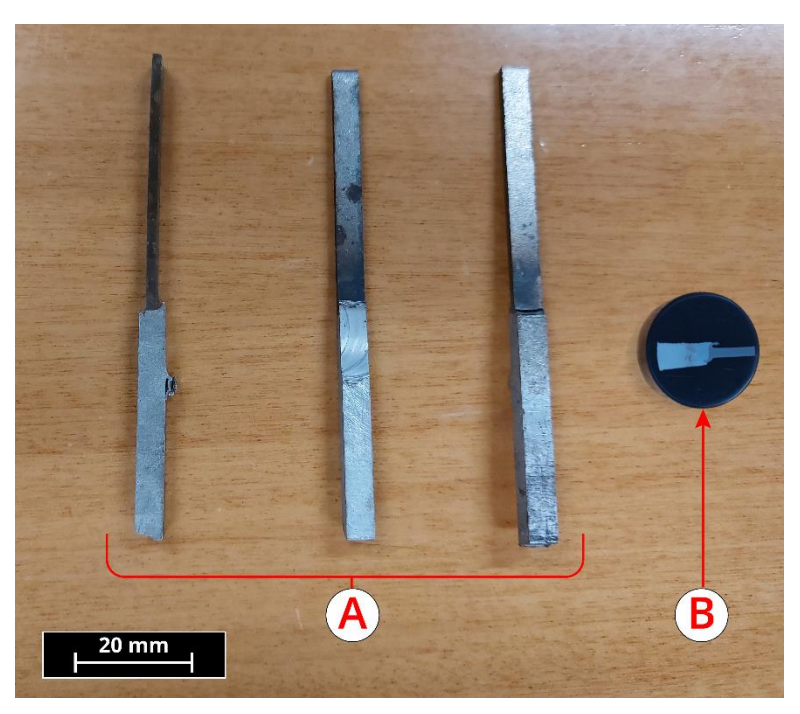


Figure 3.10 - Example of the specimens used for tensile testing and fractography (a), and sample for microstructure analysis and hardness measurements (b).

## 3.1.3.1 - SEM/EDS interface analysis

The analysis of the microstructure by SEM/EDS of the interface of the joints has three main goals: observing the microstructure and detailed geometry of the interface friction stir welded zone, otherwise challenging at a macroscale; measuring the IMC layer thickness at the Al-steel interface, allowing to draw the IMC layer growth kinetics by heat treatment and correlation with the tensile strength, joint degradation establishing cause-effect relation; and the study of the chemical composition of the joints, by performing EDS line-scans, obtaining atomic percentage across the interface.

The SEM/EDS examination was carried out using a high-resolution environmental Scanning Electron Microscope (Schottky) with X-ray Microanalysis and Analysis of Backscattered Electron Diffraction Patterns: FEI (Hillsboro, Oregon, USA) model Quanta 400FEG ESEM/ EDAX Genesis X4M. The samples were coated with Au/Pd thin films by sputtering using the SPI Module Sputter Coater for 80 s and with a 15 mA current.

The SEM/EDS analysis was divided in two sessions, the first being for the as-welded sample, named Sample00, presented in Figure 3.11 (a), which besides de aforementioned goals, had the purpose to ascertain what zones of the joints are worth of examinate in the following session, where all the heat treated samples were analysed.

For the SEM/EDS preparations, the manufactured samples were cut with a handsaw at the extremities to size and mounted in standard Epoxy preparation. The preparations were subjected to a planar griding process, going through 200p, 600p, 800p, 1200p grit discs, and finally polished in an alumina solution and finalized in a 3 µm diamond paste. To ensure the quality of the surface preparation, the samples were brought to the optical microscope and further polishing was carried, to remove all scratches and achieve a mirror-like surface. In the end, the samples were cleaned in an Isopropyl Alcohol bath.

For the first session, a sample preparation containing only the as-welded sample was analysed. The six zones studied were:

- U: upper part of the interface
- M1, M2 and M3: middle part of the interface
- L: lower tip of the interface
- **B**: bottom part of the interface

The zones examinated in the first session are represented in Figure 3.11 (b).

A 35x magnification SEM image was taken of the joint interface, and for each zone 1000x up to 30 000x magnification was used, as well as EDS line scans, enabling us to analyse the atomic percentage of Al and Fe of the interface.

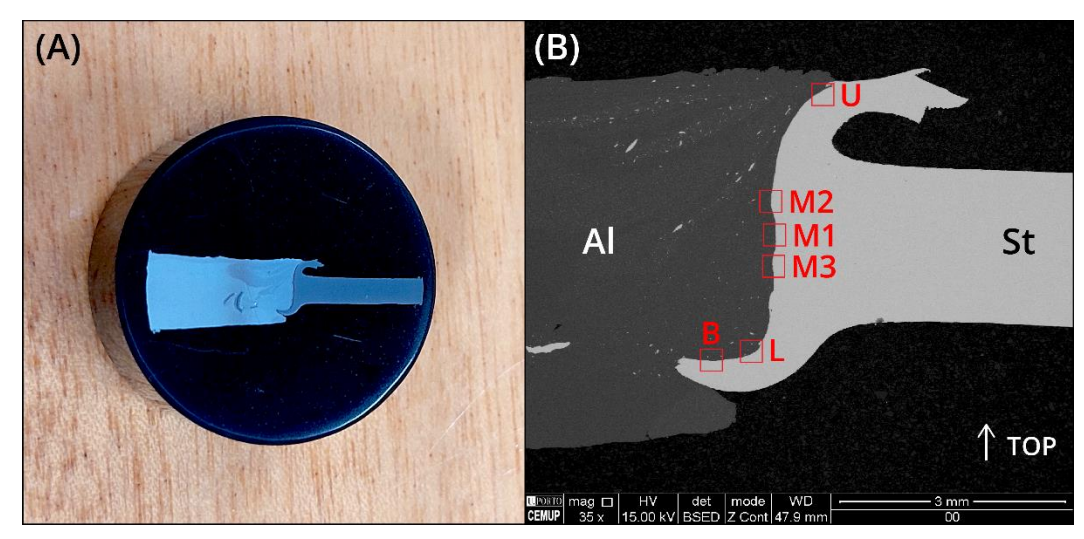


Figure 3.11 - Sample preparation for the as-welded Al/St joint (a) and joint interface – SEM image in BSE mode of the joint, at 35x magnification (b)

For the nine heat treated samples, a configuration of two preparations, one containing sample **I** to **V**, and the second sample **VI** to **IX**, represented in Figure 3.12. As observed in the first SEM/EDS session, the most compelling zones to examine for the heat-treated samples session were the upper zone **U**, the middle zone, that we called **M2**, and the bottom zone of the joint **L**.

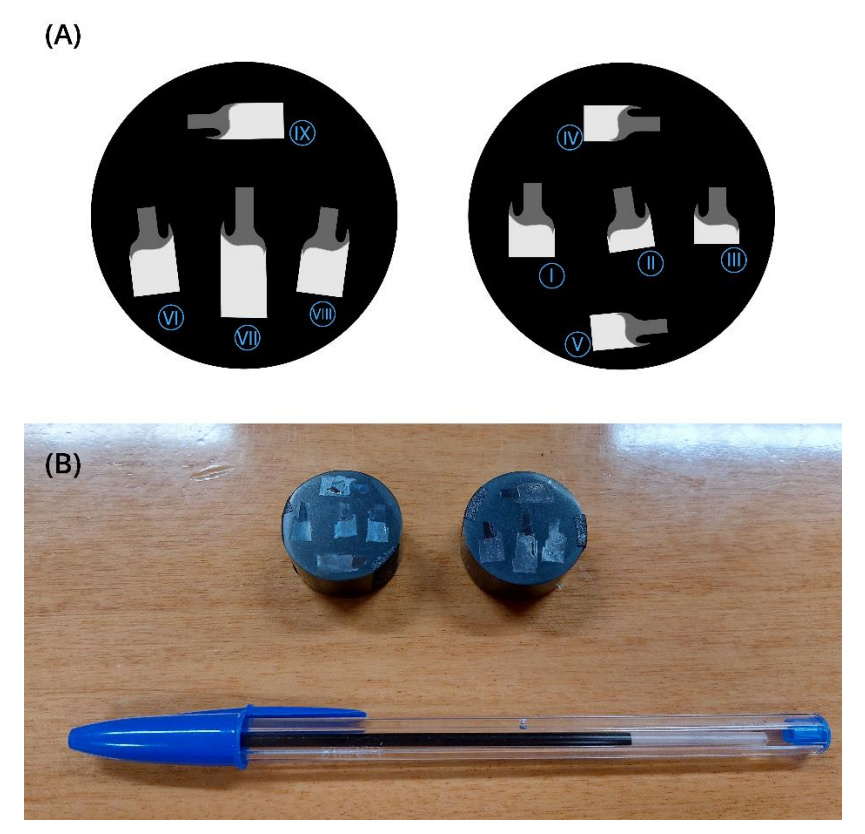


Figure 3.12 - Heat treated sample preparations for the second SEM/EDS session, (a) sample preparation photography and (b) schematic representation and identification.

For each sample, a 35x magnification SEM image of the joint was taken, along with magnification of 1000x and 10 000x imaging for all the zones, with the exception of sample **I**. An additional 30 000x image for the middle zones was recorded, as well as an EDS line scan. The magnification by zone is represented in Table 3.3.

Table 3.3 - Imaging magnification used in each zone of the sample.

Sample zones	Imaging magnification	
Joint	35x	
Upper zone <b>U</b>	1000x, 10 000x	
Middle zone M2	1000x, 10 000x, 30 000x	
Lower zone L	1000x, 10 000x	

All post-processing of the images and the consequent measurements were performed in *ImageJ* software, collecting a number of 15 to 20 thickness measurements for each zone, and averaging to an IMC layer thickness value for **U**, **M2** and **L** for every sample.

By means of EDS, line scans were performed at the zone M2 for samples III to IX, and for all the zones in the as-welded sample, collecting the atomic percentages (at.%) of Aluminium and Iron present across the joint interface. The data was plotted along the line scan length and overlayed to the line scan images, in order to have a prediction assessment of the IMC layer phases present across the interface, comparing the at.% present in the joints with an Al-Fe phase diagram.

### 3.1.3.2 - Tensile Testing

The Quasi-static tensile tests had the aim of characterizing the tensile strength of the manufactured joints, for the as-welded specimens and all the heat treatments, obtaining load-extension curves and enabling the comparison of the results and the correlation of the joint performance with the IMC layer thickness previously measured via SEM imaging.

For the tests, a universal test machine INSTRON® (Norwood, Massachusetts, USA) model 3367 was used, at a constant displacement rate of 1 mm/min at room temperature and humidity. The specimens were loaded in the longitudinal direction, with the interface facing the front of the test machine.

Additionally, the tensile tests were video recorded in Macro-mode at the joint interface with the goal of observing the failure behaviour of the specimens. The load-extension curves and the videos were time matched, and both were recorded until the complete detachment of the two failed halves. The previously mentioned interface surface of the specimens was polished before each test, removing the oxide layer present, allowing a good video recording of the joint failure. The setup for the tensile test is shown in Figure 3.13.

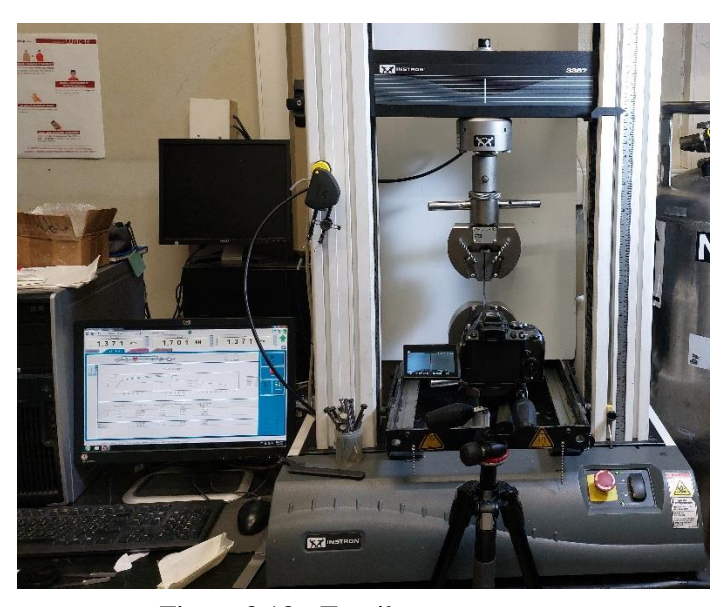


Figure 3.13 - Tensile test setup.

The simultaneous analysis of the load-extension curves and videos allows for further comprehension of the joint failure behaviour, showing the localized failure stages and mechanisms throughout the tensile tests.

The specimen's clamping system in Figure 3.14. By using the chosen clamping system, we ensure self-alignment of the specimens in a vertical direction and the accommodation of the offset seen between the top and bottom side of the joint, diminishing its possible influence upon loading.

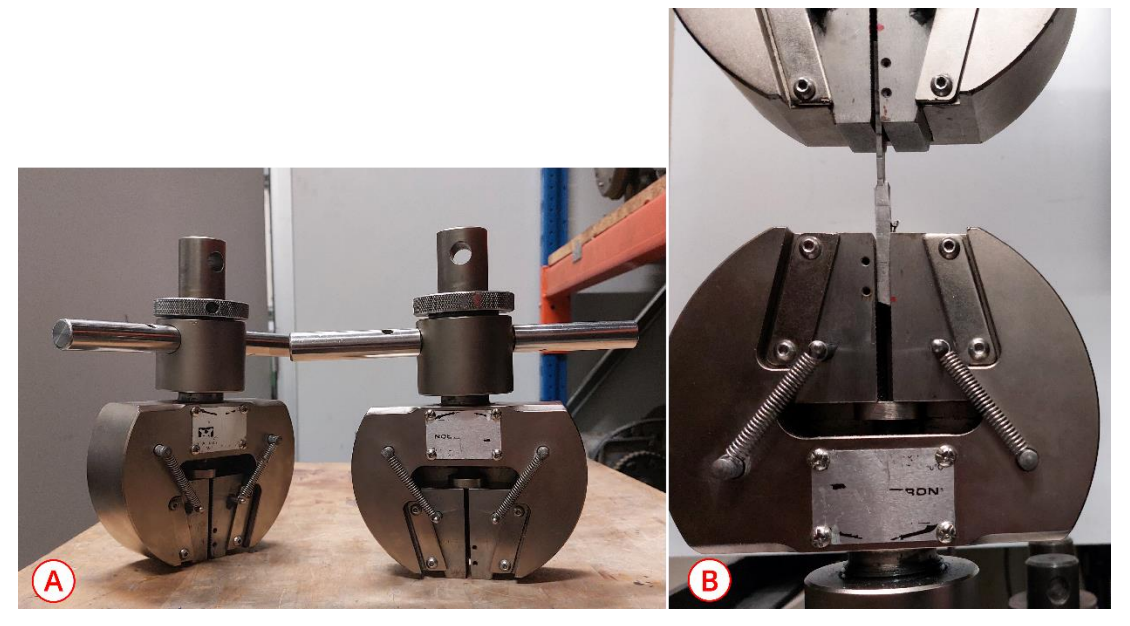


Figure 3.14 - Tensile test clamps (a) and detail of a specimen mounted in the tensile machine clamping system (b).

At the end of each tensile test, all the samples were photographed and carefully catalogued for further fractography analysis, avoiding any hand contact with the failure surfaces.

## 3.1.3.3 - Fractography

Following the tensile tests, SEM/EDS fractography was performed at the fracture surfaces, for the two halves, for three chosen specimens, resulting in the analysis of 6 samples. This analysis had the aim of studying the fracture behaviour of the joints and the failure zones intrinsic to this unique dissimilar thickness Al-steel joints, correlating these results with the tensile test data and videos of the fracture.

For the analysis, one 90 min samples for 100 °C, 250 °C and 400 °C (**III**, **VI** and **IX**, respectively) were selected, favouring the specimens that failed in the patterned manner observed in the tensile tests, disqualifying the outliers from this selection.

The two halves of each specimen were cut to the minimal height possible without compromising the failed surfaces, using a handsaw. Additionally, the surfaces were always kept protected by aluminium foil, avoiding any contamination and contact with outside agents, preserving the topology and conditions resulted in tensile tests. To ensure the sample were clean for SEM, mainly due to handling, testing and ultimately cutting, the samples were ultrasonically cleaned in Isopropyl Alcohol. Lastly, the specimens were mounted in parallel to SEM Pin Stubs using carbon tape. All the preparations were catalogued before the examination, accordingly to the heat treatment pair (III, VI or IX) and base metal half of the specimen (Al or St).

The fractography analysis was performed using a high-resolution environmental Scanning Electron Microscope (Schottky) with X-ray Microanalysis and Analysis of Backscattered and Secondary Electron Diffraction Patterns: FEI (Hillsboro, Oregon, USA) model Quanta 400FEG ESEM/ EDAX Genesis X4M.

Firstly, we examined the entire fracture surface area of the 3 specimens, for Al side and St side, then we increased the magnification in the zones of interest, both topologically and in terms of chemical composition, carrying out EDS zone analysis. All images were taken in both Secondary Electron and Backscattered Electron modes.

### 3.1.3.4 - Microhardness analysis

The selected samples to measure the Vickers microhardness along the joints were the as-welded sample **00**, and the three 90 min heat treated samples at 100 °C, 250 °C and 400 °C (**III**, **VI** and **IX**, respectively), due the same reasons discussed in the previous section. The microhardness testing machine used was a Shimadzu (Japan) model HMV-G30, equipped with a Vicker's microhardness indenter, a 10x and a 40x magnification lens.

For each sample, 3 microhardness line measurements were conducted: upper and bottom zones, designated U and B respectively, starting in the upper or bottom tip of the steel side of the joint, and continuing across the aluminium substrate, reaching the end of the sample, and a middle zone, named M, across all the joints, represented in Figure 3.15. At the upper and bottom steel tips, considering the available small area in these zones, it was impossible to conduct more than one measurement in the steel side.

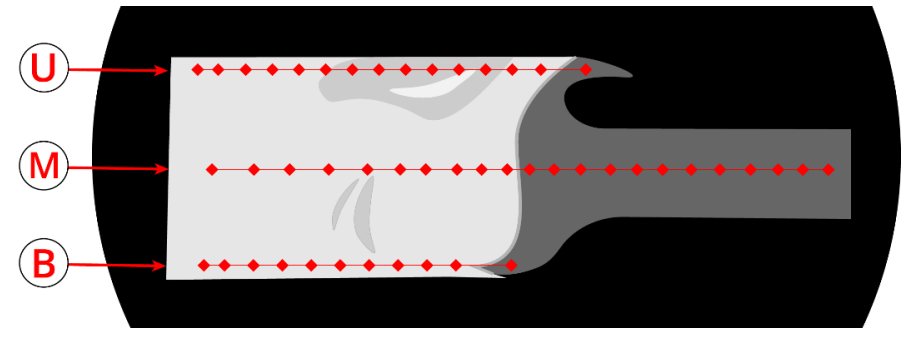


Figure 3.15 - Schematic representation of the microhardness lines measurements U, M and B, for the as-welded sample **00**.

Each microhardness line measurement started in the steel substrate and the distance between indentations was measured in conjunction with the Vickers' Hardness value. Furthermore, the results were plotted in a HV Microhardness vs. Length graph, with the origin of the later representing the first indentation of the steel substrate.

## 3.2 - Experimental results

In this subchapter, the results obtained in all the analysis performed on the Al-steel joints is presented and discussed. To start with, the data obtained in the SEM/EDS session, consisting of the IMC layer thicknesses of the samples is presented, and followed by the analysis of the microstructure and chemical composition of the interface, and surrounding areas, of the joints. Then, the results of the tensile tests are presented, sorted by heat treatment pair and specimen, and the summary of the 32 tests performed, followed by the fractography of the chosen specimens, representative of the results obtained. In the end, the third component of the results, the microhardness measurements, is discussed.

# 3.2.1 - IMC layer thickness

In the context of this work, the thickness of the IMC layer for each one of the heat treatments is one the most useful data points collected, enabling the assessment of the effectiveness of temperature and time in the microstructure of the joint's interface, drawing the kinetics of the Al-Fe IMC phases growth for this kind of FSW joints with dissimilar thickness and to study the impact of the dimensions of the IMC layer in the degradation of the joints mechanical properties.

As referenced previously, the thicknesses presented are an average of a number of measurements performed along each zone, via the post-processing of the SEM imagery of the joint samples in *ImageJ* software.

The as-welded and the heat treatment samples were measured in the three zones discussed, with the exception of the sample  $\bf I$  for 100 °C / 30 min, on account of time constraints at the SEM session where the imaging was being collected. However, due to the low thermal energy input in the interface of the sample  $\bf I$  interface and comparing to the thicknesses of the samples for the same temperature heat treatment, it is estimated that no major significant growth of the intermetallic layer took place.

	IMC layer thickness [μm]		
	Upper	Middle	Lower
as-welded	4.0	2.5	0.8
II	3.7	2.5	2.5
III	4.6	2.6	1.3
IV	3.7	2.4	1.3
V	3.3	2.1	0.8
VI	3.6	2.5	1.9
VII	4.6	3.3	2.0
VIII	5.2	3.1	2.2
IX	5.3	3.5	2.5

The IMC layer thicknesses measured in the three zones were plotted by heat treatment and a linear trendline was drawn for each one of the zones. Figure 3.16 shows the plotted measurements.

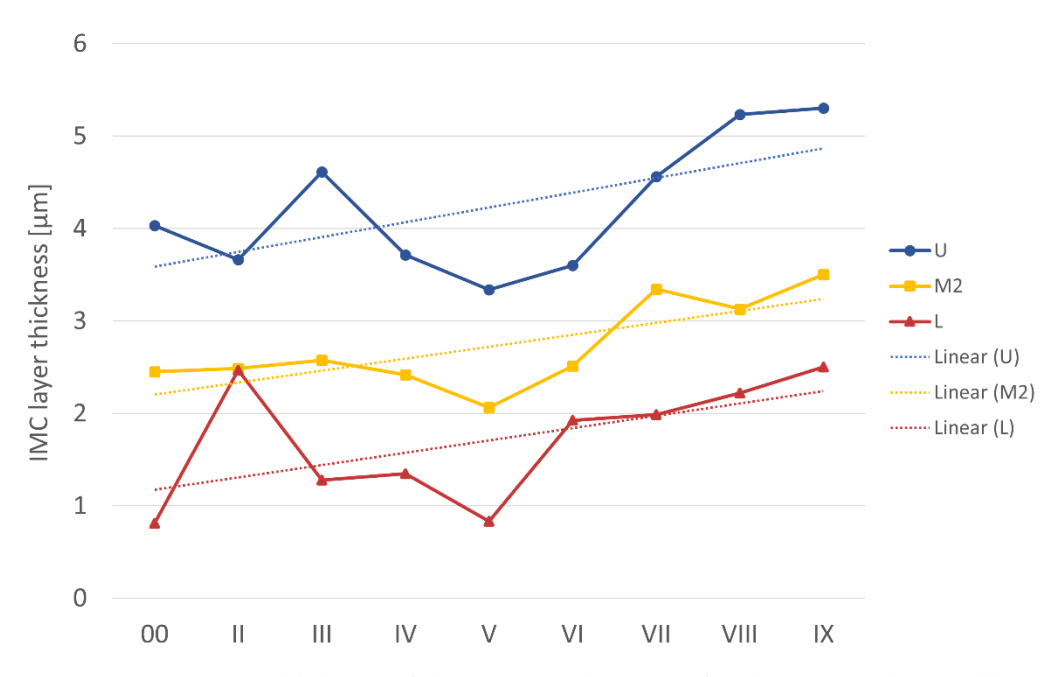


Figure 3.16 – Average IMC thickness of the U, M2 and L zones for the measured as-welded and heat treated samples, and linear regressions.

The thicknesses measured at the IMC layer, at the zones U, M2, and L, vary from the upper part of the interface to the bottom, in a decreasing order. The temperature has an influence in the growth of IMC's, increasing the diffusion rate of Al and Fe atoms and consequently forming thicker layers of IMC [95]. The shoulder of the FSW tool provides, among other functions, the necessary friction and consequent heat source for the substrates to reach high temperatures, achieving a plastic regime and forming a welded joint. These temperatures are much higher at the top part of the joint than an the bottom part, correlating to the distance from the heating source, resulting in a gradient of temperatures along the FSW process.

This phenomenon explains the thickness gradient along the IMC Layer seen in the joints present in this work. Fick's diffusion rules govern the diffusion rates, which are highly temperature dependent and for higher temperatures, the diffusion coefficient rises correspondingly, increasing atomic mobility and allowing for rapid diffusion of aluminium and iron atoms into each other's crystalline structures. This increases the total diffusion process, and facilitates the kinetics of the reaction between Al and Fe atoms, leading to a higher growth of the IMC at the interface of the base metals [98].

Since the peak temperatures reached during the welding process are higher at the top side of the joint, the IMC layer thickness is also higher in the zones, following the same correlation for the decreasing peak temperatures reached along the interface.

### 3.2.2 - Interface microstructure

### As-welded sample

The IMC layer formed as result of the weld, is not uniform along the interface of the joint, varying from thickness, morphology, and microstructure. At the top to middle zones of the joint, seen in Figure 3.17 (a) to (d), we have a homogenous layer, yet with a considerable number of cracks and discontinuities along these zones.

Additionally, some occasional inclusions of steel are present at the interface surrounded by the IMC layer, as shown at zone M2, Figure 3.17 (c), consequence of the stirring motion caused by the rotating motion of the tool, and zones of irregular highly irregular IMC growth and further morphology, likewise the zone M3, Figure 3.17 (d).

However, this is not the case at the lower zones of the joint interface, where an intermittent morphology of IMC appears along the zone, consisting in some sections of lower thickness and other sections with the occurrence of irregular IMC nodules and sporadic short thicker sections, observed in the zones L and B, Figure 3.17 (e) and (f), eventuality of an already rough surface of the metal substrates. Furthermore, only small particles of steel appear dispersed in the Al matrix along all the interface of the weld, which diminish the potential for compromising the weld integrity, in contrast with larger fragments that might appear in these types of joints.

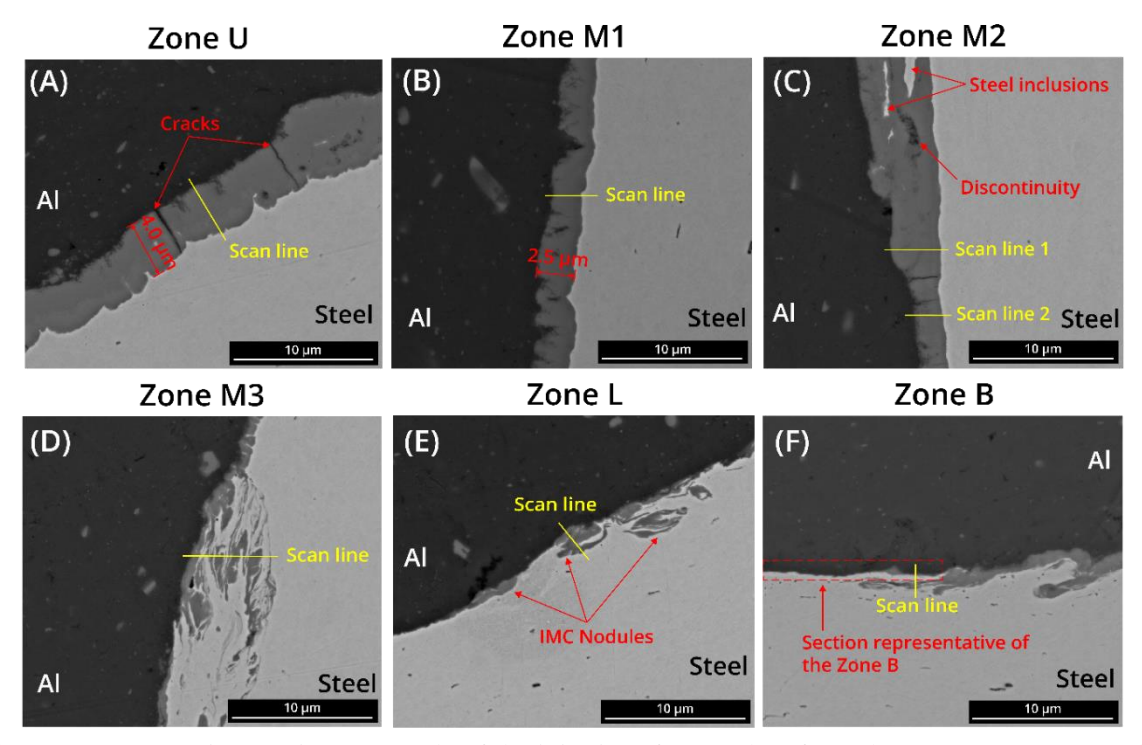


Figure 3.17 - SEM images in BSE mode of the joint interfaces, taken from the Zones M1 (a), M2 (b), M3 (c), U (d), L (e) and B (f), at 10 000x magnification.

In Figure 3.18, the EDS line-scans locations are highlighted, presenting the chemical composition across the interface of the weld. By analysing the results of the EDS line-scans performed at all the 7 locations, the zone U, zone M1 and zone M2, display a linear average atomic percentage (at. %) of Al and Fe at the centre of the IMC layer, as shown in Figure 3.18 (a) to (d).

For the upper zone U and middles zones M1 and M2 at the scan line 1, the IMC layer exhibit a 70 - 72% Al at. %, representing a Fe<sub>2</sub>Al<sub>5</sub> IMC phase. This Al-Fe phase is characterized as brittle and having a low ductility, compared with other phases, resulting in less-than-desirable joint integrity.

Furthermore, the lower ductility of Fe<sub>2</sub>Al<sub>5</sub> compounds can lead to the formation of cracks along the IMC layer of the bonded joint. The second EDS line-scan performed of the zone M2 presents an Al at % between 62-78%, leading to an unconclusive phase present at this section. Due to the non-linear and varying chemical content of the zones M3, L and B (Figure 3.18 (e), (f), and (g) respectively), correlated with the complex microstructure, the Al-Fe IMC present at these sections require further analysis to determine the corresponding phases.

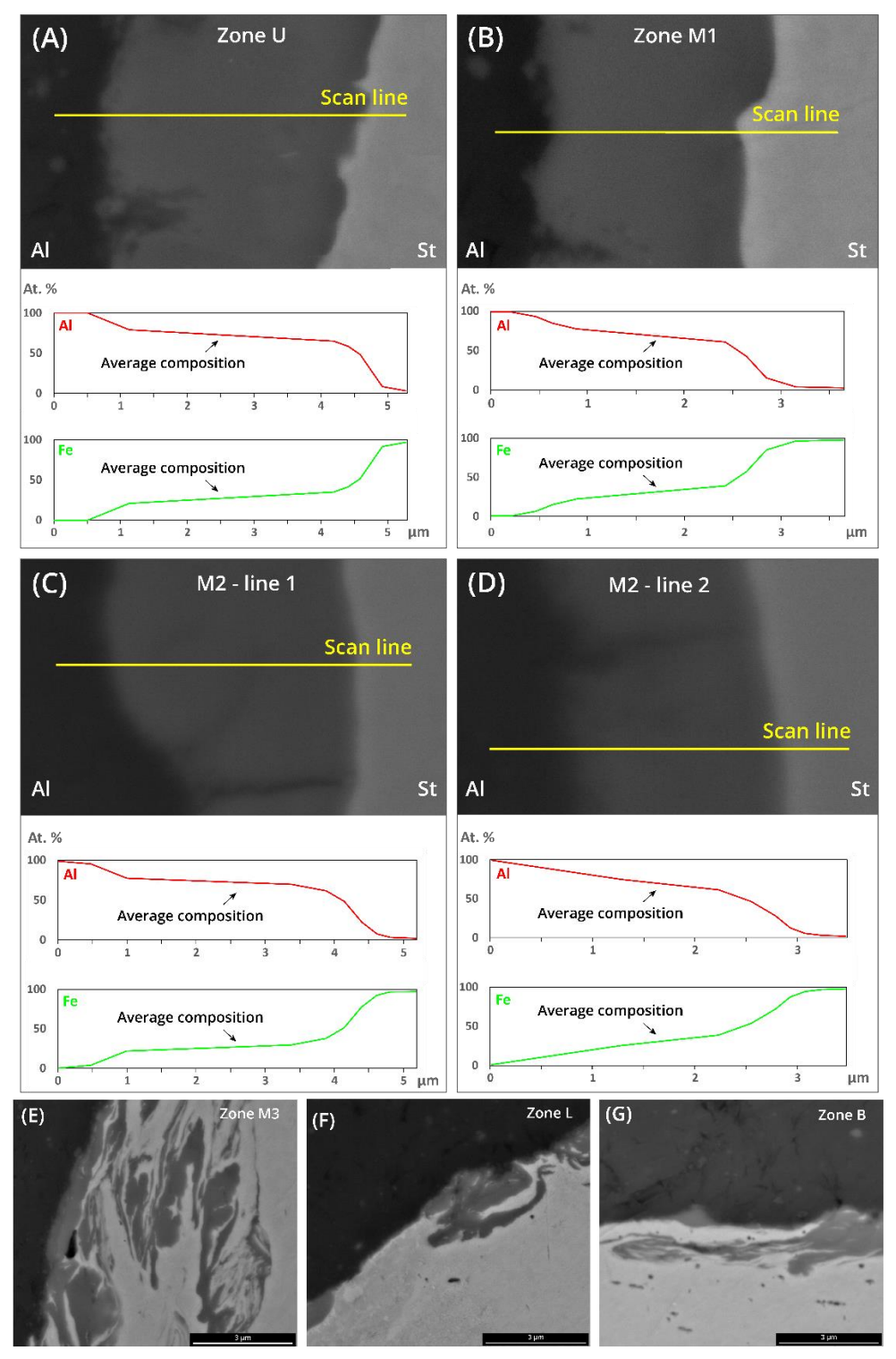


Figure 3.18 - Line-scan EDS analysis taken across the IMC layer of the zones U (a), M1 (b), M2 scan line 1 (c) and scan line 2 (d), and SEM images, 30 000x magnification, of the irregular microstructures of zone M3 (e), zone L (f) and zone B (g).

### Sample II $(100 \, ^{\circ}\text{C} / 60 \, \text{min})$

Observing the interface of the sample  $\mathbf{II}$  at the 35x magnification, as shown in Figure 3.19 (a), it is seen that the joint forms the S-shape morphology in similarity with the as-welded sample, although with less penetration of the bottom steel tip into the aluminium substrate, and with the top tip shorter than the

as-welded sample. The middle part of the interface presents good perpendicular to the joint's length and the tips of the S-shape morphology.

For the upper zone U, seen in Figure 3.19 (b) and (c), the sample presents a homogeneous IMC layer in its thickness, although with some visible discontinuities. In the upper left corner of the Figure 3.19 (b), a steel fragment is seen, with IMC a homogeneous IMC layer formation surrounding it.

The middle M2 zone presents a high degree of irregularities regarding the IMC layer, as seen in Figure 3.19 (d) and (e), presenting many discontinuities and some variation in layer thickness. The discontinuities were not corrected by the  $100 \, ^{\circ}\text{C} / 60$  min heat treatment performed in this sample.

At the lower zone L of the sample **II**, Figure 3.19 (f) and (g), we observe not only an irregular IMC layer, with varying thickness and discontinuities, but also the formation of IMCs in the steel substrate, similar to the case seen in the as-welded sample in the zone M3, Figure 3.19 (c).

An EDS analysis was not performed in the sample II.

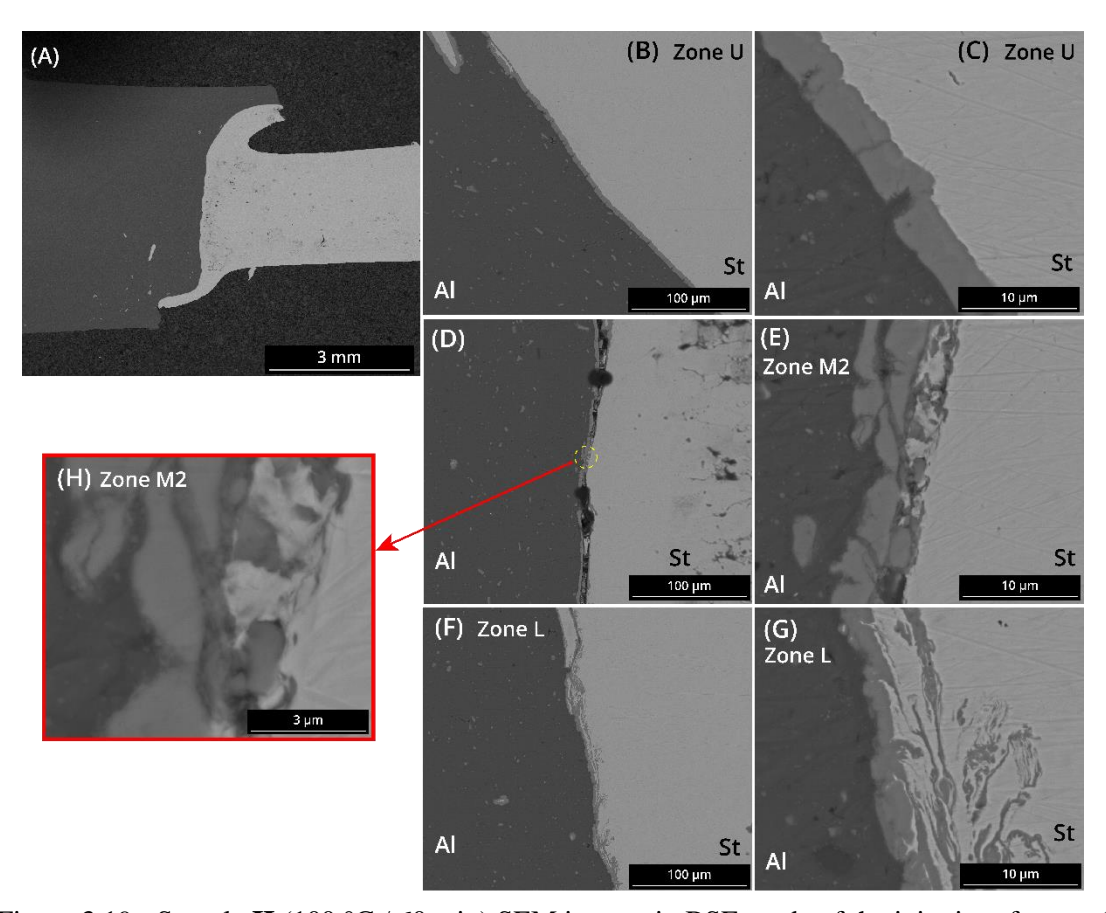


Figure 3.19 - Sample II (100 °C / 60 min) SEM images in BSE mode of the joint interfaces, taken from the zone U (b) and (c); zone M2 (d), (e) and (h); and zone L (f) and (g).

### Sample III (100 °C / 90 min)

The sample **III** presents a more curvilineal S-shape interface, seen in Figure 3.20 (a), with a deeper penetration of the bottom steel tip into the aluminium substrate, being the tip thinner than the previous examined samples. The middle zone of the interface appears in the joint in an angle, emphasising the S-shape morphology of the joint. The top steel tip encloses a substantial fragment of aluminium, result of the FSW process, promoting the penetration of the St37 into the aluminium base metal due to the forging

forces applied by the shoulder of the tool. Moreover, a high occurrence of steel fragment inclusions into the aluminium substrate, with a length as big as 0.5 mm, is visible.

At the upper zone U, an IMC layer with some degree of thickness variability and presenting some discontinuities is observed, as shown in Figure 3.20 (c) and (d).

The middle zone M2 presents a homogeneous IMC layer thickness with few discontinuities, however some steel fragments are present surrounded by the IMC layer, as seen in Figure 3.20 (f). Figure 3.20 (e) also shows the presence of the aforementioned steel fragments in the Al1050 substrate.

In Figure 3.20 (g) and (h) shows an IMC layer with a high degree of thickness variability, presenting some discontinuities and underdeveloped sections.

In this sample, a reduction in thickness from the top to the bottom zones is visible, although the confirmation of the reduction will be presented in the next subchapter.

For this sample **III**, as well as the next **IV** to **IX** samples, the EDS analysis was performed at the middle zone M2, perpendicularly to the interface, seen in Figure 3.20 (b). The IMC layer exhibits an average Al at.% of 68%, representing the presence of Fe<sub>2</sub>Al<sub>5</sub> phase.

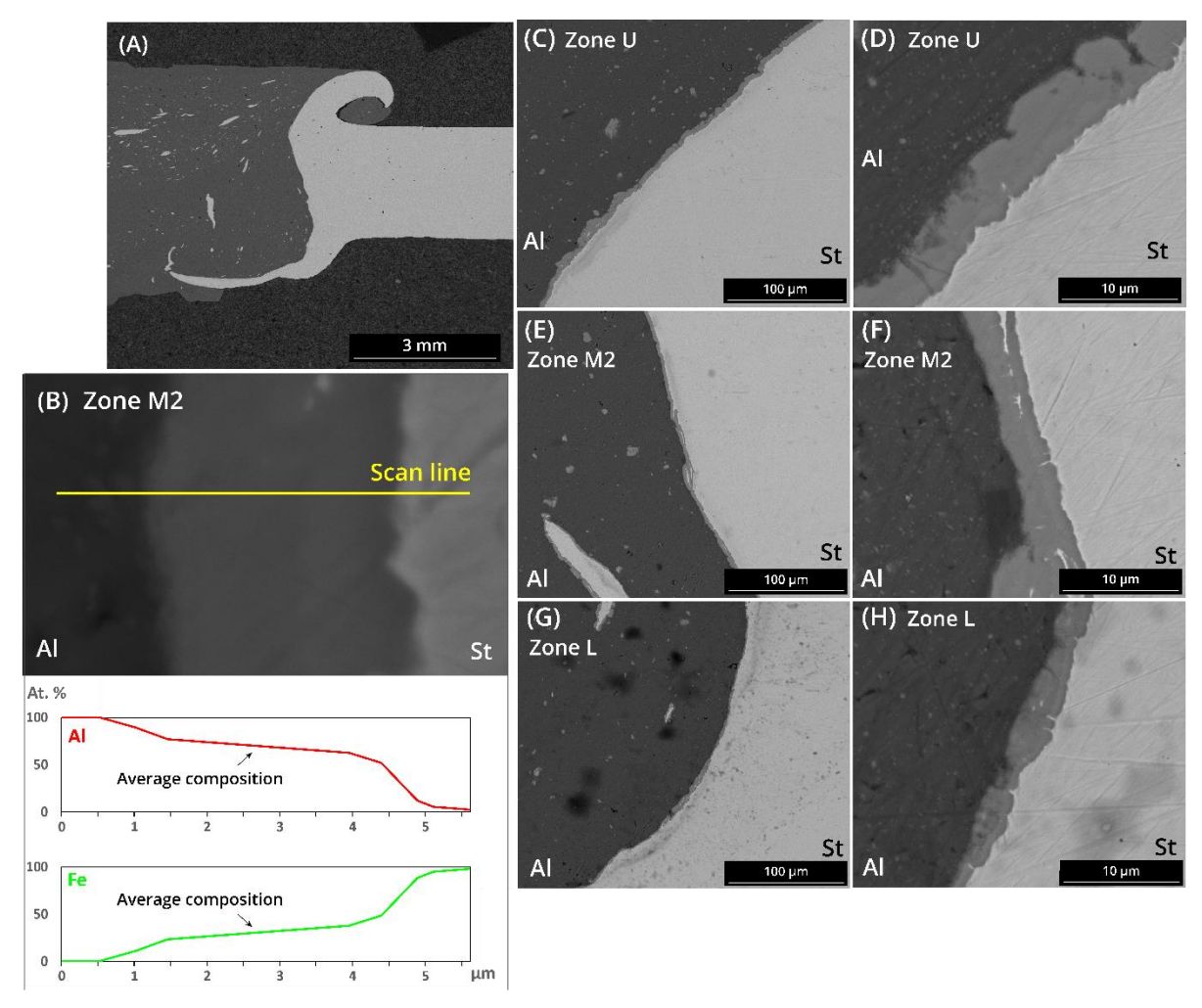


Figure 3.20 - Sample III ( $100 \,^{\circ}\text{C} / 90 \,^{\circ}\text{min}$ ) SEM images in BSE mode of the joint interfaces, taken from the zone U (c) and (d); zone M2 (e) and (f); and zone L (g) and (h). Line-scan EDS analysis taken across the IMC layer of the zone M2 (b).

### Sample IV $(250 \, ^{\circ}\text{C} / 30 \, \text{min})$

The sample **IV** presents an interface morphology similar to the previously discussed sample **III**, with an emphasized S-shape interface and deep penetration of the bottom steel tip into the aluminium substrate, as seen Figure 3.21 (a). This sample also presents the inclusion of the steel fragments in the aluminium substrate, although with lower occurrences and smaller dimensions.

The upper, middle, and lower zones of the sample **IV**, presents an IMC layer with a homogeneous thickness, and few discontinuities and steel inclusions in the layer. Additionally, the dimensions of the steel particles in the aluminium substrate are low and appears surrounded by the IMC layer as well, as seen in Figure 3.21 (c). In the middle zone, IMC fragments are seen inside the steel substrate, at a distance of the IMC layer, as seen in Figure 3.21 (f).

The EDS analysis performed at the middle zone M2, seen in Figure 3.21 (b) exhibits Al at.% between 64% and 100%, leading to an unconclusive phase present at this section.

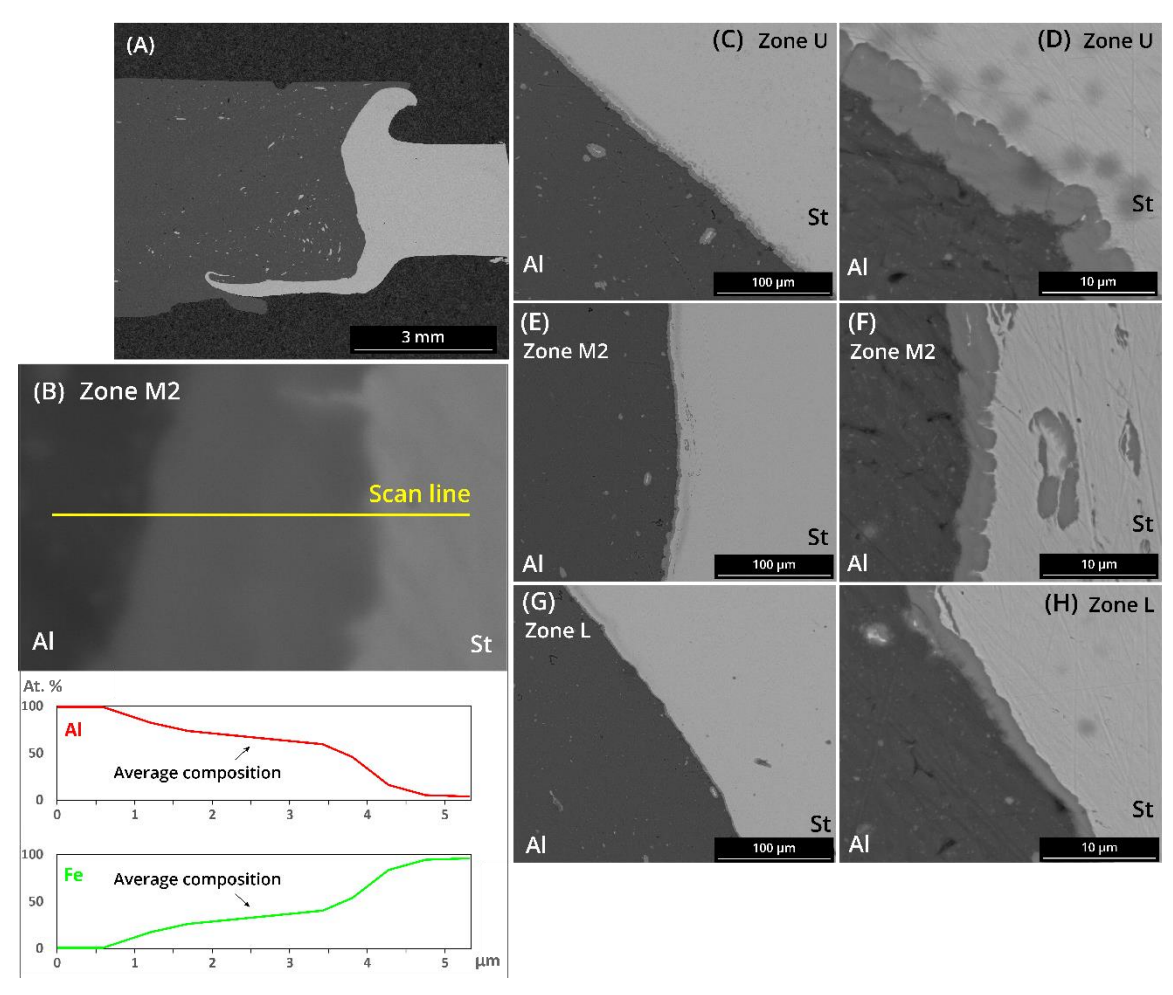


Figure 3.21 - Sample IV (250  $^{\circ}$ C / 30 min) SEM images in BSE mode of the joint interfaces, taken from the zone U (c) and (d); zone M2 (e) and (f); and zone L (g) and (h). Line-scan EDS analysis taken across the IMC layer of the zone M2 (b).

### Sample VI (250 °C / 90 min)

The sample presents a less pronounced S-shape with low penetration of the steel tip into the aluminium substrate at the lower zone of the interface and short upper zone tips, as well as a middle zone perpendicular to the joint, as shown in Figure 3.22 (a).

Observing the upper zone U, Figure 3.22 (a) and (b), a homogeneous IMC layer with some discontinuities along the section is visible. In this zone, there are no steel fragment inclusions in the IMC layer, although some small IMC fragments are visible in the Al substrate.

The middle zone M2 presents an IMC layer with no discontinuities but regular in terms of thickness along the interface. In the aluminium substrate, some IMC particles are seen detached from the IMC layer, as seen in Figure 3.22 (e) and (f).

At the lower zone L, the IMC layer appears more regular than the previous samples at the same zone, however, discontinuities exit in some sections of this zone, as seen in the top left side of Figure 3.22 (g).

The EDS analysis performed at the middle zone M2, perpendicularly to the interface, seen in Figure 3.22 (b) exhibits an average Al at.% of 69%, representing the presence of Fe<sub>2</sub>Al<sub>5</sub> phase.

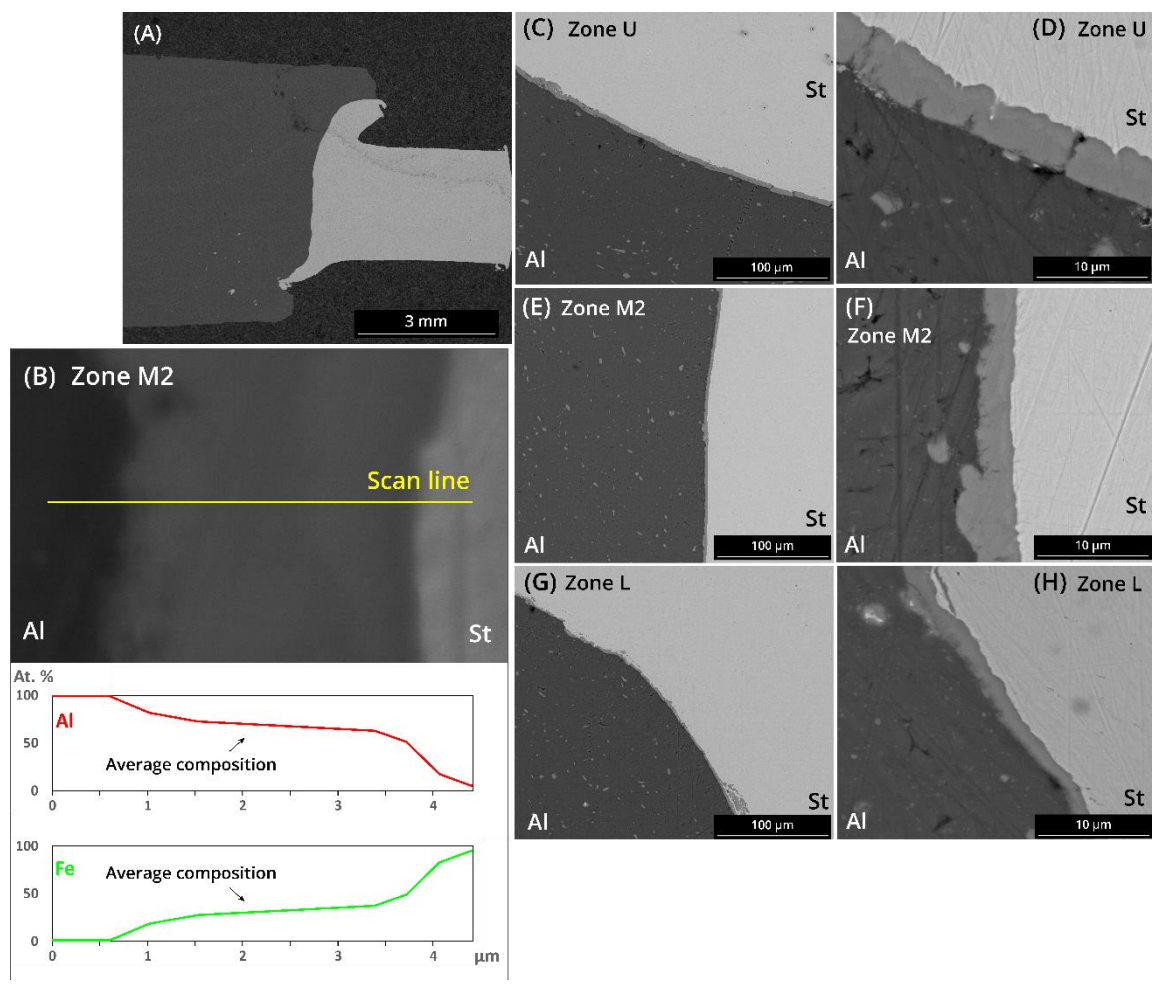


Figure 3.22 - Sample VI (250 °C / 90 min) SEM images in BSE mode of the joint interfaces, taken from the zone U (c) and (d); zone M2 (e) and (f); and zone L (g) and (h). Line-scan EDS analysis taken across the IMC layer of the zone M2 (b).

### Sample VIII (400 °C / 60 min)

Sample **VIII** presents a morphology with an upper steel tip similar to the sample **III**, trapping a piece of Al1050. However, the lower steel tips present a lower penetration in the aluminium substrate and the middle zone of the interface appear perpendicular to the joint's length.

The upper, middle, and lower zones of the interface, presents an irregularity in its thickness and the continuity of the IMC layer, as seen in Figure 3.23 (c) to (h). In Figure 3.23 (e) and (g), a substantial number of fragments of steel surrounded by an IMC layer are visible, as well as some instances of small steel inclusions in the IMC layer, seen in Figure 3.23 (h).

The EDS analysis performed at the middle zone M2, perpendicularly to the interface, seen in Figure 3.23 (b) exhibits an average Al at.% of 70%, representing the presence of Fe<sub>2</sub>Al<sub>5</sub> phase.

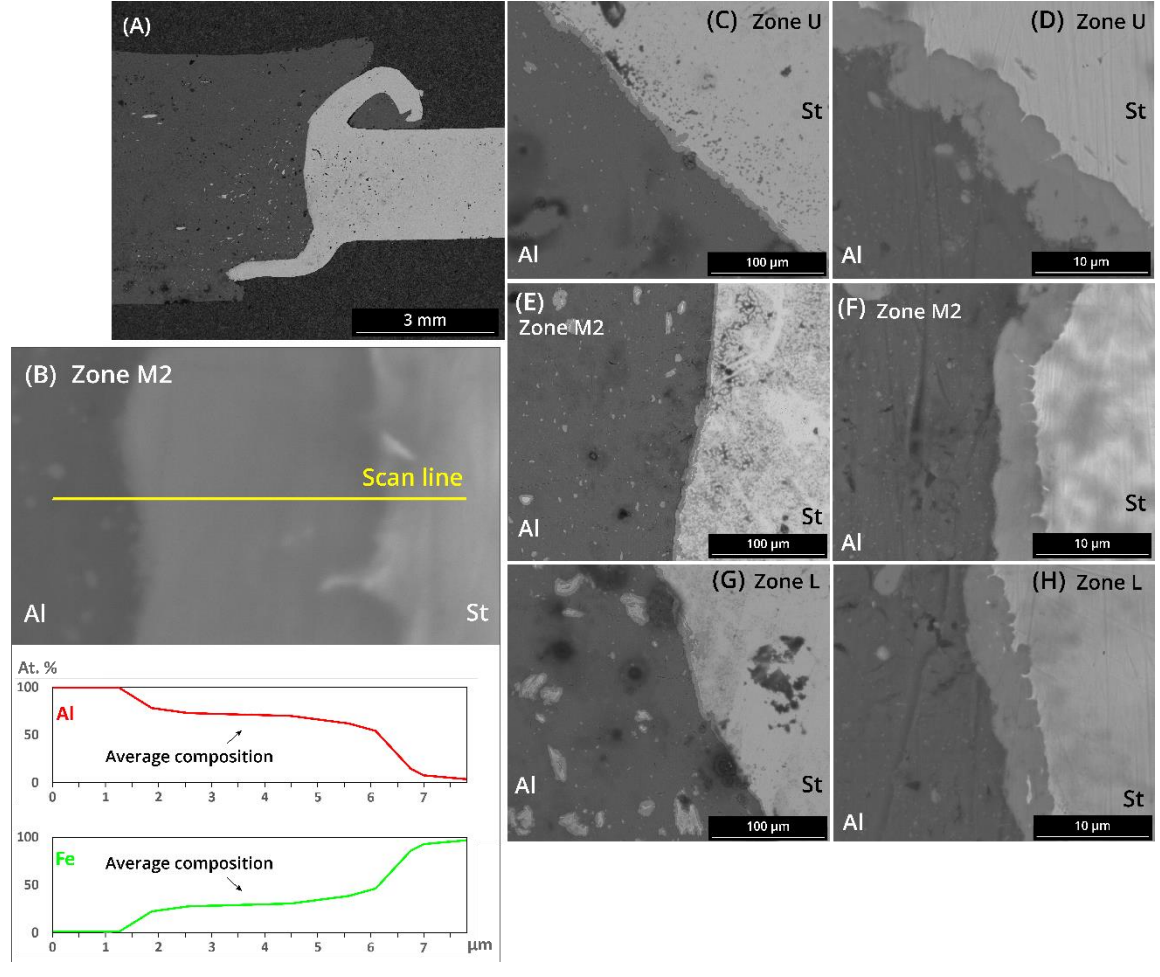


Figure 3.23 - Sample VIII ( $400 \, ^{\circ}\text{C} \, / \, 60 \, \text{min}$ ) SEM images in BSE mode of the joint interfaces, taken from the zone U (c) and (d); zone M2 (e) and (f); and zone L (g) and (h). Line-scan EDS analysis taken across the IMC layer of the zone M2 (b).

The samples V (250 °C / 60 min), VII (400 °C / 30 min), and IX (400 °C / 90min) presented an atypical morphology at the weld zone, as seen in Figure 3.24 (a), (b) and (c). The aluminium substrate of the joints contains large volumes of steel in across the weld zone, voids in the lower zones of the aluminium side and cracks at the bottom and middle zone of the interface.

Furthermore, the sample VII presents a peculiar S-shape interface, with a deeper penetration of the

bottom steel tip than all the previous discussed samples, as seen in Figure 3.24 (b). Sample V also presents a thin and deep penetration of the bottom steel tip, merging with a big volume of steel in the aluminium base metal, observed in Figure 3.24 (a).

Observing the magnified SEM images of the middle zone of the three sample, Figure 3.24 (d), (e) and (f), some additional atypical occurrences are present at the interface. The sample **V** contains a large distribution of steel fragments in the Al matrix close to the interface, with the majority of the fragments surround of an IMC layer. The IMC layer of the interface, also presence an irregular thickness, with discontinuities along it, seen in Figure 3.24 (d).

At the middle zone of the sample **VII**, an area containing large fragments of steel in the vicinity of the interface mixed in an area of IMC phases. An interfacial crack along the middle zone is present, as we can see in detail in Figure 3.24 (e). This in an abnormal occurrence for these types of joints, caused in the manufacturing process.

In Figure 3.24 (f), we observe the middle zone of the sample **IX** interface, presenting a regular IMC layer thickness with some cracks and discontinuities in the layer. Some fragments of steel are present in the Al matrix close to the interface of the joint, surrounded by an IMC layer.

These anomalies in the joints are a result of the samples' collection at the end of the weld line during the manufacturing process. Insufficient stir time, leading to lower input temperatures in the pin retraction zone, close to where these sample where collected, is a major cause for the unusual joint morphology.

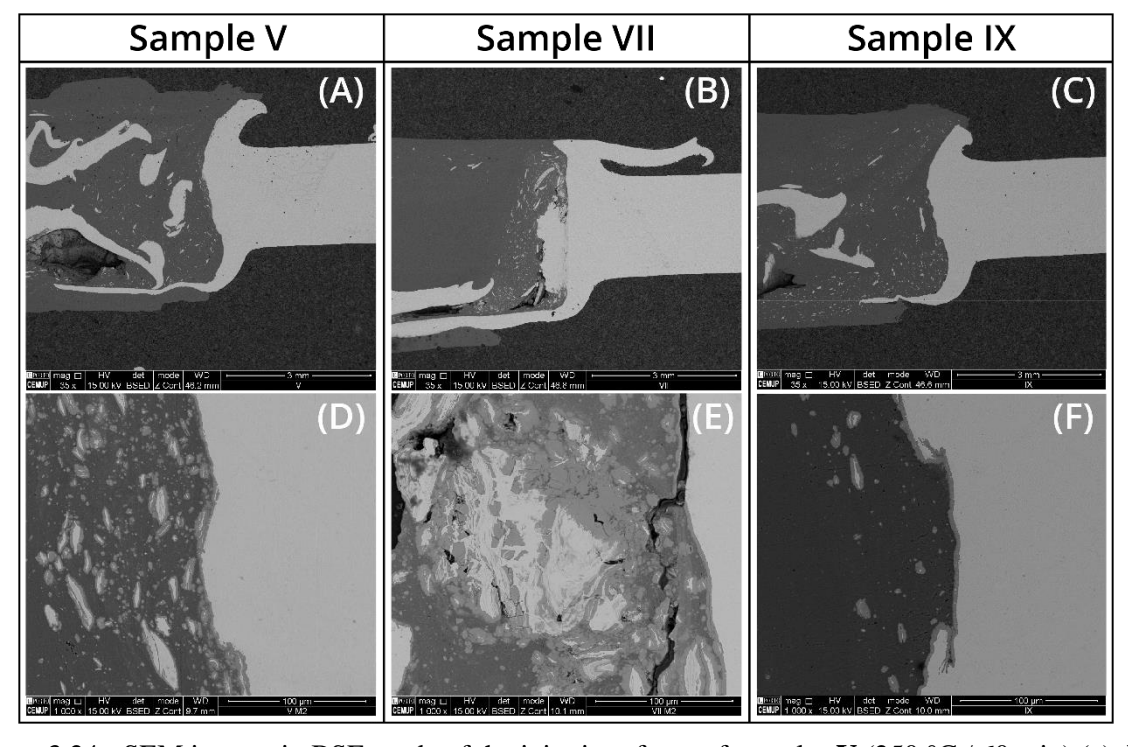


Figure 3.24 - SEM images in BSE mode of the joint interfaces of samples V (250 °C / 60 min) (a), VII (400 °C / 30 min) (b), and IX (400 °C / 90 min) (c), and details of the zone M2 (d), (e) and (f), respectively.

The EDS analysis performed at the middle zone M2 of the samples **V**, **VII** and **IX** perpendicularly to the interface, are present in Figure 3.25.

Samples V and VII exhibit an Al at.% between 65% and 100%, leading to an unconclusive phase

present at these sections. The sample **IX** presents an average Al at.% of 72%, indicative of the presence of Fe<sub>2</sub>Al<sub>5</sub> phase.

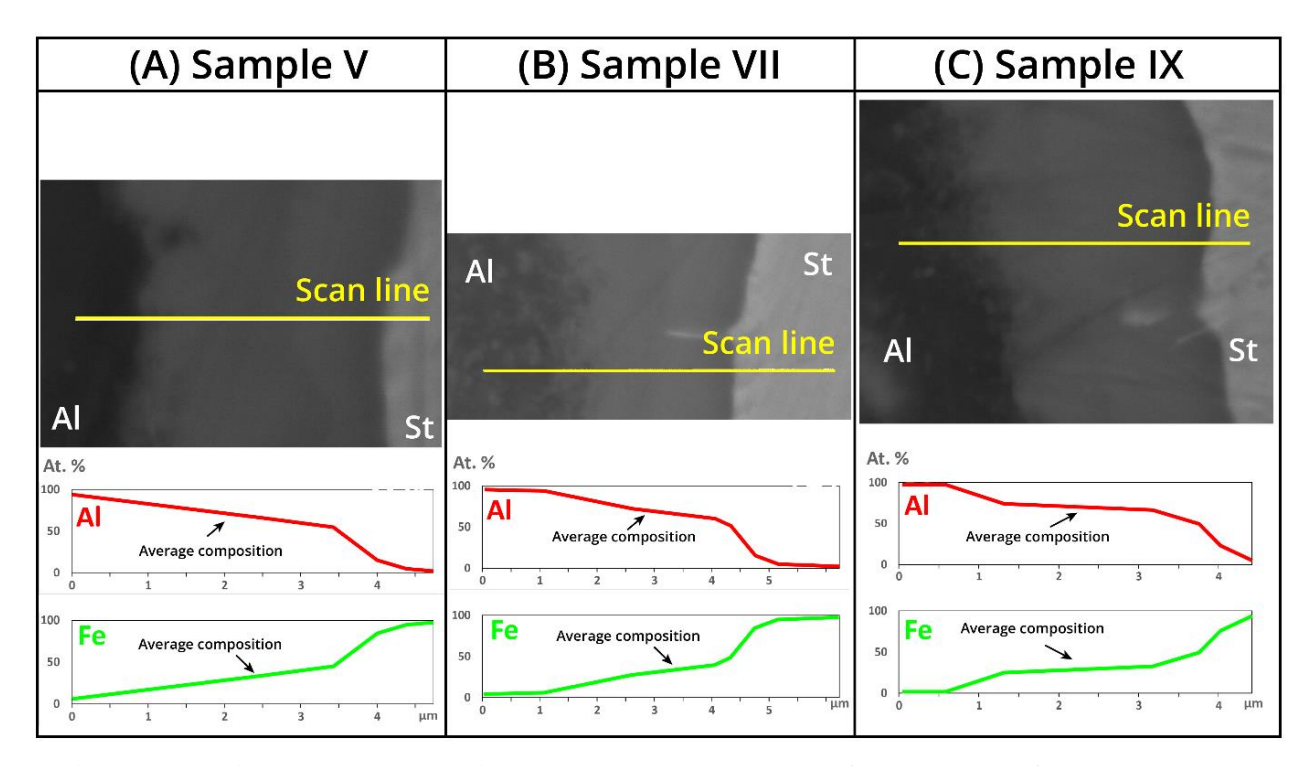


Figure 3.25 - Line-scan EDS analysis taken across the IMC layer of the zone M2 of the samples **V** (a), **VII** (b), and **IX** (c).

### 3.2.3 - Load vs. Extension results

The tensile tests allow for a compression of the failure behaviour of the joints, establishing a correlation between the strength of these with the degradation of the joint characteristics promoted by the heat treatment.

In this section, the results of the tensile tests will be presented and discussed, by pair temperature/time and for specimen tested, aided by frames of the recorded videos and images of the failed specimens at the end. The Appendix C contains the remaining frames for all the specimens mentioned. At last, a summary of the tests will be presented, in order to draw a correlation between the heat treatments performed and the joint degradation of the specimens.

For each pair temperature/time, three specimens were tested. Taking Figure 3.26 as an example, the tensile data of the three tests  $\mathbf{I} \cdot \mathbf{I} \cdot \mathbf{$ 

### Specimens I: 100 °C / 30 min heat treatment

Starting with the heat treatment pair I,  $100~^{\circ}C$  / 30~min, the lowest degradation of the joint characteristics is expected, according to the low temperature and short time of the heat treatment performed, inducing a small growth of the IMC layer.

The Load vs. Displacement curves of the I specimens is presented in the following Figure 3.26.

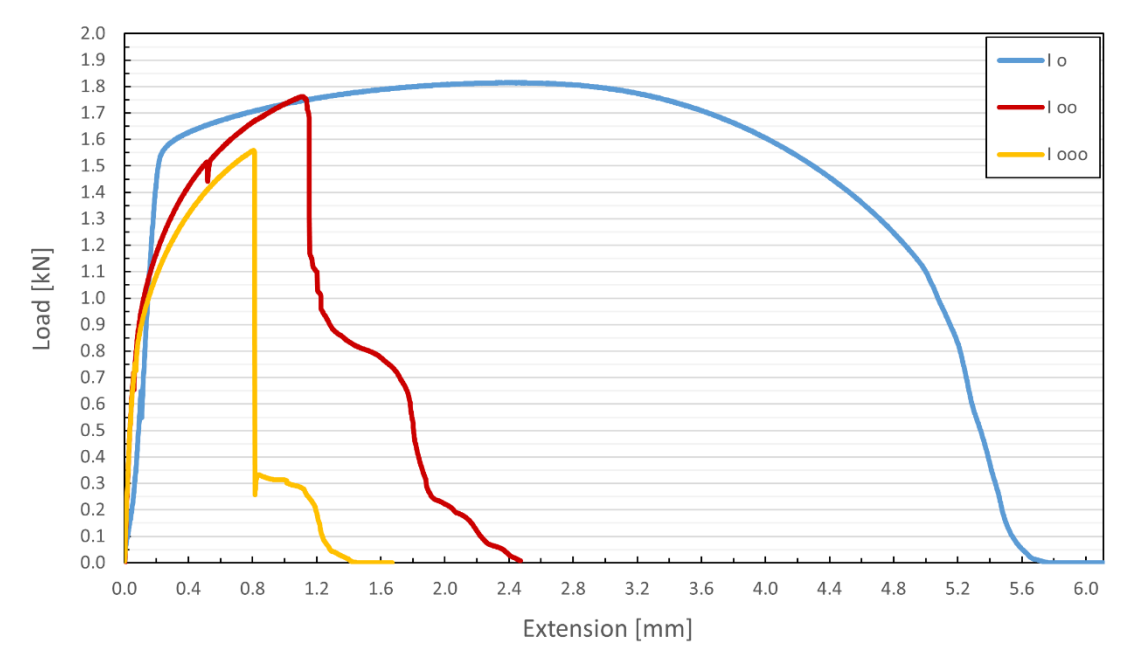


Figure 3.26 - Load vs. Extension curve of the 100 °C / 30 min heat treatment specimens.

Specimen **I** • failed at the aluminium substrate, at 1815.2 N and with an extension at failure of 2.43 mm, result of the striction on this base material, bellow the joint interface but in the weld zone of the specimen.

By failing in the aluminium substrate, the joint presents a superior mechanical strength than the other samples.

Table 3.4 - Max. Load and Extension at Max. Load of the specimen I • (100 °C / 30 min).

Max. load [N]	Extension at max. load [mm]			
1815.2	2.43			

Specimen **I** • • failed at the interface of the joint, at 1762.6 N with an extension of 1.21 mm.

It is possible to observe the Al1050 substrate entering a plastic regime before the failure at in the interface.

Table 3.5 - Max. Load and Extension at Max. Load of the specimen I • • (100 °C / 30 min).

Max. load [N]	Extension at max. load [mm]		
1762.6	1.21		

At the moment of the failure, it is possible to observe the joint failing in the middle zone of the interface, seen in Figure 3.27 (a). Afterwards, the joint fails two more times in different zones, first at the bottom zone, in the tip of S-shape interface, shown in Figure 3.27 (b) at 45 % of the max. load, followed by the failure of the top zone, Figure 3.27 (c), at a 8.5 % of the first failure load.

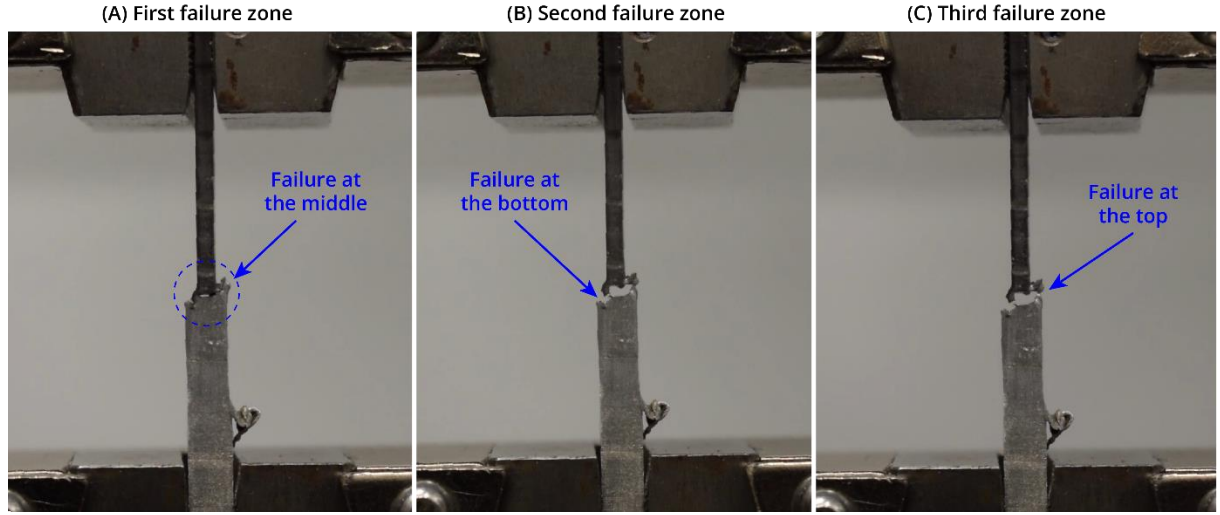


Figure 3.27 - Failure instants video frames of the specimen I • • tensile test.

In the last two failure zones, a plastic failure of the aluminium substrate occurs, as seen in video frames of Figure 3.27, and the presence of aluminium still welded to the steel substrate **I** is noticed. The presence of Al1050 at the failed tip zones will be studied in the fractography analysis in the following Section 3.2.4 -

The third specimen  $\mathbf{I} \cdot \cdot \cdot$ , failed at 1558.7 N with an extension of 0.80 mm, at the interface of the joint. The joint failed similarly to the previous  $\mathbf{I} \cdot \cdot$  specimen, starting in the middle zone of the interface, followed by the bottom zone and the top zone.

However, the failure circumstances diverge from the previous specimen. Besides the specimen **I** • • failing at lower load and extension, the secondary failure occurs at 19 % of the main failure load. The instance of complete detachment of the base metal is difficult to identify in the Load vs Extension curve, although it is possible to observe the final failure in the very last moments of the video recording.

Table 3.6 - Max. Load and Extension at Max. Load of the specimen I • • • (100 °C / 30 min).

Max. load [N]	Extension at max. load [mm]
1558.7	0.80

The specimen  $\mathbf{I} \bullet \bullet \bullet$  after failure, where the shallower S-shape, in comparison with other specimens, is possible to be observed.

The lesser curved S-shape interface is due to the location of the welded line where the specimen was cut in the manufacturing process. Noteworthy is that along the weld line made by FSW, we may not see a uniform pattern and thus we may expect some specimens differ in terms of joint interface shape.

### Specimens II: $100~^{\circ}\text{C}$ / 60~min heat treatment

The heat treatment pair **II**, for 60 min at 100 °C, no major differences from the specimens **I** were expected, in terms of max. load and fracture behaviour.

In addition, when comparing the IMC layer thickness of the as-welded sample and the sample  $\mathbf{II}$ , we identify no growth in the middle zone of the joint, which presents the largest impact in the max failure load, although the upper zone as a negligible  $0.3 \mu m$  decrease and the bottom zone an IMC layer

thickness increase of 1.7 μm.

The first specimen tested, **II** •, presented two distinct failure instants, contrasting with the specimens seen until. In the first instant, for the max. load of 1660.7 N at an extension of 0.32 mm, the joint failed at the top and middle zone simultaneously, seen in Figure 3.28 (b). The secondary failure instant occurs at 45% of the max. failure load, at the bottom zone of the joint interface.

Table 3.7 - Max. Load and Extension at Max. Load of the specimen II • (100 °C / 60 min).

Max. load [N]	Extension at max. load [mm]		
1660.7	0.32		

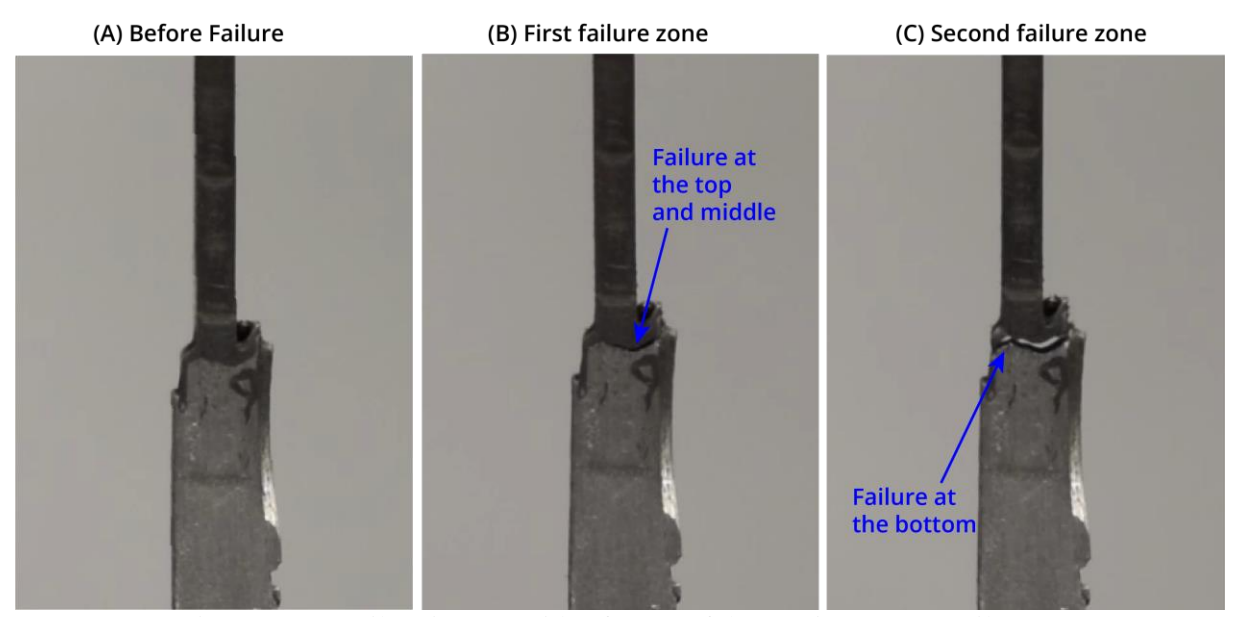


Figure 3.28 - Failure instants video frames of the specimen **II** • tensile test.

Specimen **II** • •, with a failure load of 1831.4 N and an extension at failure of 1.04 mm, failed at three zones, well identifiable in the Load vs. Extension curve and in the video.

Table 3.8 - Max. Load and Extension at Max. Load of the specimen II • • (100 °C / 60 min).

Max. load [N]	Extension at max. load [mm]			
1831.4	1.04			

Firstly, the joint failed at the middle zone, seen in Figure 3.29 (b), followed by a secondary failure instance at the top of the joint, Figure 3.29 (c), at 71% of the max. failure load. At last, the joint failed at the bottom zone. The failure of the bottom zone is characterized by the plastic deformation of the aluminium substrate throughout the loading, resulting in a piece of Al1050 still welded to the steel substrate, in the likeness of the sample  $\mathbf{I} \bullet \bullet$ , for 100 °C / 30 min heat treatment.

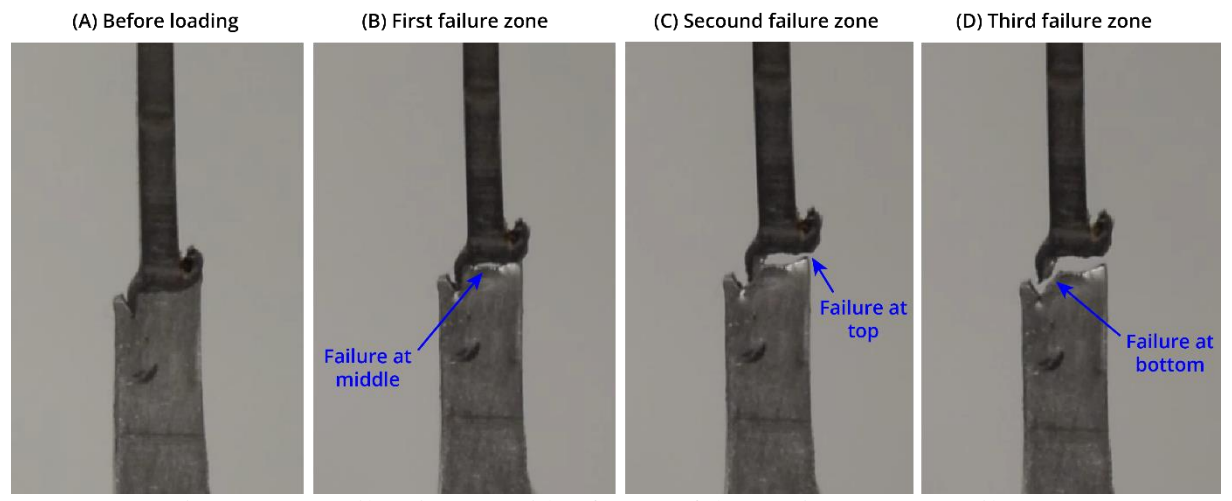


Figure 3.29 - Failure instants video frames of the specimen II • • tensile test.

The specimen II • • • failed at a 1698.2 N for an extension of 1.07 mm.

Table 3.9 - Max. Load and Extension at Max. Load of the specimen II • • • (100 °C / 60 min).

Max. load [N]	Extension at max. load [mm]		
1698.2	1.07		

In the main failure instance, is possible to observe detachment of the St37 and Al1050 substrates at middle zone of the joint and subsequently at the bottom zone. The secondary failure instance is observed at the top zone of the joint after the yielding of the aluminium part of the S-shape tip, observed in Figure 3.30.

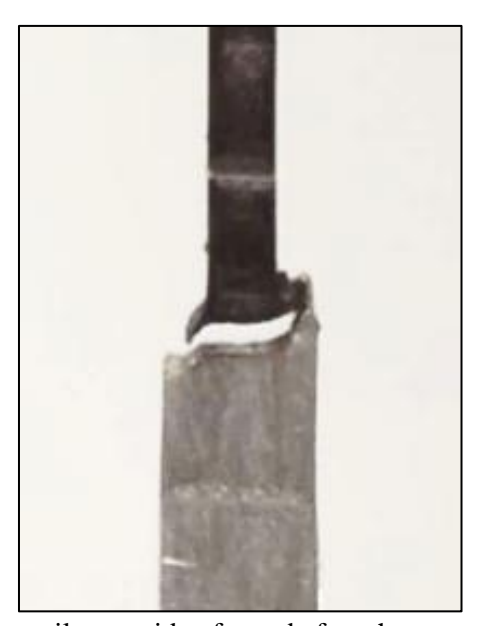


Figure 3.30 – Specimen II • • • tensile test video frame before the secondary failure instance, at the top zone of the joint.

Furthermore, at the steel half of the failed specimen, a snub of aluminium was still welded to the top side of the joint.

### Specimens III: 100 °C / 90 min heat treatment

For heat treatment pair **III**, for 90 min at 100 °C, a higher degradation of the joint properties was expected in comparison with the previous specimens with the same nominal temperature heat treatments.

Additionally, the average IMC layer thickness measured in same heat treatment sample increased in comparison to the as-welded sample in all three zones, and in the top and middle zone when compared with the sample II (100  $^{\circ}$ C / 60 min), although the negligible 0.1  $\mu$ m increase can be considered irrelevant.

The specimen **III** • failed in the aluminium substrate, in the TMAZ, with a max. load of 1894.8 N with an extension of 3.32 mm. The striction of the Al1050 base metal occurred below the interface of the joint.

In this sample the joint efficiency is 100%, as the interface did not fail. It is apparent that this specimen failed from TMAZ or HAZ.

Table 3.10 - Max. Load and Extension at Max. Load of the specimen III • (100 °C / 90 min).

Max. load [N]	Extension at max. load [mm]			
1894.8	3.32			

The specimens **III** • • and **III** • • • failed following a behaviour already observed in the previous tensile tests, starting in a first instance with the failure in the middle zone followed by the yielding of the aluminium tips of S-shape interface until reaching complete detachment from the Al1050 substrate.

The failure max. loads and extension at max. load in present in the following Table 3.11 - Max. Load and Extension at Max. Load of the specimen III • • and III • • • (100 °C / 90 min).

Table 3.11 - Max. Load and Extension at Max. Load of the specimen III • • and III • • • (100 °C / 90 min).

Specimen	Max. load [N]	Extension at max. load [mm]		
III • •	1665.7	0.62		
III•••	1978.1	2.55		

The main failure zone is the middle of the interface for the two specimens, at 63 % and 36 % of the max. loads respectively, and in addition, for the specimen III • • •, at the instant of the failure in the middle zone, a secondary failure zone at the bottom of the joint appears, visible in Figure 3.31 – Specimens III • • and III • • • tensile test video frames before loading (a) and (e), at main failure zone (b) and (f), and at the yielding of the Al1050 tips of the joint interface (c) and (g), respectively. (f).

Afterwards, tips of the aluminium substrate yield until fracture of the top tip, at 30 % max. load for specimen III • • and 10.5 % of the max. load for specimen III • • •. For the two tensile tests, the bottom zone is the last to fail.

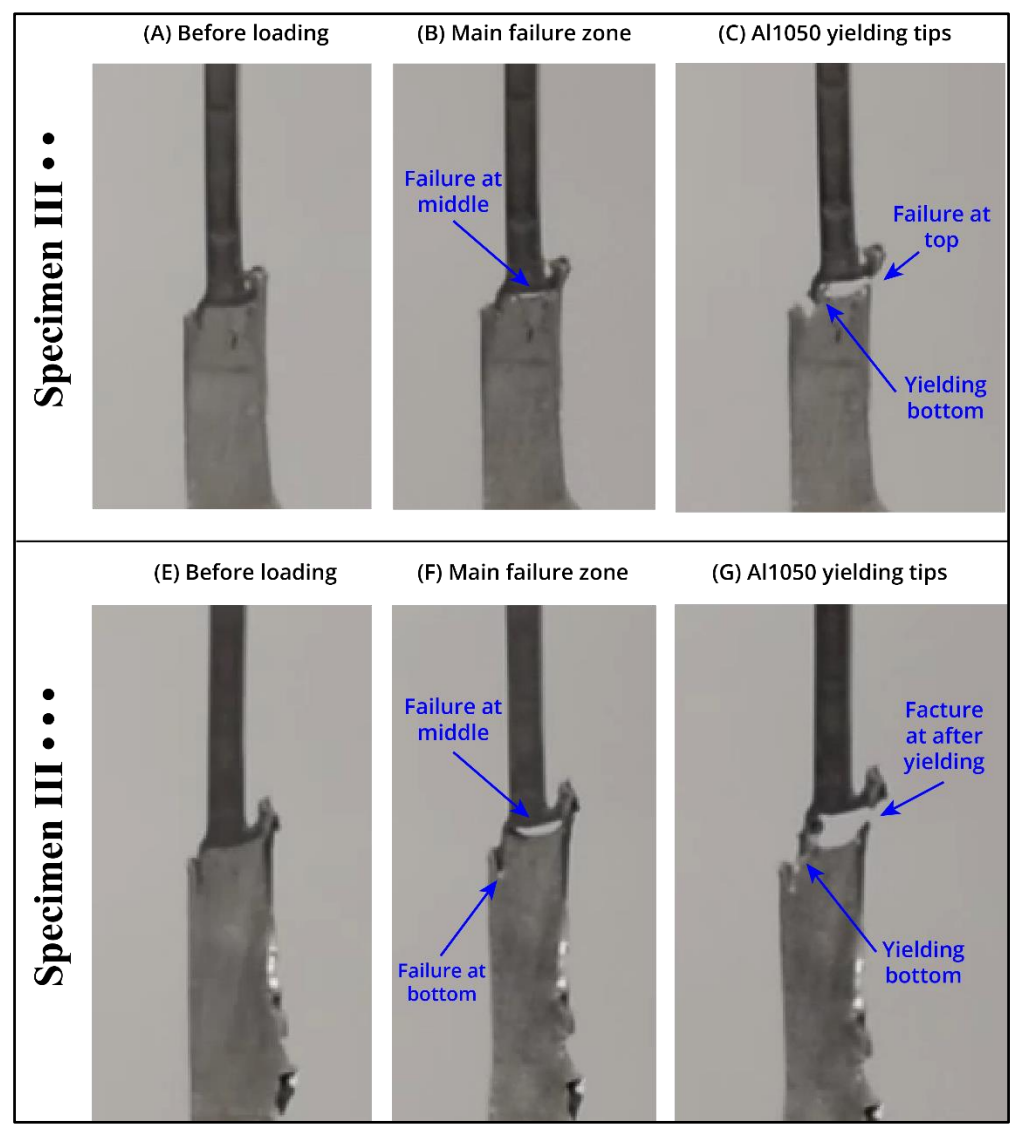


Figure 3.31 – Specimens **III** • • and **III** • • • tensile test video frames before loading (a) and (e), at main failure zone (b) and (f), and at the yielding of the Al1050 tips of the joint interface (c) and (g), respectively.

### Specimens IV: 250 °C / 30 min heat treatment

The heat treatment pair **IV**, for 30 min at 250 °C, sees a 150 °C increase from the past 9 specimens tested.

The specimen's failure loads and extension at failure are present in the Table 3.12.

Table 3.12 - Max. Load and Extension at Max. Load of the 250  $^{\circ}$ C / 30 min heat treatment specimens.

Specimen	Max. load [N]	Extension at max. load [mm]		
IV •	1514.1	0.49		
IV • •	1813.2	1.19		
IV • • •	1674.9	0.91		

The specimen **IV** • failed in a different manner from the rest of the specimens tested. At first, the joint failed at the top and middle zone simultaneously, as seen in Figure 3.32 (a), at 1514.1 N, followed

by the failure of a second half of the middle zone, close to the bottom side of the joint, Figure 3.32 (b), at 56% of the maximum load. At last, the joint failed in the bottom zone, seen in Figure 3.32 (c), at 6% of the max. load.

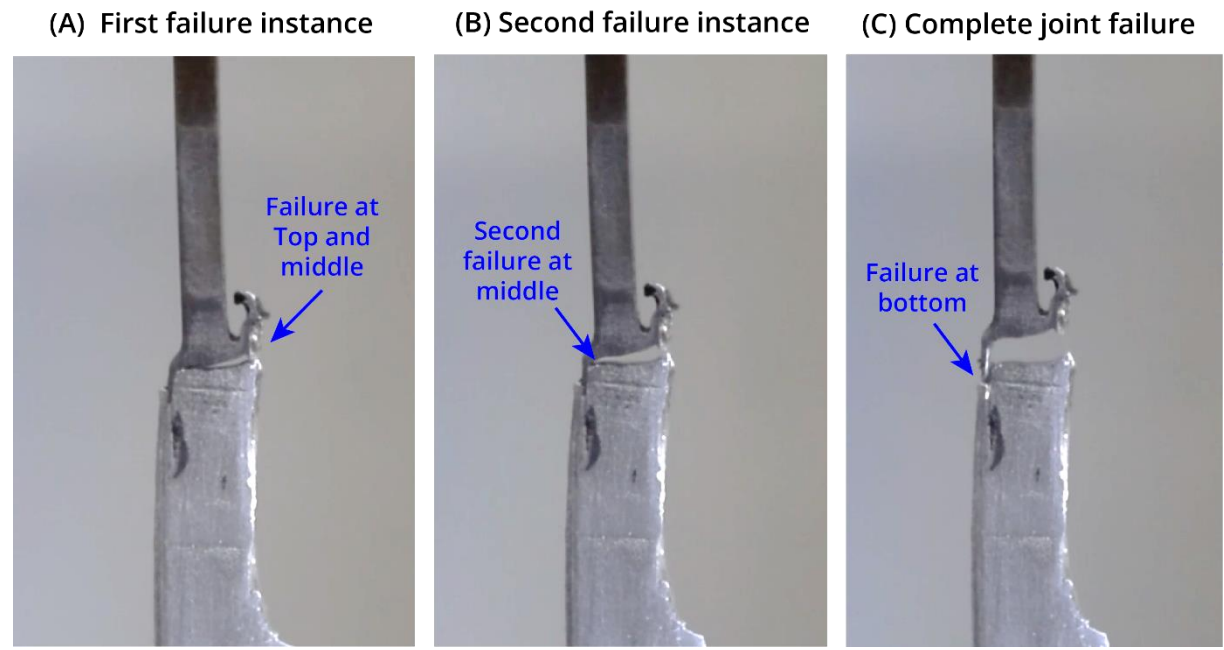


Figure 3.32 - Failure instants video frames of the specimen IV • tensile test.

Specimens **IV** • • and **IV** • • • failed in a similar manner to the previous specimen for 100 °C heat treatments, at 1813.2 N and 1674.9 N respectively.

At first, the specimens failed at the middle zone of the interface, followed by the yielding of the aluminium tips of the S-shape joint until fracture. For the specimen  $IV \bullet \bullet$ , the secondary failure occurs in top side, at 60.6% of the ultimate strength, followed by the bottom side, at 44% of the max load. In the tensile test of the specimen  $IV \bullet \bullet \bullet$ , the sequence of failure after the main failure at the middle zone is imperceptible. The Figure 3.33 represents the localized aluminium tip yielding of the specimens  $IV \bullet \bullet$  (a) and  $IV \bullet \bullet \bullet$  (b) after the main failure at the middle zone.

## (A) Specimen IV • • (B) Specimen IV • • •

Figure 3.33 – Localized yielding after main failure at the middle zone of the joints **IV** • • (a) and **IV** • • (b).

### Specimens V: 250 °C / 60 min heat treatment

The values for the ultimate loads for the tested specimens and the respective extensions are present in Table 3.13 - Max. Load and Extension at Max. Load of the 250  $^{\circ}$ C / 60 min heat treatment specimens.

Table 3.13 - Max. Load and Extension at Max. Load of the 250  $^{\circ}$ C / 60 min heat treatment specimens.

Specimen	Max. load [N]	Extension at max. load [mm]
V •	1838.5	3.29
V • •	1853.5	1.28
V • • •	1692.1	1.06

The specimen **V** •, failed at the Al1050 substrate at 1838.5 N, for an extension at the max. load of 3.29 mm

In the other hand, the specimens  $V \bullet \bullet$  and  $V \bullet \bullet \bullet$  failed in a same manner as most of the specimens observe, first at the middle zone followed by the localized yielding of the aluminium tips of the joint.

The Figure 3.34 presents the before and after of the failure instants during the tensile test of the specimen  $V \bullet \bullet$ , with the main failure at the middle, top and bottom zones, sequentially.

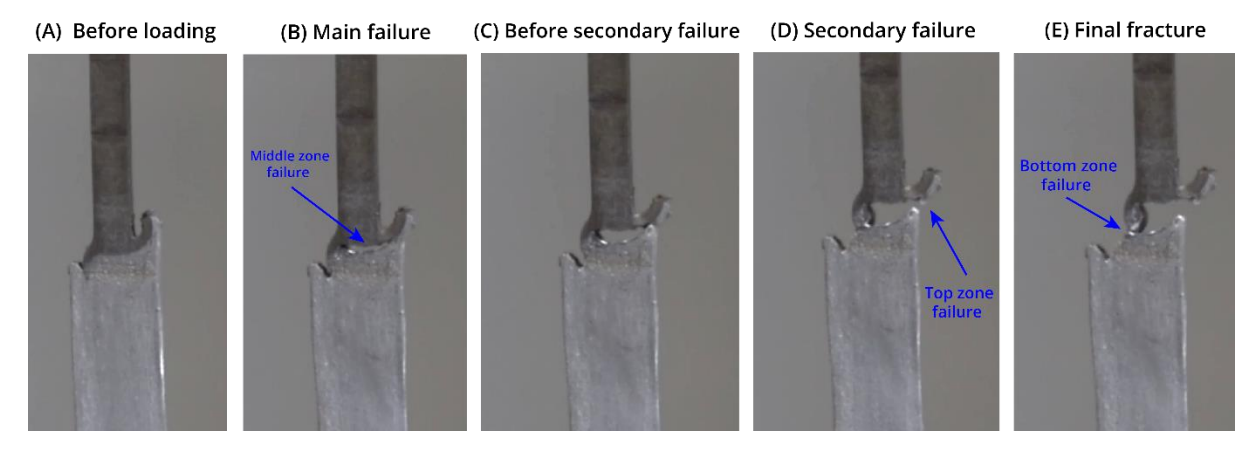


Figure 3.34 - Failure instants video frames of the specimen  $\mathbf{V} \bullet \bullet$  tensile test.

### Specimens VI: 250 $^{\circ}$ C / 90 min heat treatment

The values for max. loads for the final 250 °C heat treatment specimens and the respective extensions are present in the following Table 3.14.

Table 3.14 - Max. Load and Extension at Max. Load of the 250  $^{\circ}$ C / 90 min heat treatment specimens.

Specimen	Max. load [N]	Extension at max. load [mm]		
VI •	1662.6	0.98		
VI • •	1806.7	1.04		
VI···	1809.3	0.52		

The specimens **VI** • and **VI** • • failed in a first instance in the middle zone, at 1662.6 N / 0.98 mm and 1806.7 N / 1.04 mm, respectively followed by the yielding of the aluminium tips until fracture.

The specimen  $VI \bullet \bullet \bullet$  failed in a similar manner to the specimen  $IV \bullet$ , with the initial failure happening the top and middle zone simultaneously followed by the failure at the bottom zone, as seen in Figure 3.35.

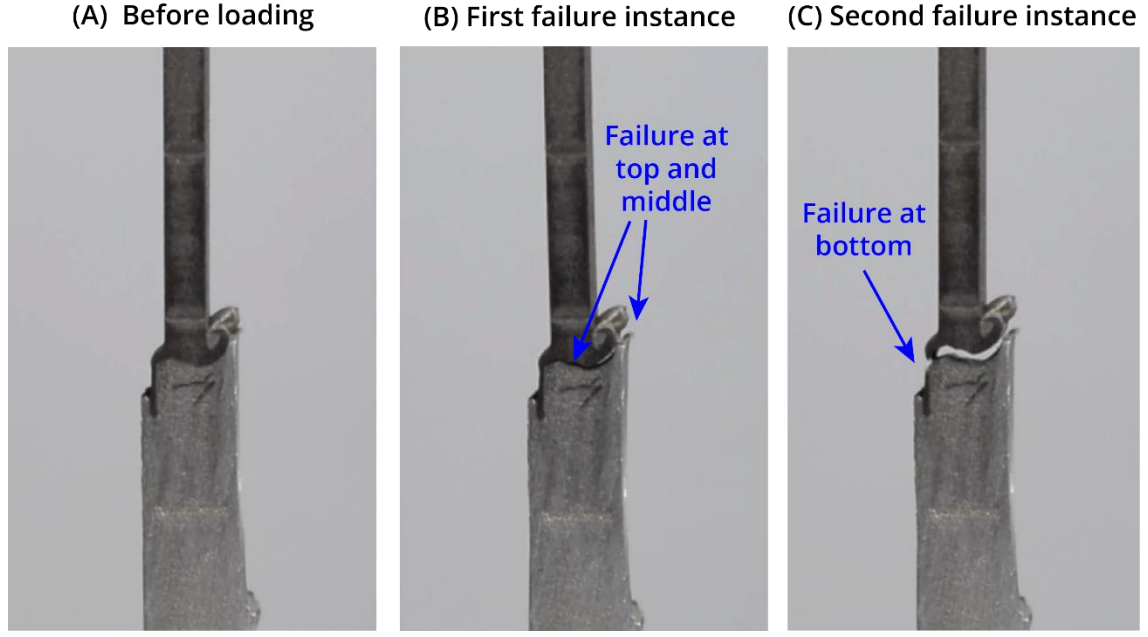


Figure 3.35 - Failure instants video frames of the specimen VI • • • tensile test.

### Specimens VII: 400 °C / 30 min heat treatment

For the specimens VII, 400 °C / 30 min heat treatment, a greater degradation of the joint properties is expected, consequence of the increase in the IMC layer thickness measured in the sample VII.

The ultimate loads and extension at failure for the three **VII** joints are present in Table 3.15.

Table 3.15 - Max.	Load and Exten	sion at Max.	Load of the	400 °C / 3	0 min hea	t treatment specimens.

Specimen	Max. load [N]	Extension at max. load [mm]
VII •	1705.7	5.72
VII • •	1695.4	4.37
VII···	1734.5	7.24

The specimens **VII** • and **VII** • • failed in with a similar behaviour of most of the joints discussed previously, failing in the middle of the joint followed by localized yielding of the Al1050 joint tips until fracture simultaneously.

However, it's possible to observe that these specimens failed at a higher extension in comparison to the previously tested heat treatment pairs, result of the annealing of the aluminium and the enhancement of the ductility of the base metal.

Specimen **VII** ••• failed at the aluminium base metal, with a max. load of 1734.5 N and a extension at failure of 7.24 mm.

### Specimens VIII: 400 °C / 60 min heat treatment

For the specimens VIII, 400 °C / 60 min heat treatment, following the trend of the past pair, the IMC layer thickness increased in comparison with the other heat treatment samples.

The maximum loads and extension at failure for the three **VIII** joints are present the following Table 3.16.

Table 3.16 - Max. Load and Extension at Max. Load of the 400 °C / 60 min heat treatment specimens.

Specimen	Max. load [N]	Extension at max. load [mm]
VIII •	1540.6	1.46
VIII • •	1690.3	3.39
VIII · · ·	1739.2	0.51

The specimens **VIII** • and **VIII** • • failed in a first instance at the middle zone of the joint, and secondly at the bottom zone and top zone, sequentially, after yielding of the Al1050 tips of the S-shape interface.

However, the specimen **VIII** ••• • failed at the three zones simultaneously in a first instance for 1739.2 N max. load and 0.51 mm extension, followed by the final fracture in the up lower point in the bottom zone. This specimen shown a more brittle behaviour in comparison with the other joint for the 400 °C heat treatment pairs.

The Figure 3.36 represents the frames before and after the main failure instance of this specimen's tensile test.

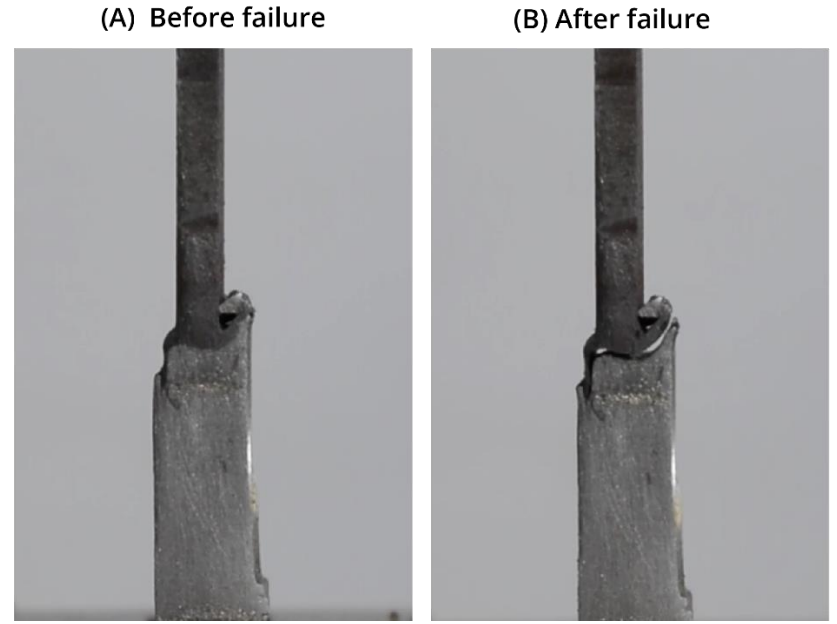


Figure 3.36 – Before and after failure instants video frames of the specimen VIII • • • tensile test.

### Specimens IX: 400 °C / 90 min heat treatment

The specimens **IX** • and **IX** • • failed accordingly to the already discusses main fracture behaviour of the joints tested: Firstly, in the middle zone followed by the tips after yielding of the aluminium, in this case first in the bottom zone and them at the top zone.

Table 3.17 presents the maximum loads and the respective extension for the **IX** specimens.

Table 3.17 - Max. Load and Extension at Max. Load of the 400 °C / 90 min heat treatment specimens.

Specimen	Max. load [N]	Extension at max. load [mm]
IX •	1684.1	4.81
IX • •	1621.8	2.61
IX • • •	1209.9	0.20

For the specimen **IX** • • •, although it failed following the sequence already discussed, demonstrated a very weak and brittle behaviour, failing at 1209.9 N and 0.20 mm of extension, and therefore considered an outlier. The frames of the tensile test for this specimen are shown in Figure 3.37.

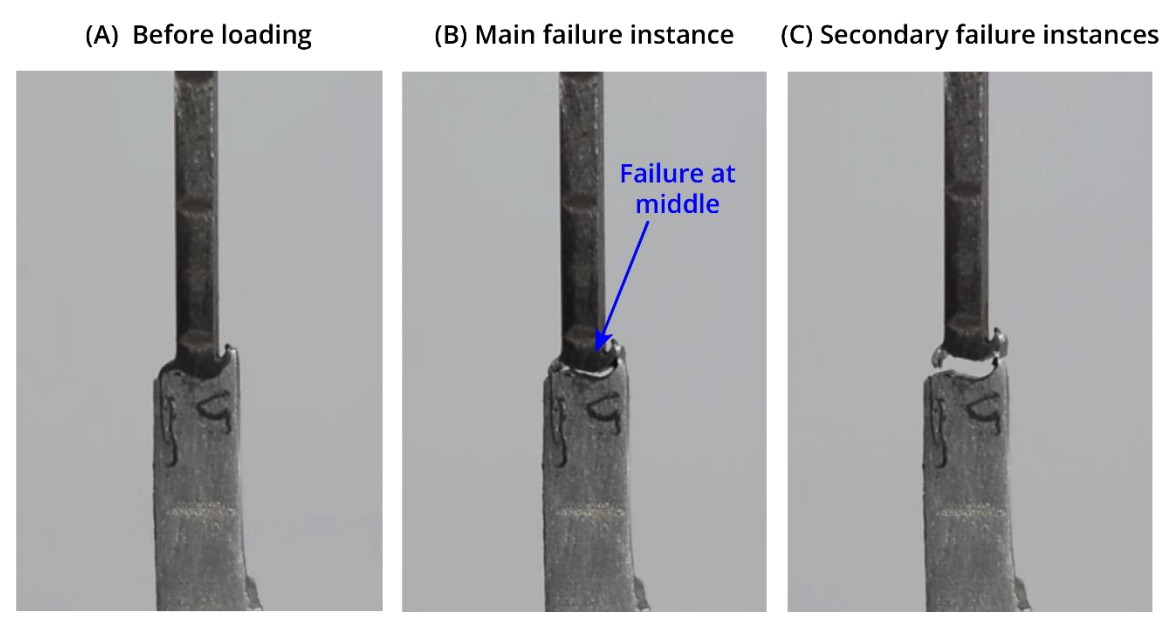


Figure 3.37 - Failure instants video frames of the specimen **IX** • • • tensile test.

In summary, 32 tensile tests were performed, for as-welded and heat treated specimens.

Averaging the results obtained for the as-welded specimens and for each heat treatment pair specimens, and eliminating the identified outliers, as shown in plot present in Figure 3.38 in blue, a decrease of the main failure load throughout the heat treatments performed is observed, as represented in the dotted black trendline in Figure 3.38, below.

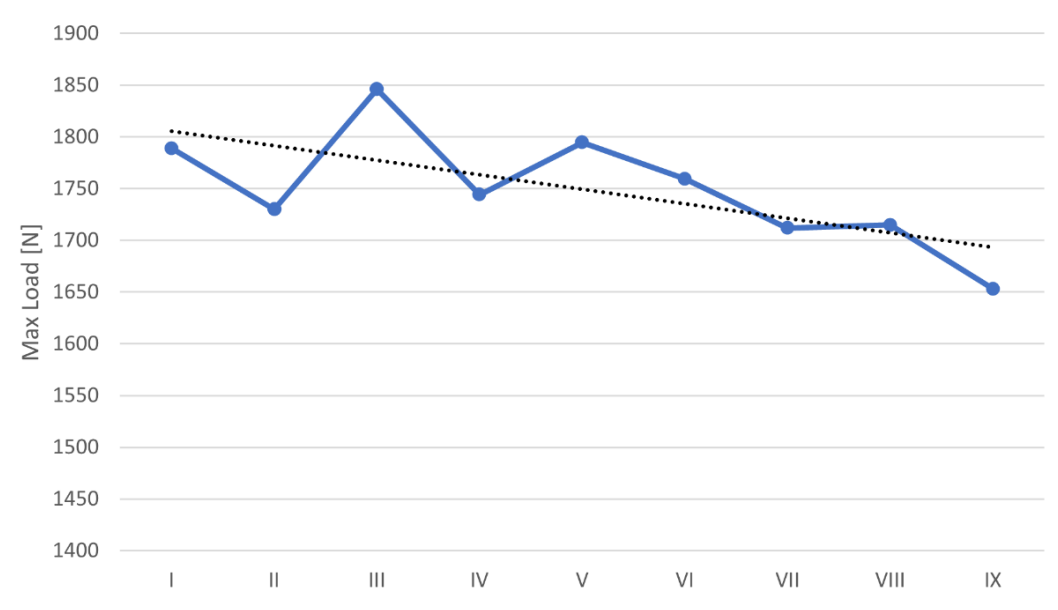


Figure 3.38 - Average max loads of each heat treatment pair and as-welded specimens (blue), and trendline (dotted black).

The temperature of the heat treatment has the largest impact on the decrease of the max. load of the specimens. By averaging the results for pair temperature/time, grouping by heat treatment duration, and varying the temperature, seen in Figure 3.39, the aforementioned impact of the temperature in the joint degradation is observable.

Moreover, it is also possible to observe that the most meaningful heat treatment duration, resulting in the highest degradation of the joint strength, are the 90min heat treatments.

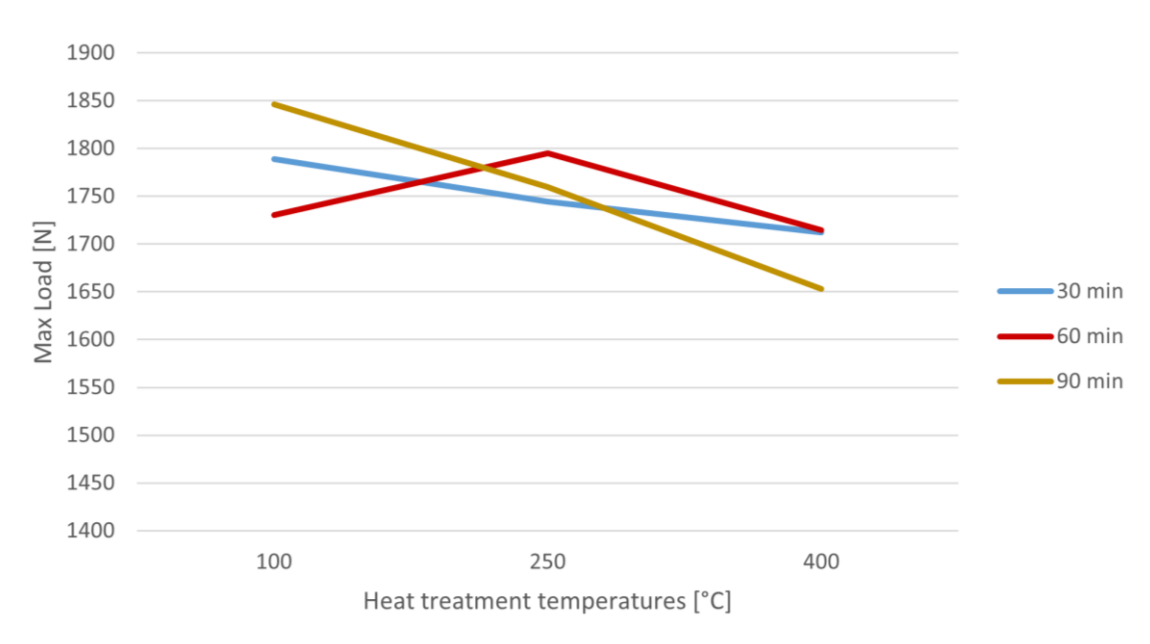


Figure 3.39 – Average max. loads by temperature, grouped by heat treatment duration.

Another factor to be considered when analysing the tensile tests results are the zones of failure and the macroscale fracture behaviour. It is observed that the majority of the specimens have 2 or 3 distinctive failure zone for different instances when loaded.

The main failure zone is at the middle of the interface, being the initial failing stage of the joint, and it is characterized as a brittle failure. In this zone, the joint is loaded in a normal direction to the interface, opposite to the forces applied in the bottom and top zones, where shear stress is applied to the interface, represented in Figure 3.40 by a schematic of the forces applied in the aforementioned joint interface zones.

This leads to a lower required load to detach the two substrates in the middle zone in comparison with the tips of the joint.

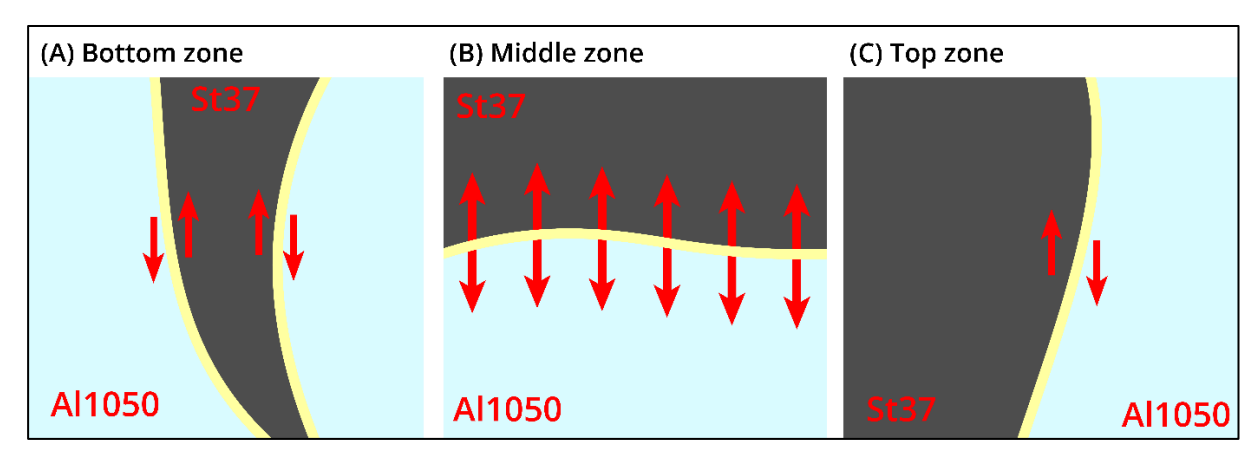


Figure 3.40 - Schematic representation of the applied forces in the bottom (a), middle (b) and top (c) zones of the joint interface. The IMC layer is represented in yellow.

The subsequent failure zones are the bottom and top zones, where yielding of the aluminium side of the joint takes place until fracture. As a consequence, fragments of Al1050 are still welded to the steel substrate in the end of the tensile test for the majority of the specimens. Further fractography analysis is required and will be performed to assess the fracture behaviour and confirm the presence of aluminium at the steel half of the failed joints.

Regarding the degradation of the joint and the impact of the IMC layer thickness on strength of the joint, the average main failure loads, and the IMC layer thicknesses of the joint samples in the middle zone throughout the heat treatments was plotted in Figure 3.41. The middle zone was chosen due to having the biggest impact on failure of the joints.

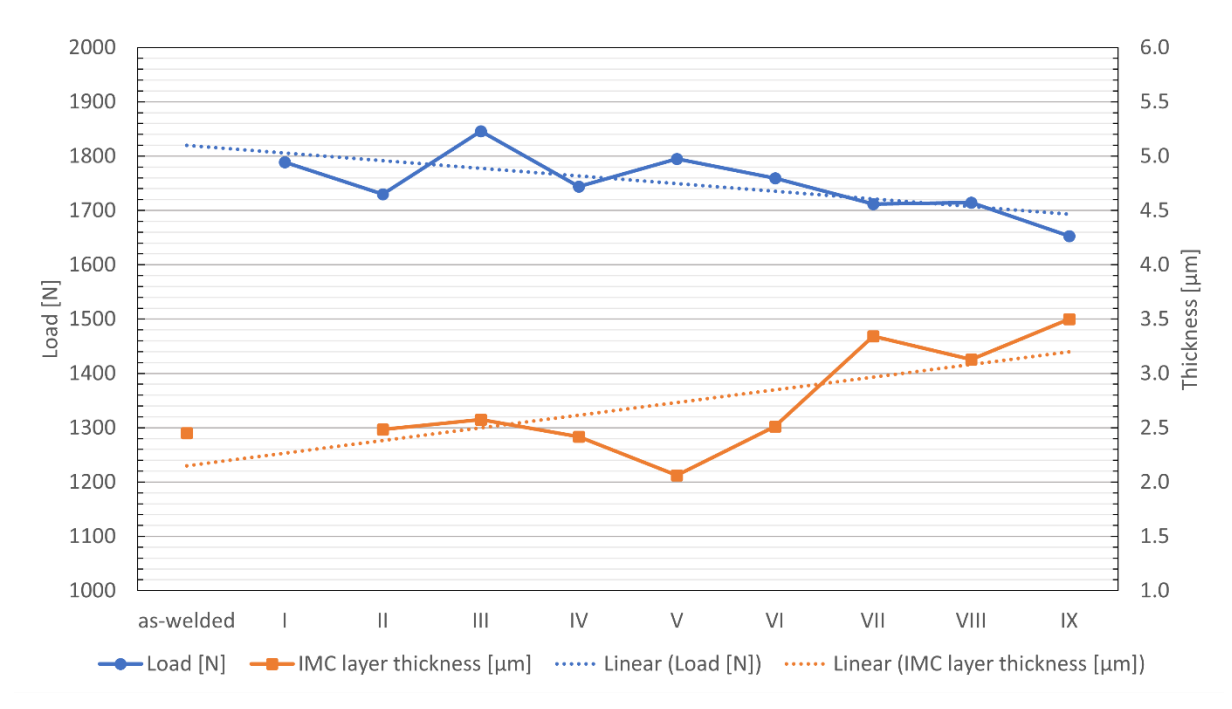


Figure 3.41 - Plotted average main failure loads and IMC layer thickness at the middle zone, with respective trendlines.

By increasing the IMC layer thickness, the strength of the joint decreases, and vice-versa. Therefore, the thickness of the IMC layer as a proportional influence on the degradation of the joint properties, as stated in the literature and confirming our expectations regarding this study.

### 3.2.4 - Fractography results

Is this section, the results of the fractography performed on the selected **III** • • (100 °C / 90 min), **VI** • (250 °C / 90 min) and **IX** • (400 °C / 90 min) samples are presented and discussed, shown in Figure 3.42

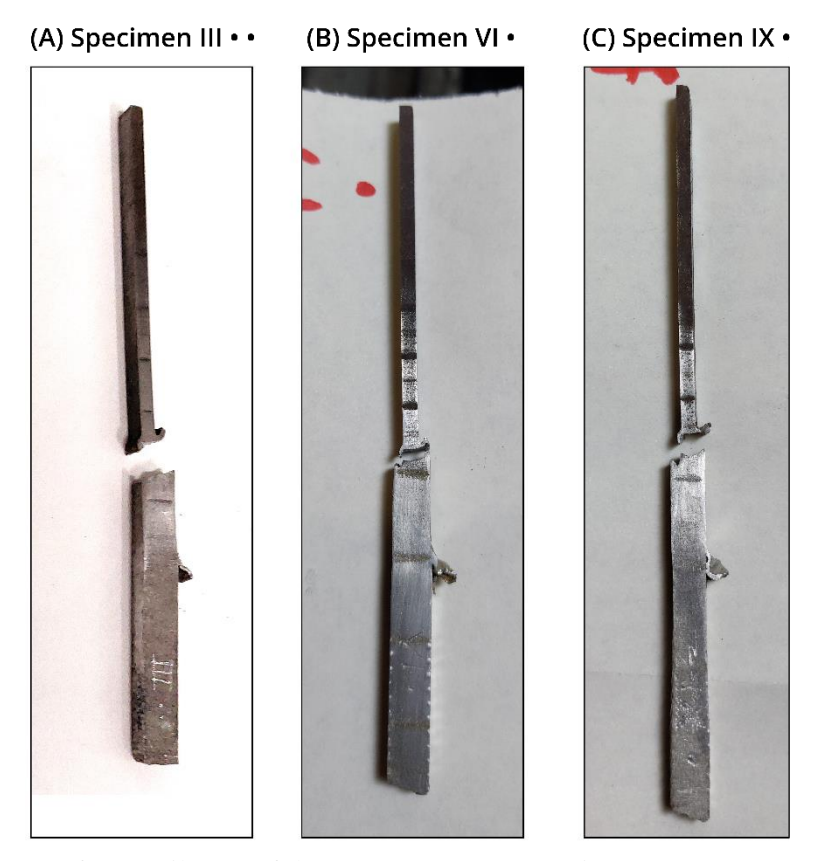


Figure 3.42 – Images after tensile test of the **III** • • (100 °C / 90 min) (a), **VI** • (250 °C / 90 min) (b), and **IX** • (400 °C / 90 min) (c) specimens.

An in-depth analysis of the fracture surfaces of the **III** ( $100 \,^{\circ}\text{C} / 90 \,^{\circ}\text{min}$ ) and **IX** ( $400 \,^{\circ}\text{C} / 90 \,^{\circ}\text{min}$ ) samples, consisting in SEM imaging, in secondary and backscattering modes, of the failed area and subsequent magnification on the zones of interest, and EDS scans of the denoted zones.

This analysis is complementary to the macro imaging via video recording, performed along the tensile tests, supporting the discussion on the previous section.

In Figure 3.43, the SEM images, in secondary mode and at 35x magnification, of the steel and aluminium side fracture surfaces are presented. The topology of the interface can be observed, as well as the failing zones discussed in the previous section: top, middle, and bottom zones of the interface.

In the steel side of the joints, Figure 3.43 (a), (c), (e) and (g), the top S-shape tip is visible, although the substantial height, perpendicular to the image plane, is not easily perceived.

At the bottom of the interface in the aluminium side, a crater along across the fracture surface is easily observed, in Figure 3.43 (b), (d), (f) and (h), where the steel tip penetrated the aluminium substrate, and the yielding of the aluminium took place, with a volume removed at the said zone.

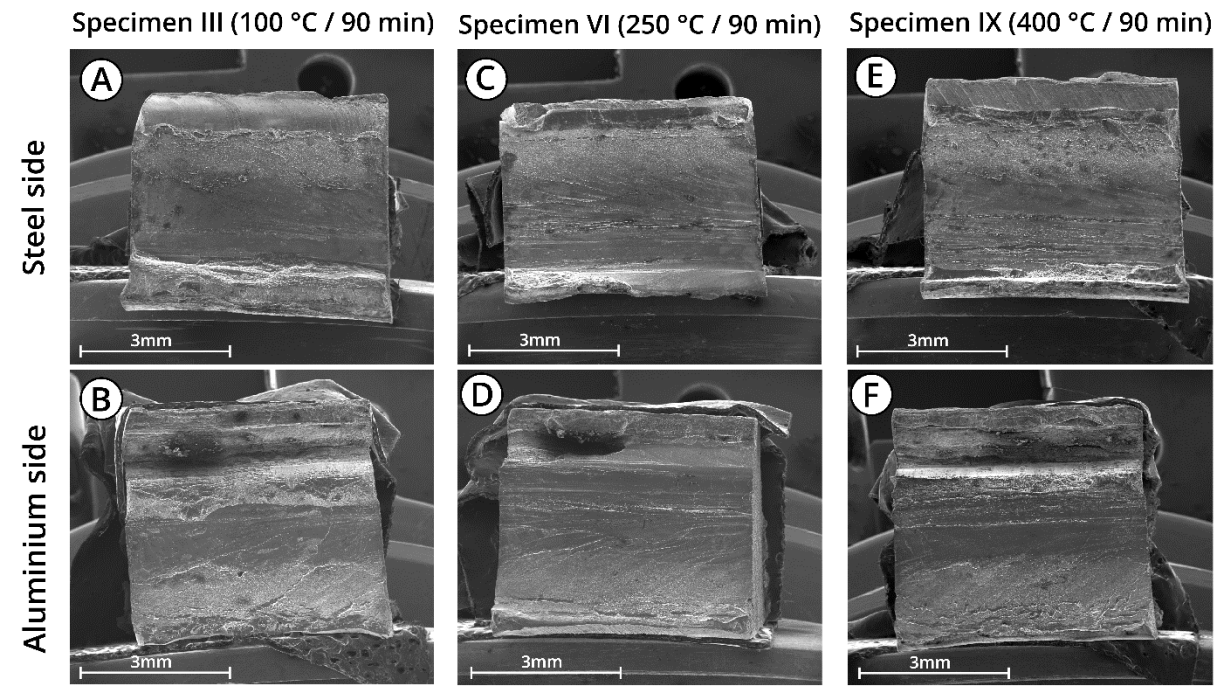


Figure 3.43 - SEM imaging, in secondary mode, of the **III**, **VI** and **IX** specimens' fracture surfaces, at 35x magnification.

For the following examination of the individual surfaces of the fracture surfaces and zone EDS analysis, backscattering mode SEM imaging will be used, in order to better differentiate the materials present at different zones on the surfaces.

### Specimens III: $100 \, ^{\circ}\text{C} / 90 \, \text{min}$ heat treatment:

For the steel side of the specimen, 4 zones were examined:

- Zones Z1 and Z2 in the middle of the interface, Figure 3.44 (a). In the EDS scan of the zone Z1, Figure 3.44 (d), and zone Z2, Figure 3.44 (e), we observe the presence of Fe-Al IMC by the constituting Al and Fe elements in the zones. However, for Z1 we have a higher count of Al comparing to Fe, opposing to Z2 where we have a higher count of Fe, therefore the presence of two Fe-Al IMC phases.
- Zones Z3 also in the middle of the interface, as seen in Figure 3.44(b), indicates the presence of A1, in a higher count, followed by Fe in a lower count, denoting the presence of Fe-Al IMC, in similarity with zone Z1, as shown in Figure 3.44 (f).
- Zone Z4 at the top of the interface, Figure 3.44(c), by analysing the EDS, we observe the presence of Al, with no counts of Fe, Figure 3.44(g), indicating to Al1050 base metal.

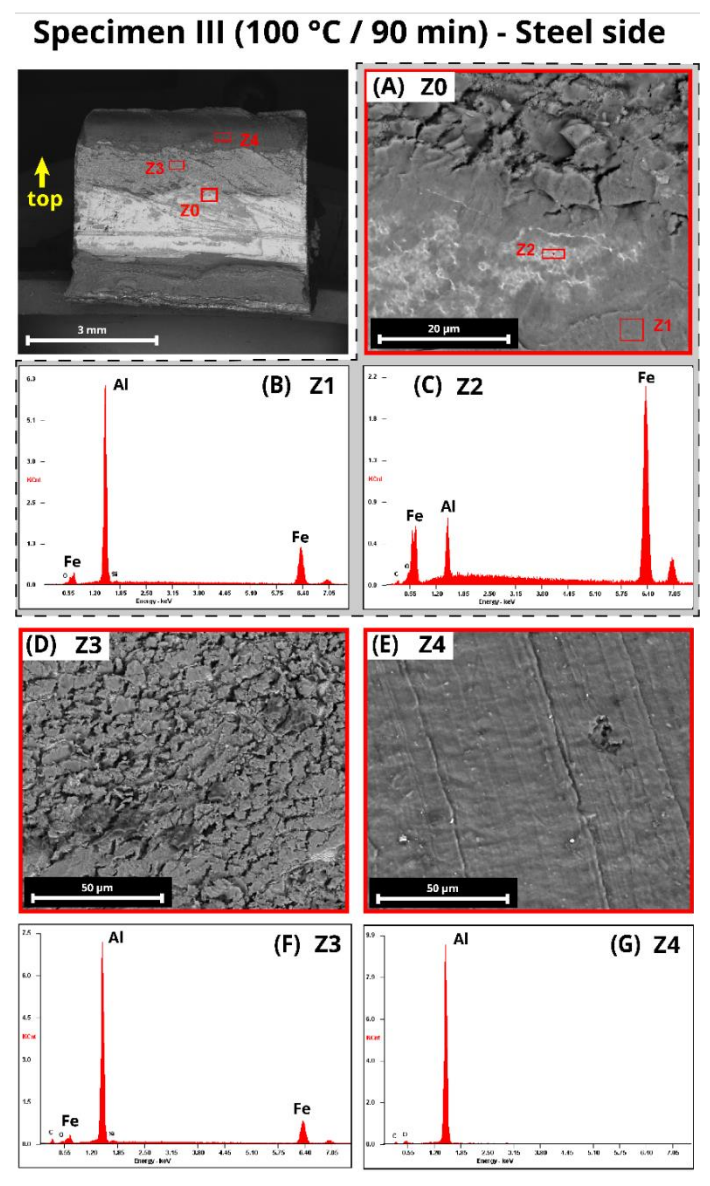


Figure 3.44 - SEM imaging, in backscattering mode, and EDS zone analysis of specimen **III** ( $100 \, ^{\circ}\text{C} / 90 \, \text{min}$ ) steel side.

For the aluminium side of the specimen, 5 zones were examined:

- Zones Z1 at the bottom side of the interface, indicates the presence of Al1050 base metal, by analysing the EDS data, with counts of Al and no presence of Fe atoms, Figure 3.45 (a).
- Zone Z2 and Z3, at the middle of the interface, Figure 3.45 (a), indicates the presence of distinct Fe-Al IMC phases in the two, having Z2 Al and Z3 Fe as the main elements in the IMC phase, Figure 3.45 (b) and (c), respectively.
- Zones Z4 and Z5 are magnification of zone Z3, as seen in Figure 3.45 (d). In Z4 we have only Al and no Fe, indicating the presence of Al1050, Figure 3.45 (e), and Z5 has Al as well as Fe in a lower count, indicating the presence of Fe-Al IMC, Figure 3.45 (f).

### Specimen III (100 °C / 90 min) - Aluminium side

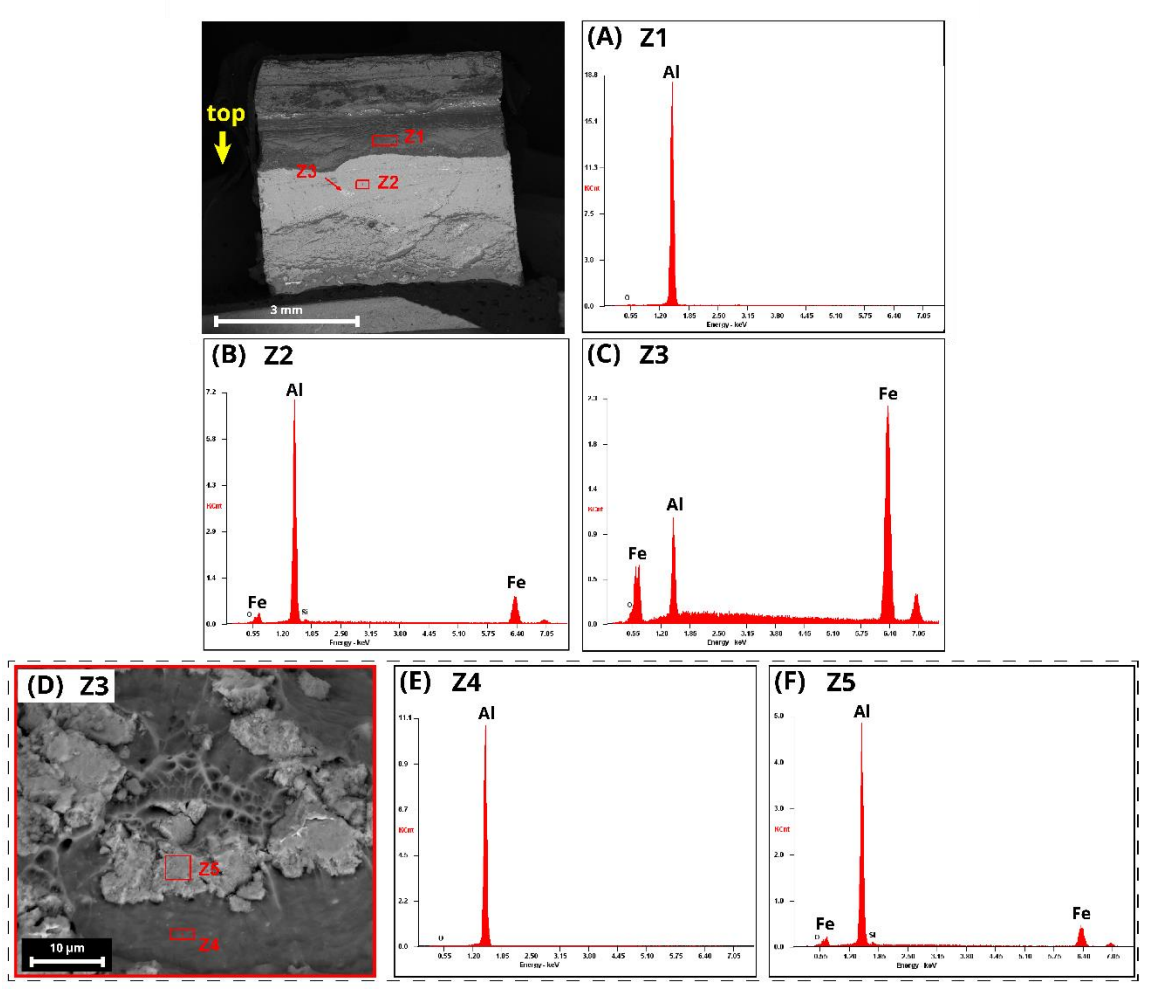


Figure 3.45 - SEM imaging, in backscattering mode, and EDS zone analysis of specimen **III** (100 °C / 90 min) aluminium side.

The presence of Al1050 substrate at the tip of the specimen III  $\bullet \bullet$  (100 °C / 90 min) is confirmed, as well as the presence of an Fe-Al IMC layer at both sides of the joint's interface, which confirms the main failure at the IMC layer of the interface, followed by the yielding of the Al1050 at the top and bottom zone of the zones.

Furthermore, we observe at zone Z4 and Z5 of the aluminium side, Figure 3.45, that the middle zone has not a homogeneous layer of IMC, but spots of IMC covering the Al1050 substrate. However, the EDS data for Z3 indicates that the IMC is predominant in the middle zone, seen in Figure 3.45 (c).

### Specimens IX: 400 °C / 90 min heat treatment

For the steel side of the specimen, 3 zones were examined:

- Zone Z1 and Z2, at the middle of the interface, as seen in Figure 3.46Figure 3.47 (a), indicates the presence of Al and Fe atoms at different counts for the two zones, where Z1 has a higher amount of Al, Z2 has a higher count of Fe atoms, seen in Figure 3.46 (c) and (d), implying two distinct Fe-Al IMC phases.
- Zone Z3 is examined at the transition of the middle to the bottom of the joint's interface. In

this zone, more specifically at the magnified zone Z3.1, we observe a high count of Al, followed by Fe, indicating the presence of Fe-Al IMC in the analysed zone. It is worth noting that in SEM image Figure 3.46 (b) we observe a darker grey area that should indicate the presence of Al1050, as seen in the previous specimens.

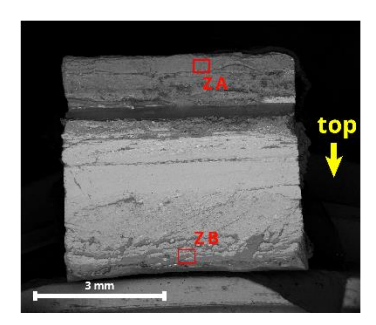
# Specimen IX (400 °C / 90 min) - Steel side (A) Z0 (B) Z1 (C) Z2 Fe (D) Z3.0 (D) Z3.0 (E) Z3.1

Figure 3.46 - SEM imaging, in backscattering mode, and EDS zone analysis of specimen IX ( $400 \, ^{\circ}\text{C} / 90 \, \text{min}$ ) steel side.

For the aluminium side of the specimen, 4 zones were examined:

- Zones Z1 and Z2, at the bottom of the interface, shown in Figure 3.47 (a), indicates the presence of Fe-Al IMC phases, distinct in the two. Z1 has a higher counter of Al atoms in comparison with Fe, Figure 3.47 (c), while Z2 has a higher count of Fe following of a meaningful presence of Al atoms, Figure 3.47 (d).
- Zones Z3 and Z4, at the top of the interface, Figure 3.47 (b), presents an Al dominated Fe-Al IMC phase for Z3 and aluminium base metal in Z4, as observed in EDS data in Figure 3.47 (e) and (f), respectively.

### Specimen IX (400 °C / 90 min) - Aluminium side



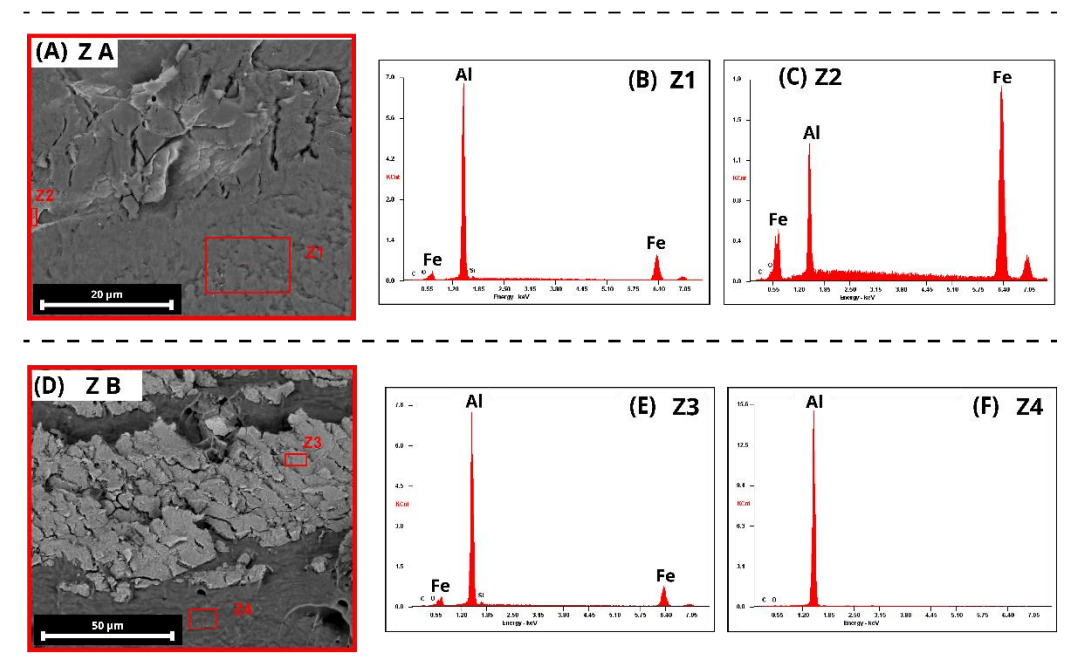


Figure 3.47 - SEM imaging, in backscattering mode, and EDS zone analysis of specimen IX ( $400 \, ^{\circ}\text{C} / 90 \, \text{min}$ ) aluminium side.

The presence of Fe-Al IMC phases in the middle of the specimen  $IX \cdot (400 \, ^{\circ}\text{C} / 90 \, \text{min})$  joint's interface, at the steel and aluminium side, corroborates the brittle main failure at the IMC layer at this zone.

Furthermore, the strain of the aluminium substrate at the top zone is confirmed by the presence of dimples in the region, indicative of this mechanical behaviour of the metal, as seen in Figure 3.48 (a) and (b), SEM images taken in secondary mode in two separate locations of the top zone of the interface.

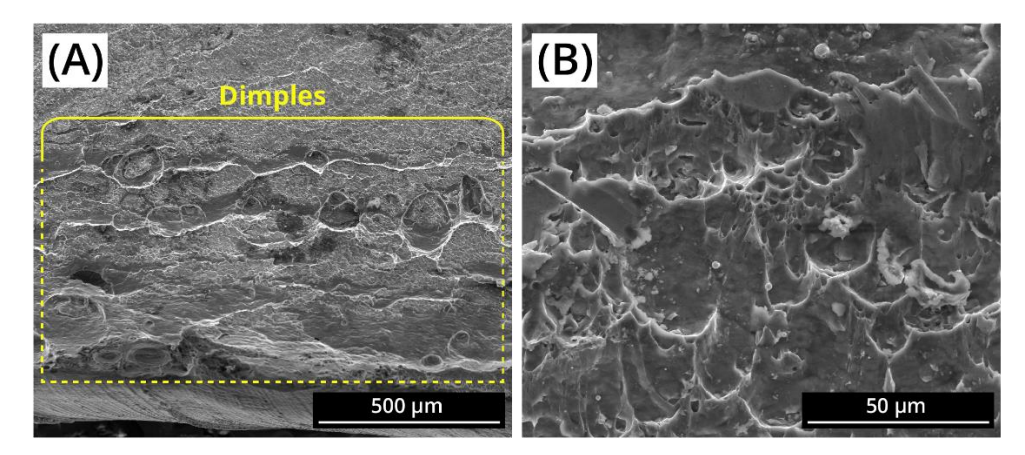


Figure 3.48 - SEM images, in secondary mode, of two sections of the top zone of the **IX** sample, Al side, (a) at 200x magnification and (b) at 2000x magnification.

At the bottom zone of the interface, is observed a crater where the steel tip was situated, as shown in Figure 3.49. The walls of the crater have the aforementioned dimples indicative of the localized plastic deformation of the aluminium and the crater base with directional grooves, indicative of the brittle fracture behaviour.

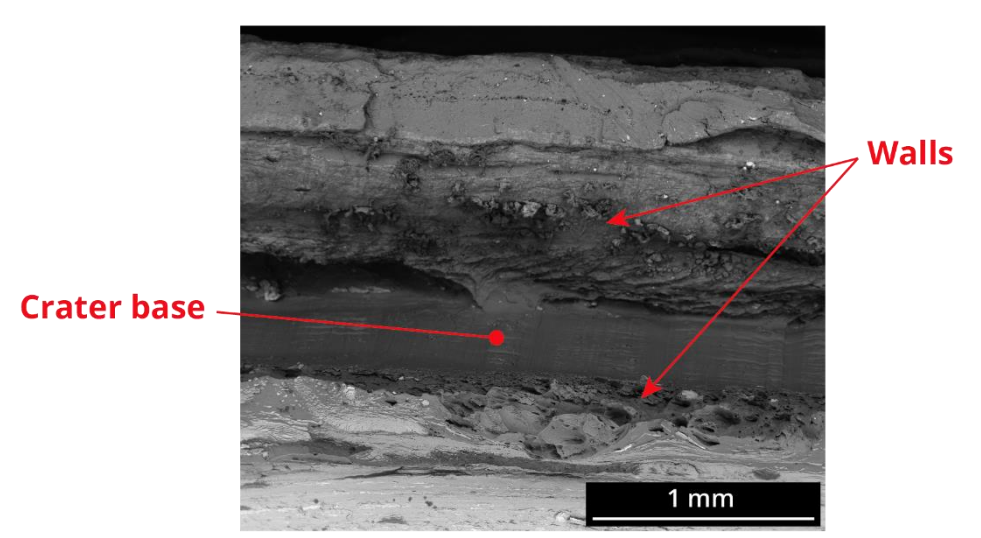


Figure 3.49 - SEM images, in secondary mode, at the bottom zone of the Al side of sample **IX**, 100x magnification.

### Specimens VI: 250 °C / 90 min heat treatment

For the specimens **VI** •, solely SEM imaging in backscattering mode and 35x magnification, was performed additionally to the examination in SEM secondary mode previously discussed.

The Figure 3.52 presents the steel side (a) and aluminium side (b) of the fracture surfaces in the mentioned parameters. As seen in the previous specimens, the middle zone and the top and bottom of the specimens **VI** • also indicates the presence of varying percentages of Al and Fe across the joint interface, denoted by the different grey shades.

### (A) Steel side (B) Aluminium side

Figure 3.50 - SEM imaging, in backscattering mode and 35x magnification of specimen **VI** (250 °C / 90 min) steel side (a) and aluminium side (b) fracture surfaces.

### 3.2.5 - Microhardness measurements

In this section, the values of the measured Vickers' microhardness will be presented firstly for each sample analysed, presenting the values for the all the zones, and plotted in a HV vs Length graph.

The negative length values correspond to the steel side and the positive to the aluminium side of the joint.

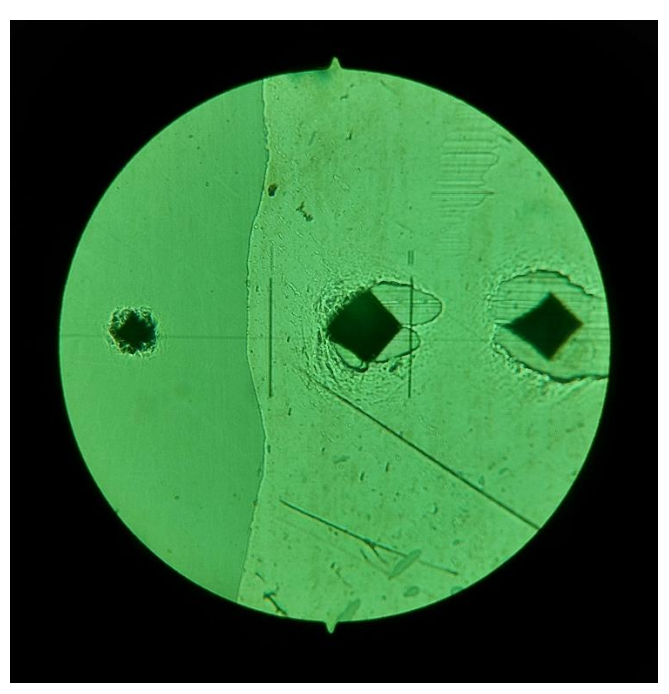


Figure 3.51 - Optical image of the as-welded sample interface, 10x magnification, during the Vicker's microhardness measurements. Noting three indentations: one at the St side and two at the Al side.

### As-welded sample 00

The hardness line measurements for the sample covers a bigger length in comparison with the heat treated samples, due to the sample preparations used, seen in Figure 3.11 and Figure 3.12. For the as-

welded sample, the lines lengths are 11.6 mm. 17.6 mm, and 9.3 mm, for the upper, middle, and bottom zone respectively.

The measured values are presented in the following Table 3.18, Table 3.19 and Table 3.20.

Table 3.18 - Upper zone Vickers' microhardness values for the as-welded sample  $\mathbf{00}$ 

Indentati	on	length [mm]	HV
St	1	-0.9	169
	2	0.9	44
	3	1.9	46
	1 2	2.8	44
	5	3.7	41
	6	4.6	43
Al	7	5.4	47
AI	8	6.3	30
	9	7.4	31
	10	8.3	34
	11	9.2	34
	12	10.1	35
	13	10.7	35

Table 3.19 - Middle zone Vickers' microhardness values for the as-welded sample 00

Indentati	ion	length [mm]	HV
	1	-8.6	116
	2	-7.4	126
	3	-6.4	119
	1 2 3 4 5 6 7 8 9 10 11 12 13 14 15 16 17	-5.7	121
C+	5	-4.9	131
31	6	-3.8	128
	7	-2.4	124
	8	-1.7	131
	9	-0.9	149
	10	-0.3	175
	11	0.3	38
	12	0.8	38
	13	1.5	43
	1 -8.6 2 -7.4 3 -6.4 4 -5.7 5 -4.9 6 -3.8 7 -2.4 8 -1.7 9 -0.9 10 -0.3 11 0.3 12 0.8 13 1.5 14 2.2 15 2.9 16 3.8	2.2	44
ΔΙ		43	
AI	16	3.8	29
	17	5.3	29
	18	6.9	30
	19	7.8	35
	20	9.0	37

Table 3.20 -Bottom zone Vickers' microhardness values for the as-welded sample **00** 

Indentati	on	length [mm]	HV
St	1	-0.6	188
	2	0.6	42
	1 -0.6	1.5	35
		28	
	5	3.3	29
Al	6 4.3	32	
AI	7	5.2	31
	8	5.6	32
	9	6.6	33
10	10	8.1	34
	11	8.8	36

When plotting the microhardness values of the as-welded sample, some observation can be taken.

Firstly, the indentations closest to the interface of the joint, the hardness values of the steel substrate decrease from the upper zone to the bottom, with 169 HV, 175 HV, and 188 HV.

Secondly, the middle zone, being the zone that we can compare the values of the St37 base metal along the length of the joint, presents an increasing hardness closest to the interface, from 116 HV in the furthest distance and 175 HV close to the interface, as observed in Figure 3.52.

For the Al1050 base metal side, all the three zone presents a pattern of higher hardness close to the interface, that decreases further from it. In the case of the upper and middle zones, we can all observe a sudden decrease in hardness from 47 HV to 30 HV at 5.4 mm from the interface, and 43 to 29 Hv at 2.9 mm from the interface, respectively.

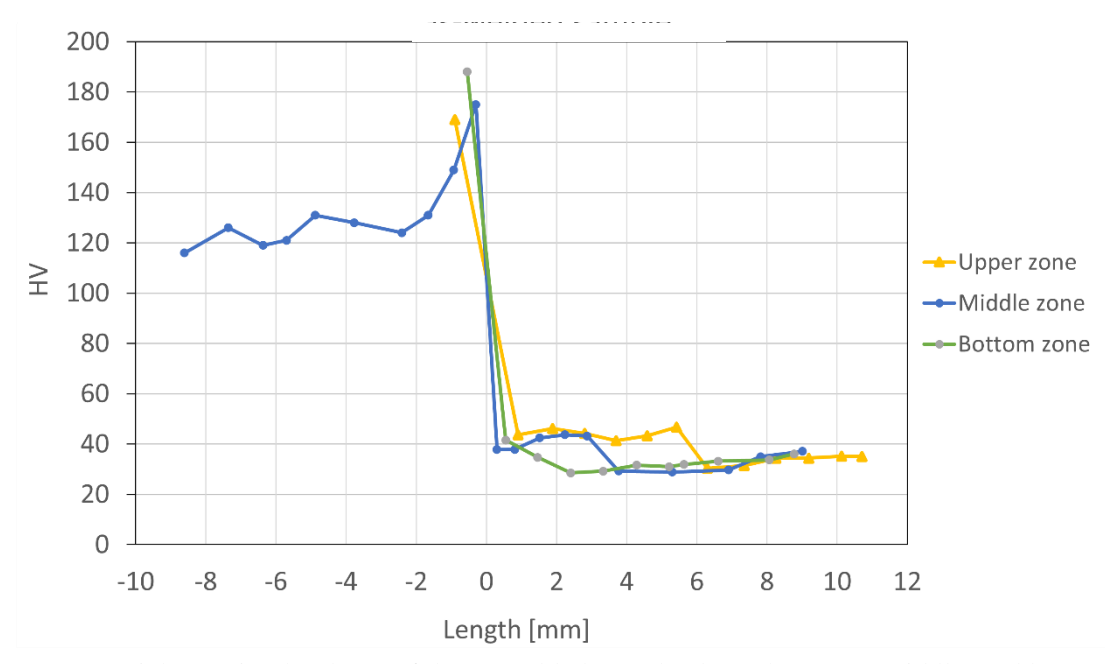


Figure 3.52 - Vickers microhardness of the as-welded sample along the upper, middle, and bottom measured lines.

### Sample III (100 $^{\circ}$ C / 90 min)

For the sample **III**, the lines lengths are 4.6 mm. 6.4 mm, and 3.7 mm, for the upper, middle and bottom zone respectively.

The measured values are presented in the following Table 3.21, Table 3.22 Table 3.23.

Table 3.21 -Upper zone Vickers' microhardness values for the sample III (100 °C / 90 min)

Indentati	on	length [mm]	HV
St	1	-0.6	146
	1 2 3 4 5 6 7	0.6	40
	3	1.1	32
	4	1.6	30
Al	5	2.1	38
	6	2.8	38
	7	3.4	39
	8	4.0	39

Table 3.22 - Middle zone Vickers' microhardness values for the sample III (100 °C / 90 min)

Indentation	on	length [mm]	HV
	1	-3.4	105
	2	-2.7	109
St	3	-2.1	104
31	4	-1.4	122
	5	-0.8	138
	6	-0.3	166
	7	0.3	52
	8	0.9	49
Al	9	1.6	46
	10	2.3	41
	11	3.0	42

Table 3.23 - Bottom zone Vickers' microhardness values for the sample **III** (100 °C / 90 min)

Indentation		length [mm]	HV
St	1	-0.4	187
	2	0.4	49
	3	0.9	55
Al	4	1.5	50
AI	5	2.1	48
	6	2.7	42
	7	3.4	45

For the sample **III**, the main hardness kinetics observed in the as-welded sample also translates for this joint: a decrease of the hardness for the steel side closest to the interface, from the upper zone to the bottom zone, with 146 HV, 166 HV, and 187 HV, respectively. In the same manner, the hardness of the steel side of the joint increases with the proximity of the interface, with a 105 HV in the furthest distance from the interface.

For the aluminium side, a slight decrease in hardness away from the interface is observed, for the middle and bottom zone. However for the upper zone, after the decrease in hardness, until the 2.1 mm point, an increase for 38 HV occurs.

### Sample VI (250 °C / 90 min)

For the sample **VI**, the lines lengths are 5.4 mm. 7.3 mm, and 4.9 mm, for the upper, middle and bottom zone respectively.

The measured values are presented in the following Table 3.24, Table 3.25, and Table 3.26.

Table 3.24 - Upper zone Vickers' microhardness values for the sample VI (250 °C / 90 min)

Indentation		length [mm]	HV
St	1	-0.3	170
	2	0.3	43
	3	0.9	42
	4	1.6	42
Al	5	2.3	47
AI	6	3.0	39
	7	3.8	43
	8	4.5	45
	9	5.1	46

Table 3.25 – Middle zone Vickers' microhardness values for the sample VI (250 °C / 90 min)

Indentatio	on	length [mm]	HV
	1	-3.0	124
	2	-2.3	136
St	3	-1.7	135
	4	-1.1	133
	5	-0.4	157
	6	0.4	29
	7	1.1	28
Al	8	1.8	30
	9	2.6	40
	10	3.4	44
	11	4.3	50

Table 3.26 - Bottom zone Vickers' microhardness values for the sample VI (250 °C / 90 min)

Indentation	on	length [mm]	HV
St	1	-0.3	160
	2	0.3	35
	3	0.9	35
Al	4	1.1	34
AI	5	1.9	30
	6	3.1	29
	7	4.0	29
	8	4.7	35

The sample **VI** presents the increase in hardness, in the steel side, towards the interface as seen in the previous samples from 124 HV to 157 HV. However, for the aluminium side of the middle zone, we observe an increase in the hardness away from the interface, from 1.8 mm onwards, an increase of 30 HV until 50 HV.

Another difference from the previous samples is hardness of the steel close to the interface of the joint, where the middle zone presents the lower value of 157 HV, followed by the bottom zone with 160 HV and the highest being the top zone with 170 HV.

#### Sample IX $(400 \, ^{\circ}\text{C} / 90 \, \text{min})$

For the sample **IX**, was performed a line measurement at the middle zone, with a total length of 9.4 mm. The measured values are presented in the following Table 3.27.

Table 3.27 - Middle zone Vickers' microhardness values for the sample IX (400 °C / 90 min)

Indentation		length [mm]	HV
	1	-4.3	122
	2	-3.7	110
St	3	-2.9	121
	4	-1.1	142
	5	-0.6	163
Al	6	0.6	40
	7	1.0	50
	8	1.4	41
	9	2.5	47
	10	3.4	33
	11	4.3	32
	12	5.1	33

The middle zone presents an increasing hardness closest to the interface, from 122 HV in the furthest distance and 163 HV close to the interface. From the interface onwards, at the aluminium zone, the hardnesses measured varied irregularly between 33 HV to 50 HV.

Additionally, the microhardness values for the middle zone were individually plotted in the following Figure 3.53

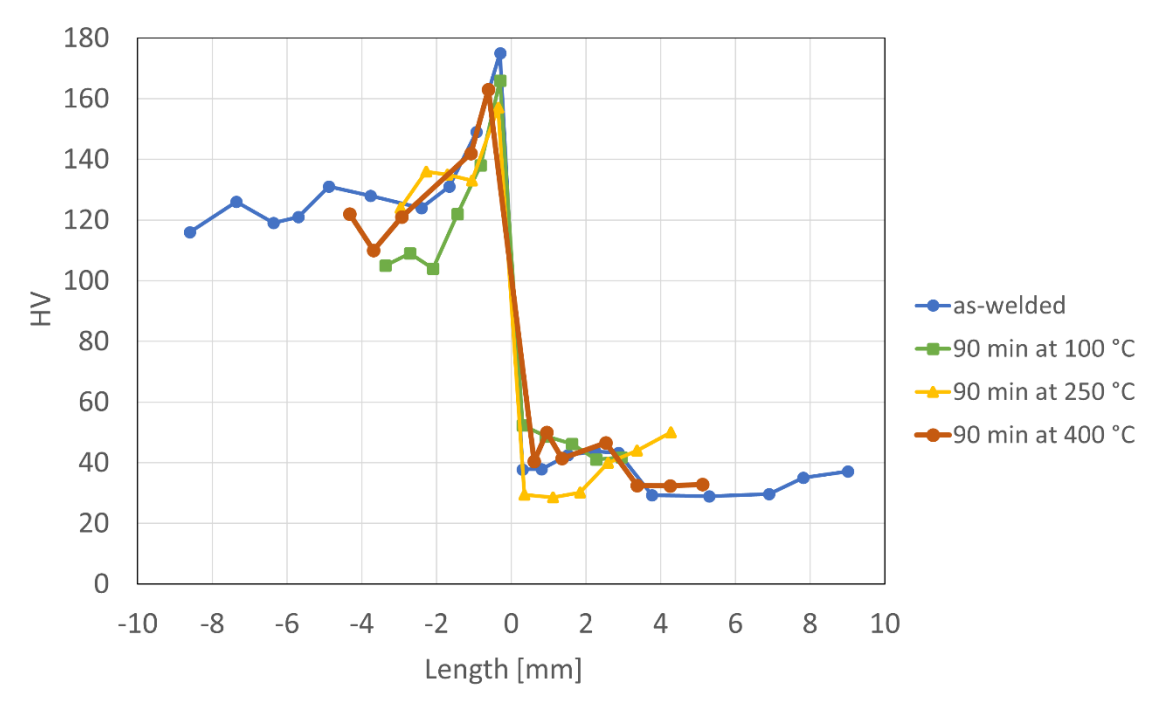


Figure 3.53 - Vickers microhardness of the middle zones of the measured samples.

For the upper zone, steel side, the as-welded and **VI** (250  $^{\circ}$ C / 90 min) samples presented 169 HV and 170 HV, respectively. For the aluminium side, the closest zone to the interface presents 44 HV 40 HV and 43 HV for the upper, middle, and bottom zones. As discussed previously, the sample **III** (100  $^{\circ}$ C / 90 min) had an opposite hardness evolution away from the interface, at the aluminium side, in comparison with the other samples: while in the sample **III** a decrease in the first millimetres after the interface, the as-welded and **VI** samples experience an increase.

For the middle zones, we observe the same increasing hardness towards the interface for the steel substrate, with the closest point having 175 HV for the as-welded sample, 166 HV for the **III** (100  $^{\circ}$ C / 90 min) and 157 HV for the **VI** (250  $^{\circ}$ C / 90 min). The aluminium side does not present a trend for the three samples, at the middle zone, as observed in Figure 3.53.

The bottom zone, aluminium side, of the sample **III** (100 °C / 90 min) presented the highest hardnesses, followed by the as-welded and **VI** (250 °C / 90 min) samples. For the steel side, the sample **VI** (250 °C / 90 min) presented the lowest hardness of 160 HV, and the as-welded and sample **III** (100 °C / 90 min) with 188 HV and 187HV, respectively.

# Chapter 4

## **Numerical Model**

#### 2.1 - Introduction

A numerical model has been devised with the primary aim of simulating the fracture behavior of joints within the context of tensile testing, as explored in the preceding chapter. The development of this numerical model has been particularly focused on the S-shaped interface geometry and the consequential influence of the diminishing thickness of the IMC layer along the interface of the two constituent base metals. In pursuit of this objective, certain simplifications have been instituted, notably the segmentation of the interface into three distinct zones (top, middle, and bottom), each endowed with individualized contact properties. Moreover, the properties ascribed to the IMC layer have been approximated based on pertinent literature, while being carefully compared against the specific case under examination.

Furthermore, the interface bonding properties characteristic of FSW joints between Al1050 and St37, facilitated by the IMC layer at the joint interface, have been modelled as cohesive contact between the substrates. This modelling approach adheres to a bilinear traction-separation law, owing to the observed similarities in the behavior of the IMC layer under both normal and shear loading conditions.

Initially, the tensile test simulation was conducted using *Abaqus CAE/Explicit* software, employing a 3D dynamic explicit analysis framework with a step time period of 1E-5 and a time scaling factor of 1. This modelling approach accounted for nonlinear effects arising from large deformations and displacements. The assembly 3D model of the specimens was based upon the average S-shape interface geometry observed in Scanning Electron Microscope (SEM) examinations, with particular emphasis on the penetration of the S-shaped steel tip into the aluminium substrate, as illustrated in Figure 4.1.

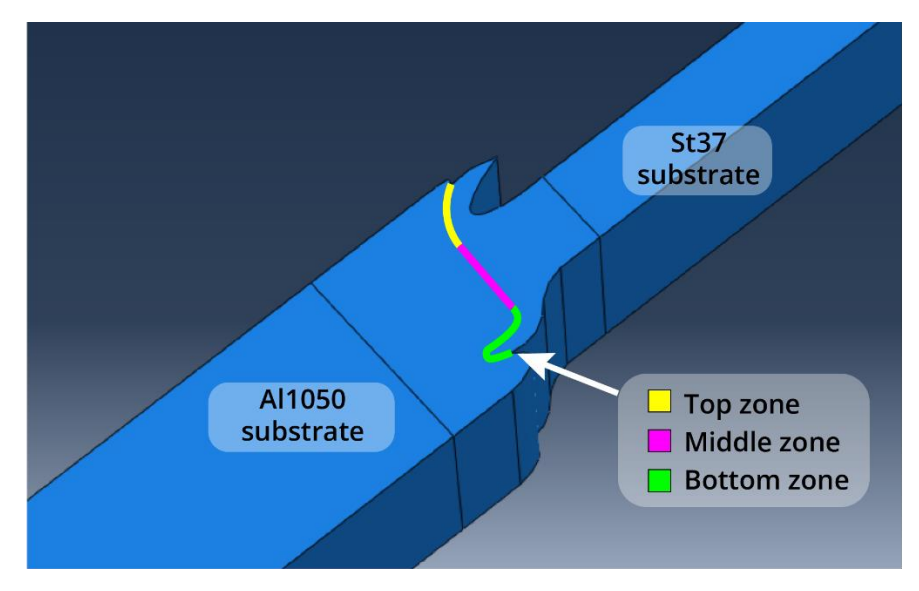


Figure 4.1 - Joint geometry used in the numerical model, in *Abaqus CAE / Explicit*.

#### 4.2 - Properties

It should be noted that the quantitative examination of the numerical findings is not entirely possible since some key material properties, such the stiffness and cohesive strength of the IMC, are not available and were not the target of characterization of this work. Thus, where possible, literature supplied data have been used in its place. The main focus of the discussion will be the behavior of the joint in comparison to its experimental fracture behavior.

The density and elastic properties for the Al1050 and St37 substrates were assigned based on the specifications outlined in Table 4.1. Moreover, the Al1050 substrate was characterized by isotropic plastic behavior to replicate the observed yielding of the base metal in the experimental investigations.

Table 4.1 – Basic materia	l properties inputted	l in numerical r	model for the substrates.
---------------------------	-----------------------	------------------	---------------------------

Material	Young's modulus [GPa]	Poisson's ratio	Mass density [kg/m³]
Al1050	71	0.33	2.71
St37	207	0.28	7.80

The cohesive contact properties of the IMC layer at the three aforementioned zones followed a bilineal traction-separation law, represented in Figure 4.2, with the a IMC layer cohesive strength of  $T_{ult}$  of 600 MPa, according to R. Mitra [99], and an estimated fracture energy  $G_c$  of 0.123 N/mm based on the tested specimens. The initial stiffness  $K_{eff}$  for the three zones were obtained by Equation 6.

$$k_{eff} = \frac{E_{IMC}}{\rho} \tag{6}$$

The value of the IMC stiffness is  $E_{IMC}$  261GPa [99] and the IMC layer thickness e varies for the three zones according to sample IX, with 5.3  $\mu$ m at the top, 3.5  $\mu$ m at the middle, and 2.5  $\mu$ m at the

bottom zone of the interface, resulting in 49.2E6 N/mm<sup>3</sup>, 74.6E6 N/mm<sup>3</sup>, and 104.4E6 N/mm<sup>3</sup>, respectively. A general contact interaction was given between the Al1050 and St37 surfaces, assigning the cohesive properties for the three respective zones.

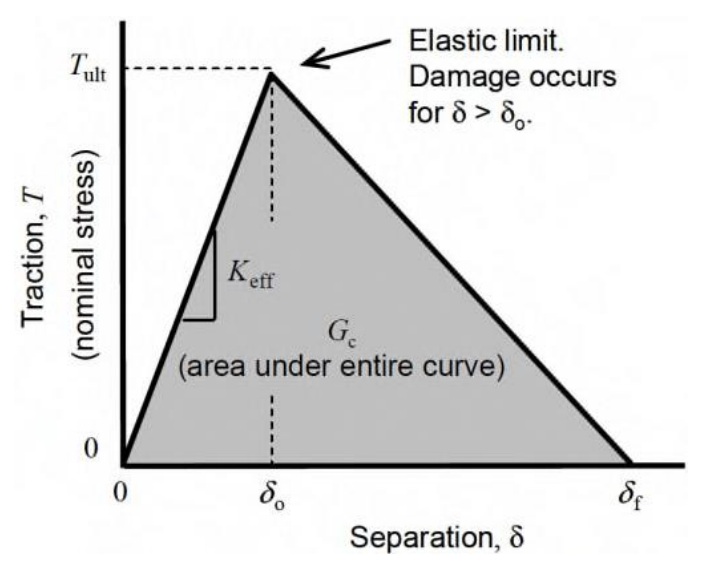


Figure 4.2 - Bilineal traction-separation law diagram.

#### 4.3 - Meshing and boundary conditions

Two boundary conditions were created at the initial step and propagated to the first step, one being the encastre at the aluminium side base and the other a 4mm total displacement throughout the step, represented in Figure 4.3 (a).

For each substrate, three mesh partitions were created. Variable meshing was employed, leading to an approximate element size of 2 mm at the encastre, an element size of 1 mm at the across the substrates, using C3D8R elements, as seen in Figure 4.3 (b). Free C3D4 tetrahedron elements, approximately 0.1 mm in size, were used close to the interface, represented in Figure 4.3 (c).

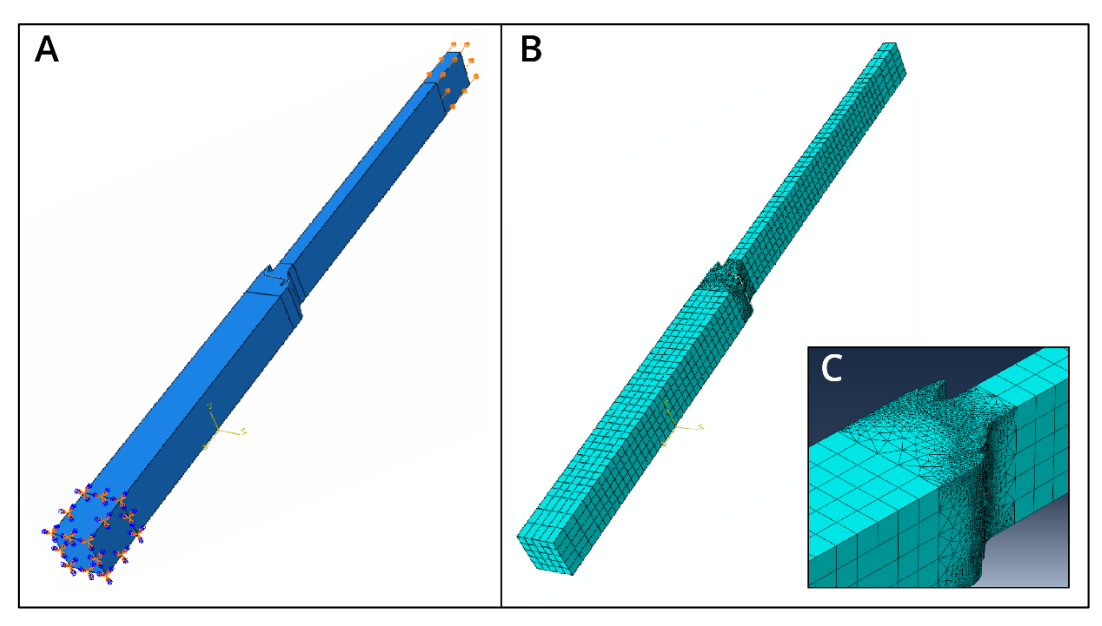


Figure 4.3 – Model boundary conditions (a), and variable meshing of the part (b).

#### 4.4 - Results

An analysis of the cohesive surface's (CSMAXSCRT) damage initiation in the Al1050 substrate indicates a slow degradation of the joint. Figure 4.4 illustrates the observed damage initiation, which starts from the middle zone of the interface and propagates to the top zone. The middle zone notably undergoes total damage initiation, as observed in Figure 4.4 (d).

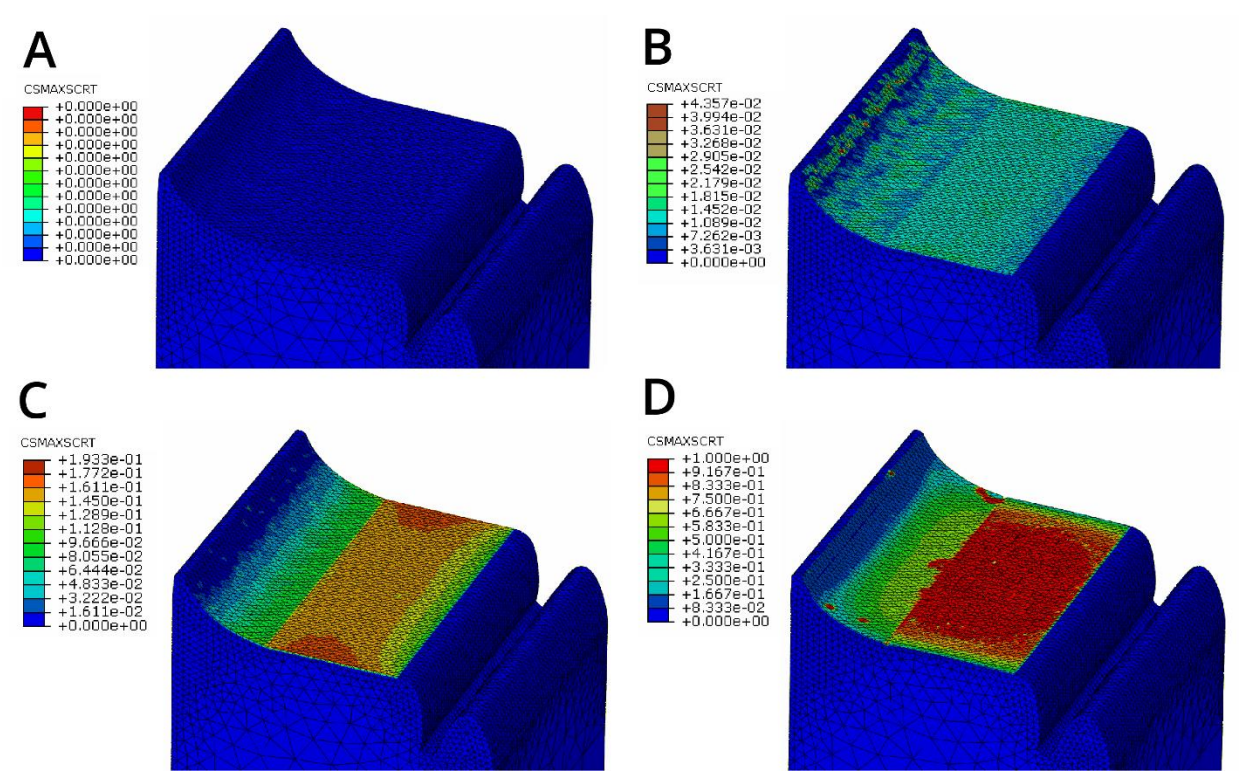


Figure 4.4 – Cohesive surface damage initiation (CSMAXSCRT) results, at the Al1050 substrate interface, of the tensile test simulation.

Upon observing the plastic deformation depicted in Figure 4.5, noticeable yielding of the Al1050 substrate and subsequent necking close to the joint interface are evident. The yielding of the aluminium is particularly predominant at the bottom and top S-shaped tips. Notably, the bottom aluminium tip undergoes partial detachment from the ST37 substrate, as illustrated in Figure 4.5 (c) and (d).

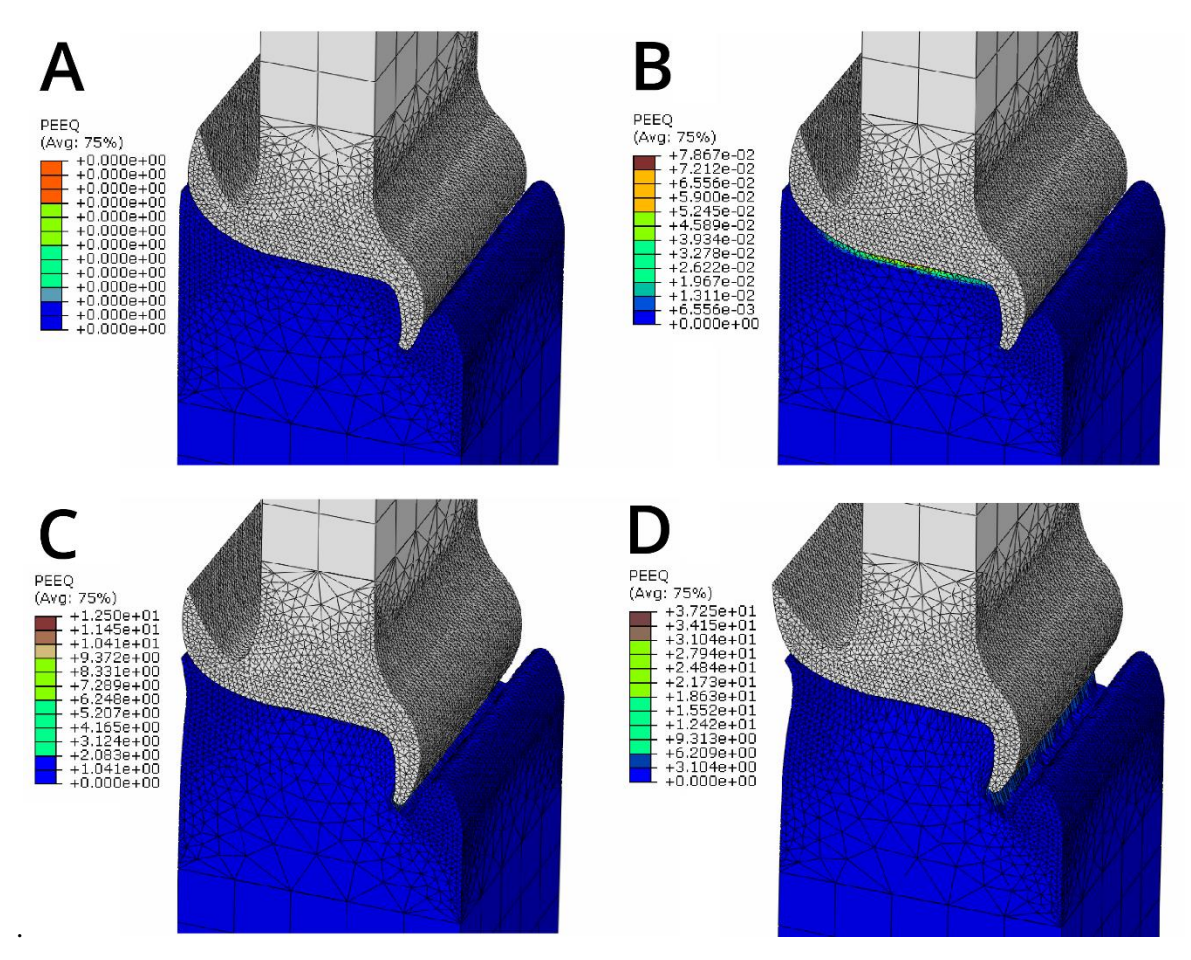


Figure 4.5 - Plastic strain equivalent (PEEQ) results of the tensile test simulation.

As seen in the last frame of the tensile test simulation (Figure 4.6) total damage of the cohesive surface, which represents the IMC layer behaviour, is present at the middle and top zone of the interface. Large plastic deformation occurs at the bottom zone of the aluminium side, in a similar manner to the failure behaviour of the experimental joints.

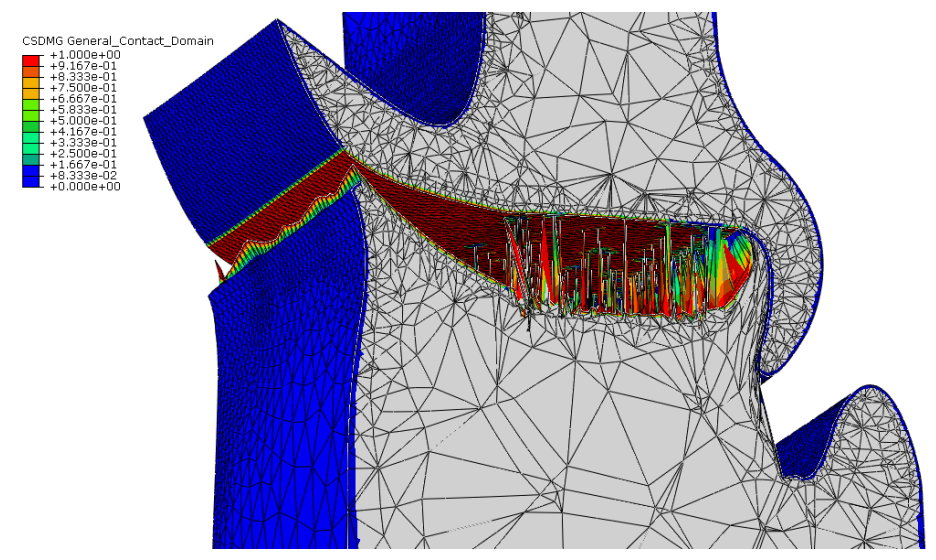


Figure 4.6 – Cohesive damage (CSDMG) results for the joint interface. View cut of the last simulation frame

These results show that the model is quite capable of modelling in detail the process of failure of these joints configurations and thus it can be used in subsequent works to enable a more precise outlook of the failure process of a dissimilar FSW. Supplied with more accurate material characterization data of the welded region (especially of the intermetallic region), this model can eventually also allow for a precise estimation of the joint performance, especially in what regards joint stiffness and failure load.

.

# Chapter 5

## Conclusions and future work

In conclusion, this study has provided valuable insights into the realm of dissimilar welding of aluminium and steel with unequal thicknesses.

First of all, the welding of St37 and Al1050 with novel dissimilar thickness of 2 mm and 5 mm, respectively, joint geometry via FSW was achieved successfully, with a low defect rate. This joint presented a sound integrity, with an average IMC layer thickness of 4.0 μm to 0.8 μm, from top to bottom of the interface, where the common Fe-Al IMC phase present at the dissimilar joint interface is Fe<sub>2</sub>Al<sub>5</sub>, denoted by an average Al at.% of the IMC layer of 68% to 72%. As a consequence of the novel dissimilar thickness geometry, promoted by the material flow during the FSW processes, the joint obtained exhibited a normal and two parallel interface surfaces, that we named S-shape geometry, allowing for more load bearing capacity and distributing the loads in normal and shear stresses in the interface.

Secondly, an increase in the IMC layer thickness was observed throughout the heat treatments performed, with special attention to the influence of the temperature, as expected from past studies present in the literature, and the prominent impact of the 90 min duration time of the annealing of the joints in the joint integrity.

Another important result was the way the interfaces failed during tensile testing. In normal loading condition in the middle of the interface a fully brittle fracture was observed, while in shear loading at the top and bottom of the interface (in the curves parts of the S-shape interface) a ductile fracture was observed. In the latter, the aluminium was observed on the fracture surface of the steel side indicating the interface did not fail. This contributes to an enhancement of the joint strength and ductility and gives a good insight to the design of the dissimilar joints.

Additionally, through the tensile tests results, the decrease in the ultimate failing loads throughout the heat treatment pairs is observed, notably for the 400 °C. The joint strength reduces with increasing IMC layer thickness and vice versa. Thus, as indicated by the literature and supporting our predictions for this work, the thickness of the IMC layer has a proportional impact on the deterioration of the joint characteristics.

Regarding the numerical model, damage initiation is observed starting from the middle zone and to the top zone. The middle zone experiences total damage, while the bottom zone experiences high plastic deformation, obtaining a model with a failure behavior similar to the experimental joints.

Overall, this study underscores the importance of interdisciplinary approaches and innovative strategies in addressing complex engineering challenges. The findings presented here hold significant implications for the automotive industry, offering potential pathways to enhance vehicle performance,

reduce emissions, and minimize environmental impact.

While this study has made significant strides in advancing our understanding of dissimilar welding techniques, it is essential to acknowledge its limitations and areas for further exploration. Future research endeavours may focus on refining numerical models, exploring alternative welding techniques, such as buttering the carbon steel substrate with a high alloy steel, and investigating the long-term durability employing higher annealing temperatures, and reliability of dissimilar joints in real-world applications.

# References

- 1. Nonnenmann, T., et al., Feasibility study on hybrid weld-bonding between dissimilar material for automotive industry. International Journal of Adhesion and Adhesives, 2023. 121: p. 103316.
- 2. Robinson, A.L., A.I. Taub, and G.A. Keoleian, Fuel efficiency drives the auto industry to reduce vehicle weight. MRS Bulletin, 2019. 44(12): p. 920-923.
- 3. Beygi, R., et al., A comprehensive analysis of a pseudo-brittle fracture at the interface of intermetallic of  $\eta$  and steel in aluminum/steel joints made by FSW: Microstructure and fracture behavior. Materials Science and Engineering: A, 2021. 824: p. 141812.
- 4. Kayode, O. and E.T. Akinlabi, An overview on joining of aluminium and magnesium alloys using friction stir welding (FSW) for automotive lightweight applications. Materials Research Express, 2019. 6(11): p. 112005.
- 5. Zhao, H., R. Zhang, and Z. Bin. A Review of Automotive Lightweight Technology. in 2018 International Conference on Mechanical, Electronic, Control and Automation Engineering (MECAE 2018). 2018. Atlantis Press.
- 6. Busarac, N., et al. *Lightweight Materials for Automobiles*. in *IOP Conference Series: Materials Science and Engineering*. 2022. IOP Publishing.
- 7. Dauguet, M., et al., Recycling of CFRP for high value applications: Effect of sizing removal and environmental analysis of the SuperCritical Fluid Solvolysis. Procedia Cirp, 2015. 29: p. 734-739.
- 8. Tisza, M. and I. Czinege, *Comparative study of the application of steels and aluminium in lightweight production of automotive parts.* International Journal of Lightweight Materials and Manufacture, 2018. 1(4): p. 229-238.
- 9. Kaushik, P. and D.K. Dwivedi, *Al-steel dissimilar joining: challenges and opportunities.* Materials Today: Proceedings, 2022. 62: p. 6884-6899.
- 10. Bahador, A., E. Hamzah, and M.F. Mamat, Effect of filler metals on the mechanical properties of dissimilar welding of stainless steel 316L and carbon steel A516 GR 70. J. Teknol, 2015. 75: p. 61-65.
- 11. Shravan, C., et al., A review on welding techniques: properties, characterisations and engineering applications. 2023.
- 12. Jones, D.R. and M.F. Ashby, *Engineering materials 2: an introduction to microstructures and processing.* 2012: Butterworth-Heinemann.
- 13. Pujari, K. and D. Patil, *A review on GTAW technique for high strength aluminium alloys (AA 7xxx series)*. Int. J. Eng. Res. Technol, 2013. 2: p. 2477-2490.

- 14. Sarolkar, A. and K. Kolhe, *A Review of (GTAW) Gas Tungsten Arc Welding and its Parameters for Joining Aluminium Alloy*. International Journal for Science and Advance Research In Technology, 2017. 3(8): p. 361.
- 15. Kutelu, B.J., et al., *Review of GTAW welding parameters*. Journal of Minerals and Materials Characterization and Engineering, 2018. 6(5): p. 541-554.
- 16. Madhavan, S., et al., Microstructure and mechanical properties of aluminium/steel dissimilar weldments: effect of heat input. Materials Science and Technology, 2017. 33(2): p. 200-209.
- 17. Jamaludin, S.B., et al. *Joining Dissimilar Metals between Steel and Aluminum by TIG Welding*. in *Materials Science Forum*. 2015. Trans Tech Publ.
- 18. Singh, R., B.J. Singh, and E.M. Singh, *EFFECT OF CARBIDE PRECIPITATION ON 316L AUSTENITIC*.
- 19. Pal, K. and S.K. Pal, Effect of pulse parameters on weld quality in pulsed gas metal arc welding: a review. Journal of materials engineering and performance, 2011. 20(6): p. 918-931.
- 20. Weman, K. and G. Lindén, MIG welding guide. 2006: Woodhead Publishing.
- 21. Kumar, K.S., S. Gejendhiran, and M. Prasath, *Comparative investigation of mechanical properties in GMAW/GTAW for various shielding gas compositions*. Materials and Manufacturing Processes, 2014. 29(8): p. 996-1003.
- 22. Mandal, N.R. and N.R. Mandal, *Fusion Welding Methods*. Ship Construction and Welding, 2017: p. 175-220.
- 23. Abioye, T., T. Olugbade, and T. Ogedengbe, Welding of dissimilar metals using gas metal arc and laser welding techniques: a review. Journal of Emerging Trends in Engineering and Applied Sciences, 2017. 8(6): p. 225-228.
- 24. Dissimilar Metals, Welding Handbook. Vol. 4. 1982, Miami, USA: AWS. 514-547.
- 25. Sun, Y., et al., Effects of dilution on alloy content and microstructure in multi-pass steel welds. Journal of Materials Processing Technology, 2019. 265: p. 71-86.
- 26. Banovic, S., J. DuPont, and A. Marder, *Dilution and microsegregation in dissimilar metal welds between super austenitic stainless steel and nickel base alloys*. Science and Technology of welding and Joining, 2002. 7(6): p. 374-383.
- 27. Meseguer-Valdenebro, J.L., E. Martínez-Conesa, and A. Portoles, *Influence of welding parameters on grain size*, *HAZ and degree of dilution of 6063-T5 alloy: optimization through the Taguchi method of the GMAW process*. The International Journal of Advanced Manufacturing Technology, 2022. 120(9-10): p. 6515-6529.
- 28. Rizvi, S.A. and M. Ahamad, Effect of heat input on the microstructure and mechanical properties of a Welded joint-A Review. International Journal of Applied Engineering Research, 2018. 13(6): p. 184-188.
- 29. Liu, X., et al., Review of electron beam welding technology in space environment. Optik, 2021. 225: p. 165720.
- 30. Martukanitz, R.P., *A critical review of laser beam welding*. Critical Review: Industrial Lasers and Applications, 2005. 5706: p. 11-24.
- 31. Palani, P. and N. Murugan, Selection of parameters of pulsed current gas metal arc welding. Journal of Materials Processing Technology, 2006. 172(1): p. 1-10.
- 32. Goyal, V., P. Ghosh, and J. Saini, *Influence of pulse parameters on characteristics of bead-on-plate weld deposits of aluminum and its alloy in the pulsed gas metal arc welding process.* Metallurgical and Materials Transactions A, 2008. 39: p. 3260-3275.

- 33. Chaudhari, R., R. Parekh, and A. Ingle. *Reliability of dissimilar metal joints using fusion welding: A Review.* in *International Conference on Machine Learning, Electrical and Mechanical Engineering (ICMLEME: 2014).-2014.* 2014.
- 34. Cai, W., et al., A state-of-the-art review on solid-state metal joining. Journal of Manufacturing Science and Engineering, 2019. 141(3): p. 031012.
- 35. Kah, P., M. Shrestha, and J. Martikainen, *Trends in joining dissimilar metals by welding*. Applied Mechanics and Materials, 2014. 440: p. 269-276.
- 36. Munoz, A.C., et al., Comparison of TIG welded and friction stir welded Al-4.5 Mg-0.26 Sc alloy. Journal of materials processing technology, 2008. 197(1-3): p. 337-343.
- 37. Shi, Y., et al., *Corrosion behavior of aluminum-steel weld-brazing joint*. Journal of Materials Engineering and Performance, 2016. 25: p. 1916-1923.
- 38. Davis, J. and A.-A.S.f. Metals, *Corrosion of dissimilar metal weldments*. ASM-American Society for Metals, Corrosion of Weldments, 2006: p. 170.
- 39. Khedr, M., et al., Review on the Solid-State Welding of Steels: Diffusion Bonding and Friction Stir Welding Processes. Metals, 2022. 13(1): p. 54.
- 40. Akca, E. and A. Gürsel, *The importance of interlayers in diffusion welding-A review*. Periodicals of engineering and natural sciences, 2015. 3(2).
- 41. Yang, W., An investigation of bonding mechanism in metal cladding by warm rolling. 2011: Texas A&M University.
- 42. Khaledi, K., et al., *Modeling of joining by plastic deformation using a bonding interface finite element.* International Journal of Solids and Structures, 2019. 160: p. 68-79.
- 43. Pouranvari, M., A. Ekrami, and A. Kokabi, *Effect of bonding temperature on microstructure development during TLP bonding of a nickel base superalloy*. Journal of Alloys and Compounds, 2009. 469(1-2): p. 270-275.
- 44. Kwon, Y.-S., et al., *Transient liquid phase bonding process using liquid phase sintered alloy as an interlayer material*. Journal of materials science, 2000. 35: p. 1917-1924.
- 45. Findik, F., Recent developments in explosive welding. Materials & Design, 2011. 32(3): p. 1081-1093.
- 46. Imak, A., Overview of friction welding processes for different metallic materials. Materials Testing, 2022. 64(9): p. 1372-1382.
- 48. Goldsmith, W. and S. Finnegan, *Normal and oblique impact of cylindro-conical and cylindrical projectiles on metallic plates*. International journal of impact engineering, 1986. 4(2): p. 83-105.
- 49. Mousavi, S.A. and P.F. Sartangi, Experimental investigation of explosive welding of cptitanium/AISI 304 stainless steel. Materials & Design, 2009. 30(3): p. 459-468.
- 50. Lee, D., E. Kannatey-Asibu, and W. Cai, *Ultrasonic welding simulations for multiple layers of lithium-ion battery tabs*. Journal of Manufacturing Science and Engineering, 2013. 135(6): p. 061011.
- 51. Siddiq, A. and E. Ghassemieh, *Thermomechanical analyses of ultrasonic welding process using thermal and acoustic softening effects.* Mechanics of Materials, 2008. 40(12): p. 982-1000.
- 52. Dhamothara Kannan, T., et al., *Unsymmetric rod to plate rotary friction welding of dissimilar martensitic stainless steel and low carbon steel for automotive applications-mathematical modeling and optimization*. International Journal on Interactive Design and Manufacturing (IJIDeM), 2023: p. 1-29.
- 53. Hattingh, D., et al., Friction processing as an alternative joining technology for the nuclear industry. Journal of the Southern African Institute of Mining and Metallurgy, 2015. 115(10): p. 903-912.

- 54. Thomas, W., et al., *International patent application no.* 1991, PCT/GB92/02203 and GB patent application.
- 55. Mishra, R.S., et al., *Friction stir processing*. Friction stir welding and processing: science and engineering, 2014: p. 259-296.
- 56. Chauhan, P., et al., Modeling of defects in friction stir welding using coupled Eulerian and Lagrangian method. Journal of Manufacturing Processes, 2018. 34: p. 158-166.
- 57. Fraser, K., L. St-Georges, and L.I. Kiss, *A mesh-free solid-mechanics approach for simulating the friction stir-welding process.* Joining technologies, 2016: p. 27-52.
- 58. Kumar, K. and S.V. Kailas, *The role of friction stir welding tool on material flow and weld formation*. Materials Science and Engineering: A, 2008. 485(1-2): p. 367-374.
- 59. Hossfeld, M., Shoulderless Friction Stir Welding: A low-force solid state keyhole joining technique for deep welding of labile structures. Production Engineering, 2022. 16(2-3): p. 389-399.
- 60. Ambrosio, D., et al., *Material flow in friction stir welding: A review*. Journal of Materials Processing Technology, 2023: p. 118116.
- 61. Chen, S., et al., Study on in-situ material flow behaviour during friction stir welding via a novel material tracing technology. Journal of Materials Processing Technology, 2021. 297: p. 117205.
- 62. Miah, M.H., D.S. Chand, and G.S. Malhi, A novel technique for repairing Keyhole in the aircraft assembly technology employing friction stir additive manufacturing. Materials Today: Proceedings, 2022.
- 63. Zhang, Y., et al., *Review of tools for friction stir welding and processing*. Canadian Metallurgical Quarterly, 2012. 51(3): p. 250-261.
- 64. Singh, S., C. Prakash, and M.K. Gupta, *On friction-stir welding of 3D printed thermoplastics*. Materials forming, machining and post processing, 2020: p. 75-91.
- 65. Thomas, W., et al., International Patent Application No. PCT/GB92/02203 and GB Patent Application No. 9125978 8 and US Patent Application No. 5,460,317. 1991.
- 66. Chaturvedi, M., et al., *Friction Stir Welding and Design*. Advanced Welding Techniques: Holistic View with Design Perspectives, 2021: p. 133-165.
- 67. Sidhu, M.S. and S.S. Chatha, *Friction stir welding-process and its variables: A review*. International Journal of Emerging Technology and Advanced Engineering, 2012. 2(12): p. 275-279.
- 68. Penner, S. and M. Armbrüster, Formation of intermetallic compounds by reactive metal-support interaction: a frequently encountered phenomenon in catalysis. ChemCatChem, 2015. 7(3): p. 374-392.
- 69. Albannai, A.I., *Review the common defects in friction stir welding*. Int. J. Sci. Technol. Res, 2020. 9(11): p. 318-329.
- 70. Penalva, M., et al. *Development of a new joint geometry for FSW*. in *AIP Conference Proceedings*. 2009. American Institute of Physics.
- 71. Ferreira Magalhães, A.C., Thermoelectric Measurements for Temperature Control of Robotic Friction Stir Welding. 2020, University West.
- 72. Mendes, N., et al., *Machines and control systems for friction stir welding: a review.* Materials & Design, 2016. 90: p. 256-265.
- 73. Fonda, R. and J. Bingert, *Microstructural evolution in the heat-affected zone of a friction stir weld*. Metallurgical and materials transactions A, 2004. 35: p. 1487-1499.
- 74. Arbegast, W.J., *Modeling friction stir joining as a metal working process*. Hot deformation of aluminum alloys III, 2003: p. 313-327.

- 75. Liu, F. and T. Nelson, *In-situ material flow pattern around probe during friction stir welding of austenitic stainless steel*. Materials & Design, 2016. 110: p. 354-364.
- 76. Liu, F., et al., A review of friction stir welding of steels: Tool, material flow, microstructure, and properties. Journal of Materials Science & Technology, 2018. 34(1): p. 39-57.
- 77. Safeen, M.W. and P. Russo Spena, Main issues in quality of friction stir welding joints of aluminum alloy and steel sheets. Metals, 2019. 9(5): p. 610.
- 78. Podržaj, P., B. Jerman, and D. Klobčar, *Welding defects at friction stir welding*. Metalurgija, 2015. 54(2): p. 387-389.
- 79. Zeng, X., et al., Effect of processing parameters on plastic flow and defect formation in friction-stir-welded aluminum alloy. Metallurgical and Materials Transactions A, 2018. 49: p. 2673-2683.
- 80. Martinsen, K., S. Hu, and B. Carlson, *Joining of dissimilar materials*. Cirp Annals, 2015. 64(2): p. 679-699.
- 81. Kimapong, K. and T. Watanabe, *Friction stir welding of aluminum alloy to steel*. Welding journal, 2004. 83(10): p. 277.
- 82. Elrefaey, A., et al., *Characterization of aluminum/steel lap joint by friction stir welding.*Journal of materials engineering and performance, 2005. 14: p. 10-17.
- 83. Watanabe, T., H. Takayama, and A. Yanagisawa, *Joining of aluminum alloy to steel by friction stir welding*. Journal of Materials Processing Technology, 2006. 178(1-3): p. 342-349.
- 84. Chen, T., *Process parameters study on FSW joint of dissimilar metals for aluminum-steel.*Journal of materials science, 2009. 44: p. 2573-2580.
- 85. Figner, G., et al., Friction stir spot welds between aluminium and steel automotive sheets: influence of welding parameters on mechanical properties and microstructure. Welding in the World, 2009. 53: p. R13-R23.
- 86. Tanaka, T., T. Morishige, and T. Hirata, *Comprehensive analysis of joint strength for dissimilar friction stir welds of mild steel to aluminum alloys*. Scripta Materialia, 2009. 61(7): p. 756-759.
- 87. Abd Elnabi, M.M., T. Osman, and A. El Mokadem, Evaluation of the formation of intermetallic compounds at the intermixing lines and in the nugget of dissimilar steel/aluminum friction stir welds. Journal of Materials Research and Technology, 2020. 9(5): p. 10209-10222.
- 88. Beygi, R., et al., *Design of friction stir welding for butt joining of aluminum to steel of dissimilar thickness: Heat treatment and fracture behavior*. The International Journal of Advanced Manufacturing Technology, 2021. 112: p. 1951-1964.
- 89. Westbrook, J.H. and R.L. Fleischer, *Intermetallic compounds*. Vol. 378. 1967: Wiley New York.
- 90. Paul, A.R., M. Mukherjee, and D. Singh, A critical review on the properties of intermetallic compounds and their application in the modern manufacturing. Crystal Research and Technology, 2022. 57(3): p. 2100159.
- 91. Liu, Z., et al., *Electrically reversible cracks in an intermetallic film controlled by an electric field.* Nature communications, 2018. 9(1): p. 41.
- 92. Naoi, D. and M. Kajihara, *Growth behavior of Fe2Al5 during reactive diffusion between Fe and Al at solid-state temperatures*. Materials Science and Engineering: A, 2007. 459(1-2): p. 375-382.
- 93. Chen, N., et al., *Microstructural and mechanical evolution of Al/steel interface with Fe2Al5 growth in resistance spot welding of aluminum to steel*. Journal of Manufacturing Processes, 2018. 34: p. 424-434.

- 94. Shi, L., et al., Role of Fe2Al5 in fracture of novel dissimilar aluminum-steel resistance spot welds using multi-ring domed electrodes. Materials Science and Engineering: A, 2022. 831: p. 142233.
- 95. Wang, T., et al., Evaluation of intermetallic compound layer at aluminum/steel interface joined by friction stir scribe technology. Materials & Design, 2019. 174: p. 107795.
- 96. Bouayad, A., et al., *Kinetic interactions between solid iron and molten aluminium*. Materials science and engineering: A, 2003. 363(1-2): p. 53-61.
- 97. Tang, N., et al., *Interfacial reactions of solid Co and solid Fe with liquid Al.* Corrosion Science, 2012. 60: p. 32-37.
- 98. Cao, F., et al., The formation and growth of intermetallic compounds during interdiffusion of Al/Cu bimetals. Materials Research Express, 2022. 9(5): p. 056503.
- 99. Mitra, R., Structural intermetallics and intermetallic matrix composites. Vol. 6. 2015: CRC press.

# **Appendices**

# Appendix A

# **Paper**

# The effect of heat treatment on the joint characteristics of dissimilar thickness aluminium-steel joints

TOG Teixeira<sup>1</sup>, R Beygi <sup>2</sup>, RJC Carbas<sup>2</sup>, EAS Marques<sup>1</sup>, AQ Barbosa<sup>2</sup>, LFM da Silva<sup>1</sup>

<sup>1</sup> Department of Mechanical Engineering, Faculty of Engineering of the University of Porto, Rua Dr. Roberto Frias, 4200-465 Porto, Portugal.

<sup>2</sup> Institute of Science and Innovation in Mechanical and Industrial Engineering (INEGI), Rua Dr. Roberto Frias, 4200-465 Porto, Portugal.

#### **Abstract**

The automotive sector is increasingly employing dissimilar welding methods, especially for lightweight alloys, to minimize vehicle weight and enhance fuel efficiency. This transition is prompted by the intricate manufacturing process and limited recyclability of lightweight structures, which contribute to reduced emissions and a diminished carbon footprint. Joining dissimilar metals, such as aluminium and steel, presents an appealing approach for creating lightweight yet durable structures. However, challenges arise from the formation of brittle intermetallic compounds (IMCs) at the interface of dissimilar joints, which significantly affect joint strength under load and often lead to brittle failure. Heat treatments offer a feasible solution to alter the thickness and characteristics of IMCs, thereby modifying joint properties. This research introduces a straightforward design for joining a thin steel sheet (2 mm thickness) to an aluminium sheet (5 mm thickness) in a butt configuration, resulting in an S-shaped Al/St interface due to the offset of the Friction Stir Welding (FSW) tool into the steel. The study aims to explore the effects of various heat treatments on steel and aluminium joints produced through FSW. A thorough analysis will be conducted on a series of St37 carbon steel/ Al1050 aluminium specimens, encompassing examination of the microstructure of the welded joint interface using Scanning Electron Microscopy (SEM) and Electron-dispersive Spectroscopy (EDS) for chemical composition analysis and IMC layer thickness measurements. Mechanical properties will be assessed through tensile testing, while fracture behavior during loading will be investigated by analysing fracture surfaces and examining hardness distribution across the joint. The primary objective is to ascertain the optimal temperature and duration for achieving optimal mechanical properties while managing IMC formation at the joint interface. The study will delve into the kinetics of IMC growth, establishing correlations between temperature, time, IMC layer thickness, and joint strength.

Keywords: Friction Stir Welding, Intermetallic Compounds, Dissimilar metal welding

#### 1. Introduction

In recent times, the automotive sector has dedicated significant time and resources to the search for lightweight substitutes for its structural elements [1]. These include the substitution of high strength-to-weight alloys like aluminium (Al) for the commonly used steel (St) [2] and the adoption of greener and more energy-efficient technologies [3]. The Friction Stir Welding (FSW) joining process makes it possible to create a solid-state weld (SSW) between two different metals using a non-consumable rotating tool[4]. The tool creates the heat required for the substrates to become plastic by causing friction, which enables the two to mix and stir until a weld is formed [5]. Conventional fusion based methods are often unable different metals together [6] and the FSW approach has the added benefit of not being energy intensive and ecologically benign. It does not require the use of flux or cover gas during the welding process [7].

The production of hard and brittle Al-Fe intermetallic compounds (IMC) at the interface poses a significant barrier to dissimilar metal welding [8], particularly for Al/St [9]. This phenomenon leads to inferior mechanical characteristics of the joint, ultimately diminishing its structural dependability [10]. The high friction temperatures attained during the FSW process and the stirring of the two metals facilitate the diffusion of Al and Fe elements across the joint interface and the ensuing solid-state reaction of the atoms [11], which in turn leads to the nucleation and additional growth of IMCs along the bonded interface. Furthermore, annealing the joint after the manufacturing promotes the formation of IMCs, enabling the study of the IMC layer growth kinetics [12].

In this study, a unique welding configuration was used to combine dissimilar materials with distinct thickness (Al-St). In order to do this, a unique butt arrangement was created to connect 5-mm-thick AA1050 to 2-mm-thick St37 carbon steel substrates. In order to investigate the fracture behavior of the joints, tensile tests were applied to the fabricated specimens, and energy-dispersive spectroscopy (EDS) and scanning electron microscopy (SEM) were used to analyse the fracture surfaces and the IMC interface of the welded samples.

Table A.1 - Mechanical properties and chemical compositions of St37 carbon steel and 1050 Aluminium.

St37 Carbon Steel	1050 Aluminium	
Tensile strength - 370 MPa	Tensile strength - 100-135 MPa	
Yielding strength - 300 MPa	Yielding strength - 85 MPa	
Vicker's hardness - 120 HV	Vicker's hardness - 41 HV	
Chemical composition:	Chemical composition:	
Fe: 99.43 - 99.75%	Al: 99.5 %	Иg: 0.05 %
C: 0.08%	Si: 0.25 %	n: 0.07 %
Mn: 0.25 - 0.4%	Fe: 0.40 %	ī: 0.05 %
S: 0.05%	Cu: 0.05 %	Others: 0.03 %
P: 0.04%	Mn: 0.05 %	

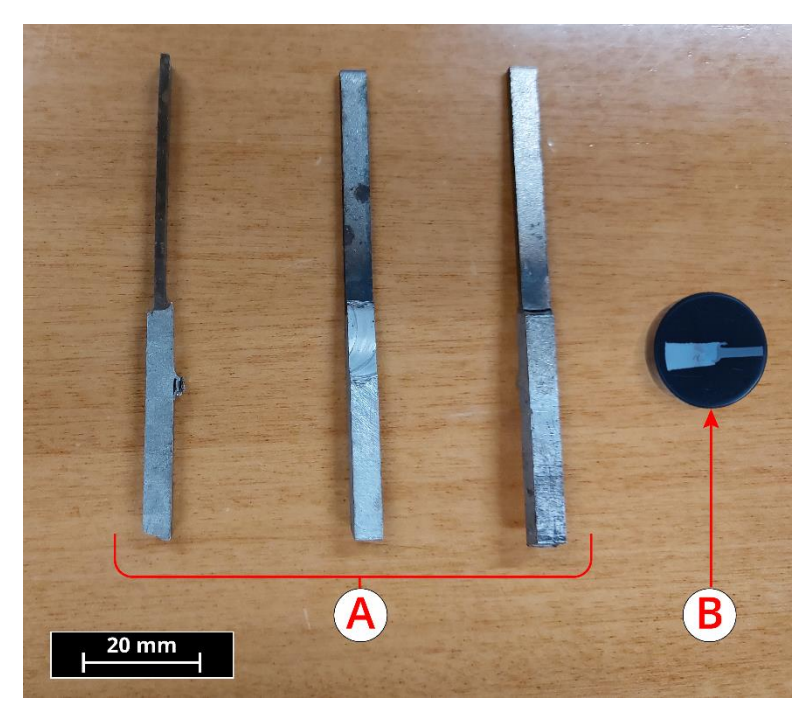


Figure A.1 - Example of the specimens used for tensile testing and fractography (a), and sample for microstructure analysis and hardness measurements (b).

#### 2. Experimental Procedure

#### 2.1 Heat treatments

With the objective of assessing the influence of temperature on the degradation of Al-St joint properties through Friction Stir Welding (FSW), a sequence of thermal treatments was conducted on the manufactured joints, promoting the growth of the Intermetallic Compound (IMC) layer at the joint's interface. To monitor the kinetics of IMC layer growth, a total of 9 combinations of temperature and duration were chosen, spanning from 100°C to 400°C, and from 30 minutes to 90 minutes. For each temperature/duration pair, three specimens were designated for tensile testing, while one additional sample was set aside for SEM/EDS analysis. The distribution of samples across each temperature/duration combination was carefully arranged to ensure uniformity and minimize potential biases inherent in the manufacturing process, which could otherwise introduce erroneous conclusions and correlations. The designation of each heat treatment pair is represented in the Figure A.2.

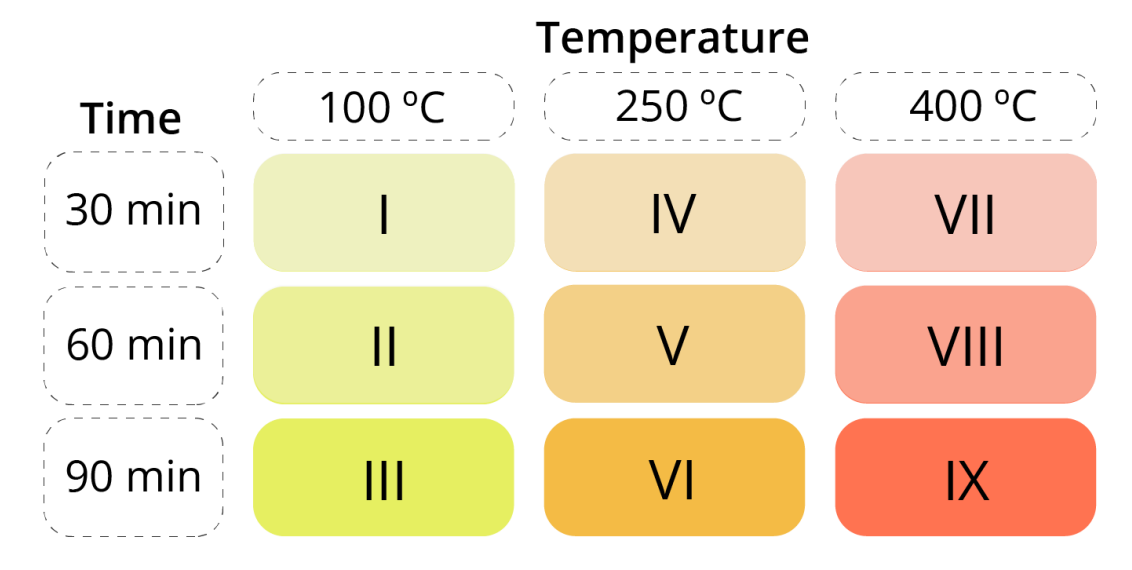


Figure A.2 - Schematic of the heat treatment pairs.

For each combination of treatment temperature and duration, the heat treatment protocol proceeded as follows: Initially, the tensile test specimens and the SEM/EDS sample were positioned with a precise placement of a thermocouple at the joint interface to ensure accurate temperature monitoring throughout the heat treatment process. Subsequently, the joints were protected with aluminium foil to mitigate the impact of the oxidizing atmosphere within the oven. A steel plate was then layered atop the aluminium foil to ensure continuous contact between the thermocouple tip and the joint throughout the duration of the heat treatment. This preparatory procedure served to maintain ideal conditions during heat treatment. Upon reaching the target temperature, as indicated by the oven's thermometer, the prepared specimens were introduced into the oven. Following the completion of the designated heat treatment period, the joints were allowed to cool naturally to room temperature.

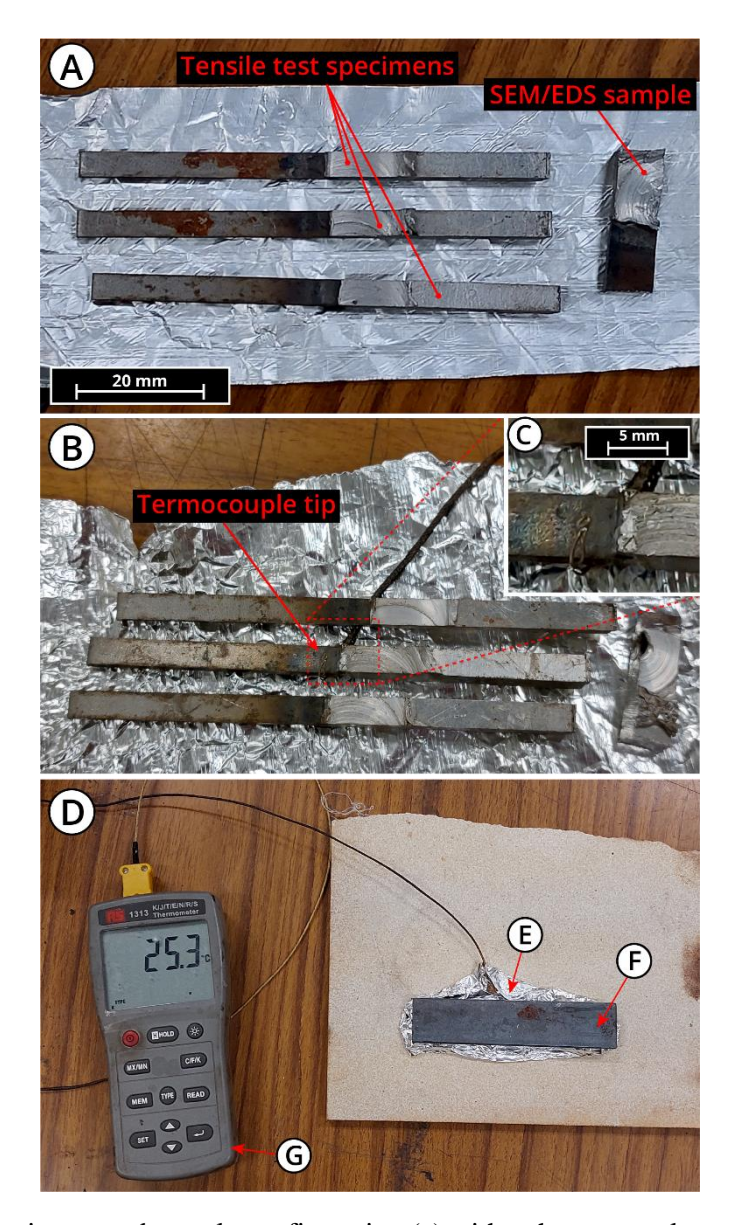


Figure A.3 - Specimens and sample configuration (a) with a thermocouple attached one of the specimens at the interface of the joint (b). Close-up of the thermocouple tip located at the joint (c), and preparation for heat treatment(d), with the aluminium foil wrap (e) and steel plate (f). In (g) we have the thermometer used in the preparation.

The joint temperature was regularly compared to the temperature displayed in the oven controller and the nominal temperature during heat treatments. Offsets were observed between the measured and nominal temperatures. The maximum offset was 9.9°C for pair **VII** (30 min at 400°C), resulting in a heat treatment of 390.1°C. To address this, an increase of 5°C was set to oven temperature for pairs **VIII** and **IX**, resulting in a decrease of approximately 5°C between nominal and joint temperatures.

#### 2.2 SEM/EDS analysis

The study of the microstructure of joints' interfaces using SEM/EDS aims to observe the friction stir welded zone, measure IMC layer thickness at the Al-St interface and study the chemical composition of the joints through EDS line-scans, obtaining atomic percentages across the interface, and to establish cause-effect relationships between IMC layer growth kinetics, joint degradation, and tensile strength.

The SEM/EDS examination was carried out using a high-resolution environmental Scanning Electron Microscope (Schottky) with X-ray Microanalysis and Analysis of Backscattered Electron Diffraction Patterns: *FEI Quanta 400FEG ESEM/ EDAX Genesis X4M*. The samples were coated with Au/Pd thin films by sputtering using *the SPI Module Sputter Coater*. Furthermore, the fractography analysis follows the aforementioned procedure.

During this session, three distinct zones were examined and identified as illustrated in Figure A.4: the upper portion of the interface labelled as **U**, the middle section as **M**, and the lower tip as **L**. These zones were subjected to detailed scrutiny and analysis to discern potential variations and characteristics within each region.

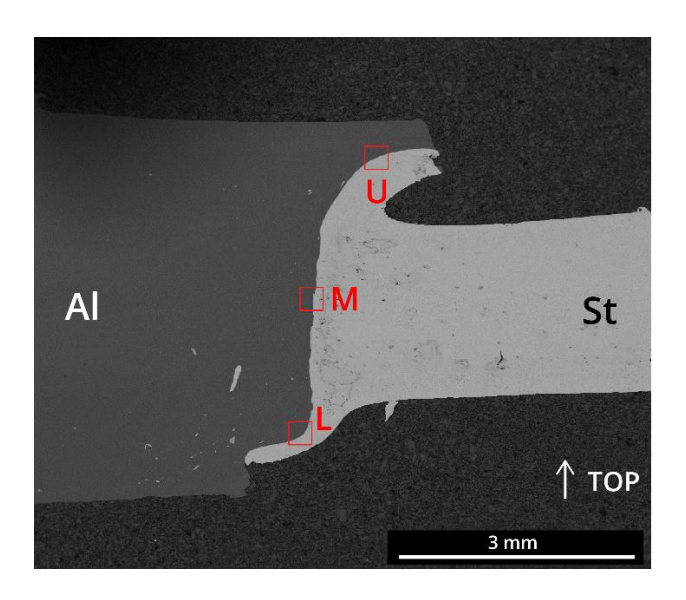


Figure A.4 – Joint interface with the represented examination zones U, M and L. SEM image in BSE mode of the joint, at 35x magnification.

The study examined nine heat-treated samples in a configuration of two preparations, one containing sample I to V and the other VI to IX, as shown in Figure A.5.

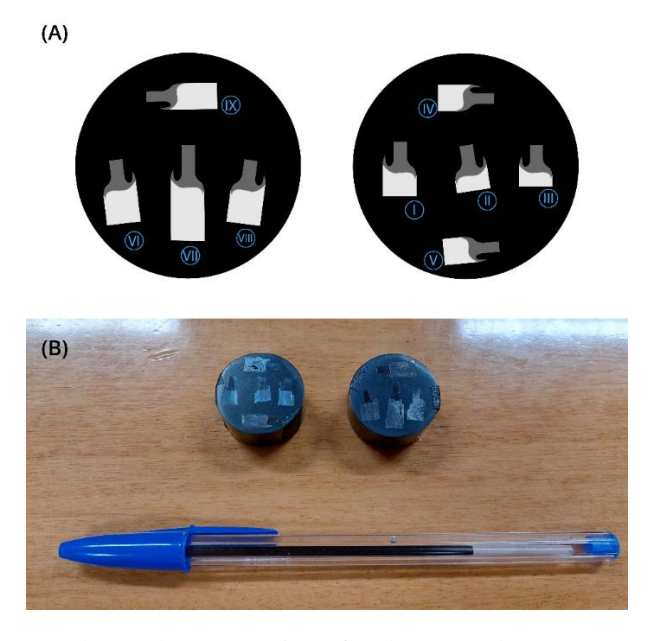


Figure A.5 – Heat treated sample preparations for the second SEM/EDS session, (a) sample preparation photography and (b) schematic representation and identification.

The study used ImageJ software for post-processing the images and extracting measurements, collecting 15-20 thickness measurements for each zone and averaging them to determine the IMC layer thickness for U, M, and L for each sample. Line scans were performed at zone M for samples III to IX and all zones in the as-welded sample, collecting atomic percentages of Aluminium and Iron present across the joint interface. Data was plotted along the line scan length and overlayed to predict IMC layer phases, comparing the at.% in the joints with an Al-Fe phase diagram.

#### 2.3 Mechanical tests

Quasi-static tensile tests were conducted to characterize the tensile strength of manufactured joints. The tests were conducted using a universal test machine INSTRON® (Norwood, Massachusetts, USA), model 3367, at a constant displacement rate of 1 mm/min at room temperature and humidity. The specimens were loaded in the longitudinal direction, with the interface facing the front of the test machine. The tests were recorded using a high resolution video camera in macro-mode at the joint interface to observe failure behavior. The load-extension curves and videos were time-matched until the failure of the two failed halves. The interface surface of the specimens was polished before each test to remove oxide layers.

The Vickers microhardness was measured in three heat-treated samples at different temperatures. Each sample had three microhardness measurement lines: upper and bottom zones (U and B) starting at the steel side of the joint, and a middle zone (M) across all joints. Due to the small area of these zones, multiple measurements were not possible. The distance between indentations was measured in conjunction with the Vickers' hardness value. The results were plotted in a HV Microhardness vs. Length graph, with the origin representing the first indentation of the steel substrate.

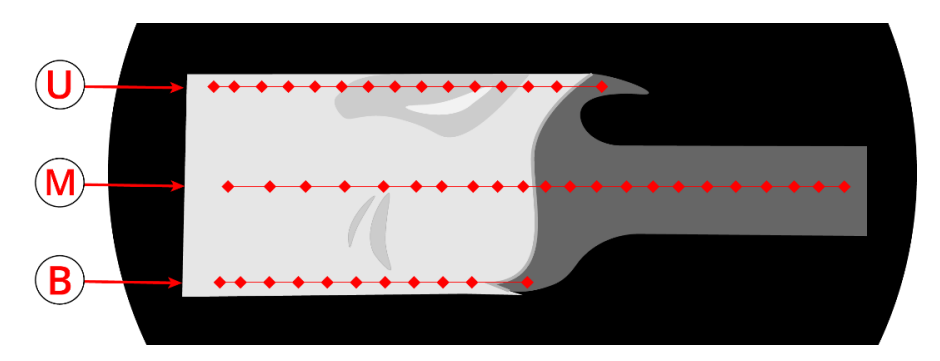


Figure A.6 - Schematic representation of the microhardness lines measurements U, M and B.

#### Results and discussion

#### 3.1 Interface microstructure and IMC layer thickness

Sample III ( $100 \,^{\circ}\text{C} / 90 \,^{\circ}\text{min}$ ) presents a more curvilineal S-shape interface, seen in Figure A.7 (a), with a deeper penetration of the bottom steel tip into the aluminium substrate, being the tip thinner than the previous examined samples. The middle zone of the interface appears in the joint in an angle, emphasising the S-shape morphology of the joint. The top steel tip encloses a substantial fragment of aluminium, result of the FSW process, promoting the penetration of the St37 into the aluminium base metal due to the forging forces applied by the shoulder of the tool. Moreover, a high occurrence of steel fragment inclusions into the aluminium substrate, as large as 0.5 mm in length, is visible.

At the upper zone U, an IMC layer with some degree of thickness variance and presenting some discontinuities is observed, as shown in Figure A.7 (c) and (c). The middle zone M2 presents

a homogeneous IMC layer thickness with few discontinuities, however some steel fragments are present surrounded by the IMC layer, as seen in Figure A.7 (f). Figure A.7 (e) also shows the presence of the aforementioned steel fragments in the Al1050 substrate. Figure A.7 (g) and (h) shows an IMC layer with a high degree of thickness variance, presenting some discontinuities and underdeveloped sections.

In this sample, a reduction in thickness from the top to the bottom zones is visible. For this sample **III**, as well as **IV** to **IX** samples, EDS analysis was performed at the middle zone M2, perpendicularly to the interface, seen in Figure A.7 (b).

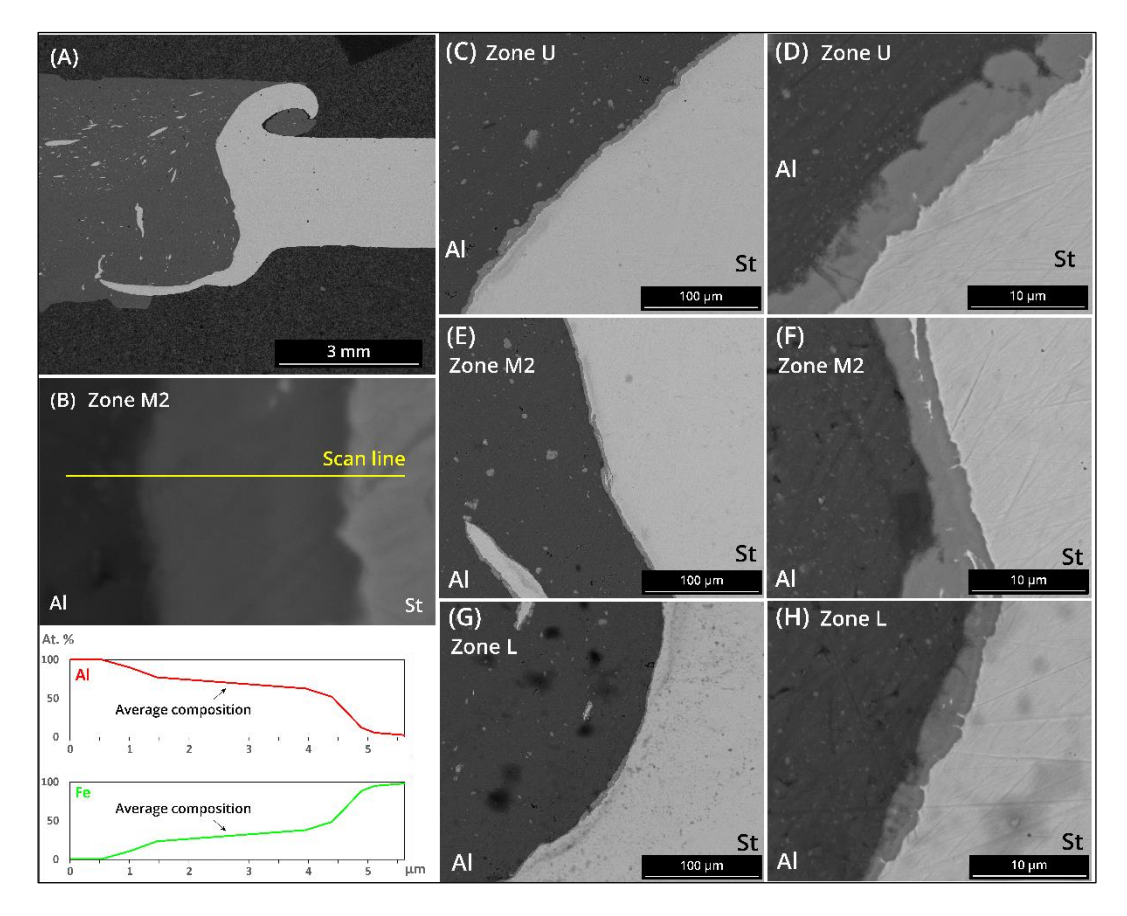


Figure A.7 - Sample **III** (100 °C / 90 min) SEM images in BSE mode of the joint interfaces, taken from the zone U (c) and (d); zone M2 (e) and (f); and zone L (g) and (h). Line-scan EDS analysis taken across the IMC layer of the zone M2 (b).

Sample VI (250 °C / 90 min) presents a less pronounced S-shape with low penetration of the steel tip into the aluminium substrate at the lower zone of the interface and short upper zone tips, as well as a middle zone perpendicular to the joint, as shown in Figure A.8 (a). Observing the upper zone U, Figure A.8 (a) and (b), a homogeneous IMC layer with some discontinuities along the section is visible. In this zone, there are no steel fragment inclusions in the IMC layer, although some small IMC fragments are still visible in the Al substrate.

The middle zone M2 presents an IMC layer with no discontinuities but with regular thickness along the interface. In the aluminium substrate, some IMC particles are seen detached from the IMC layer, as seen in Figure A.8 (e) and (f). At the lower zone L, the IMC layer appears more regular than the previous samples at the same zone, however, discontinuities exit in some sections of this zone, as seen in the top left side of Figure A.8 (g).

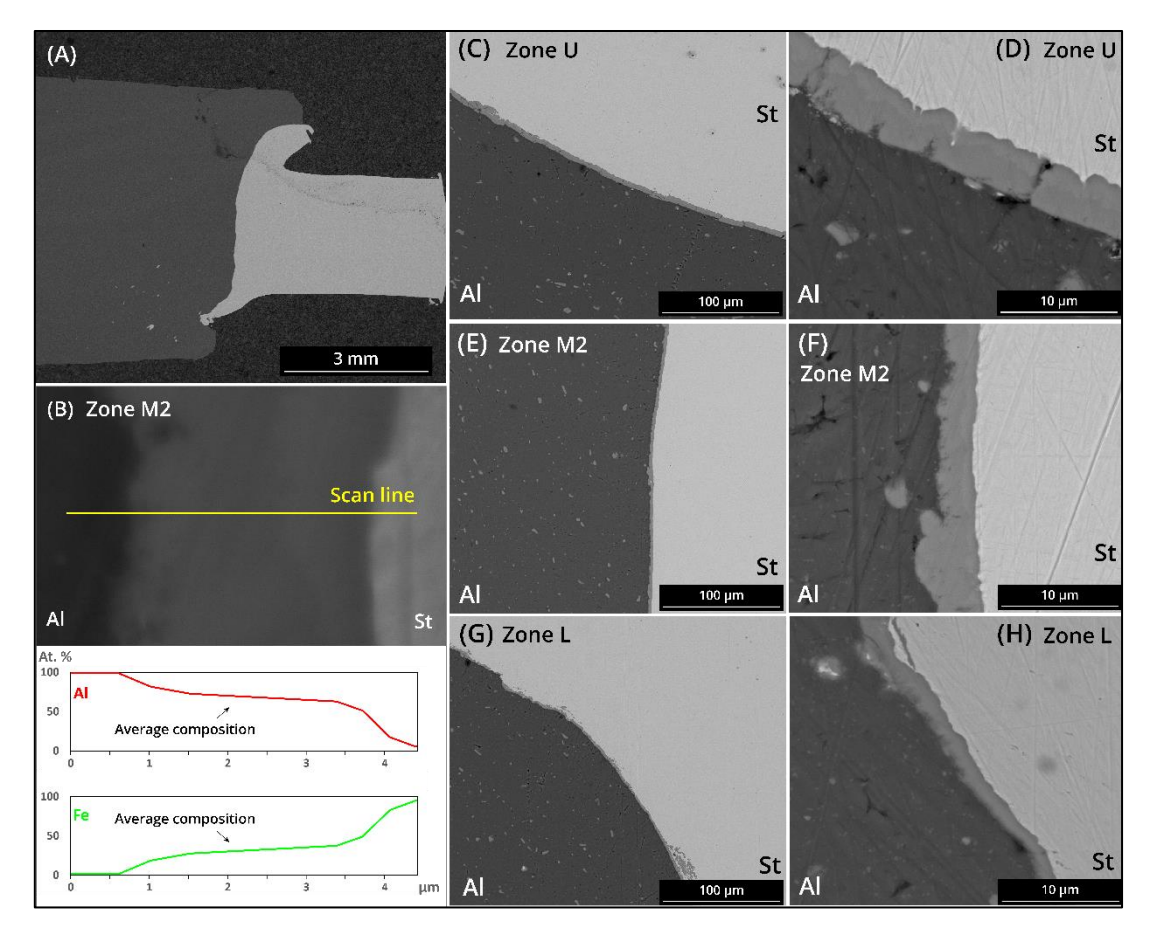


Figure A.8 - Sample VI (250 °C / 90 min) SEM images in BSE mode of the joint interfaces, taken from the zone U (c) and (d); zone M2 (e) and (f); and zone L (g) and (h). Line-scan EDS analysis taken across the IMC layer of the zone M2 (b).

The IMC layers exhibits an average Al at.% of 70%, denoting the presence of the  $Fe_2Al_5$  phase. The Al at.% analysed in the middle zone of the samples, as well as the corresponding Fe-Al IMC phase are present in Table A.2. The EDS scanlines exhibiting a high Al at.% gradient, present an unconclusive phase present at this section due to a lack of a quasi-constant average chemical composition at the IMC layer of the interface of the joints.

Table A.2 - Al at.% and the corresponding Fe-Al IMC phases for sample III to IX

Sample	Al at.%	Fe-Al IMC phase
III	68%	Fe <sub>2</sub> Al <sub>5</sub>
IV	64% - 100%	unconclusive
V	65% - 100%	unconclusive
VI	69%	Fe <sub>2</sub> Al <sub>5</sub>
VII	65% - 100%	unconclusive
VIII	70%	Fe <sub>2</sub> Al <sub>5</sub>
IX	72%	Fe <sub>2</sub> Al <sub>5</sub>

This study uses the thickness of the IMC layer for each heat treatment to joints and effectiveness of temperature and time on the microstructure of the joint's interface, draw the kinetics of Al-Fe IMC phases growth for dissimilar thickness FSW joints, and study the impact of IMC layer dimensions on the degradation of the join's mechanical properties. The as-welded and heat treatment samples were measured in three zones, except for sample I at  $100^{\circ}$ C / 30 minutes due to time constraints during the SEM session. Due to low thermal energy input and by comparing samples for the same temperature heat treatment, it was estimated that no significant growth of the intermetallic layer occurred.

Table A.3 – IMC layer thickness of the samples at the upper, middle and lower zones.

	IMC layer thickness [µm]			
Sample	Upper	Middle	Lower	
as-welded	4.0	2.5	0.8	
II	3.7	2.5	2.5	
III	4.6	2.6	1.3	
IV	3.7	2.4	1.3	
V	3.3	2.1	0.8	
VI	3.6	2.5	1.9	
VII	4.6	3.3	2.0	
VIII	5.2	3.1	2.2	
IX	5.3	3.5	2.5	

The IMC layer thicknesses measured in the three zones were plotted as a function of the heat treatment variables and a linear trendline was drawn for each one of the zones. Figure A.9 shows these plotted measurements.



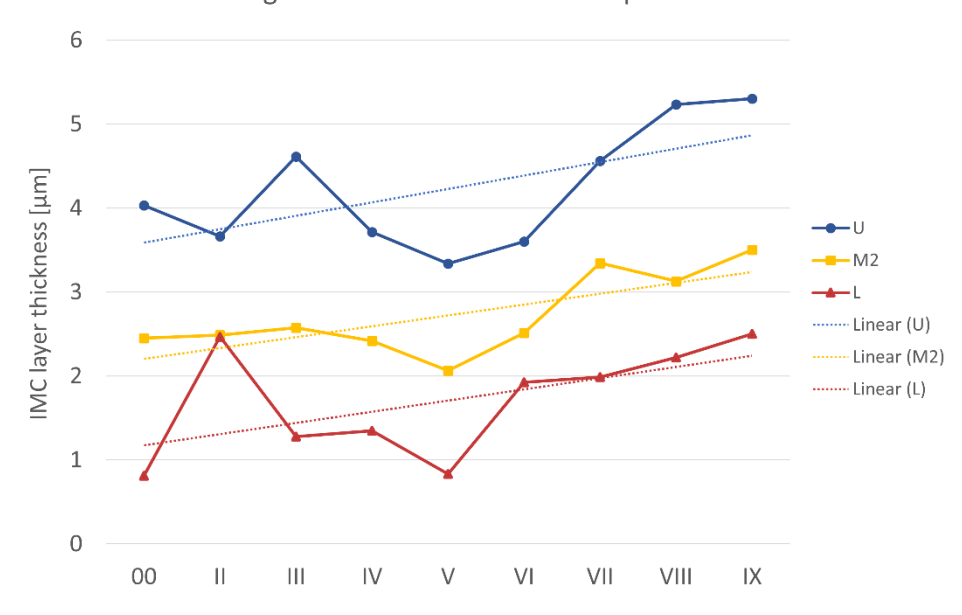


Figure A.9 - Average IMC thickness of the U, M2 and L zones for the measured as-welded and heat treated samples, and linear regressions.

The thicknesses measured at the IMC layer, at the zones U, M2, and L, vary from the upper part of the interface to the bottom, in a decreasing order. The temperature has an influence in the growth of IMC's, increasing the diffusion rate of Al and Fe atoms and consequently forming thicker layers of IMC [13]. The shoulder of the FSW tool provides, among other functions, the necessary friction and consequent heat source for the substrates to reach high temperatures, achieving a plastic regime and forming a welded joint. These temperatures are much higher at the top part of the joint, compared to the bottom part, correlating well to the distance from the heating source and resulting in a gradient of temperatures along the FSW process.

This phenomenon explains the thickness gradient along the IMC Layer seen in the joints present in this work. Fick's diffusion rules govern the diffusion rates, which are highly temperature dependent. For higher temperatures, the diffusion coefficient rises correspondingly, increasing atomic mobility and allowing for rapid diffusion of aluminium and iron atoms into each other's crystalline structures, thus increasing the total diffusion process, and facilitating the kinetics of the reaction between Al and Fe atoms, leading to a higher growth of the IMC at the interface of the base metals [14].

Since the peak temperatures reached during the welding process are higher at the top side of the joint, the IMC layer thickness is also higher in the zones, following the same correlation for the decreasing peak temperatures reached along the interface.

#### 3.2 Microhardness results

In the upper zone on the steel side, both the as-welded and **VI** (250°C / 90 min) samples exhibited hardness values of 169 HV and 170 HV, respectively. Conversely, on the aluminium side, hardness values of 44 HV, 40 HV, and 43 HV were recorded for the upper, middle, and bottom zones closest to the interface. Notably, sample **III** (100°C / 90 min) demonstrated an opposing trend in hardness evolution away from the interface on the aluminium side compared to other samples: while sample **III** exhibited a decrease in hardness in the initial millimetres after the interface, the as-welded and **VI** samples experienced an increase. Regarding the middle zones, a consistent trend of increasing hardness towards the interface was observed for the steel substrate, with hardness values of 175 HV for the as-welded sample, 166 HV for sample **III** (100°C / 90 min), and 157 HV for sample VI (250°C / 90 min). However, no clear trend was discernible for

the aluminium side across the middle zones for the three samples. In the bottom zone on the aluminium side, sample **III**  $(100^{\circ}\text{C} / 90 \text{ min})$  exhibited the highest hardness values, followed by the as-welded and VI  $(250^{\circ}\text{C} / 90 \text{ min})$  samples. On the steel side, sample **VI**  $(250^{\circ}\text{C} / 90 \text{ min})$  displayed the lowest hardness at 160 HV, while the as-welded and sample **III**  $(100^{\circ}\text{C} / 90 \text{ min})$  recorded hardness values of 188 HV and 187 HV, respectively.

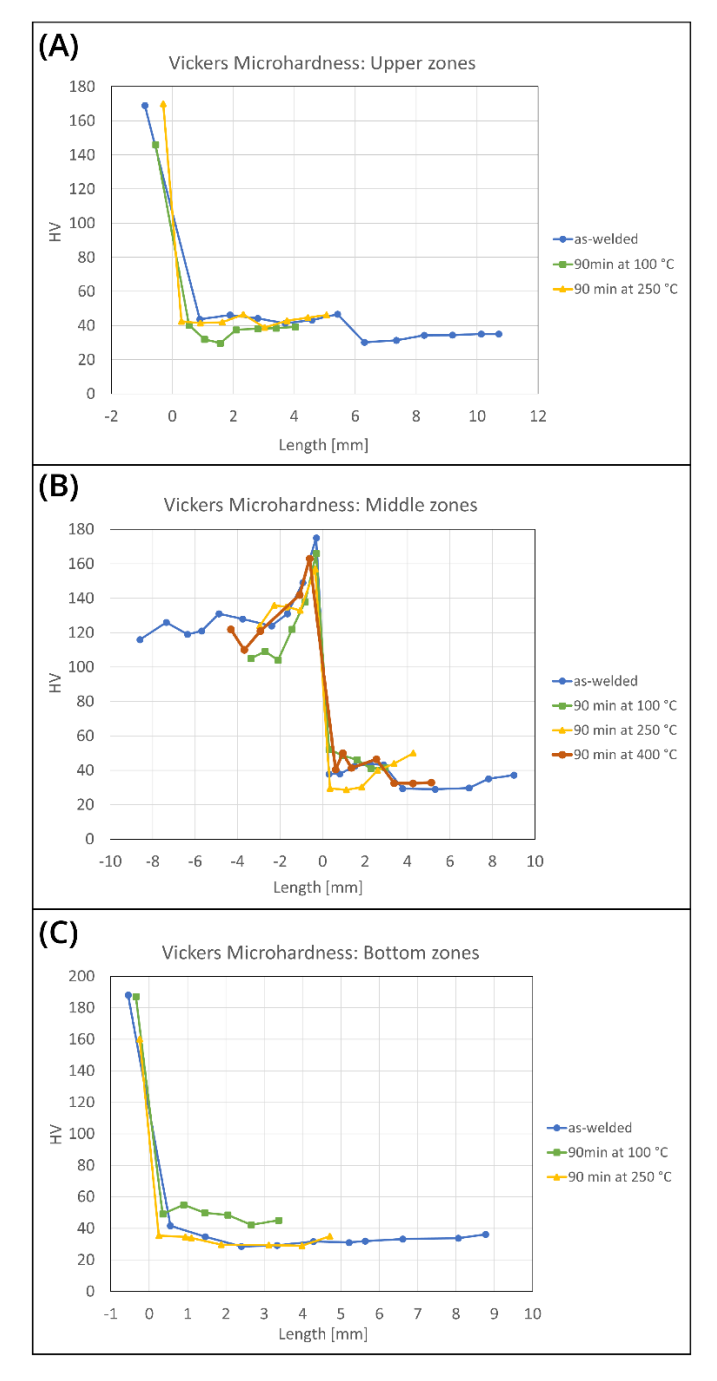


Figure A.10 - Vickers microhardness along the interface length of the three zones of the measured as-welded,  $100~^{\circ}\text{C}$ ,  $250~^{\circ}\text{C}$  and  $400~^{\circ}\text{C}$  (90 min duration) samples.

#### 3.3 Tensile tests

Upon analysing the specimens for each heat treatment pair and excluding identified outliers, as illustrated in the blue curve of Figure A.11, a discernible decrease in the main failure load

across the performed heat treatments is evident, as indicated by the dotted black trendline in the same figure. Notably, the temperature of the heat treatment emerges as the primary factor contributing to the reduction in the maximum load of the specimens. By aggregating results for each temperature/time pair, grouped by heat treatment duration and varying temperature, depicted Figure A.12, the significant impact of temperature on joint degradation becomes apparent. Particularly noteworthy is the observation that heat treatments lasting 90 minutes result in the most substantial degradation of the joints.

Concerning joint degradation and the influence of the IMC layer thickness on joint strength, the average main failure loads, and IMC layer thicknesses of joint samples in the middle zone throughout heat treatments were plotted in Figure A.11. The selection of the middle zone for analysis was motivated by its significant impact on joint failure. Notably, an increase in IMC layer thickness correlates with a decrease in joint strength, and vice versa. Consequently, the thickness of the IMC layer exerts a proportional influence on the degradation of joint properties, aligning with existing literature and affirming the expectations of this study.

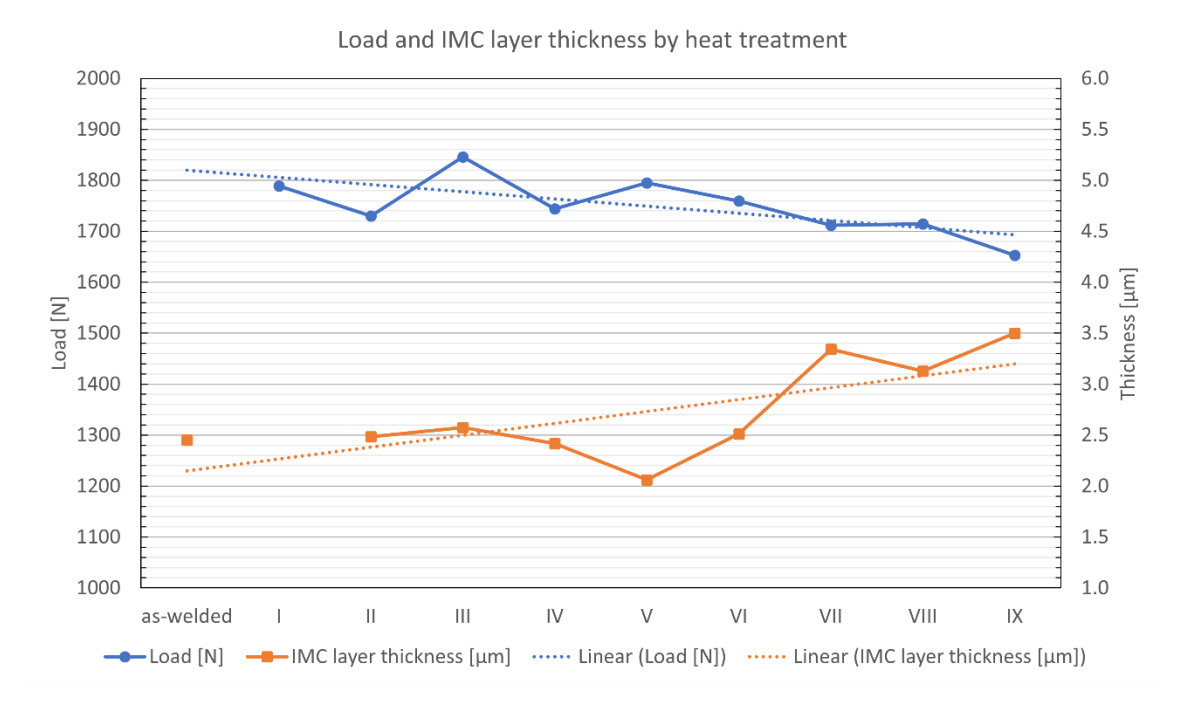


Figure A.11 - Plotted average main failure loads and IMC layer thickness at the middle zone, with respective trendlines.



Figure A.12 - Average max. loads by temperature, grouped by heat treatment duration.

250
Heat treatment temperatures [°C]

400

#### 3.4 Fracture behaviour

100

The examination of tensile test results necessitates consideration of failure zones and macroscale fracture behavior. It is observed that the majority of specimens exhibit 2 or 3 distinct failure zones under varying loading conditions. The principal failure zone lies in the middle of the interface, representing the initial stage of joint failure and characterized by a brittle fracture mode, seen in the specimens III • • and III • • • examples in Figure A.13. Conversely, the bottom and top zones experience yielding of the aluminium side of the joint until fracture occurs. Consequently, fragments of Al1050 remain welded to the steel substrate at the conclusion of the tensile test for most specimens. Further fractography analysis is imperative to evaluate fracture behavior and confirm the presence of aluminium on the steel side of the failed joints. The main failure zone is at the middle of the interface, corresponding to the initial locus of failure, and it is characterized as a brittle failure. In this zone, the joint is loaded in a normal direction to the interface, opposite to the forces applied in the bottom and top zones, where shear stress is applied to the interface, represented in Figure A.14 by a schematic of the forces applied in the aforementioned joint interface zones.

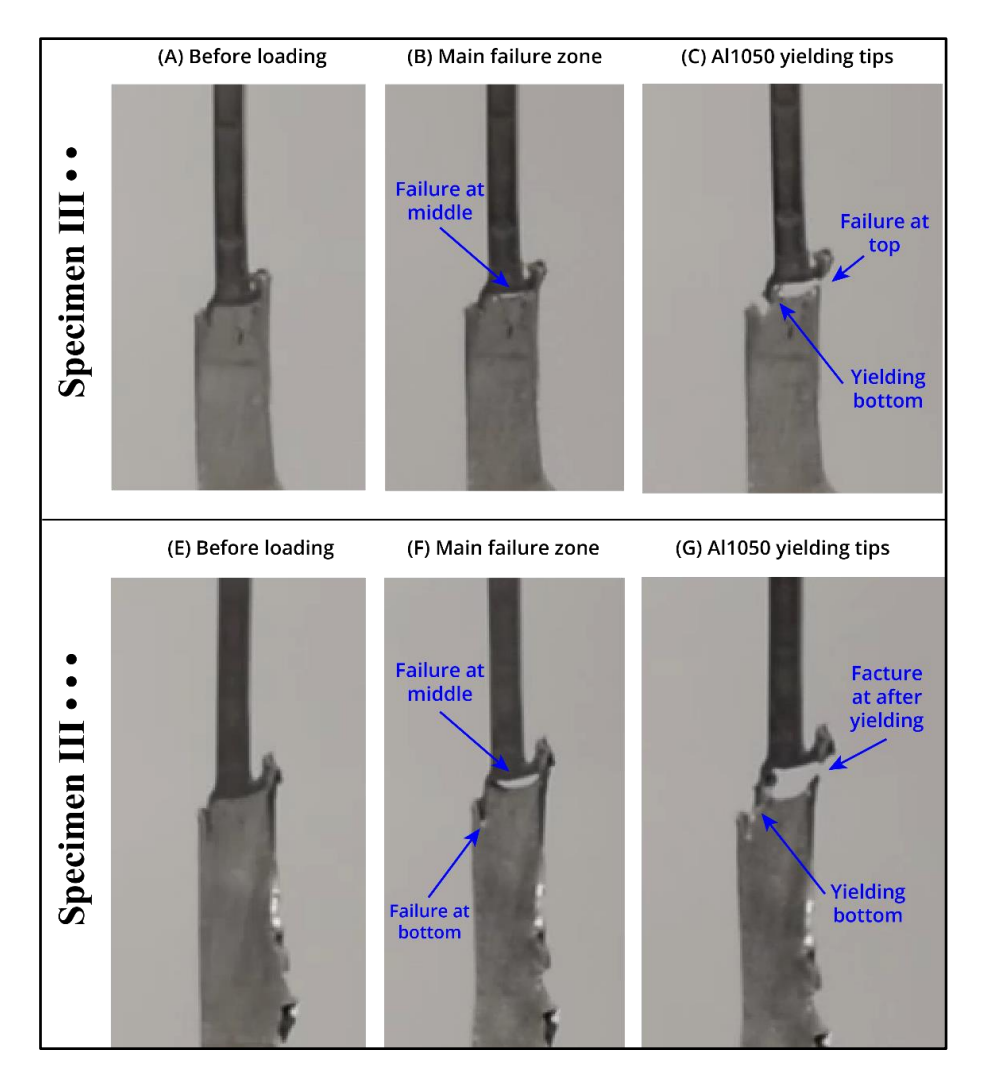


Figure A.13 - Specimens III • • and III • • • tensile test video frames before loading (a) and (e), at main failure zone (b) and (f), and at the yielding of the Al1050 tips of the joint interface (c) and (g), respectively.

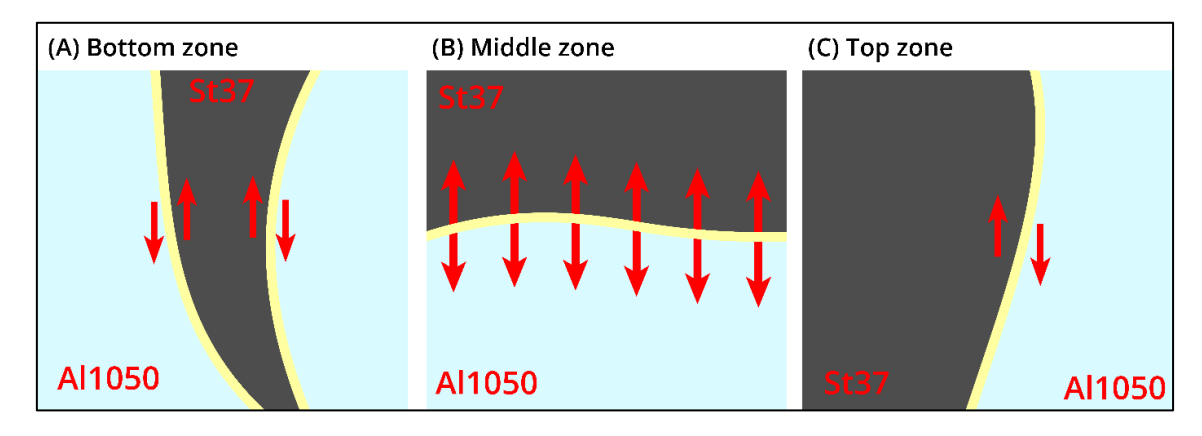


Figure A.14 - Schematic representation of the applied forces in the bottom (a), middle (b) and top (c) zones of the joint interface. The IMC layer is represented in yellow.

At the lower interface on the aluminum side, distinct crater form across the fracture surface, indicating penetration by the steel tip into the aluminum substrate, resulting in volume removal due to aluminum yielding. subsequent analysis of individual fracture surfaces and zone EDS analysis, backscattering mode SEM imaging will be employed to differentiate materials across various zones on the surfaces. Regarding Specimens III subjected to 100°C / 90 min heat

treatment, four zones were examined on the steel side Figure A.16 (c). Zones Z1 and Z2 in the middle of the interface exhibited Fe-Al IMC, with Z1 showing higher Al counts and Z2 higher Fe counts. Zone Z3 also displayed Al and Fe, like Z1. Zone Z4 at the interface's top showed solely Al. On the aluminum side, Figure A.16 (a), five zones were examined, with Z1 at the interface's bottom showing Al1050, while Z2 and Z3 at the middle indicated distinct Fe-Al IMC phases. Zones Z4 and Z5 magnified from Z3 displayed Al and Fe, suggesting Fe-Al IMC presence.

In Specimen IX, exposed to the 400°C / 90 min heat treatment, steel-side analysis revealed Fe-Al IMC in Z1 and Z2, Figure A.16 (i), with varying Al and Fe counts. Zone Z3 at the middle-bottom transition exhibited significant Al and Fe, indicating Fe-Al IMC presence. On the aluminum side, Figure A.16 (f), Z1 and Z2 at the interface's bottom displayed Fe-Al IMC, with Z1 showing more Al, while Z3 and Z4 at the top showed Al-dominated IMC and Al base metal, respectively. For Specimens VI undergoing 250°C / 90 min heat treatment, SEM imaging revealed varying Al and Fe percentages across the interface on both steel and aluminum sides, consistent with previous specimens.

Furthermore, the strain of the aluminium substrate at the top zone is confirmed by the presence of dimples in the region, indicative of this mechanical behaviour of the metal, as seen in <u>Figure</u> A.15 (a) and (b), SEM images taken in secondary mode in two separate locations of the top zone of the interface. At the bottom zone of the interface, a crater is observed where the steel tip was situated, as shown Figure A.15 (c). The walls of the crater have the aforementioned dimples indicative of the localized plastic deformation of the aluminium and the crater base with directional grooves, indicative of the brittle fracture behaviour.

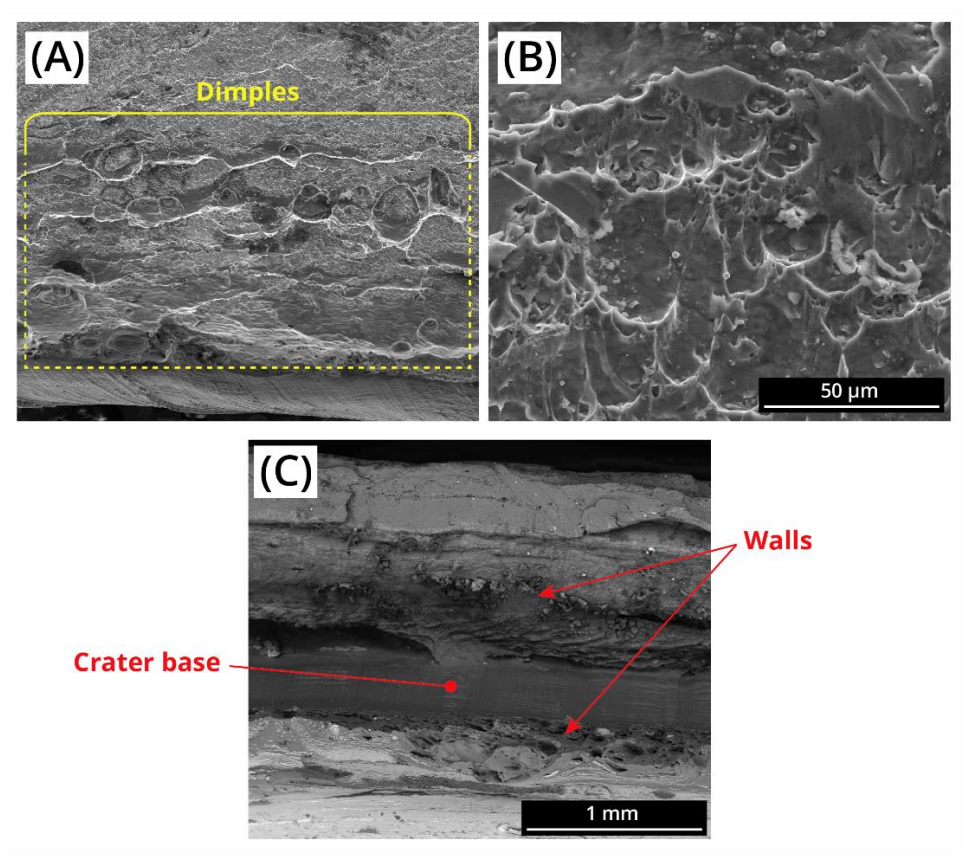


Figure A.15 - SEM images, in secondary mode, of two sections of the top zone of the **IX** sample, Al side, (a) at 200x magnification and (b) at 2000x magnification, and at the bottom zone of the Al side of sample **IX**, 100x magnification (c).

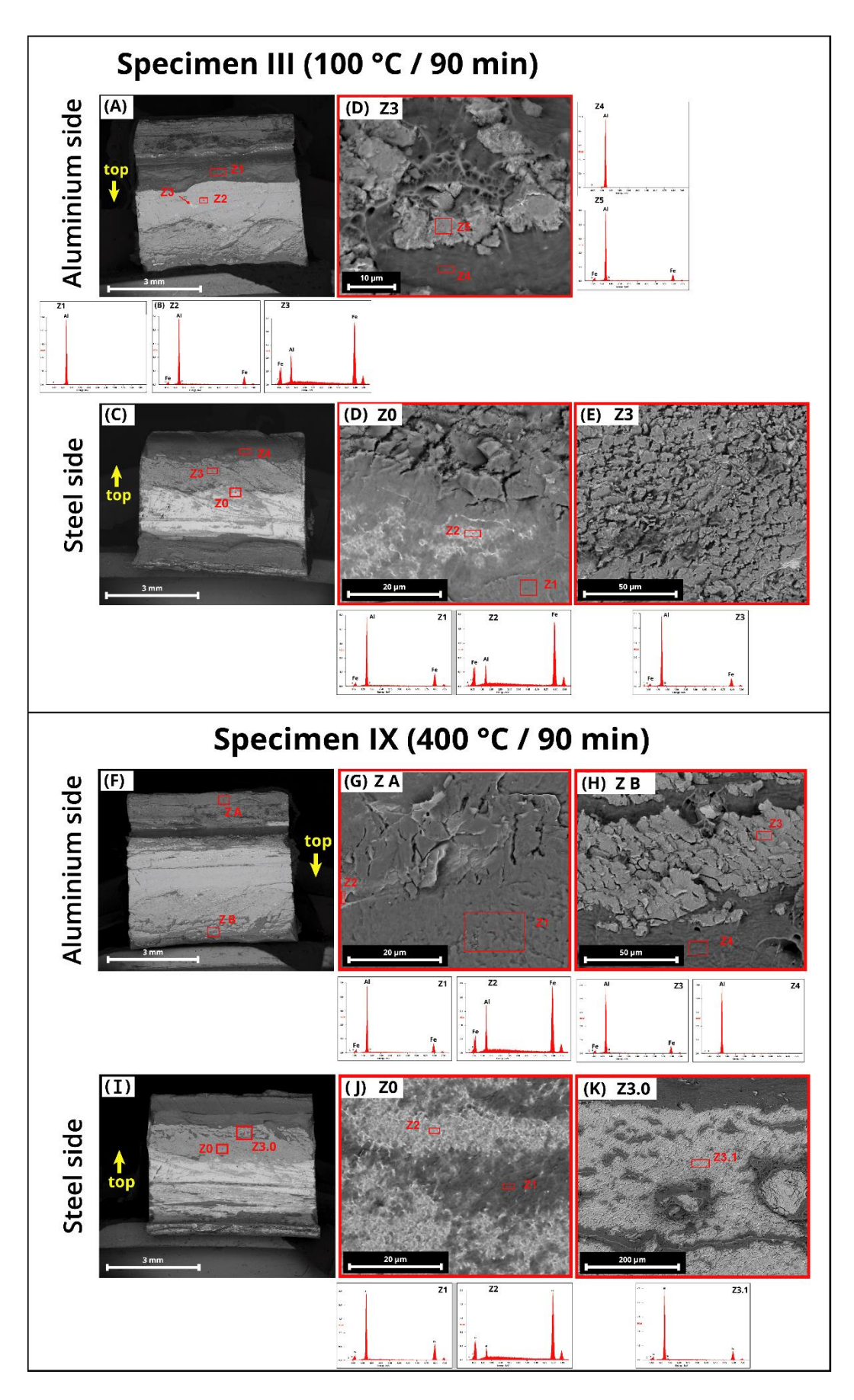


Figure A.16 - SEM imaging, in backscattering mode, and EDS zone analysis of specimens  ${\bf III}$  and  ${\bf IX}$ , for aluminium and steel sides.

#### 4. Conclusions

This study has contributed to a further understanding the influence of temperature on the degradation of dissimilar FSW Al/St joints' degradation, as a result of the IMC layer growth. In more detail, the conclusions of this study are the following:

- Successful welding of St37 and Al1050 with dissimilar thicknesses of 2 mm and 5 mm, respectively, was achieved via FSW achieved with low defect rates. The welded region featured an S-shape geometry with normal and two parallel interface surfaces, facilitating mechanical interlocking and distributing loads in normal and shear stresses within the interface.
- 2. The resulting joint exhibited sound integrity with an average IMC layer thickness ranging from  $4.0 \mu m$  to  $0.8 \mu m$  across the interface, attributed to the novel dissimilar thickness geometry and material flow during FSW processes.
- 3. The most common Fe-Al IMC phase present at the dissimilar joint interface is Fe<sub>2</sub>Al<sub>5</sub>, denoted by an average Al at.% of the IMC layer of 68% to 72%.
- 4. Observations during heat treatments revealed an increase in IMC layer thickness, particularly notable with higher temperatures and longer duration, such as the 90-minute annealing period, which significantly influenced joint integrity.
- 5. Tensile test results indicated a decrease in ultimate failure loads across heat treatment pairs, especially evident at 400°C. Joint strength showed a proportional reduction with increasing IMC layer thickness and vice versa, consistent with literature findings and aligning with predictions for this study.

#### References

- 1. Nonnenmann, T., et al., Feasibility study on hybrid weld-bonding between dissimilar material for automotive industry. International Journal of Adhesion and Adhesives, 2023. **121**: p. 103316.
- 2. Liedl, G., et al., *Joining of aluminum and steel in car body manufacturing*. Physics Procedia, 2011. **12**: p. 150-156.
- 3. Gohoungodji, P., et al., What is stopping the automotive industry from going green? A systematic review of barriers to green innovation in the automotive industry. Journal of Cleaner Production, 2020. 277: p. 123524.
- 4. Zhang, Y., et al., *Review of tools for friction stir welding and processing*. Canadian Metallurgical Quarterly, 2012. **51**(3): p. 250-261.
- 5. Mishra, R.S. and Z. Ma, *Friction stir welding and processing*. Materials science and engineering: R: reports, 2005. **50**(1-2): p. 1-78.
- 6. Chaudhari, R., R. Parekh, and A. Ingle. *Reliability of dissimilar metal joints using fusion welding: A Review.* in *International Conference on Machine Learning, Electrical and Mechanical Engineering (ICMLEME: 2014).*—2014. 2014.
- 7. Munoz, A.C., et al., *Comparison of TIG welded and friction stir welded Al–4.5 Mg–0.26 Sc alloy*. Journal of materials processing technology, 2008. **197**(1-3): p. 337-343.

- 8. Xue, P., B.a. Xiao, and Z. Ma, Effect of interfacial microstructure evolution on mechanical properties and fracture behavior of friction stir-welded Al-Cu joints. Metallurgical and Materials Transactions A, 2015. **46**: p. 3091-3103.
- 9. Hussein, S.A. and A. Hadzley, *Characteristics of aluminum-to-steel joint made by friction stir welding: A review.* Materials Today Communications, 2015. **5**: p. 32-49.
- 10. Prangnell, P., F. Haddadi, and Y. Chen, *Ultrasonic spot welding of aluminium to steel for automotive applications—microstructure and optimisation*. Materials Science and Technology, 2011. **27**(3): p. 617-624.
- 11. Penner, S. and M. Armbrüster, Formation of intermetallic compounds by reactive metal—support interaction: a frequently encountered phenomenon in catalysis. ChemCatChem, 2015. **7**(3): p. 374-392.
- 12. Beygi, R., et al., *Design of friction stir welding for butt joining of aluminum to steel of dissimilar thickness: Heat treatment and fracture behavior.* The International Journal of Advanced Manufacturing Technology, 2021. **112**: p. 1951-1964.
- 13. Wang, T., et al., Evaluation of intermetallic compound layer at aluminum/steel interface joined by friction stir scribe technology. Materials & Design, 2019. **174**: p. 107795.
- 14. Cao, F., et al., *The formation and growth of intermetallic compounds during interdiffusion of Al/Cu bimetals.* Materials Research Express, 2022. **9**(5): p. 056503.

# Appendix B

# Load vs. Extension curves

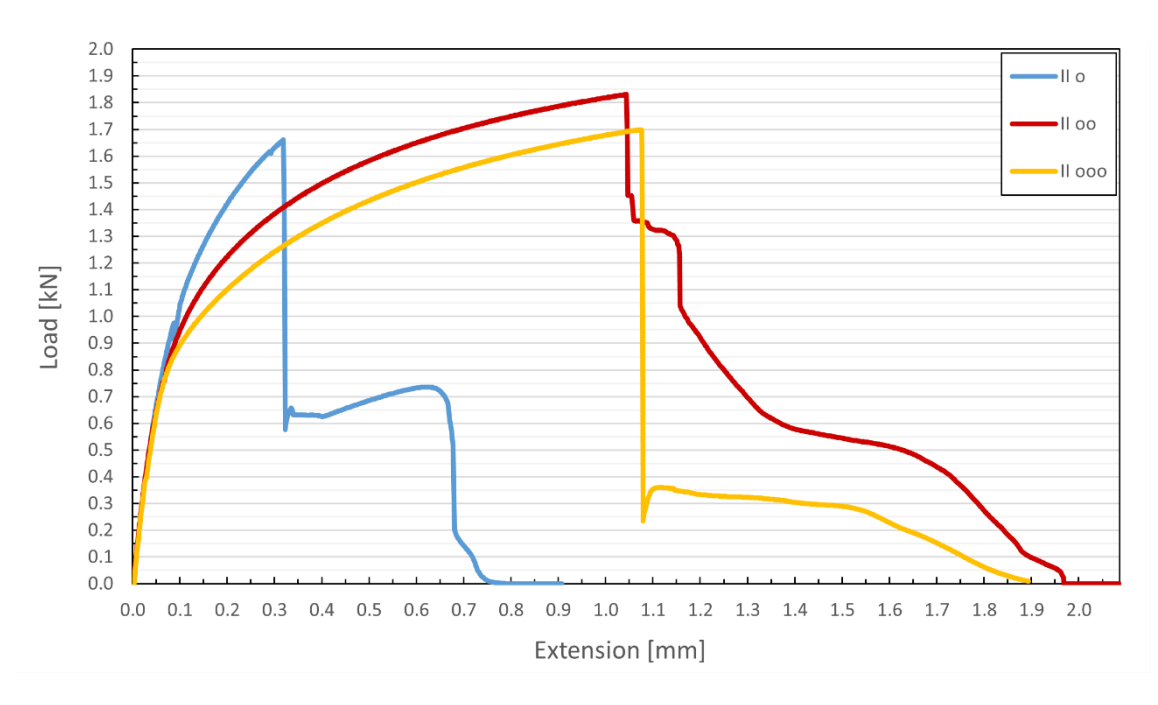


Figure B.1 - Load vs. Extension curve of the  $100 \, ^{\circ}\text{C} \, / \, 60$  min heat treatment specimens.

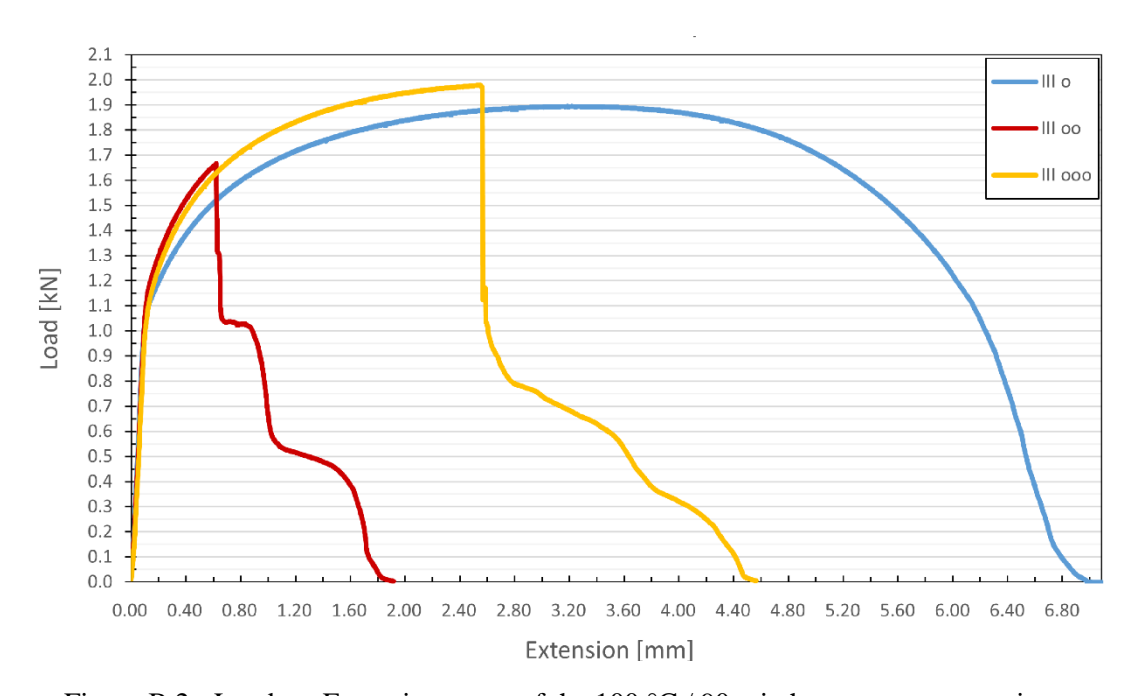


Figure B.2 - Load vs. Extension curve of the 100  $^{\circ}\text{C}$  / 90 min heat treatment specimens.

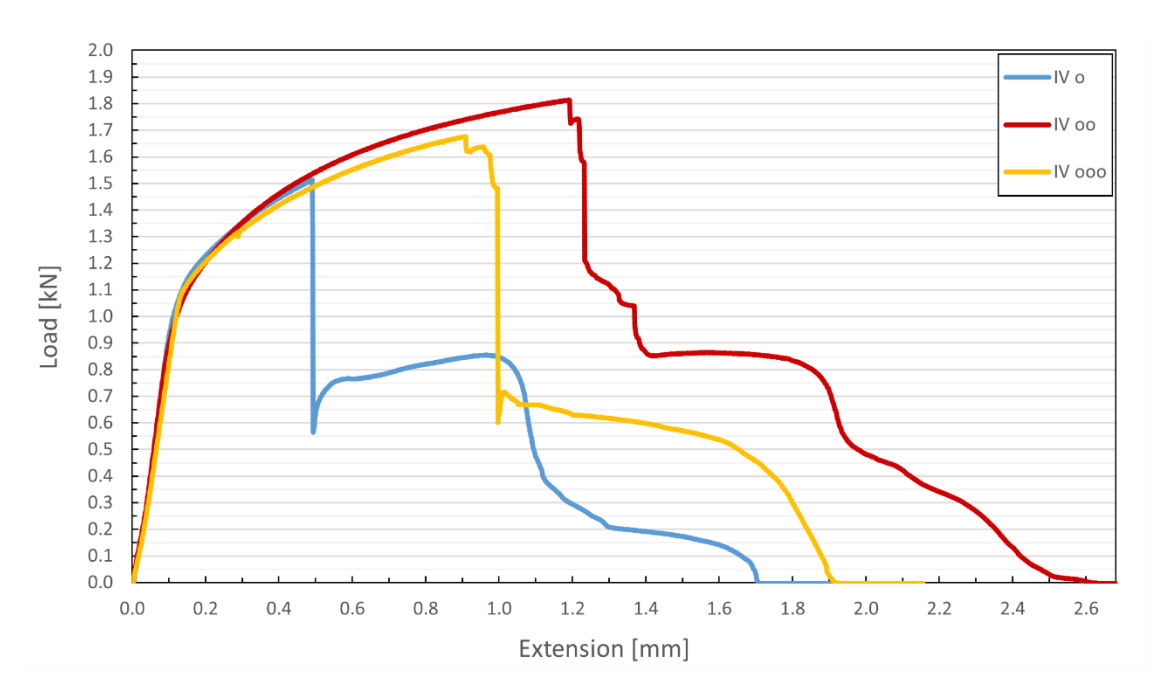


Figure B.3 - Load vs. Extension curve of the 250  $^{\circ}$ C / 30 min heat treatment specimens.

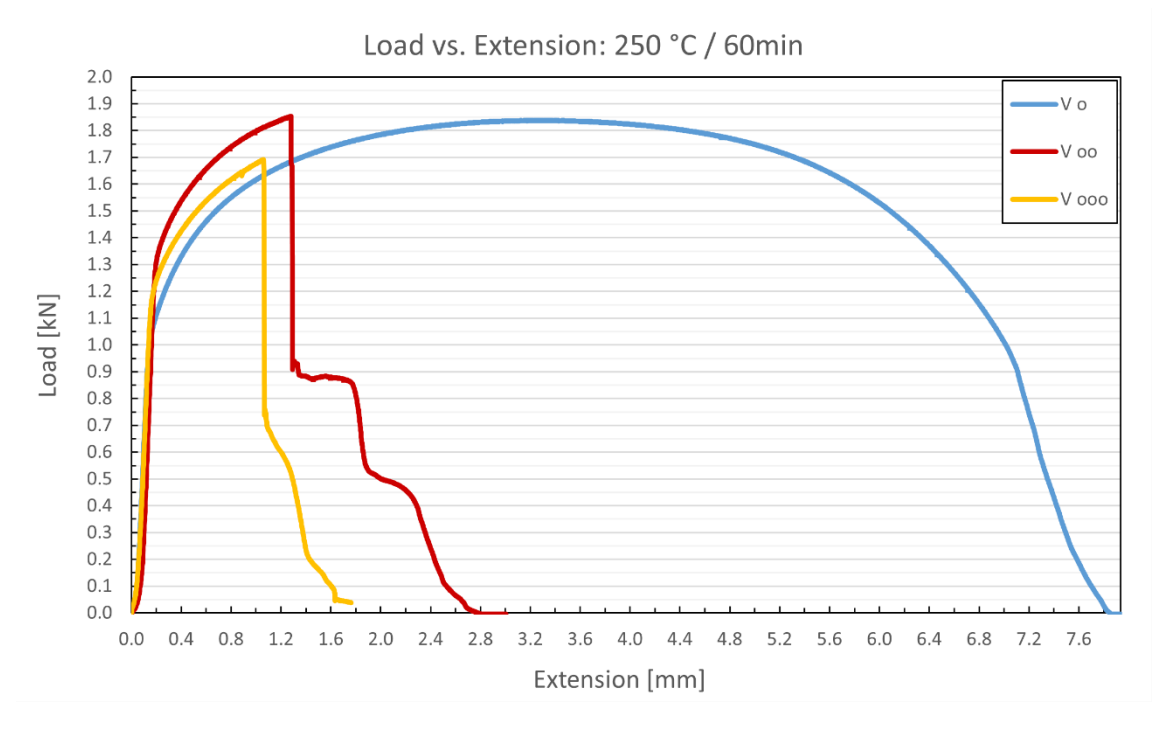


Figure B.4 - Load vs. Extension curve of the 250  $^{\circ}\text{C}$  / 60 min heat treatment specimens.

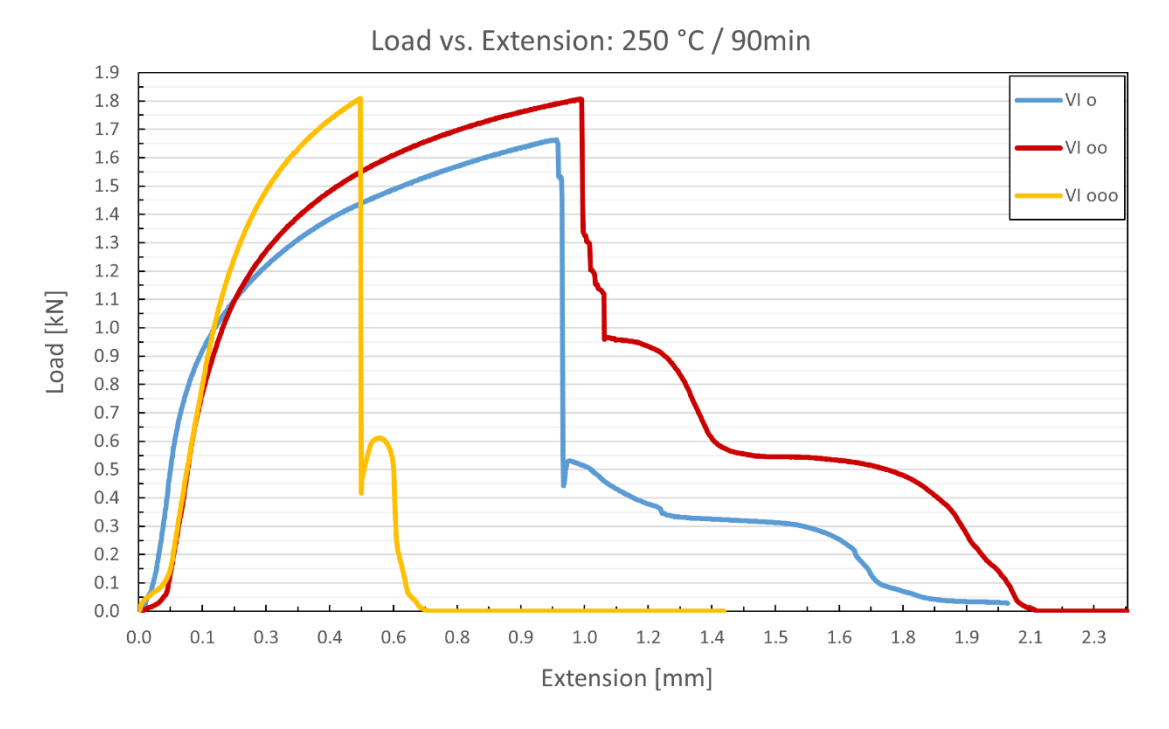


Figure B.5 - Load vs. Extension curve of the 250  $^{\circ}$ C / 90 min heat treatment specimens.

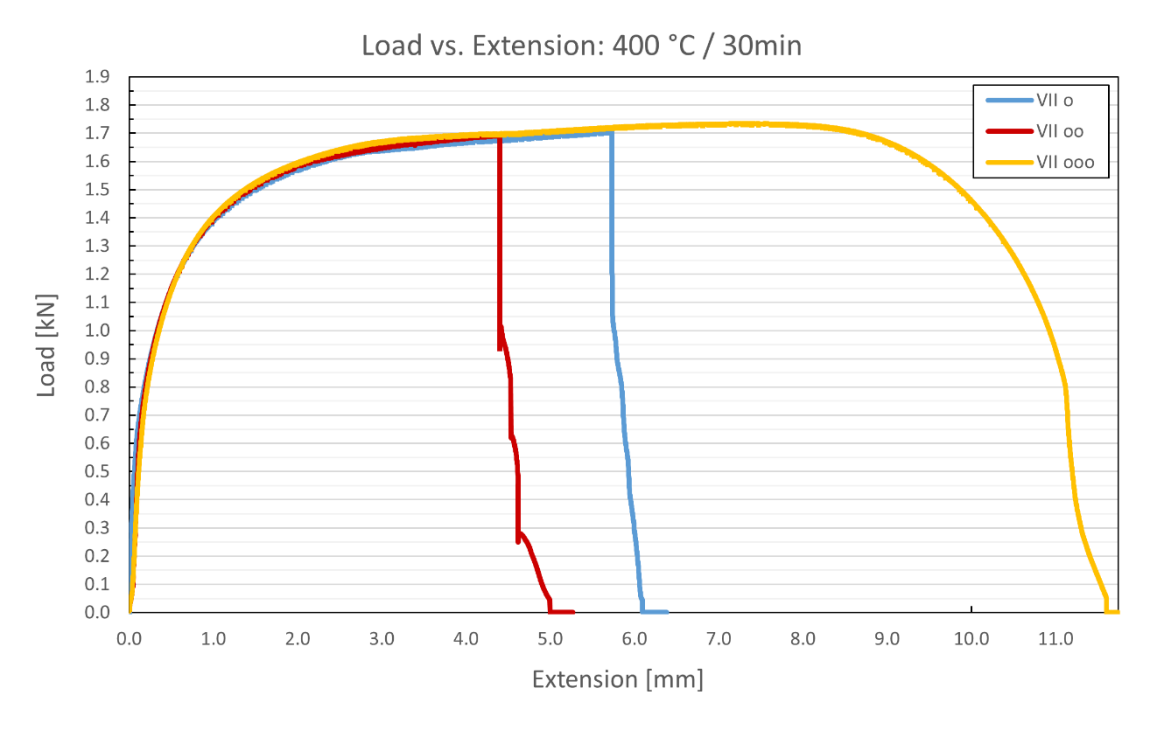


Figure B.6 - Load vs. Extension curve of the  $400\,^{\circ}\text{C}$  /  $30\,\text{min}$  heat treatment specimens.

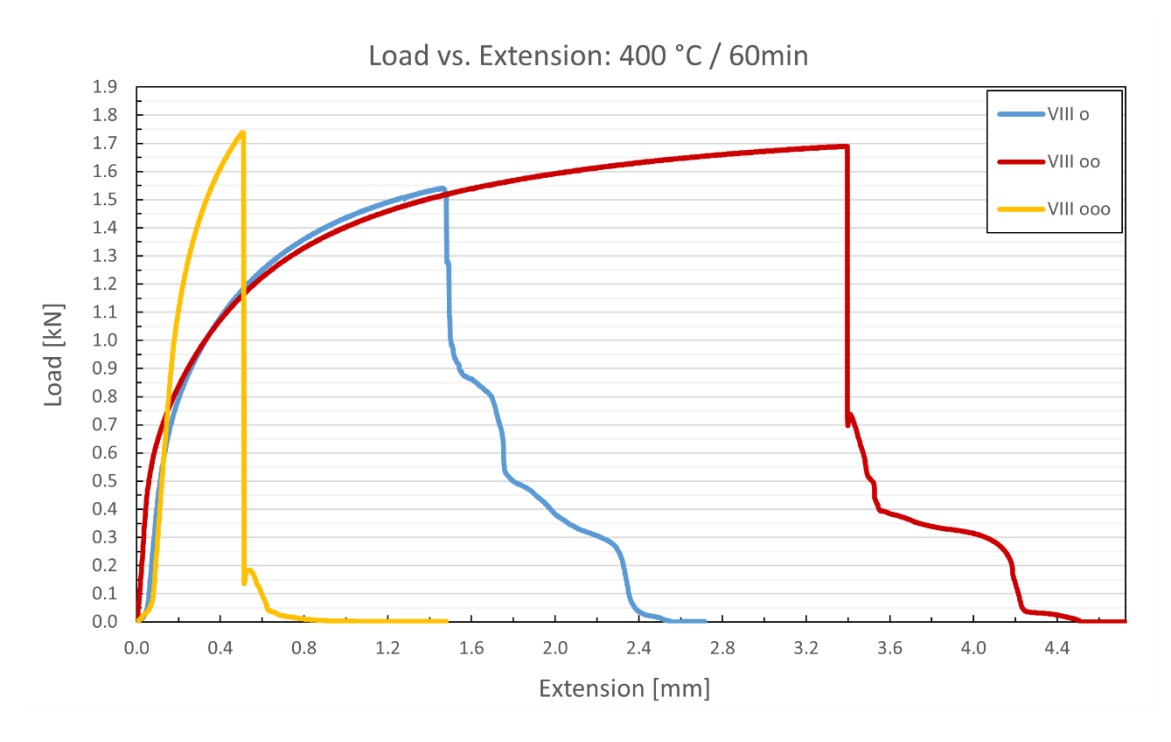


Figure B.7 - Load vs. Extension curve of the  $400\,^{\circ}\text{C}$  /  $60\,\text{min}$  heat treatment specimens.

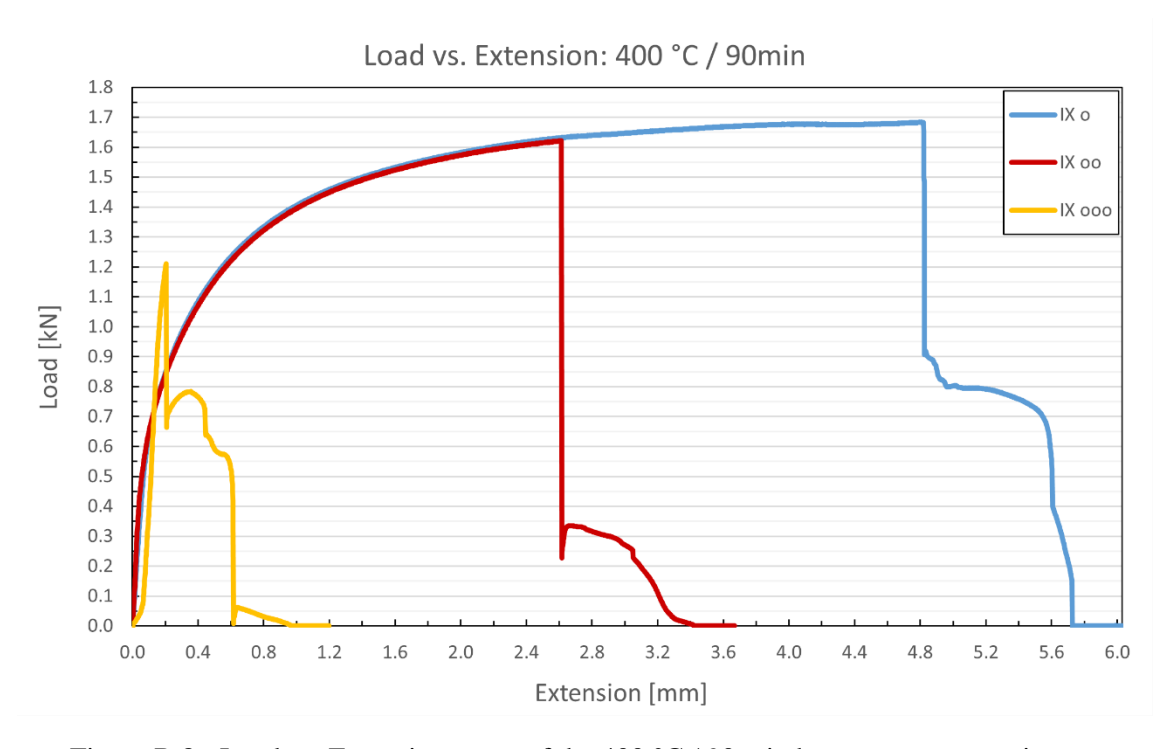


Figure B.8 - Load vs. Extension curve of the 400  $^{\circ}\text{C}$  / 90 min heat treatment specimens.

# Appendix C

# Tensile test video frames

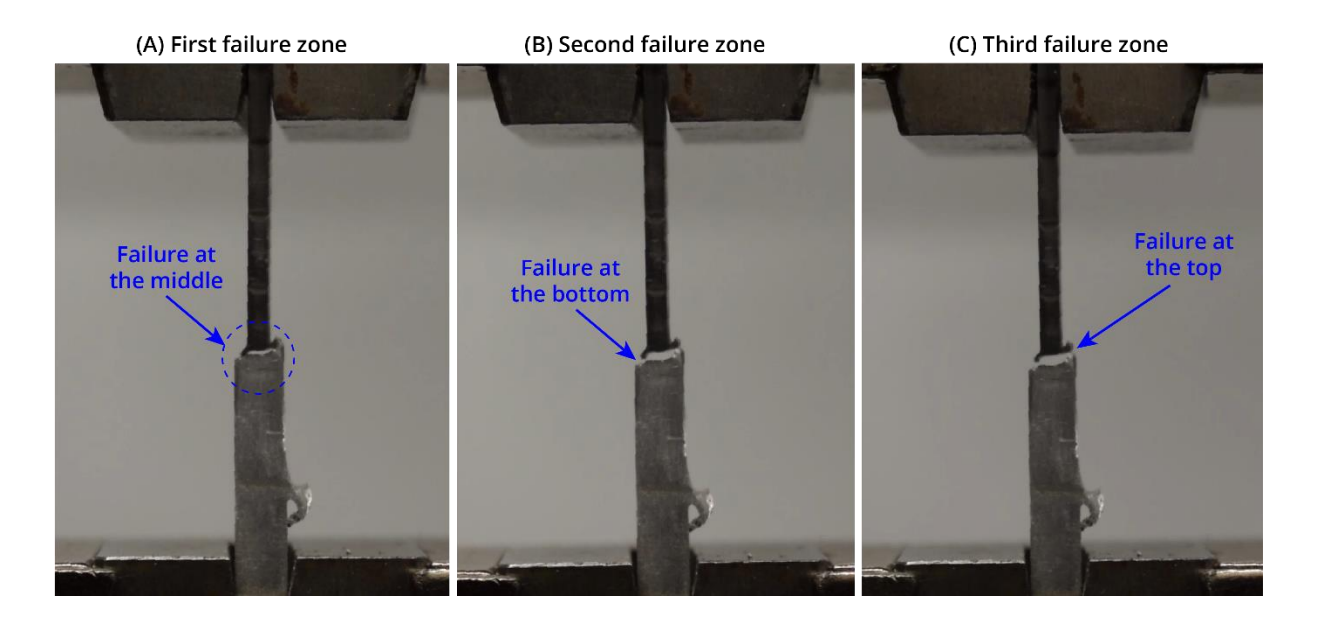


Figure C.1 - Failure instants video frames of the specimen I • • • tensile test.

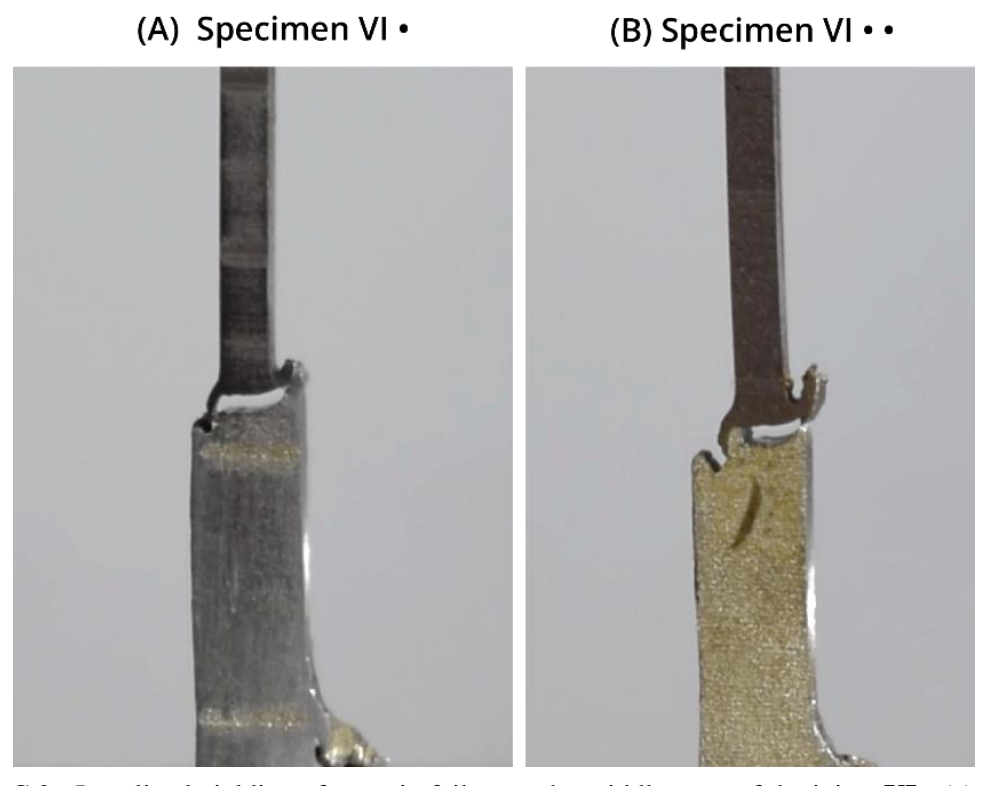


Figure C.2 - Localized yielding after main failure at the middle zone of the joints  $VI \bullet (a)$  and  $VI \bullet \bullet (b)$ .

# (A) Specimen VII • • (B) Specimen VII • •

Figure C.3 - Localized yielding after main failure at the middle zone of the joints  $VII \bullet (a)$  and  $VII \bullet \bullet (b)$ .



Figure C.4 - Localized yielding after main failure at the middle zone of the joints **VIII** • (a) and **VIII** • • (b).

# Appendix D

# Microhardness plots

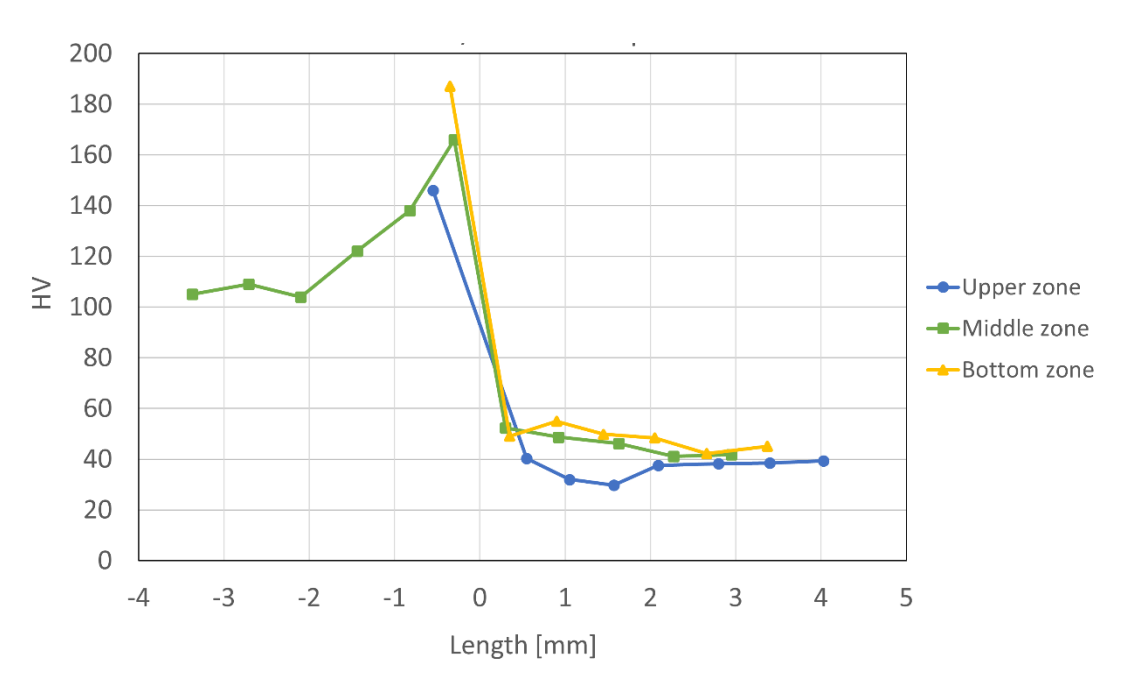


Figure D.1 - Vickers microhardness of sample III ( $100\,^{\circ}\text{C}$  /  $90\,\text{min}$ ) sample along the upper, middle, and bottom measured lines.

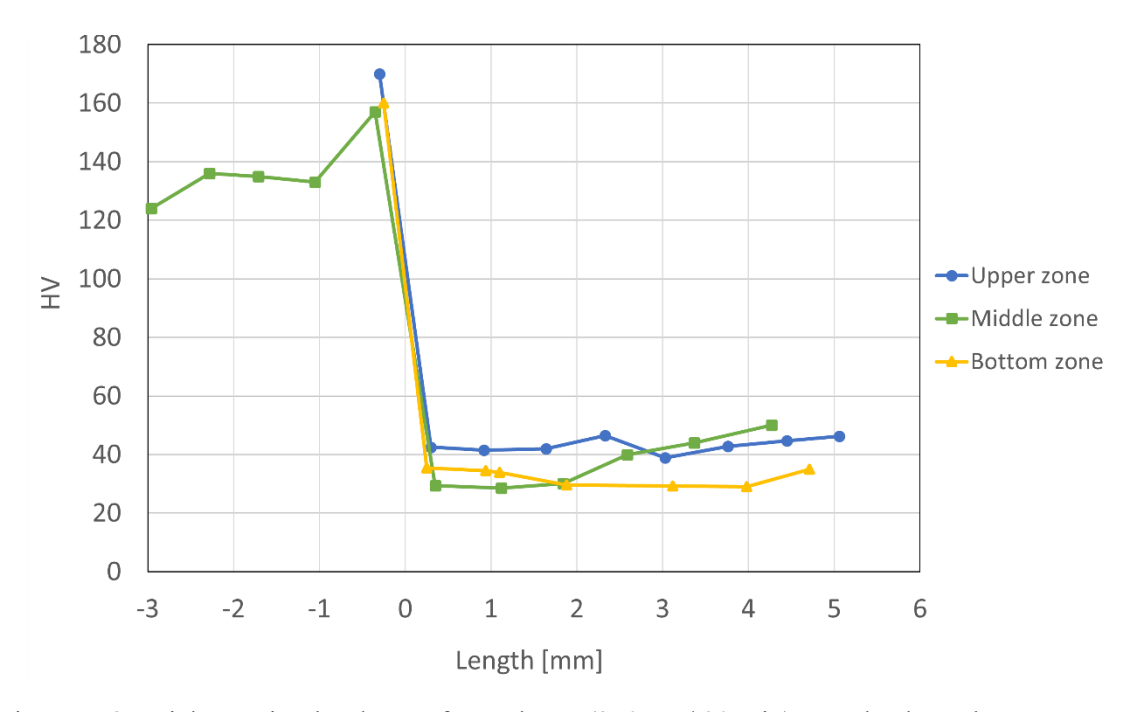


Figure D.2 - Vickers microhardness of sample VI (250  $^{\circ}$ C / 90 min) sample along the upper, middle, and bottom measured lines.

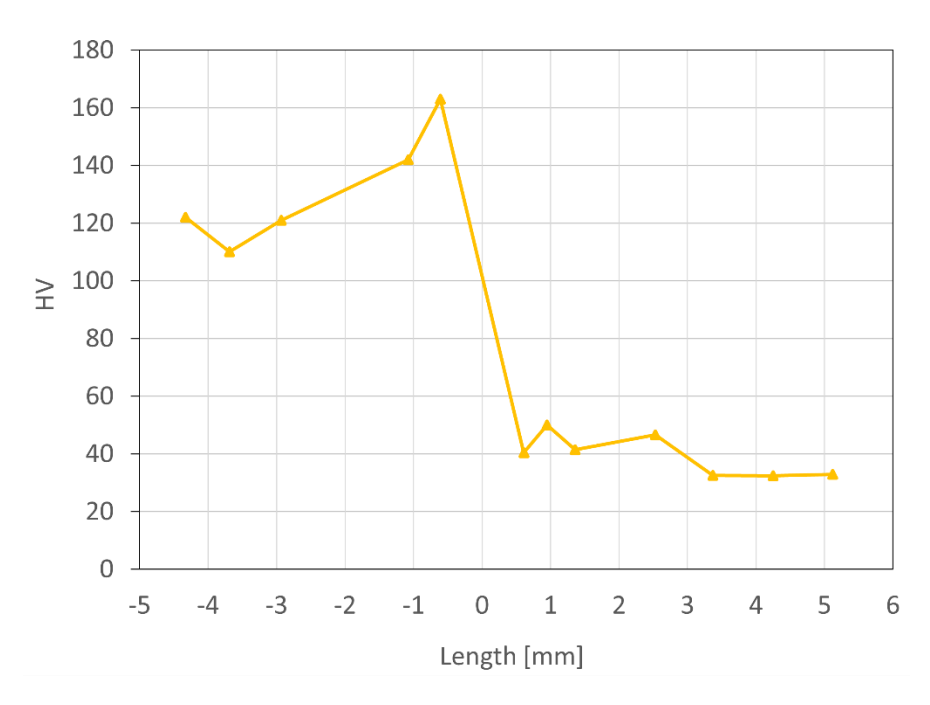


Figure D.3 - Vickers microhardness of sample IX (400  $^{\circ}\text{C}$  / 90 min) sample along the middle measured lines.

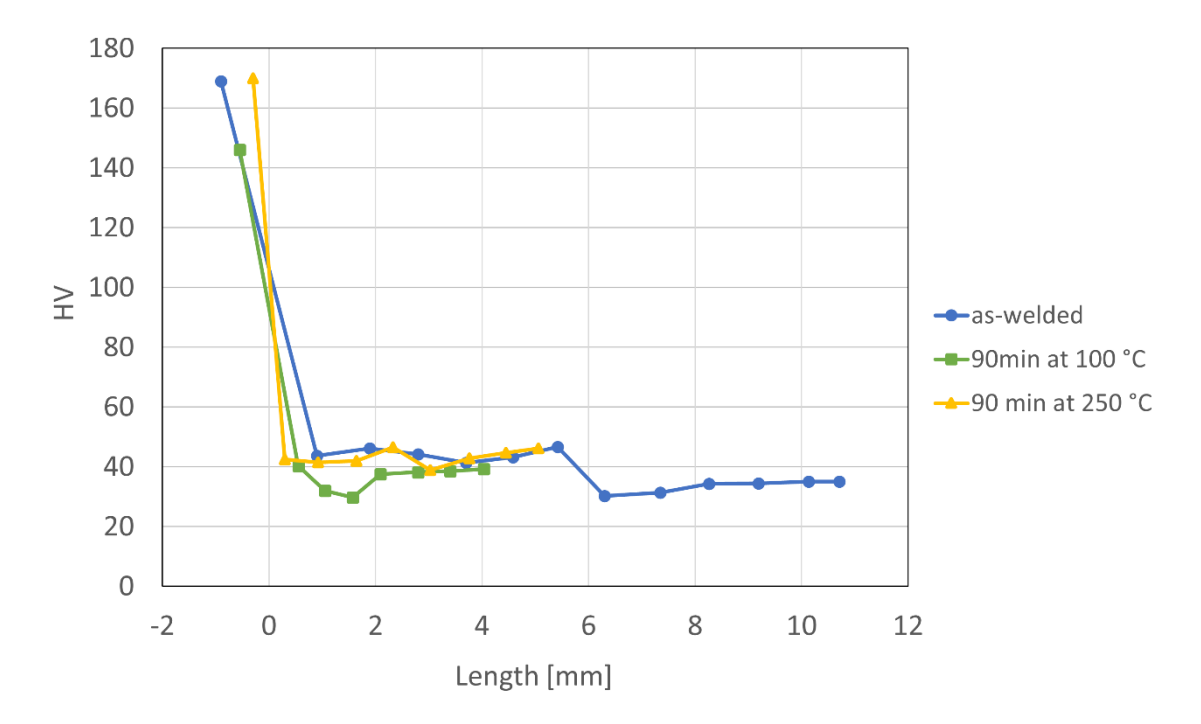


Figure D.4 - Vickers microhardness of the upper zones of the measured samples.

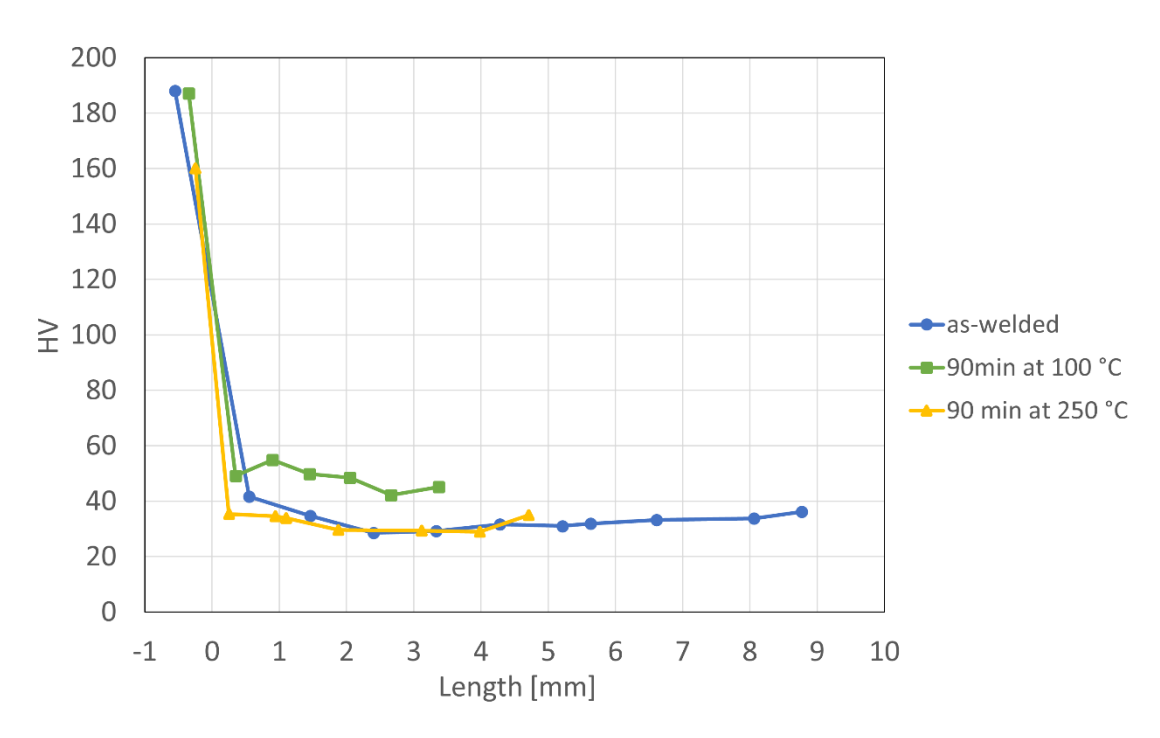


Figure D.5 - Vickers microhardness of the bottom zones of the measured samples.